The Physics of Phase-Noise Mitigation: Signal Generation and Filtering Using Microwave-Photonic Links

by

William Loh
M.S. Electrical Engineering
Massachusetts Institute of Technology, 2009
B.S. Electrical Engineering
University of Michigan, 2007

Submitted to the Department of Electrical Engineering and Computer Science
in partial fulfillment of the requirements for the degree of

Doctor of Philosophy in Electrical Engineering

at the

MASSACHUSETTS INSTITUTE OF TECHNOLOGY

September 2013

©2013 MIT, MMXIII. All rights reserved.
The author hereby grants to MIT permission to reproduce and distribute publicly
paper and electronic copies of this thesis document in whole or in part

Author_____
Department of Electrical Engineering and Computer Science
July 26, 2013

Certified by_____
Paul W. Juodawlkis
Assistant Group Leader, Group 83, MIT Lincoln Laboratory
Thesis Supervisor

Certified by_____
Rajeev J. Ram
Professor of Electrical Engineering
Thesis Co-Supervisor

Accepted by_____
Leslie A. Kolodziejski
Chair, Committee for Graduate Students

The Physics of Phase-Noise Mitigation: Signal Generation and Filtering Using Microwave-Photonic Links

by

William Loh

Submitted to the Department of Electrical Engineering and Computer Science
on July 26, 2013, in partial fulfillment of the requirements for the degree of
Doctor of Philosophy in Electrical Engineering

Abstract

The spectral purity of every oscillator system is limited by noise. This thesis explores the physics and measurements of noise fundamental to oscillators operating in the electrical and optical domains. Our analysis leads to a unified theory of phase noise applicable to perturbations whose characteristics are both white and colored. To minimize phase noise, the oscillator delay length must be made long. This principle motivates us to study a recent class of hybrid optoelectronic oscillators (OEOs) that operate based on concepts of microwave-photonic (MWP) gain. The delay of an OEO is made long (1-15 km) by taking advantage of the low losses afforded by optical fiber. Furthermore, the additional sidemodes are suppressed by a process of super-homogeneous gain exhibited by the MWP link. In this work, we demonstrate an OEO comprising of high-power low-noise slab-coupled optical waveguide (SCOW) components. The use of SCOW technology enables low-noise oscillation without the need for additional external amplification. We also show results of a similar system based on a SCOW coupled optoelectronic oscillator (COEO) configuration whose operation resembles that of a regeneratively modelocked laser. Both oscillators achieve phase noise significantly lower than that of conventional free-running microwave oscillators. Our ultimate goal is the monolithic integration of the OEO onto a single chip of InP. Towards that end, we will show our development of a SCOW distributed feedback laser (DFB) as a replacement to the bulky pump laser currently employed in the OEO.

Thesis Supervisor: Dr. Paul W. Juodawlkis
Title: Assistant Group Leader Group 83

Thesis Supervisor: Rajeev J. Ram
Title: Professor of Electrical Engineering

Acknowledgements

First and foremost, I would like to thank my advisor, Dr. Paul Juodawlkis, for his dedication towards my Ph.D. His extensive knowledge and fantastic guidance have proven to be invaluable for overcoming many of the challenges that I have faced. Perhaps most striking about Paul is his overwhelming supply of enthusiasm, which has made working with him a truly enjoyable experience over all of these years. I am also grateful to my co-advisor, Professor Rajeev Ram, whose advice I have greatly benefitted from, both inside and outside of research. His dedication to student learning combined with his incredible insight over a wide range of topics have made this Ph.D very rewarding. I am also thankful to both my advisors for giving me the opportunity 1) to actively enroll in classes and 2) to define my own areas of research. This has allowed me the freedom to explore the limits of my imagination.

I would like to thank the excellent staff members at MIT Lincoln Laboratory for their help over my graduate career. In particular, I have had the good fortune to learn from my interactions with many of the members of Group 83. Siva Yegnanarayanan acted the role of a third advisor, with whom I enjoyed sharing numerous discussions and ideas. Siva always offered a unique perspective and was always free for a "quick" conversation. Jason Plant was my first point of contact at Lincoln, and I benefitted greatly from his expertise on device fabrication. I am indebted to Jason for his help on the fabrication of DFB lasers. I similarly would like to thank Kevin Ray for his generous help with the DFB laser fabrication and also to thank Doug Oakley for his generous help with the DFB laser growth. Finally, I would like to express my gratitude to Fred O'Donnell for all of his help over the years. I am moved by the willingness of the Group 83 staff members to devote time out of their busy schedules for the benefit of a single graduate student. I should also mention my colleague and fellow graduate student, Kevin Anglin, whose antics and humor kept me company through months of writing. I would like to acknowledge Groups 67, 82, and 86 for their generosity in lending me almost all of the equipment necessary to conduct my research. Needless to say, none of this would be possible without the support of the Lincoln staff.

On the MIT campus side, I would like to thank my peers in the Physical Optics and Electronics Group for always making me feel welcome in the group, even with most of my time spent at Lincoln Laboratory. I also thank my colleagues and mentors in the Integrated Photonics

Intiative (IPI), with whom I've shared many discussions and ideas over the course of my Ph.D. I would like to express my gratitude to Professor Erich Ippen for agreeing to serve as the final committee member for this thesis. I am also grateful to the many officers/residents of the Sidney-Pacific dormitory with whom I've gotten to know from my involvement with the house government.

Last and most important, I am indebted to my parents (Cindy and Hai-Yu) and my brother (Jonathan) for their encouragement throughout my studies. Their loving support is all the motivation I need to face whatever comes next.

Contents

1 Introduction 29

1.1 Oscillator Phase Noise 30

1.1.1 The Importance of Low Phase Noise 32

1.1.2 Applications of Low-Noise Oscillators 33

1.2 Optoelectronic Oscillator Systems 36

1.2.1 The Optoelectronic Oscillator (OEO) 37

1.2.2 Analysis of OEO Operation 39

1.2.3 The Coupled Optoelectronic Oscillator (COEO) 41

1.2.4 RF Oscillator Comparisons 43

1.3 Slab-Coupled Optical Waveguide (SCOW) Gain Medium 46

1.3.1 Slab-Coupled Optical Waveguide Amplifier (SCOWA) 49

1.3.2 Slab-Coupled Optical Waveguide External Cavity Laser (SCOWECL) 51

1.3.3 Slab-Coupled Optical Waveguide Distributed Feedback Laser (SCOW-DFB) 54

1.3.4 Slab-Coupled Optical Waveguide Photodiode (SCOWPD) 56

1.3.5 Comparison Between Optical Device Technology 57

2 Oscillator Phase Noise – White Noise 60

2.1 Oscillator Phase Noise Theories 62

2.1.1 LTI Theories of Oscillator Phase-Noise 62

2.1.2 LTV Theories of Oscillator Phase-Noise 65

2.1.3 Time-Domain Theories of Oscillator Phase-Noise 67

2.2 Unified Theory of Phase Noise 69

2.2.1 Phase-Noise Theory 69

2.2.2 Unification with Laser Theory 75

2.3 Experimental Results of Oscillator Phase-Noise 76

2.3.1 Comparisons to Measurement: Electrical Oscillator 77
2.3.2 Comparisons to Measurement: Optoelectronic Oscillator 82
2.3.3 Discussion 86
2.4 Conclusion 87

3 Oscillator Phase Noise – Flicker Noise 88
3.1 Oscillator Spectrum Perturbed by Noise 90
3.2 Unified Theory of Phase Noise 93
3.2.1 Description of an Oscillator Under Noise Perturbation 93
3.2.2 Flicker Noise in Oscillators 99
3.2.3 Oscillator Phase-Noise Spectrum 101
3.2.4 Modeling Procedure: Oscillator Phase-Noise 105
3.3 Experimental Results of Oscillator Phase-Noise 106
3.3.1 Comparisons to Measurement: Electrical Oscillator 107
3.3.2 Comparisons to Measurement: Optoelectronic Oscillator 118
3.4 Conclusion 123

4 Slab-Coupled Optical Waveguide Optoelectronic Oscillators (SCOW-OEOs) 124
4.1 SCOW-OEO System and Operation 125
4.1.1 SCOW-OEO Threshold Analysis 127
4.1.2 SCOW-OEO System and Environmental Isolation 129
4.2 SCOW-OEO Components and Noise 132
4.2.1 SCOWECL Relative Intensity Noise 132
4.2.2 VC-SCOWPD AM and PM Noise 135
4.2.3 Discovery Semiconductor DSC50S AM and PM Noise 137
4.2.4 Stimulated Brillouin Scattering (SBS) Noise 138
4.3 SCOW-OEO Experimental Measurements 140
4.3.1 SCOW-OEO Phase-Noise Measurements 141
4.3.2 SCOW-OEO RF Spectrum Measurements 150

4.3.3 Discussion 152
4.4 Conclusion 154

5 Super-Homogeneous Gain in Microwave-Photonic Links 155
5.1 Super-Homogeneous Gain 157
5.1.1 Theory of Two-Tone MWP Gain 158
5.1.2 Super-Homogeneous Gain Measurement Results 161
5.1.3 Discussion – Super-Homogeneous Gain 165
5.2 SCOW-OEO Simulation and Experimental Results 166
5.2.1 SCOW-OEO Parameters and Experimental Configuration 166
5.2.2 SCOW-OEO Steady-State Simulation 168
5.2.3 SCOW-OEO Sidemode Simulation and Experimental Results 171
5.3 Nonlinear Filtering Using MWP Links 180
5.3.1 Theory of Two-Tone Gain Over a MWP Link 180
5.3.2 Nulling Behavior Under Amplitude Modulation 185
5.3.3 Nulling Behavior Under Phase Modulation 187
5.4 Experimental Verification of MWP Filtering 188
5.5 Conclusion 198

6 Slab-Coupled Optical Waveguide Coupled Optoelectronic Oscillators (SCOW-COEOs) 199
6.1 SCOW-COEO System and Operation 200
6.1.1 SCOW-COEO Configuration 200
6.1.2 SCOW-COEO Equivalent Circuit 203
6.1.3 Noise Measurements of the SCOWA 204
6.2 SCOW-COEO Measurement Results and Discussion 206
6.2.1 Comparison of SCOW-COEO Systems 207
6.2.2 SCOW-COEO Comparisons: Constant Intracavity Power 212
6.2.3 SCOW-COEO Open-Loop Measurements 217
6.2.4 SCOW-COEO Optimization 222

6.3 Conclusion 227

7 Slab-Coupled Optical Waveguide Distributed Feedback Lasers (SCOW-DFBs) 229

7.1 Design of First Generation SCOW-DFB 231

7.1.1 Overview of DFB Grating Operation 231

7.1.2 Selection of SCOW-DFB Grating Parameters 234

7.1.3 Optimization of SCOW-DFB Structure 236

7.2 SCOW-DFB Fabrication 240

7.2.1 SCOW-DFB Grating Process 240

7.2.2 SCOW-DFB Fabrication Process 244

7.2.3 SCOW-DFB Fabrication AFM Scans 245

7.3 First Generation SCOW-DFB Measurements 246

7.3.1 SCOW-DFB L-I-V 247

7.3.2 SCOW-DFB Optical Spectrum 248

7.3.3 SCOW-DFB Gain 250

7.3.4 SCOW-DFB Mode Profile 251

7.4 Analysis of First Generation SCOW-DFB Deficiencies 253

7.4.1 SCOW-DFB Electrical Simulation 253

7.4.2 SCOW-DFB Post-Fabrication SEM Images 256

7.5 Design of Second Generation SCOW-DFB 259

7.5.1 Second Generation SCOW-DFB Structure 259

7.5.2 Second Generation SCOW-DFB Optical Simulations 261

7.5.3 Second Generation SCOW-DFB Electrical Simulations 262

7.6 Fabrication of Second Generation SCOW-DFB 265

7.7 Conclusion 267

8 Conclusions and Future Work 269

A Appendix: Chapter 2 276

A.1 Derivation of the Phase-Noise Spectrum 276

A.2 Vector Combination of Noise Sources 278

A.3 Effects of Oscillator Non-uniformity 279

B Appendix: Chapter 3 281

B.1 Derivation of the Mixer (IF) Voltage Output 281

List of Figures

1-1 Illustration of oscillator spectrum under ideal conditions (dashed line) and with effects of linewidth broadening (solid line). 31

1-2 (a) Schematic of a system that downconverts an input signal into an intermediate frequency (IF) and (b) illustration of the system output in the presence of an interferer. 31

1-3 Illustration of backreflected Doppler radar signal with the object signature masked by the clutter. 31

1-4 Mixer stage of a swept-tuned spectrum analyzer whose IF output is contaminated by the noise of the internal local oscillator. 31

1-5 Typical configuration of an optoelectronic oscillator comprising a pump laser, Mach-Zehnder (MZ) modulator, fiber delay, and photodiode in the optical cavity. The electrical cavity consists of an RF amplifier, phase shifter, filter, and output coupler. 31

1-6 Typical configuration of a coupled optoelectronic oscillator comprising a Mach-Zehnder (MZ) modulator, fiber delay, optical amplifier, optical coupler, and photodiode as the optical elements. The electrical elements consist of an RF amplifier, RF phase shifter, RF filter, and RF output coupler. 31

1-7 Phase noise comparison between several high-performance oscillator technologies normalized for operation at 10 GHz. For the Wenzel OCXO operating at 10 MHz, ideal frequency multiplication was assumed resulting in a phase noise degradation of 60 dB. 44

1-8 Slab-Coupled Optical Waveguide Cross Section. 48

1-9 Measured packaged SCOWA fiber-to-fiber gain as a function of wavelength and bias current. 49

1-10 Measured packaged SCOWA noise figure as a function of wavelength and bias current. 50

1-11 Packaged SCOWECL (a) schematic and (b) photograph consisting of a double-pass curved-channel (CC) SCOWA, anti-reflection (AR) coated lensed fiber, fiber Bragg grating, and isolator. 51

1-12 Measured packaged SCOWECL output power and efficiency versus bias current. The SCOWECL is operated at 1550 nm wavelength. 52

1-13 Measured packaged SCOWECL normalized spectrum and its associated Voigt fit. The SCOWECL is operated at 4 A bias and 1550 nm wavelength. 53

1-14 Illustration of a grating stack in a DFB laser along with the corresponding intracavity field profile of the lasing mode. $A(z)$ and $B(z)$ denote the forward and backward propagating fields, respectively. 54

1-15 Illustration of intrinsic RIN suppression characteristic of a saturated device. 58

2-1 Block diagram illustration of phase noise in an oscillator consisting of an amplifier, delay line, and filter wrapped in a positive feedback circuit. 31

2-2 Illustration of noise that is added (a) in-phase and (b) out-of-phase to an oscillating signal. The relative phase between noise and signal results in a perturbation to amplitude, phase, or a combination of the two. 65

2-3 Vector-based description of an oscillator's field under noise perturbation. 70

2-4 Circuit schematic of an RF oscillator operating at 2.5 GHz. The system delay is defined by various configurations of RF filters controlling the net group delay per cavity roundtrip. The RF signal is coupled out prior to filtering allowing for direct measurement of the noise added in each roundtrip. 77

2-5 Measured RF oscillator phase-noise and amplitude-noise. (a) Measured phase-noise spectra and theory at -10.0 dBm RF power. (b) Amplitude-noise spectra at -10.0 dBm RF power. (c) Measured phase-noise spectra and theory at -6.5 dBm RF power. (d) Amplitude-noise spectra at -6.5 dBm RF power. The RF oscillator of Fig. 2-4 was tested with three filter configurations including 1) a tunable filter, 2) a tunable filter + 5.5 m delay, and 3) a fixed filter. The various filter configurations change the effective roundtrip delay through the associated resonances of the filters. 78

2-6 Measured and theoretical power dependence of oscillator phase-noise. 80

2-7 Measured RF amplifier small-signal gain and noise figure as a function of bias voltage. 82

2-8 Configuration of an optoelectronic oscillator operating at 3.0 GHz. Microwave-photonic (MWP) gain is achieved by the combination of a high-power, low-noise slab-coupled optical waveguide external cavity laser (SCOWECL), Mach-Zehnder modulator (MZ Modulator) and photodiode. 83

2-9 RF spectrum of the OEO corresponding to Fig. 2-8 when the laser is operated under mode-hopping conditions. The spectrum for normal operation is also provided. 85

2-10 Phase-noise of the OEO corresponding to Fig. 2-8 operated under laser mode-hopping conditions. The white injected noise dominates resulting in a Lorentzian phase-noise spectrum.....86

3-1 Measured phase noise of a 2.5 GHz fixed-filter oscillator as a function of RF output power. The system oscillates from gain supplied by Amplifier 1. 90

3-2 Measured phase noise of a 2.5 GHz fixed-filter oscillator as a function of RF output power. The system oscillates from gain supplied by Amplifier 2. 91

3-3 Measured phase noise of a 2.5 GHz fixed-filter oscillator as a function of RF output power. The system oscillates from gain supplied by Amplifier 3. 91

3-4 Illustration of the total noise power that results from a combination of both flicker and white noise. Since flicker noise is proportional to the signal power, a change in the signal level causes the intercept of flicker and white noise to shift (a). Thus, the spectrum of the total noise becomes dependent on the signal power (b). 92

3-5 Vector-based diagram of oscillator field under noise perturbation. 94

3-6 Generic system diagram employed for three RF oscillators comprising different types of RF amplifiers. The system delay is defined by various configurations of RF filters controlling the net group delay per cavity roundtrip. The RF signal is coupled out prior to filtering allowing for direct measurement of the noise added in each roundtrip.....107

3-7 Measured (solid lines) and theoretical (solid circles) RF oscillator phase-noise for three different types of amplifiers. (a) Phase noise for Amplifier 1 at 9.12 dBm RF power. (b) Phase noise for Amplifier 1 at 11.17 dBm RF power. (c) Phase noise for Amplifier 2 at 7.27 dBm RF power. (d) Phase noise for Amplifier 2 at 10.26 dBm RF power. (e) Phase noise for Amplifier 3 at 3.85 dBm RF power. (f) Phase noise for Amplifier 3 at 6.28 dBm RF power. The RF oscillator of Fig. 3-6 was tested with three filter configurations including 1) a tunable filter, 2) a tunable filter + 5.5 m delay, and 3) a fixed filter. The Lorentzian phase noise predictions (dashed line) are also shown.....108

3-8 Measured normalized phase noise at 100 Hz offset frequency as a function of the normalized delay for Amplifier 1 (12.0 V), Amplifier 2 (7.2 V), and Amplifier 3 (13.5 V). The phase noise is plotted for the tunable filter, tunable filter + 5.5 m, and fixed filter configurations, normalized to the tunable filter case. The delay is similarly normalized to the delay of the tunable filter. The ideal $1/T^2$ dependency of phase noise on delay (dashed line) is also provided.....110

3-9 Diagram of the system used to measure the residual phase-noise added by an RF amplifier. 112

3-10 Measured phase-noise (solid line) with asymptotic fits (dashed line) for three different types of RF amplifiers. (a) Amplifier 1 phase noise with 9.12 dBm output RF power. (b) Amplifier 1 phase noise with 11.17 dBm output RF power. (c) Amplifier 2 phase noise with 7.27 dBm output RF power. (d) Amplifier 2 phase noise with 10.26 dBm output RF power. (e) Amplifier 3 phase noise with 3.85 dBm output RF power. (f) Amplifier 3 phase noise with 6.28 dBm output RF power. The phase-noise slope is also indicated for each case. 114

3-11 Configuration of an optoelectronic oscillator (OEO) operating at 3.0 GHz. Microwave-photonic (MWP) gain is achieved by the high-power, low-noise slab-coupled optical waveguide external cavity laser (SCOWECL), Mach-Zehnder modulator (MZ Modulator) and photodiode. 118

3-12 Measured (solid line) and theoretical phase noise (solid circles) of an OEO corresponding to the configuration of Fig. 3-11. The SSA measurement noise floor (dash-dot line) and Lorentzian theory (dashed line) are also provided. 120

3-13 Schematic of a system that measures the residual phase-noise of an OEO. The system is similar to that of Fig. 3-9 but measures the phase noise of the combined amplifier (MWP link + RF amplifier). 121

3-14 Measured residual phase-noise of an OEO system consisting of a MWP link + RF amplifier. In addition to the OEO residual noise (solid line), the asymptotic fit (dashed line) and measurement noise floor (dash-dot line) are also provided. 122

4-1 Schematic of a 1.5 km cavity length SCOW-OEO system that oscillates due to MWP gain supplied by the SCOWECL, Mach-Zehnder (MZ) modulator, and VC-SCOWPD. Oscillation was achieved at 3 GHz without the use of RF amplification. 126

4-2 Simulation of an OEO's small-signal net power gain (gain – loss) as a function of photocurrent for V_π between 1.5 V and 5.0 V. The threshold condition is determined when the net gain becomes greater than 0 dB (dashed line).....128

4-3 SCOW-OEO system resting on an optical table and employing passive vibration control. Rubber blocks are used to isolate the SCOWECL, VC-SCOWPD, and passive optical fiber from environmental perturbations.....130

4-4 SCOW-OEO isolation box for temperature and environmental stabilization of a 1.5-km fiber spool. This box is also shared by many other passive optical and RF cavity elements.....130

4-5 Fiber and electrical cable routing assembly for SCOW-OEO system. The front panel of the isolation box provides the connections between the active and passive components of the OEO. 131

4-6 Measured RIN of a SCOWECL (solid squares) and commercial ECL (open circles) at low-frequencies (10 Hz – 2 MHz) with the corresponding shot-noise floor indicated (solid line). The reported RIN of a Lightwave Electronics Nd:YAG laser (dashed line) is also provided for comparison.....133

4-7 Measured RIN of a SCOWECL (solid squares) and commercial ECL (open circles) at high-frequencies (10 Hz – 10 GHz) with the corresponding shot-noise floor indicated (solid line). The RIN of a Lightwave Electronics Nd:YAG laser (dashed line), which is assumed to be shot-noise limited at high frequencies, is also provided for comparison. 134

4-8 Measured dependence of the VC-SCOWPD phase (solid squares) and amplitude (open circles) on DC photocurrent at 3 GHz operation and -3.5 V DC bias. 136

4-9 Measured dependence of the DSC50S phase (solid squares) and amplitude (open circles) on DC photocurrent for operation at 3 GHz and -9.0 V DC bias. 137

4-10 Diagram of the measurement technique used to determine transmitted and backreflected signals from a spool of optical fiber. The variable optical attenuator (VOA) is used for control over the SCOWECL power. 138

4-11 Measured backscatter relative to the signal input for various fiber types and lengths. Input powers between 0.67 mW and 67 mW were used in this measurement. 139

4-12 Measured phase noise of a 3 GHz SCOW-OEO operating at 27.3 mA and using 1.5-km delay. The phase modulation peaks at 60 kHz and 120 kHz can be observed, while the sidemodes at 135 kHz are below the measurement noise floor (dashed line). 141

4-13 Measured phase noise of a 3 GHz SCOW-OEO operating at 35 mA and using 1.5 km delay. Both the phase modulation peaks at 60 kHz and 120 kHz and the sidemodes at 135 kHz harmonics can be observed. The SSA noise floor (dashed line) is also provided. 142

4-14 Measured phase noise of a 3-GHz SCOW-OEO operating without the use of phase modulation. No sidemodes are visible above the measurement noise floor (dashed line) in the spectrum. 144

4-15 Measured phase noise of a 3-GHz SCOW-OEO operating with the use of RF amplification. The phase modulation and sidemode spurs are noticeably visible in the spectrum. The measurement noise floor (dashed line) is also provided. 145

4-16 Measured 3-GHz SCOW-OEO phase-noise for two configurations: one comprising a VC-SCOWPD and another comprising a DSC50S + low-noise RF amplifier. Cross-correlation averaging (1000x) was employed to reduce the noise-floor (dashed line) of the measurement system.....147

4-17 Measured 3-GHz SCOW-OEO phase-noise comprising an intracavity Covega semiconductor optical amplifier. Cross-correlation averaging (10x) was employed to reduce the noise-floor (dashed line) of the measurement system. 149

4-18 Measured 3-GHz SCOW-OEO RF spectrum with/without RF amplification and phase modulation. The frequency ranged tested was +/- 2.5 kHz centered around the carrier with a resolution bandwidth of 100 Hz.....151

4-19 Measured 3-GHz SCOW-OEO RF spectrum with/without RF amplification. The frequency ranged tested was +/- 175 kHz centered around the carrier with a resolution bandwidth of 3 kHz.....151

5-1 Microwave-Photonic (MWP) amplification of V_{in} by signal transmission over an intensity modulated direct detection (IMDD) optical link.....155

5-2 Illustration of homogeneous, inhomogeneous, and superhomogeneous gain saturation for two input tones (one small, one large). 156

5-3 Illustration of the two-tone interaction between a mainmode and a sidemode of an OEO. The amplitudes of the tones v_1, v_2, v_3 and their corresponding frequencies $\omega_1, \omega_2, \omega_3$ are also indicated. 159

5-4 Simulated (solid line) and experimentally measured (solid squares/triangles) voltage gain for two tones amplified over an IMDD link. The gain is normalized to a peak value of 1 and plotted versus the voltage of the larger signal.....162

5-5 Experimental setup for measuring the MWP gain over an IMDD link. Here, the noise acts as the small tone and the synthesizer acts as the large tone. 163

5-6 Illustration of Agilent E8241A synthesizer spurs at harmonic multiples of 30 MHz. The synthesizer power was set to 24 dBm for this measurement. 164

5-7 Configuration of the SCOW-OEO comprising a high-power, low-noise SCOWECL pump laser and a high-current variable confinement (VC)-SCOW photodiode. 167

5-8 Simulation of SCOW-OEO RF power versus DC photocurrent using the parameters of Table 5.1. 169

5-9 Simulation of SCOW-OEO RF power gain versus DC photocurrent using the parameters of Table 5.1 170

5-10 Simulation of SCOW-OEO SMSR versus DC photocurrent using the parameters of Table 5.1. 171

5-11 Measured SCOW-OEO amplitude-noise spectrum with estimated sidemode spur levels indicated. 173

5-12 Measured SCOW-OEO amplitude-noise spectrum under varying optical attenuation (4.8 dB – 2.3 dB). 175

5-13 Measured SCOW-OEO amplitude-noise spectrum under varying optical attenuation (1.8 dB – 0.3 dB). 176

5-14 Measured SCOW-OEO phase-noise spectrum for 4.3 dB (solid line) and 0.8 dB (dashed line) optical attenuation. 178

5-15 Measured SCOW-OEO phase-noise spectrum for 0.3 dB optical attenuation. 179

5-16 Diagram of two input tones, one large tone at ω_1 and one small tone at ω_2, generating an intermodulation output at ω_3 181

5-17 Measured and simulated values of the normalized voltage gain magnitudes corresponding to the larger signal, smaller signal, and intermodulation spur for $0 < \pi v_1 / V_\pi < 10$. The input power of the smaller tone was -26.6 dBm, while the photocurrent was maintained near 4 mA over the course of the measurement. 182

5-18 Measured and simulated values of the normalized voltage gain magnitudes corresponding to the larger signal, smaller signal, and intermodulation spur for $3.0 < \pi v_1 / V_\pi < 4.6$. The input power of the smaller tone was -26.6 dBm, while the photocurrent was maintained near 4 mA over the course of the measurement. 183

5-19 Diagram of the setup used to measure the gain of the larger signal, smaller signal, and intermodulation spur transmitted over a MWP link. The 1 GHz synthesizer serves as the larger input tone, while the 1 GHz + Δf synthesizer serves as the smaller input tone. The MWP link consists of a distributed feedback (DFB) laser, optical isolators, polarization controller, Mach-Zehnder (MZ) modulator, and photodiode. 184

5-20 MWP link operation under small-signal frequency modulation of a larger tone in the presence of a secondary tone. The total modulator input corresponding to P_{large} = 19.9 dBm and P_{small} = -26.3 dBm is provided for reference. A comparison of the MWP outputs for P_{large} ranging from 19.8 dBm to 20.0 dBm is also shown. At P_{large} = 19.9 dBm, the suppression of the larger tone is at its maximum. 189

5-21 MWP link operation under small-signal amplitude modulation of a larger tone in the presence of a secondary tone. The total modulator input corresponding to P_{large} = 19.9 dBm and P_{small} = -26.3 dBm is provided for reference. A comparison of the MWP outputs for P_{large} ranging from 19.8 dBm to 20.0 dBm is also shown. At P_{large} = 19.9 dBm, the suppression of the larger tone is at its maximum. 190

5-22 MWP link operation under large-signal frequency modulation (FM) of an RF tone. The modulator RF input is provided corresponding to an applied RF power of P_{large} = 19.9 dBm. The MWP link input and output when the FM modulation is turned off is also provided for reference. 191

5-23 MWP link operation under large-signal amplitude modulation (AM) of an RF tone. The modulator RF input is provided corresponding to an applied RF power of P_{large} = 19.9 dBm. The MWP link input and output when the AM modulation is turned off is also provided for reference. 192

5-24 Phase-noise suppression of a 1-GHz larger signal (P_{large} = 19.9 dBm) in the presence of a smaller signal (P_{small} = -61.6 dBm) spaced 3.5 Hz away. The smaller signal normally hidden underneath the phase noise of the larger tone is uncovered after transmission over the MWP link. The noise floor of the measurement is provided for reference. 193

5-25 Phase-noise suppression of a 1-GHz larger signal (P_{large} = 19.9 dBm) in the presence of a 10-Hz amplitude-modulated smaller signal (P_{small} = -76.6 dBm) spaced 35 Hz away. The smaller signal normally hidden underneath the phase noise of the larger tone is uncovered after transmission over the MWP link. The noise floor of the measurement is provided for reference. 195

5-26 Suppression of a 1-GHz larger signal (P_{large} = 19.9 dBm) in the presence of a smaller signal (P_{small} = -76.6 dBm) spaced 300 kHz away. The noise floor of the measurement is provided for reference. 196

5-27 Output behavior for two RF tones transmitted over a MWP link. The larger tone is applied at 1 GHz with a RF power fixed at 19.9 dBm, while the smaller tone is applied at 1 GHz + 30 kHz with its power varied between -29.6 dBm and 6.4 dBm. 197

6-1 Schematic of the RF amplifier-free SCOW-COEO configuration exhibiting a total delay of ~310 m. 201

6-2 Equivalent circuit of the SCOW-COEO in Fig. 6-1 where the optical cavity has been replaced by an equivalent filter with delay T and net gain G. 203

6-3 Relative intensity noise of a SCOWECL and a commercial SECL for three cases of operation: unamplified, amplified by a SCOWA, and amplified by a commercial EDFA. The shot-noise floor (dashed line) corresponding to 7 mA photocurrent is also provided.....205

6-4 Measured phase-noise of a VC-SCOWPD SCOW-COEO system (blue dashed-line) and of a DSC50S + RF amplifier SCOW-COEO system (red line). The phase-noise floor (black dashed line) is also provided. 207

6-5 Measured normalized RF spectrum of a VC-SCOWPD SCOW-COEO system (blue dashed-line) and of a DSC50S + RF amplifier SCOW-COEO system (red line). The spectrum was centered at 10 GHz with a corresponding resolution bandwidth of 100 kHz.....209

6-6 Comparison of the SCOW-COEO optical pulses with and without 60 m DCF compression for (a) the VC-SCOWPD system and (b) the DSC50S + RF Amp system. 210

6-7 Comparison of the SCOW-COEO optical spectra with and without 60 m DCF compression for (a) the VC-SCOWPD system and (b) the DSC50S + RF Amp system. 211

6-8 Measured phase-noise of a DSC50S + RF amplifier SCOW-COEO system (red line) using a 90:10 coupler (a) without cross-correlation averaging and (b) with 1000 cross-correlation averaging. The measured phase-noise of the VC-SCOWPD system (80:20 coupler) is also shown for comparison (blue dashed-line). The measurement noise-floor is indicated by the black dashed-line. 213

6-9 Measured phase-noise of a 90:10 output coupler DSC50S + RF amplifier SCOW-COEO system with varying intracavity optical power. The intracavity power was varied across two measurement trials (Trial 1: 7-11 dBm and Trial 2: 16-20 dBm). 215

6-10 Measured phase-noise of a 90:10 output coupler DSC50S + RF amplifier SCOW-COEO system at 2 kHz offset frequency as a function of intracavity power. The intracavity power was varied across two measurement trials (Trial 1: 7-11 dBm and Trial 2: 16-20 dBm). 216

6-11 Schematic of the system used to probe the S21 response of the SCOW-COEO's optical cavity. The operating conditions of the individual components are maintained at their levels during COEO operation. 218

6-12 Measured open-loop phase noise of a 90:10 output coupler DSC50S + RF amplifier SCOW-COEO with varying intracavity optical power. Also provided is the noise of the reference RF source (black line) used as the probe for this measurement.....219

6-13 Measured open-loop amplitude noise of a 90:10 output coupler DSC50S + RF amplifier SCOW-COEO with varying intracavity optical power. The noise of the reference RF source (black line) and measurement noise-floor (gray dashed-line) are also provided.....220

6-14 Measured phase-noise of a VC-SCOWPD SCOW-COEO system exhibiting a resonance near 30 kHz. The phase-noise floor (black dashed-line) is also provided. 221

6-15 DSC50S + RF amplifier SCOW-COEO phase-noise comparison for delays lengths of (a) 21 m and 60 m and (b) 81 m and 60 m delay in the optoelectronic loop. The measurement noise-floor (black dashed-line) is also provided.....223

6-16 Measured DSC50S + RF amplifier SCOW-COEO phase-noise as a function of the coupling ratio between optical and optoelectronic cavities. The measurement noise-floor (black dashed-line) is also provided. 224

6-17 Measured DSC50S + RF amplifier SCOW-COEO phase-noise for a coupling ratio of 99-1 between optical and optoelectronic cavities. The measurement noise-floor (black dashed-line) is also provided. 225

6-18 Measured DSC50S + RF amplifier SCOW-COEO phase-noise for a delay of 500 m in the optical loop and a delay of 60 m in the optoelectronic loop. The measurement noise-floor (black dashed-line) is also provided. 226

7-1 Grating structure from the perspective of the light beam consisting of two alternating refractive indices. The reflections from each period add constructively. 231

7-2 Grating analysis in spatial domain and spatial frequency domain. The grating can be spatially represented as a product of a rect function and a periodic impulse train. In the frequency domain, this becomes a convolution of a sinc function with a second impulse train. 233

7-3 Possible grating locations in the SCOW-DFB structure: (i) surface of the slab waveguide, (ii) surface of the SCOW ridge, (iii) above n-InP substrate, (iv) above quantum wells. 237

7-4 Structure of the SCOW-DFB with 0.1 μm InGaAsP grating layer above the quantum well active region. 238

7-5 SCOW-DFB modes for both grating cross sections with the grating layer (dashed line) indicated. The values of the effective modal index are also provided. 239

7-6 SCOW-DFB 1st and 2nd higher-order modes with the grating layer (dashed line) indicated. 239

7-7 SCOW-DFB grating etch as a function of the exposure dose (12 mJ – 30 mJ). 241

7-8 SCOW-DFB grating process beginning from the developing of the photoresist to the sulfuric clean of the grating grooves. 242

7-9 SEM photograph of a 6 minute SCOW-DFB grating etch under 10% RF power. 243

7-10 SCOW-DFB fabrication process starting from (a) an InP wafer grown up to the grating layer and ending with (f) the patterned and metalized SCOW-DFB structure.....244

7-11 AFM images superimposed on the image of an InP chip indicating the location of the scans. The grating etch depths averaged 96.3 nm across the chip.....246

7-12 SCOW-DFB output light power (AR facet) and voltage versus bias current (0 A – 5 A). The extracted turn-on voltage and series resistance are also provided. 247

7-13 SCOW-DFB AR facet optical spectrum for a bias current of 4.5 A. 249

7-14 SCOW-DFB AR facet optical spectrum for a bias current of 3.8 A. The resolution bandwidth for this measurement was 0.2 pm. 249

7-15 AR-AR SCOW-DFB single-pass gain for wavelengths between 1454 nm and 1641 nm. The gain spectrum was measured for bias currents ranging from 0.5 A to 4.0 A.....251

7-16 SCOW-DFB mode profiles as a function of bias for currents between 1.5 A and 4.5 A. The dimensions of the modes are also provided. The first number denotes the X dimension, whereas the second number denotes the Y dimension.....252

7-17 Band diagram of the SCOW-DFB for operation at (a) 0 V bias and at (b) 1.2 V bias. The electron and hole quasi-Fermi levels are also provided. 254

7-18 Carrier concentrations as a function of position within the SCOW-DFB structure for voltage biases of 0.9 V – 1.8 V. 255

7-19 Simulated I-V relations for the standard SCOW structure and for the SCOW-DFB. The turn-on voltage for each respective device is also provided. 256

7-20 SEM image of the SCOW-DFB gratings after regrowth. The measured average grating height is indicated. The average grating period can be found from the measured length over 6 grating periods. 257

7-21 AFM scans for three different InGaAsP compositions with bandgaps corresponding to the wavelengths of (a) 1055 nm, (b) 1256 nm, and (c) 1545 nm. The grating heights (H) are provided in each case. 258

7-22 SEM scans for three different InGaAsP compositions with bandgaps corresponding to the wavelengths of (a) 1055 nm, (b) 1256 nm, and (c) 1545 nm. The grating heights (H) are provided in each case. 258

7-23 Revised SCOW-DFB structure with 0.02 μm InGaAsP buffer layer, 0.001 μm InP etch stop layer, and 0.04 μm variable-width InGaAsP grating layer. 260

7-24 SCOW-DFB modes for both grating cross sections with the grating layer (dashed line) indicated. The values of the effective modal index are also provided. 261

7-25 Higher-order SCOW-DFB modes for both grating cross sections with the grating layer (dashed line) indicated.....262

7-26 Band diagram of the SCOW-DFB for operation at (a) 0 V bias and at (b) 1.2 V bias. The electron and hole quasi-Fermi levels are also provided. 263

7-27 Carrier concentrations as a function of position within the SCOW-DFB structure for voltage biases of 0.9 V – 1.8 V. 263

7-28 Simulated I-V relations for the standard SCOW structure and for the second-generation SCOW-DFB. The turn-on voltage for each respective device is also provided. 264

7-29 SCOW-DFB fabrication process starting from (a) an InP wafer grown up to the grating layer and ending with (f) the patterned and metalized SCOW-DFB structure. 265

A-1 RF oscillator consisting of three amplification stages, an RF filter, and an output coupler. Points (i), (ii), and (iii) label the outputs of RF Amplifiers 1, 2, and 3, respectively. 279

List of Tables

1-1 Comparison of parameters between several high-performance oscillators. The specifications for the OCXO are for 10 MHz operation and does not account for the multiplication step required to achieve 10 GHz. 46

1-2 Comparison of parameters for optical devices developed from fiber, SCOW, and semiconductor technologies. 57

3-1 Summary of RF amplifier residual phase-noise measurements corresponding to Amplifiers 1, 2, and 3. 115

5-1 Summary of measured SCOW-OEO parameters used in the simulation 168

Chapter 1

Introduction

Oscillators are essential components enabling operation for a wide variety of systems. Their applications span multiple disciplines of science, and their use is ubiquitous at frequencies ranging from optical to microwave and below. The spectral purity of every oscillator system is limited by noise. This purity is captured by a parameter termed the oscillator's phase noise. Currently, the separate communities of optical and electrical oscillators do not interact, resulting in a divergence in their individual understanding of phase noise. One major goal of this thesis is to provide a general theory that unifies the concepts of phase noise across both communities (Chapters 2 and 3). Among other parameters, we will see that a large roundtrip delay is critically important to achieve high oscillator performance.

Our analysis on roundtrip delay motivates us to search for oscillators whose cavity length can be made long. This is typically difficult to achieve in most oscillator systems due to high attenuation from propagation. However, using optical fiber as the guiding medium, this loss can be reduced below 0.2 dB/km. From this, one would then expect large improvements in phase noise by using a long fiber delay in a laser cavity. This is true to some extent but ignores the behavior of the other modes, which increases in number with a longer delay. As a consequence of the inhomogeneous broadening mechanisms of the gain medium, these modes are only partially suppressed in the cavity. In the worst-case scenario, the laser becomes multi-moded.

In this thesis, we will consider an alternative type of oscillator that takes advantage of the low optical fiber loss to generate a spectrally pure microwave tone. This oscillator (Chapter 4), termed the optoelectronic oscillator (OEO) in literature, uses principles of microwave-photonic (MWP) gain to achieve net amplification in a single cavity roundtrip. Unlike the case of the laser, the OEO gain is super-homogeneous (Chapter 5) which intrinsically suppresses the oscillation of sidemodes. These unique features make the OEO the ideal oscillator for operation with long cavity delays.

Typical OEOs require the use of additional external RF amplification, as the MWP gain is generally insufficient to overcome cavity losses. This RF amplifier degrades the OEO's size, weight, and power (SWaP) and injects further noise into the system. One of the central underlying themes of this thesis will be the use of high-power low-noise slab-coupled optical waveguide (SCOW) technology to enhance the functionality of the OEO. The use of SCOW components not only offers the advantage of lower noise but also enables oscillation without need of an RF amplifier. In the end, we will find the SCOW-OEO's phase noise performance to be superior to any free-running microwave oscillator operating in the same frequency range. The SCOW technology will also be applied (Chapter 6) to a coupled optoelectronic oscillator (COEO), whose configuration resembles that of a regeneratively modelocked laser.

The ultimate goal for the OEO technology would be to transfer its functionality in full onto an integrated chip. This ideal requires the miniaturization of several key components of the system. We will describe these efforts for the pump laser (Chapter 7), choosing a distributed-feedback laser (DFB) as suitable replacement. The DFB is designed based on a SCOW waveguide structure so that both high power and low noise operation can be achieved.

In this chapter, we review some of the principles regarding OEOs emphasizing the importance of achieving low phase-noise. We also discuss potential applications for low-noise microwave oscillators and present a comparison between the various competing oscillator approaches. We conclude with an overview of the SCOW technology, highlighting the devices that have been demonstrated to date. By the end, it will be clear that the SCOW technology offers unique benefits for OEOs beyond that of fiber and traditional semiconductor approaches.

1.1 Oscillator Phase Noise

Noise is an inescapable phenomenon present in all physical systems. Fundamentally, noise can be treated as a perturbation producing fluctuations decomposed along the amplitude and phase axes. By equipartition, the noise in each quadrature is (for most cases) exactly equal in strength. This equality of amplitude noise and phase noise reflects the fact that noise is random and does not preferentially align along any particular direction. Note that there exist non-classical realizations of noise where this equipartitioning becomes violated.

We are specifically interested here in the effects of noise on the behavior of oscillators. Although both amplitude and phase fluctuations can occur, the disturbances in phase are usually orders of magnitude larger than its amplitude counterpart. This dominance is a result of two mechanisms of amplitude-noise suppression fundamental to the operation of an oscillator. The first mechanism is related to an oscillator's intrinsic negative feedback, which maintains the net gain at the level of the cavity losses. Any amplitude fluctuations slower than the roundtrip time are effectively corrected by this feedback response. The second amplitude-limiting mechanism occurs due to device saturation during oscillation. This saturation suppresses the ability of an input (amplitude) fluctuation to induce a variation in the output. Together, these two processes eliminate the need for considerations of amplitude noise in virtually all oscillator systems. For the rest of this thesis, we will therefore restrict our attention primarily to perturbations of phase.

It is natural at this point to ask what does phase noise mean in an oscillator. For this discussion, we consider the following equation

$$E(t) = \left[E_0 + \Delta E(t)\right]\cos\left(2\pi f_0 t + \phi(t)\right) \tag{1.1}$$

which describes an ideal oscillator field perturbed by both amplitude and phase noise. In

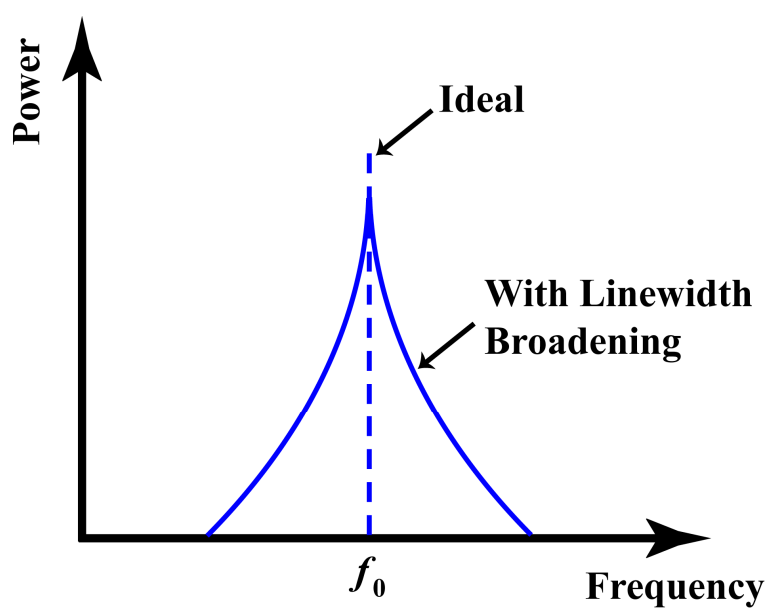

Figure 1-1: Illustration of oscillator spectrum under ideal conditions (dashed line) and with effects of linewidth broadening (solid line).

Eq. (1.1), E_0 is the field amplitude without effects of noise, $\Delta E(t)$ is the noise-induced amplitude perturbation, f_0 is the oscillation frequency, $\phi(t)$ is the noise-induced phase perturbation, and t is the time variable of the system. Under ideal conditions ($\Delta E(t)$, $\phi(t) \sim 0$), the field consists of a delta function at the frequency of oscillation. However, taking into account effects of the finite oscillator lifetime, the field is no longer a pure sinusoid and thus broadens over a band of frequencies. The oscillator's phase noise creates additional broadening beyond this limit. The phase fluctuations can be thought of as perturbations to the oscillator's instantaneous frequency, which acts to spread the signal across a distribution of frequencies. These cases are illustrated in Fig. 1-1. Note that power conservation has been employed in Fig. 1-1 so that the total powers in the ideal and broadened oscillators are equal (ignoring the power contributions added by noise).

There are two common definitions of phase noise used to describe the spectral broadening observed in Fig. 1-1. This topic will be a subject of considerable discussion in Chapter 3. For now, we will only provide the definition that we prefer, which specifies phase noise as the (phase) noise power stored within the electric field in a 1 Hz bandwidth and normalized to the total power of the carrier. Defined in this way, it is clear that phase noise becomes directly related to the oscillator's spectrum, as one might intuitively expect from Fig. 1-1.

1.1.1 The Importance of Low Phase Noise

Our goal in this section is to motivate why low oscillator phase noise is important. Central to our discussion is the link of Fig. 1-2 (a), which downconverts an input signal into its corresponding intermediate frequency (IF). This link is generic and may belong to a wireless network receiver or instead to a number of other systems. Due to the presence of an unwanted interferer, the actual input contains both the signal-of-interest and also a strong contribution of the interferer (Fig. 1-2 (b)). The proximity of the interferer frequency to the signal frequency prevents the interferer from being rejected by the bandpass filter. The RF amplifier similarly does not provide any discrimination, amplifying both of the inputs equally. The signal and interferer are then passed to a mixer, whose operation multiplies (in the time domain) both inputs by a separate local oscillator (LO). The resulting spectrum is found from the convolution of the individual

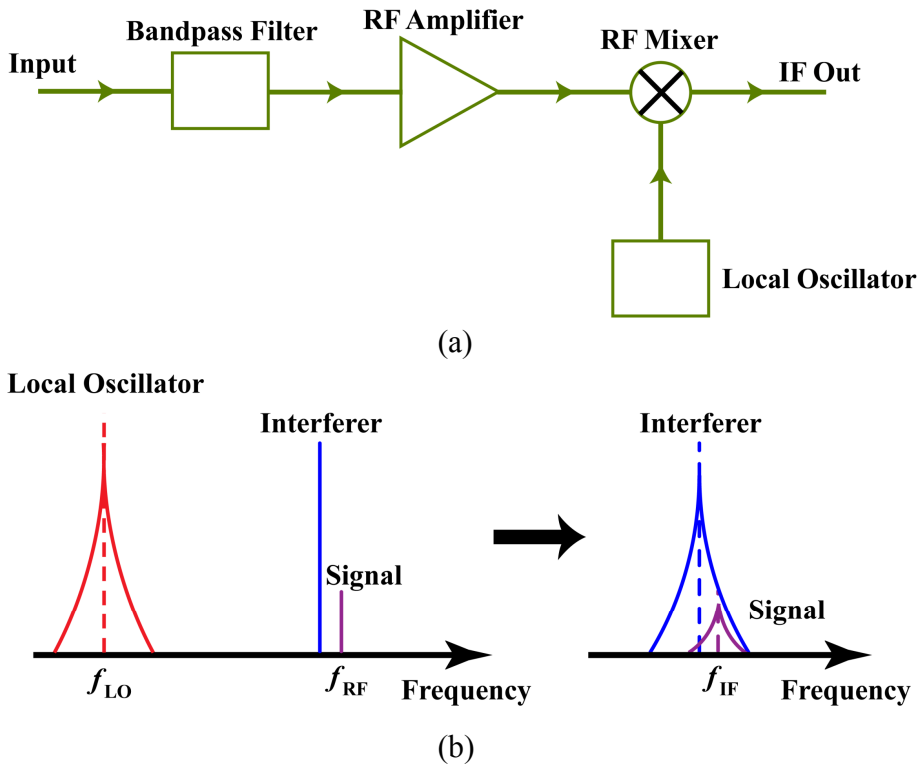

Figure 1-2: (a) Schematic of a system that downconverts an input signal into an intermediate frequency (IF) and (b) illustration of the system output in the presence of an interferer.

spectra yielding a downconverted version of the inputs. If the signal, interferer, and local oscillator are all ideal delta functions, the interferer contribution can be readily removed by efficient narrowband filtering at the IF frequency. However, if even just the local oscillator is non-ideal (Fig. 1-2 (b)), the spectral spread of the downconverted interferer may be enough to completely mask any trace of the desired signal.

1.1.2 Applications of Low-Noise Oscillators

Here, we discuss some applications for oscillators with low phase noise. Our examples will be focused primarily on RF oscillators, but numerous applications can also be found for oscillators operating at other frequencies (e.g. optical) or operating in other domains (e.g. mechanical). Low-noise oscillators are required whenever the impurities of the spectrum prevent the detection

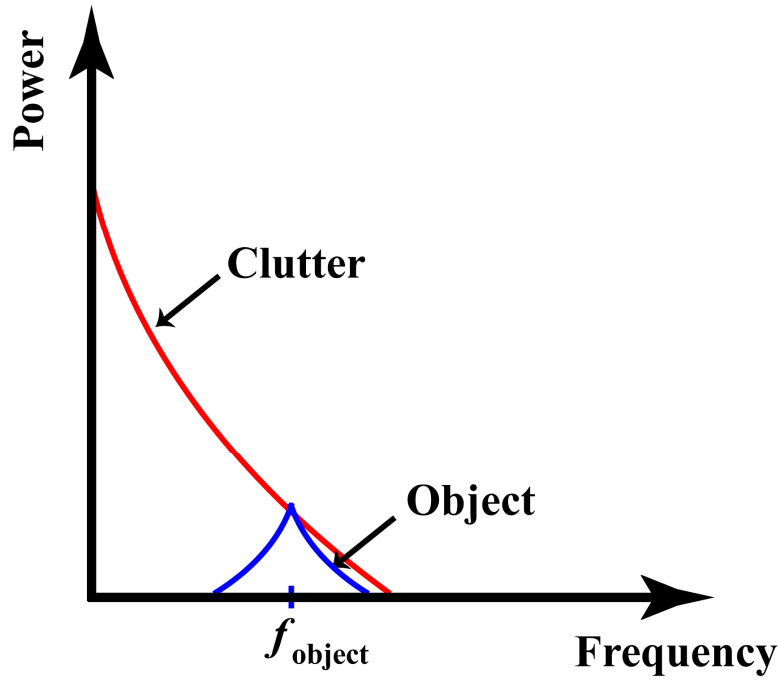

Figure 1-3: Illustration of backreflected Doppler radar signal with the object signature masked by the clutter.

of a weak signal. One general example of this was provided in Fig. 1-2, but here we would like to discuss specifically applications related to radar.

In a Doppler radar system, an RF waveform is transmitted that scatters off of nearby objects in the environment. The scattered energy is detected, with the corresponding spectral content Doppler-shifted based on the velocity of each object. In addition to the target, there is unfortunately a large amount of clutter (from mountains, etc) that provides a strong backscattered signal. An illustration of the combined backscattered spectrum is shown in Fig. 1-3. The local oscillator phase noise determines the spectral width imprinted on each of the return signals. With enough spectral broadening, the reflections due to clutter can completely mask the presence of the object. For the detection of objects that are either small or slow-moving, low phase noise oscillators become a critical requirement. Typical Doppler radars operate near 10 GHz using a frequency-multiplied quartz crystal oscillator for signal generation. In this operating frequency range, the phase-noise level is usually near -75 dBc/Hz at 10 Hz offset and near -115 dBc/Hz at

1 kHz offset. These low levels of phase noise are even more challenging to meet in airborne systems where significant noise is introduced through vibration.

Low phase noise RF oscillators are also used in the global positioning system (GPS) where navigation is accomplished through the use of one-way time measurements. The position of an object is triangulated from a set of three or more satellites. Due to the high propagation speeds for electromagnetic waves and also to the long travel distances, the accuracy of the clock becomes critical for estimating target range. For example, at speeds of 3×10^8 m/s, a clock inaccuracy of 1 μs would yield a range error of 300 m. The oscillators used on board each satellite typically consist of high-performance atomic clocks (Rubidium and Cesium). These oscillators achieve excellent phase noise while also offering the benefit of stability at long time scales. Typical GPS systems operate at center frequencies of 1575.42 MHz and 1227.60 MHz. However, to provide a better comparison against other X-band oscillators, we specify the Rubidium oscillator phase-noise frequency multiplied to 10 GHz. For this frequency range, the phase noise of Rubidium oscillators are ~-80 dBc/Hz at 10 Hz offset. The short-term phase noise

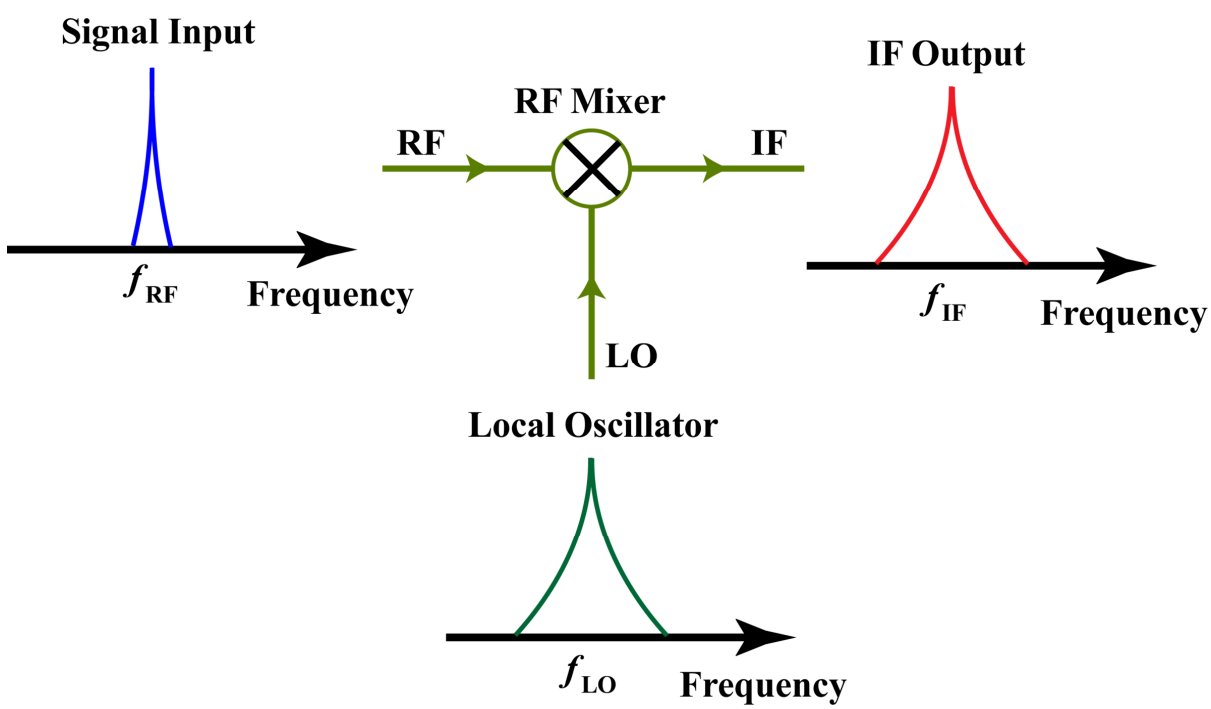

Figure 1-4: Mixer stage of a swept-tuned spectrum analyzer whose IF output is contaminated by the noise of the internal local oscillator.

affects navigation accuracy and jamming resistance, while the long-term stability is important for reducing the time interval between oscillator tune-ups [1]. The clocks used in GPS receivers are usually compact oven-controlled or temperature-controlled crystal oscillators steered to the GPS reference.

We will discuss one more application here on the use of high precision clocks in measurement instrumentation. This topic encompasses equipment such as spectrum analyzers where the accuracy of the internal reference determines the resolution that can be measured. To illustrate this point, we consider the mixing stage of a swept-tuned spectrum analyzer, which downconverts an RF input into a suitable IF frequency where it can be filtered and measured. The mixer output is the convolution of the individual input spectra of the signal and local oscillator. If the phase noise of the local oscillator is large compared to that of the signal, the spectrum of the signal effectively becomes a delta function during the convolution. At the mixer output, a replica of the local oscillator is then recovered at the IF frequency thus corrupting the spectrum measurement. Only when the spectral content of the signal is much wider than that of the local oscillator can the absolute noise of the signal be obtained. For intermediate levels of noise, the final spectrum would contain a mixture of the features present in the signal and local oscillator. Therefore, it is clear that the spectral purity of the reference oscillator becomes critical for making accurate measurements of low-noise signals. This statement, although specifically justified for the case of a spectrum analyzer, applies generally across any oscillator measurement.

Other applications of low phase-noise RF oscillators include cellular phone transmission, high-quality analog-to-digital conversion, and space exploration [1].

1.2 Optoelectronic Oscillator Systems

In the following sections, we describe the operation of oscillators whose cavity consists of both optical and electrical elements. The fundamental process of signal amplification is achieved through MWP gain. There are currently two types of oscillators exhibiting these properties, and we will cover each system in turn. Both oscillators share in common the use of a long optical delay as the key feature that enables low phase noise.

1.2.1 The Optoelectronic Oscillator (OEO)

The concept of an optoelectronic oscillator (OEO) was first proposed by Kersten in 1978 [2] and later demonstrated in 1980 [3] based on electrical feedback into an optically-driven modulator. Over 30 years later, significant research is still ongoing in this field, with much of the underlying theory developed by Yao in 1996 [4, 5]. The configuration of a typical OEO is illustrated in Fig. 1-5. The optical cavity comprises a continuous wave (CW) pump laser that drives a Mach-Zehnder (MZ) modulator. The modulated output is sent through a long optical fiber delay before detection by a photodiode. In the electrical cavity, an RF amplifier boosts the incoming photodetected signal and sends its output to a phase shifter. Afterwards, the signal is directed to an RF filter, which serves the dual purpose of defining the center oscillation frequency and also filtering out any unwanted disturbances that are out-of-band. Next, a fraction of the signal is

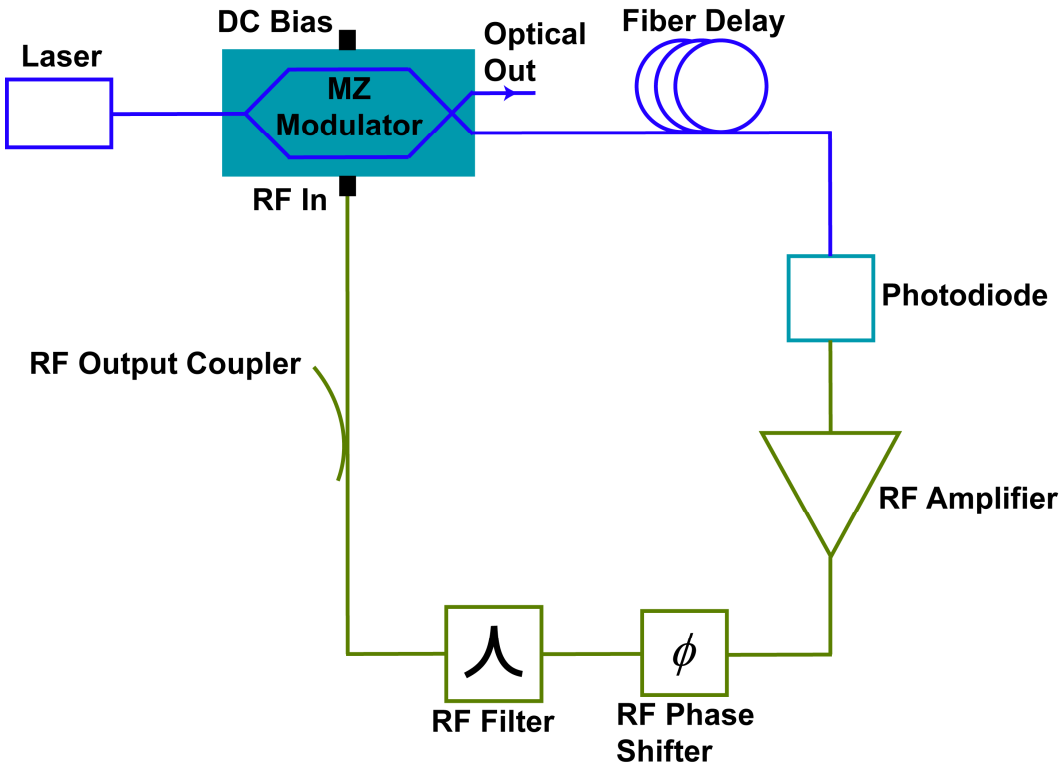

Figure 1-5: Typical configuration of an optoelectronic oscillator comprising a pump laser, Mach-Zehnder (MZ) modulator, fiber delay, and photodiode in the optical cavity. The electrical cavity consists of an RF amplifier, phase shifter, filter, and output coupler.

coupled out of the cavity, while the remainder is fed into the modulator's RF port to drive self-oscillation.

The RF signal amplification occurs through a process of MWP gain that can be understood by tracing through a single roundtrip of the cavity. We do this starting from the perspective of a signal input on the modulator. The RF signal modulates a CW laser resulting in sidebands equally spaced around the carrier by the modulation frequency. The envelope is detected by the photodiode generating RF beating from the modulation. The RF voltage is then amplified, filtered, and sent back to drive modulation for the next roundtrip. Oscillation occurs if a small-signal voltage receives net gain from one cycle of the cavity. Although we have traced through the OEO assuming coherent signal modulation, we wish to make clear that ultimately it is noise that starts this process.

It is useful at this point to discuss how to achieve low phase-noise performance from an OEO. We will show in Chapters 2 and 3 that for *any* oscillator system, the phase noise can be made lower if the roundtrip delay is increased or if the noise injected in each roundtrip is decreased. The best phase noise is achieved only when both the roundtrip delay and injected noise are optimized. For now, let us take these principles as given and apply them to the design of a low-noise OEO. To obtain the lowest level of noise injection, it becomes necessary to remove the RF amplifier from the system. This has the added benefit of reducing system SWaP. With a large optical pump, high-efficiency modulator, and high-power photodetector, the OEO can oscillate from gain supplied solely by the MWP link [6].

The modulator requirements are the simplest to meet as commercial $LiNbO_3$ modulators are readily available rated for ~1 W optical power with a halfwave switching voltage (V_π) below 2.5 V. On the other hand, the photodetector and laser requirements are significantly more difficult to realize with no commercial options currently viable. The photodiode ideally should have >30 mA current handling at >10 GHz RF bandwidth (unterminated). Note that typical photodiodes include a 50 Ω output termination that halves the effective load impedance seen by the device. The net result is a doubling of bandwidth (in the RC limit) but at a cost of 6 dB to the generated electrical power. In a similar vein, the laser should exhibit low relative intensity noise (RIN) from 1 Hz to 10 GHz while maintaining an optical power >200 mW. The RIN requirements are challenging for fiber and solid state lasers to achieve as usually the RIN is too high, and large relaxation oscillation peaks are observed near ~100 kHz. On the other hand, both

the power and RIN requirements are challenging for semiconductor lasers to meet as these lasers typically operate with ~20 mW power and also exhibit large relaxation oscillations near ~5-10 GHz. In this thesis, we will be exploring the use of high-power low-noise slab-coupled optical waveguide devices to meet the demands of the OEO system. The operation of the individual components will be described in Section 1.3. One potential challenge to using high-powers is that nonlinear noise processes within the optical fiber can become significant. This topic will be addressed in Chapter 4.

1.2.2 Analysis of OEO Operation

Let us now analyze the operation of the OEO [4] treating the modulation function as an ideal sinusoid with input-output characterized by

$$P(t) = \frac{\alpha P_O}{2}\left(1 - \cos\left[\Gamma_0 + \frac{\pi}{V_\pi} V_{in}(t)\right]\right) \tag{1.2}$$

In Eq. (1.2), $P(t)$ is the optical power (time dependent) at the output of the modulator, α is the loss of the modulator, P_O is the optical power supplied by the laser, Γ_0 is the modulator's bias point, V_π is the modulator's half-wave switching voltage, and $V_{in}(t)$ is the input RF voltage drive. After photodetection, the optical power is converted to an electrical voltage through a responsivity $\Re$ and a load resistance R yielding

$$V(t) = \Re R P(t) = V_{ph}\left(1 - \cos\left[\Gamma_0 + \frac{\pi}{V_\pi} V_{in}(t)\right]\right) \tag{1.3}$$

Here, $V_{ph} = \alpha P_O \Re R/2$ is the detected voltage resulting from the DC photocurrent flowing through R when the modulator is biased for maximum RF output ($\Gamma = \pi/2$). Equation (1.3) is nonlinear due to the cosine dependence of the modulator's transfer function. We consider as input a sinusoidal voltage generated through self-oscillation of the form

$$V_{in}(t) = v \sin(\omega t) \tag{1.4}$$

The output voltage can then be expanded in Bessel functions as

$$V(t) = V_{ph}\left(1 - \sum_{n\geq 0}\begin{cases} \cos\Gamma_0 J_0\left(\frac{\pi v}{V_\pi}\right) & n = 0 \\ 2\cos\Gamma_0 J_n\left(\frac{\pi v}{V_\pi}\right)\cos(n\omega t) & n \text{ even} \\ -2\sin\Gamma_0 J_n\left(\frac{\pi v}{V_\pi}\right)\sin(n\omega t) & n \text{ odd} \end{cases}\right) \tag{1.5}$$

where the nonlinearity-induced harmonics of ω have now been made explicit. We are specifically interested in the component of the signal at ω, which yields a gain of

$$G = 2V_{ph}\sin(\Gamma_0)J_1\left(\frac{\pi v}{V_\pi}\right)\Big/ v \tag{1.6}$$

from voltage input to voltage output. For low values of v, the gain converges to a constant

$$G\big|_{v=0} = \pi V_{ph}\sin(\Gamma_0)/V_\pi \tag{1.7}$$

dependent only on the operating conditions of the system. When v becomes large-signal compared to V_π, the gain response of Eq. (1.6) saturates and begins to decrease (in a nonlinear fashion). Note that at large enough optical powers, net gain ($G > 1$) is possible through the microwave downconversion process [6]. However, in a typical OEO, additional RF amplification is usually necessary (Fig. 1-5) to achieve self-oscillation.

Once net gain is established, the modes of the OEO are defined through the frequencies where the roundtrip phase shift is a multiple of 2π. These frequencies are dependent on the sign of the gain (Eq. (1.6)), as an extra π phase shift is induced if the voltage becomes inverted. Mathematically, the oscillator phase condition can thus be summarized as

$$\begin{aligned} 2\pi f_k T &= 2\pi k && \text{for } G > 0,\ k = 0, 1, 2... \\ 2\pi f_k T &= 2\pi k + \pi && \text{for } G < 0,\ k = 0, 1, 2... \end{aligned} \tag{1.8}$$

where T is the roundtrip time delay and f_k represent the individual mode frequencies indexed by k. The RF phase shifter of Fig. 1-5 controls the accumulated roundtrip phase and thus allows

fine-tuning for the exact value of f_k. It is clear from Eq. (1.8) that the free-spectral range (FSR) reduces with a longer delay, and therefore the modes become more finely interleaved in the spectrum.

1.2.3 The Coupled Optoelectronic Oscillator (COEO)

In this section, we discuss a variant of the OEO whose configuration consists of two coupled cavities in simultaneous oscillation (Fig. 1-6), termed the coupled optoelectronic oscillator (COEO) [7, 8]. The optical cavity comprises an optical amplifier, MZ modulator, optical delay line, and optical coupler. When the gain provided by the optical amplifier is enough to overcome the losses, this cavity (by itself) behaves analogous to a multi-mode laser. The optoelectronic

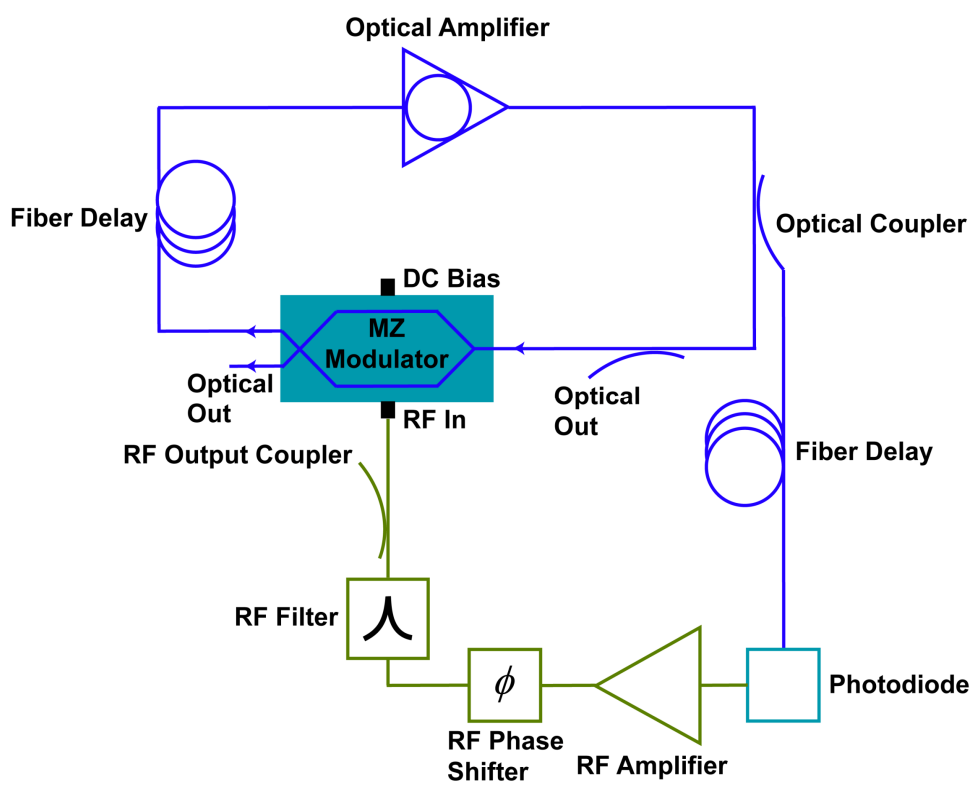

Figure 1-6: Typical configuration of a coupled optoelectronic oscillator comprising a Mach-Zehnder (MZ) modulator, fiber delay, optical amplifier, optical coupler, and photodiode as the optical elements. The electrical elements consist of an RF amplifier, RF phase shifter, RF filter, and RF output coupler.

cavity comprises the same cavity elements but also includes the photodiode, RF amplifier, RF phase shifter, RF filter, and RF output coupler. The behavior of the optoelectronic cavity resembles that of an OEO driven by amplified spontaneous emission (ASE) rather than by a coherent laser source. The ASE alone usually does not provide sufficient gain to allow for self-oscillation. However, when the operations of the individual cavities are combined, their characteristics synergize to drive coherent oscillation of the complete system. The multi-mode optical cavity generates RF beating at the harmonics of its mode spacing. The RF filter then picks out the signal of interest and uses this power for modulation of the optical cavity. The modulation frequency aligns with a harmonic of the optical cavity FSR and thus reinforces its energy upon photodetection. After all the dynamics settle, the end result is coherent harmonic modelocking in the optical cavity. In addition, self-oscillation builds up simultaneously in the optoelectronic cavity from modulator voltage in to voltage out.

The COEO of Fig. 1-6 is similar to a regeneratively modelocked laser (RML) as both systems have identical configurations consisting of similar loop delays [7-9]. In the literature, it is often cited that the difference between the two systems is related to the purpose of the electronic feedback. In a COEO, the feedback forms a secondary coupled-cavity of the system, while in a RML, the feedback is intended to stabilize the optical cavity against fluctuations. While this is true, it is unclear whether this distinction plays any role during experimental operation of either system. From our perspective, the difference between a COEO and a RML appears to be related to the performance metrics that each system is optimized for. A COEO primarily serves the role of a pristine microwave source and is therefore usually optimized for low phase-noise [9]. Historically, the RML has been designed for the generation of high repetition-rate, short-pulse trains where phase-noise was more of a secondary concern [10]. In this thesis, we use the terms COEO and RML to be consistent with this definition.

The coupled oscillation of the individual cavities has important consequences on the operation of the combined system. In particular, the oscillation frequency is the same for both cavities and thus must independently correspond to valid modes in each cavity. This is typically accomplished with relative ease if the cavity lengths are made sufficiently long such that many modes are allowed to form. Through fine control of the modes in the optoelectronic cavity (via the phase shifter), one can always tune the system so that a pair of modes overlap at the desired oscillation frequency. In general, this overlap will not be satisfied between the other modes of

the optical and optoelectronic cavities (near the vicinity of the operating point) as the length of the two cavities are not equal. Therefore, by a Vernier effect [7, 8], oscillation is largely suppressed at the various sidemode frequencies corresponding to each cavity. Note that it is possible for a mode pair to eventually find overlap when there is a common multiple between the individual cavity FSRs. These frequencies can be designed to occur far away from the oscillation frequency where they are rejected by the RF filter.

As in the case of the OEO, the COEO can be made to self-oscillate on solely the MWP gain available to the system. Removal of the RF amplifier provides savings in SWaP and also reductions in the noise added in each cavity roundtrip. To achieve self-oscillation, the optical amplifier/photodiode must be able to supply/handle significant amounts of power to drive oscillation in both the optical and optoelectronic cavities. From Fig. 1-6 and principles of power conservation, it can be seen that there is an inherent tradeoff in the optical power coupled into each cavity. The requirements placed on the optical amplifier are even more stringent as the RIN of the amplifier must be low to achieve good oscillator phase-noise performance. In comparison to fiber technology, semiconductor optical amplifiers (SOAs) possess significant advantages in RIN when the amplifiers are operated in saturation. As will be discussed in Section 1.3 and Chapter 6, the amplifier RIN becomes suppressed when the fluctuations occur slower than the response time of the carriers. For SOAs, RIN suppression occurs at frequencies below 10 GHz. In this thesis, we will explore the use of high-power low-noise SCOW amplifiers and photodiodes to optimize the performance of the COEO.

1.2.4 RF Oscillator Comparisons

Here, we compare the performance of several key oscillator technologies at microwave frequencies. In general, this comparison is difficult to perform as many of these oscillators operate under dramatically different conditions. For example, the majority of the oscillators described here achieve low phase noise through a variety of cavity stabilization techniques. In contrast, both the OEO and COEO technologies operate completely free-running. The improvement afforded by cavity stabilization is large. For example, in the realm of optical frequencies, free-running laser linewidths of 10-100 kHz can be stabilized to below 1 Hz by locking to a high Q optical cavity. This represents an improvement in phase noise of 40-50 dB.

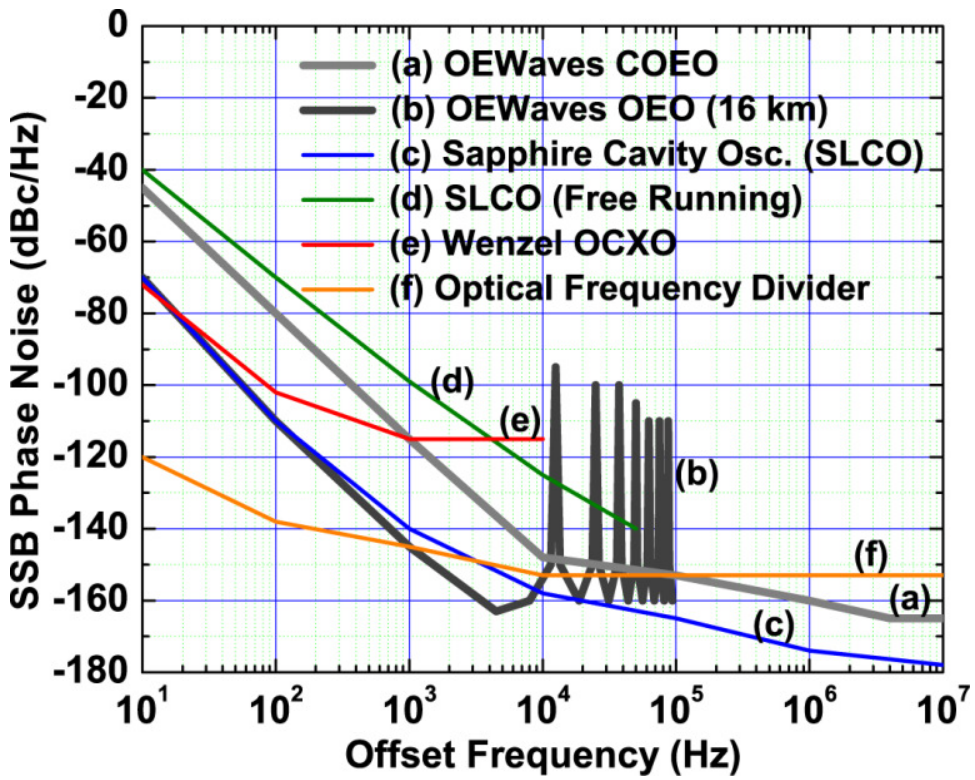

Figure 1-7: Phase noise comparison between several high-performance oscillator technologies normalized for operation at 10 GHz. For the Wenzel OCXO operating at 10 MHz, ideal frequency multiplication was assumed resulting in a phase noise degradation of 60 dB.

However, even without the benefits gained through stabilization, the OEO remains competitive compared to the highest performance microwave oscillators.

Figure 1-7 illustrates the phase-noise of the OEWaves COEO and OEO [11] compared to a variety of other oscillator technologies operating at 10 GHz. Note that the OEO/COEO can be made to operate with the same performance at any RF frequency (tuned by the RF filter) as long as the other cavity components (laser, modulator, photodetector) do not degrade at these frequencies. (c) shows a comparison to a commercial sapphire loaded cavity oscillator (SLCO) manufactured by Poseidon Scientific Instruments (now acquired by Raytheon). These oscillators function with a sapphire whispering gallery mode resonator serving the dual purpose of an intracavity filter and also as a discriminator for stabilization against phase errors. In regards to phase noise, the OEO and SLCO exhibit similar performance at lower offset frequencies. The cavity modes of the OEO eventually spoil its phase-noise performance beyond 12.5 kHz offset.

In Chapter 5, we will describe in detail how these modes can be effectively *eliminated* within the oscillator spectrum. (d) shows the phase noise of a free-running SLCO using the sapphire resonator only as an intracavity filter [12, 13]. The performance of the free-running SLCO lags behind that of the locked SLCO by ~30 dB. When only free-running oscillators are compared, it can be seen that both the OEO and COEO achieve lower phase noise than the SLCO. (e) shows the phase noise of an oven controlled crystal oscillator (OCXO) manufactured by Wenzel. These oscillators operate using quartz crystals as the intracavity filter element with the crystal housed in a temperature controlled oven. The resonant frequencies of quartz allow for oscillation only in a limited frequency range 0.5-300 MHz. The 10 GHz oscillator data was generated by multiplying up the frequency (and phase noise) assuming ideal multiplication. From Fig. 1-7, the OCXO appears to be competitive with the OEO below 100 Hz offset. At higher offset frequencies, the performance of the OCXO quickly reaches the limit set by its noise floor. (g) shows the phase noise of a recently demonstrated optical frequency divider (OFD) based on using MWP downconversion of a stabilized optical frequency comb [14]. This oscillator functions by locking the operation of the comb to a stabilized CW laser (linewidth ~1 Hz) while simultaneously stabilizing the carrier-envelope offset by f-2f interferometry [15]. Subsequent photodetection of the frequency comb divides both the optical carrier and its associated phase noise into the microwave frequency regime. It is clear from Fig. 1-7 that the OFD approach provides large improvements to phase noise at low offset frequencies (<1 kHz). This oscillator may be a potential insertion point for SCOW technology in the future. However, we should note that the performance advantages come at a significant cost of SWaP and system complexity. The full functionality of the oscillator requires locking a frequency comb to a CW laser, which itself is locked to a high Q optical cavity. The carrier-envelope offset locking requires frequency doubling of the comb lines and stabilization of the resulting offset against a reference. This added complexity makes a compact solution for the OFD difficult to realize. For completeness, we note that typical atomic clocks (Rubidium, etc) have phase-noise performance comparable to that of the OCXO. On the other hand, the long-term stability of the atomic reference is excellent, making them currently the ideal choice for GPS applications.

A comparison of the system properties for each oscillator is provided in Table 1-1. The OEO, COEO, and OFD yield the additional benefit of providing both optical and RF outputs during

Table 1-1: Comparison of parameters between several high-performance oscillators. The specifications for the OCXO are for 10 MHz operation and does not account for the multiplication step required to achieve 10 GHz.

Parameters	Coupled Optoelectronic Oscillator	Optoelectronic Oscillator	Sapphire Loaded Cavity Oscillator	Oven Controlled Crystal Oscillator	Optical Frequency Divider
Size (cm^3)	15×11.5×2	19″ rack-mount	22×22×6.5	4.4×7.5×2.5	Optical Bench
Power Consumption (W)	28	Unspecified (Assumed large)	<200	2.5 (at 10 MHz)	Unspecified (Assumed large)
Output Power (dBm)	RF: 13	RF: 13	RF: 13	RF: 13 (at 10 MHz)	RF: >0
	Op: -3	Op: 0	N/A	N/A	Op: Unspecified

operation. On the other hand, the OCXO has significant advantages in size and power consumption, which makes them suitable for applications requiring portability. The goal of this thesis is to demonstrate a SCOW-based OEO and COEO that leverages the capabilities of high optical power to achieve oscillation without the need for RF amplification. This provides significant reductions in SWaP (particularly in system power consumption) as we will show in Chapters 4 and 6. As a second benefit, the SCOW devices exhibit low RIN, which results in large improvements to oscillator phase noise. Our target is to obtain an order of magnitude phase-noise improvement in comparison to the OEO systems of Fig. 1-7. The final goal of this work would be to integrate the full functionality of the OEO onto a single chip of InP and thus allow the OEO to compete in the same application space as the OCXO.

1.3 Slab-Coupled Optical Waveguide (SCOW) Gain Medium

In Section 1.1, we motivated the need for low phase-noise RF oscillators. This led us towards a discussion of the optoelectronic oscillator, which we compared against conventional microwave

oscillator approaches in Section 1.2. The OEO is unique in that it is the optical components that provide the gain necessary for RF amplification. To achieve the highest OEO performance, these components are required to exhibit both high circulating power and low (relative intensity) noise. In this section, we will show that SCOW devices are the ideal choice for meeting these requirements.

The SCOW gain medium [16–18] is unique in that the waveguide operates single transverse mode despite the fact that its dimensions (5.8 μm ridge width, 5 μm waveguide thickness) are large compared to the optical wavelength (1.55 μm). Fig. 1-8 shows a cross-section of the SCOW waveguide. The waveguide is engineered for single-mode operation by use of small index contrast in the lateral and vertical dimensions. Through careful design, phase-matching can be established between all the higher-order modes of the ridge and the modes of the slab such that these higher-order modes become leaky. The fundamental mode, however, does not have a direct phase-match counterpart and is thus confined to the ridge. By itself, this is typically not enough to guarantee that the fundamental mode dominates as the slab modes do not see a large difference in loss. The mode contrast is instead provided by the quantum wells which introduce gain primarily into the fundamental guided mode.

As a result of the large waveguide dimensions, the effective mode areas of typical SCOW devices are in the range of 5 μm (vertical) × 7 μm (lateral). There are a few important and unique advantages afforded by a large mode structure. One principal advantage is a significant reduction to the confinement factor (Γ), which is a measure of the mode overlap with the active region. In a typical SCOW structure, $\Gamma \sim 0.5\%$, which is over 10 times smaller than Γ of conventional semiconductor devices. For the same optical power, a lower Γ results in less saturation of the quantum wells since only the optical power overlapped with the active region undergoes stimulated emission. By storing most of the power in the waveguide, SCOW structures can achieve over an order of magnitude higher power before the active region saturates. The large mode area is also beneficial for reducing effects of two-photon absorption (TPA) [19, 20]. The optical power is spread over a larger area, thus maintaining a low optical power density. Beyond device characteristics, the SCOW structure is ideal for link applications due to its near-ideal coupling efficiency ($\eta_c \sim 90\%$) to optical fiber. This efficient coupling results from the excellent overlap of the SCOW mode to a 6.5 μm × 6.5 μm mode of commercial lensed fiber. Two other

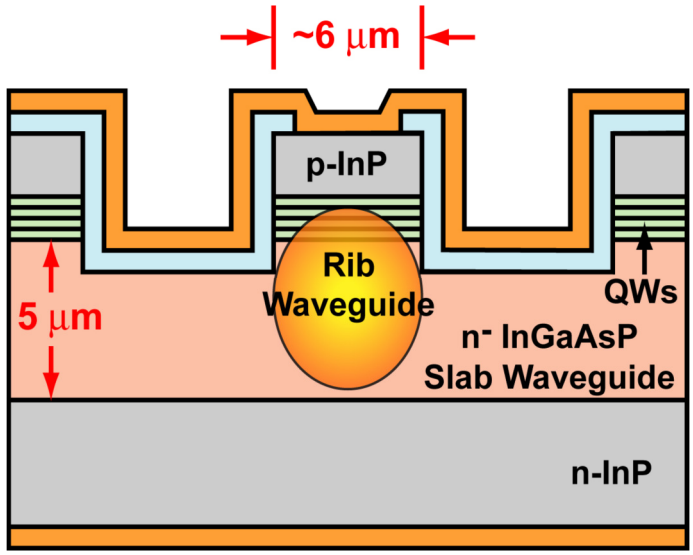

Figure 1-8: Slab-Coupled Optical Waveguide Cross Section.

notable advantages characteristic of SCOW devices are low series resistance and superior heat removal both due to the SCOW's inherent large area design.

One consequence of a low-confinement structure is that internal losses (α_i) become significant compared to the available gain. The total gain (G) accumulated through propagation is given by

$$G = e^{(\Gamma g_m - \alpha_i)L} \tag{1.9}$$

where g_m is the material gain of the active medium and L is the length of the device. A low confinement structure is limited by low modal gain (Γg_m), so that α_i must be reduced similarly in order to obtain net amplification. Typical SCOW waveguides have $\alpha_i \sim 0.5$ cm^{-1}, which is an order of magnitude below α_i of conventional semiconductor structures. The low SCOW α_i results from a reduced overlap of the guided mode with the lossy p-InP regions. The length of a SCOW waveguide is typically 1 cm (over 10× longer than conventional devices) to compensate for the overall net decrease in $\Gamma g_m - \alpha_i$.

The SCOW technology is applicable across a wide variety of applications. We will mention some of these applications below when we discuss each of the individual SCOW devices. An analysis regarding the suitability of SCOW devices for OEOs will be presented at the end.

1.3.1 Slab-Coupled Optical Waveguide Amplifier (SCOWA)

The SCOW concept can be applied to improve the capabilities of a number of semiconductor devices. Here, we will describe the operation of a slab-coupled optical waveguide amplifier (SCOWA) [21–23], designed, fabricated, and packaged by the technical staff at MIT Lincoln Laboratory. These amplifiers are angled at 5° and anti-reflection (AR) coated on both facets to suppress lasing from unintentional cavity feedback. Previous SCOWAs have demonstrated a fiber-coupled saturation output power (P_{sat}) of ~0.8 W (~0.9 W free space) with ~14 dB gain at λ=1540 nm [22] (Fig. 1-9). This value of P_{sat} improves on previous semiconductor optical

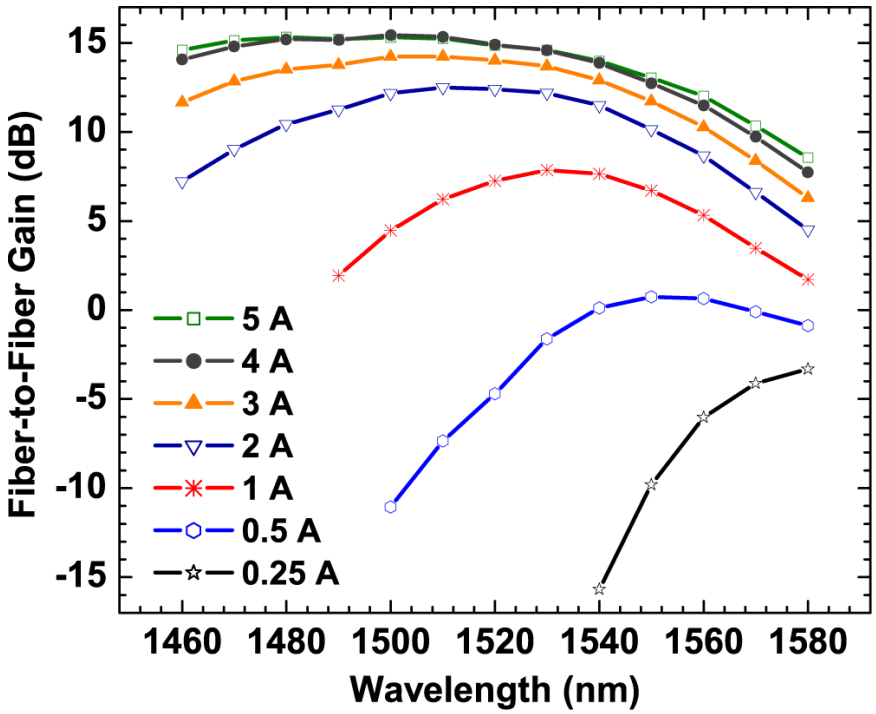

Figure 1-9: Measured packaged SCOWA fiber-to-fiber gain as a function of wavelength and bias current.

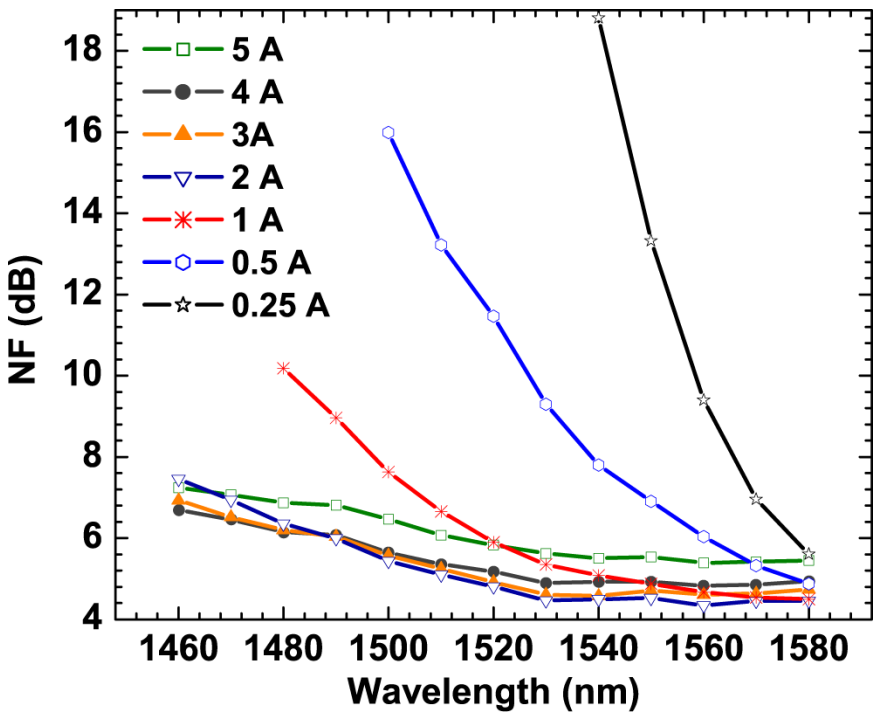

Figure 1-10: Measured packaged SCOWA noise figure as a function of wavelength and bias current.

amplifier (SOA) record results [24, 25] by a factor of 2. The noise figure (NF) of the fiber coupled SCOWA is < 5.5 dB [22, 23], which is the lowest demonstrated among any packaged SOA (Fig. 1-10). The low SCOWA NF is primarily attributed to its near-optimal coupling efficiency. Any input coupling loss directly reduces the signal power but does not affect the amplified spontaneous emission (ASE) noise added by the amplifier. As a result, the noise figure degrades beyond its ideal 3 dB limit. The output powers of SCOWAs are currently limited by two-photon absorption (TPA) in the waveguide [19] and can be flared to achieve operation beyond one Watt.

Currently, the SCOWA is most directly applicable as a power amplifier for boosting signals generated by a lower power source. In this application, high power and gain is essential, while low NF becomes a more secondary concern. The SCOWA may also be suitable as an in-line or pre-amplifier in the future but is currently limited by its polarization sensitivity for these applications. Today, the optical fibers deployed for telecommunication applications are primarily non-polarization maintaining. As a result, the polarization is completely scrambled before signal

arrival at any of the components along the fiber. Erbium doped fiber amplifiers (EDFAs) with their inherent polarization-insensitive operation are currently the dominant amplifier technology used in telecommunication networks. Compared to the SCOWA, high-power EDFAs exhibit larger P_{sat}, higher gain, and similar NF. EDFAs also have carrier lifetimes ~10 ms which render EDFAs less susceptible to the pattern effect. On the other hand, the SCOWA exhibits lower SWaP and can be integrated with other components to enable system-scale functionality on chip.

1.3.2 Slab-Coupled Optical Waveguide External Cavity Laser (SCOWECL)

Single longitudinal mode lasers can be realized using frequency selective feedback from either

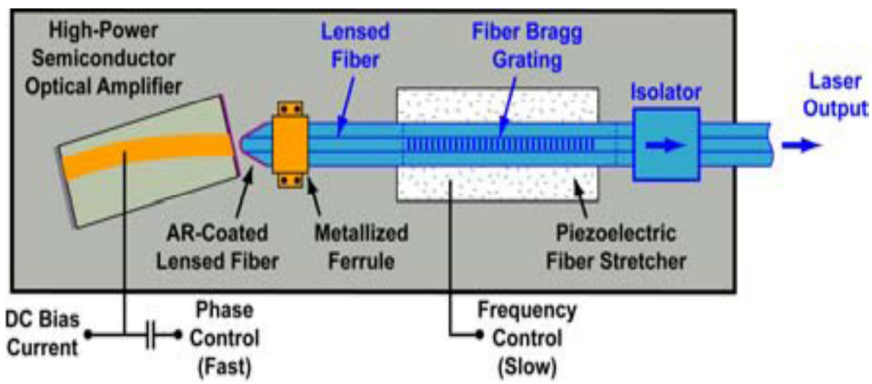

(a)

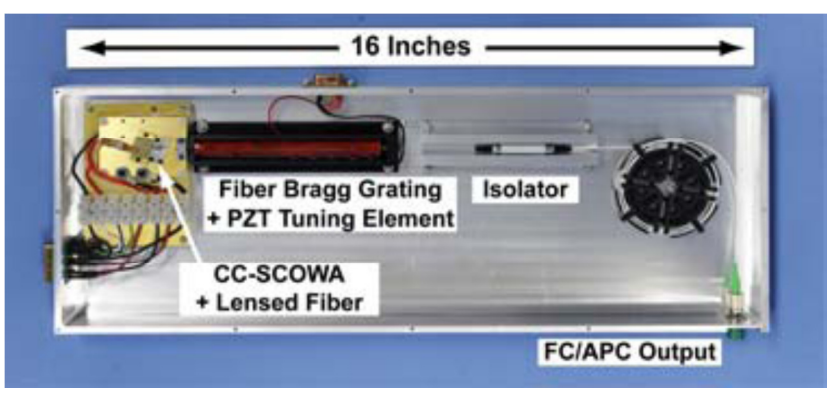

(b)

Fig. 1-11. Packaged SCOWECL (a) schematic and (b) photograph consisting of a double-pass curved-channel (CC) SCOWA, anti-reflection (AR) coated lensed fiber, fiber Bragg grating, and isolator.

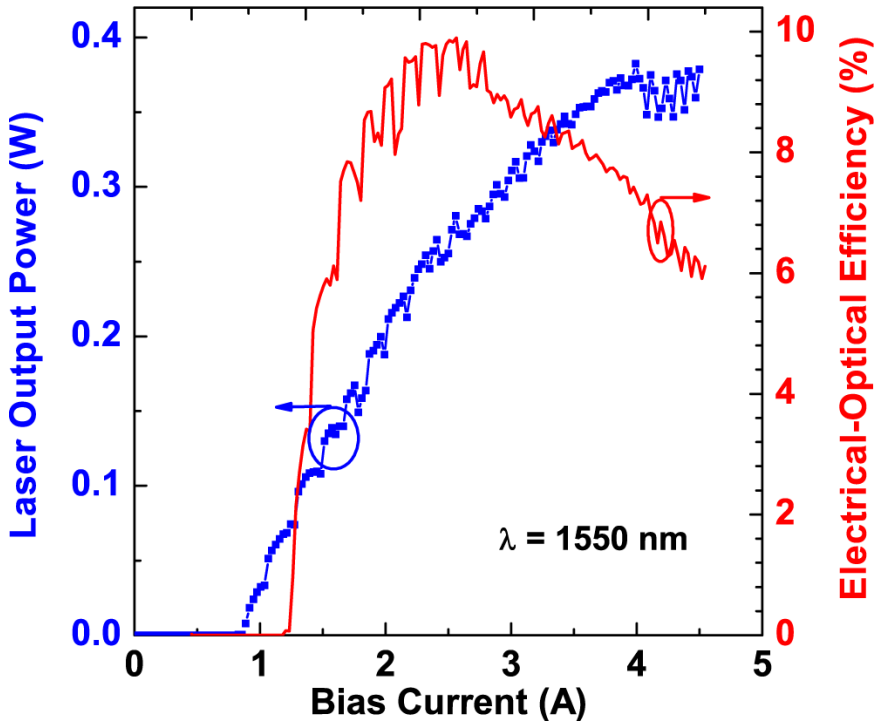

Figure 1-12: Measured packaged SCOWECL output power and efficiency versus bias current. The SCOWECL is operated at 1550 nm wavelength.

monolithic gratings or gratings in an external passive cavity. In this section, we describe the slab-coupled optical waveguide external cavity laser (SCOWECL) [26–28] and defer the discussion of monolithic grating lasers to the next section. A schematic and photograph of the SCOWECL (fabricated and packaged by MIT Lincoln Laboratory) is shown in Fig. 1-11. The SCOWECL cavity comprises a 1-cm-long double-pass curved-channel (CC) SCOWA, an anti-reflection-coated lensed fiber, a fiber Bragg grating (FBG) (λ_c = 1550 nm, $\Delta\lambda$ = 20 pm, R = 20%), and a fiber-pigtailed 60-dB optical isolator. The lensed fiber, FBG, and isolator are interfaced via fusion splicing. Care was taken to minimize the length of lensed fiber (3 cm) to prevent multi-mode lasing. Although the initial SCOWECL package spans an area of 16 in. × 6 in. (comparable to fiber lasers), efficient utilization of space would result in >2 times savings in size. The packaged SCOWECL exhibits >350 mW output power (Fig. 1-12) with ~35 kHz (1 kHz) Gaussian (Lorentzian) linewidth (Fig. 1-13) operated at 1550 nm wavelength [27]. Compared to

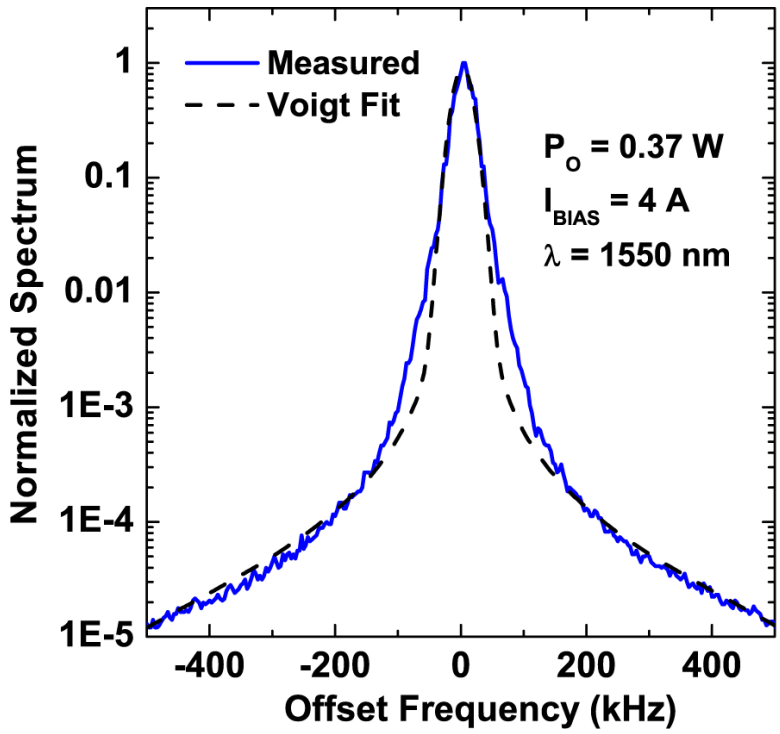

Figure 1-13: Measured packaged SCOWECL normalized spectrum and its associated Voigt fit. The SCOWECL is operated at 4 A bias and 1550 nm wavelength.

other semiconductor lasers at 1550 nm, the SCOWECL's output power is larger by a factor of ~10.

Its relative intensity noise (RIN) is shot-noise limited (<-160 dBc/Hz) at high frequencies. At low frequencies, the RIN degrades due to effects of flicker noise. Even then, the SCOWECL's RIN remains superior compared to the RIN of other lasers irrespective of their technology (semiconductor, fiber, or solid state) as we will see in Chapter 4. The SCOWECL's excellent power and noise characteristics are useful for a variety of applications. In this thesis, we will be primarily interested in applying the SCOWECL as a pump laser for use in a high-performance OEO.

1.3.3 Slab-Coupled Optical Waveguide Distributed Feedback Laser (SCOW-DFB)

Monolithic single longitudinal mode lasers can also be realized by etching gratings directly into the semiconductor active cavity. By integrating gratings into a SCOW laser, very-compact high-power single-mode lasers can be realized. Both the distributed feedback laser (DFB) and the distributed Bragg reflector (DBR) laser are possible configurations for achieving monolithic single-wavelength operation. In comparison to DBR lasers, DFBs are typically more compact and obtain higher optical output powers. However, DFBs also suffer from low yield due to the sensitivity of lasing operation to the position of the facet cleave. DBR lasers are more complex to fabricate than their DFB counterparts but offer the potential for separate wavelength tuning of the Bragg mirrors. DBR lasers also do not face complications from the position of the facet cleave. In this thesis, we choose to demonstrate slab-coupled optical waveguide lasers based on the DFB configuration primarily due to its inherent simplicity. The fabrication details and experimental findings of these devices are deferred to Chapter 7. Here, we will instead briefly review the principles fundamental to DFB operation.

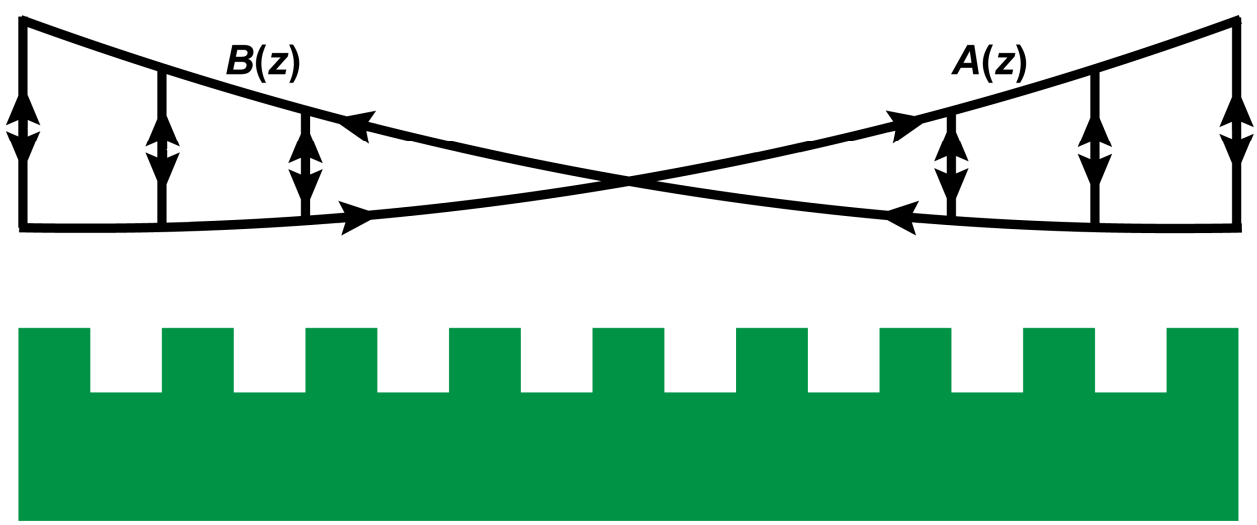

Figure 1-14: Illustration of a grating stack in a DFB laser along with the corresponding intracavity field profile of the lasing mode. $A(z)$ and $B(z)$ denote the forward and backward propagating fields, respectively.

Figure 1-14 shows an example of a grating stack found in a DFB laser along with the corresponding intracavity field profile of the lasing mode. The forward $\left(A(z)\right)$ and backward $\left(B(z)\right)$ propagating fields are coupled through their reflection at each grating interface. This coupling between fields is illustrated for some (but not all) of the reflection interfaces in Fig. 1-14. The total electric field $\left(E(z)\right)$ is given by the sum of the forward and backward components through

$$E(z) \cong A(z)e^{-j\beta z} + B(z)e^{+j\beta z} \tag{1.10}$$

Here, β denotes the average propagation constant of the wave along the laser cavity. The interaction of the forward and backward waves is conventionally analyzed through a set of coupled-mode equations with the form [29, 30]

$$\begin{aligned} \frac{dA(z)}{dz} &= -j\kappa_{+l}e^{+2j\Delta\beta z}B(z) \\ \frac{dB(z)}{dz} &= +j\kappa_{-l}e^{-2j\Delta\beta z}A(z) \end{aligned} \tag{1.11}$$

In Eq. (1.11), $\Delta\beta$ denotes the detuning (including effects of gain or loss) from the Bragg resonance and κ_{+l} (κ_{-l}) denotes the coupling coefficient to the forward (reverse) wave due to scattering from the lth grating order. Combined, the coupled-mode equations have the interpretation that the forward and reverse waves continuously feed each other as they both propagate through the cavity. Furthermore, the detuning from the Bragg resonance can be seen to yield an additional phase shift along z to the propagating wave or to yield attenuation/gain for complex values of propagation constants. Eq. (1.11) can be solved to determine the threshold condition of the DFB [29], which depends strongly on the feedback supplied by the grating through κ_{+l},κ_{-l}. In Chapter 7, we will show how to design a DFB so that κ_{+l},κ_{-l} is optimized.

Previous demonstrations of semiconductor DFB lasers have mostly achieved output powers limited to <50 mW at 1550 nm wavelength. However, higher power DFBs have also been demonstrated [31, 32] with output powers approaching 440 mW (340 mW fiber-coupled) [32] using 2 mm of cavity length. The lasers of [32] also exhibited <2 MHz linewidth with ~30 dB of

side mode suppression and unspecified RIN performance. The performance of DFBs based on high-power low-noise SCOW technology will be the subject of our discussions in Chapter 7.

1.3.4 Slab-Coupled Optical Waveguide Photodiode (SCOWPD)

All the devices discussed previously have normal operation in the forward-bias regime, generating gain by the process of stimulated emission. Reverse-biased devices can also be implemented with SCOW technology, and we describe one example of this (the SCOWPD [33, 34]) here. The SCOWPD is a waveguide photodiode developed by MIT Lincoln Laboratory based on a low-confinement design. The advantage of using a low-confinement photodiode is that large optical powers can be absorbed before suffering limitations due to device saturation and thermal failure. The absorption is distributed over a longer device length, thereby limiting the power absorbed per unit length. Photocurrents of 250 mA at 0.8 A/W responsivity [33] have been achieved using these principles. In conventional photodiode structures, most of the optical power is absorbed near the device input since the power diminishes with each additional propagation step. This leads to premature photodiode saturation as any further device length effectively becomes unutilized. To prevent these undesirable effects, variable confinement SCOWPD structures (VC-SCOWPD) have been designed where Γ increases with device length to obtain nearly uniform power absorption [34]. Various VCSCOWPDs have demonstrated performance ranging from 40 mA saturation currents (at 1 GHz) with bandwidths of 12.6 GHz to >100 mA saturation currents (at 1 GHz) with bandwidths of 2.5 GHz [34]. Although these particular VC-SCOWPDs exhibited responsivities of (~0.7-0.8 A/W), other structures have achieved $\Re \sim 1$ A/W. Note that these SCOWPDs are also all unterminated and thus do not suffer any inherent 6 dB loss in their delivered electrical power.

Despite the advantages of higher power handling, a large waveguide design comes with the tradeoff of lower bandwidth (via an increase in device capacitance). Ideally travelling-wave structures [35] can be employed to overcome these limitations, potentially allowing for both high optical powers and unrestricted operating bandwidth. However, these structures are typically complicated to successfully implement, especially for photodiodes of longer lengths. In many cases, it may be sufficient to simply design a photodiode using conventional means while reaching a suitable optimum in its parameters.

1.3.5 Comparison Between Optical Device Technology

In this section, we provide a comparison between a few of the technologies that can be used to make optical devices (Table 1-2). The key technologies considered here are those of fiber, semiconductor, and SCOW operating at 1550 nm wavelength. The highest output powers are generally obtained by fiber devices with optical powers >1 W commercially available. For OEO applications, this power is excessive as it becomes greater than the amount necessary to achieve net MWP gain. In most cases, this power is even detrimental due to the nonlinear noise processes incurred from propagation over a long optical delay. The SCOW technology thus supplies the optimum amount of power for operation of the OEO. The gain provided by SCOW devices is generally lower than that achieved by fiber and traditional semiconductor devices. Even so, this gain is enough for the purpose of enabling oscillation in a laser or COEO. The size and efficiency of SCOW devices also lag behind that of semiconductor technology but become tradeoffs necessary to obtain high output power.

Perhaps the most important parameter for an OEO/COEO is RIN as it determines the level of noise injection and therefore directly influences oscillator phase noise. The RIN of semiconductor and SCOW devices are generally lower than that of fiber components due to their intrinsic suppression of intensity noise under saturation [36]. This suppression can be understood from Fig. 1-15 taking as an example an amplifier whose gain has been depleted by a large signal

Table 1-2: Comparison of parameters for optical devices developed from fiber, SCOW, and semiconductor technologies.

	Fiber	SCOW	Semiconductor
Output Power	>1 W	0.5-1 W	10-50 mW
Gain	40 dB	15-30 dB	40 dB
Size	>1 m	~1 cm	~100-500 μm
Efficiency	Low	Medium	Medium-High
RIN	Moderate *Large relaxation oscillation ~100 kHz*	Low *No relaxation oscillations*	Low-Moderate *Large relaxation oscillation 5-10 GHz*

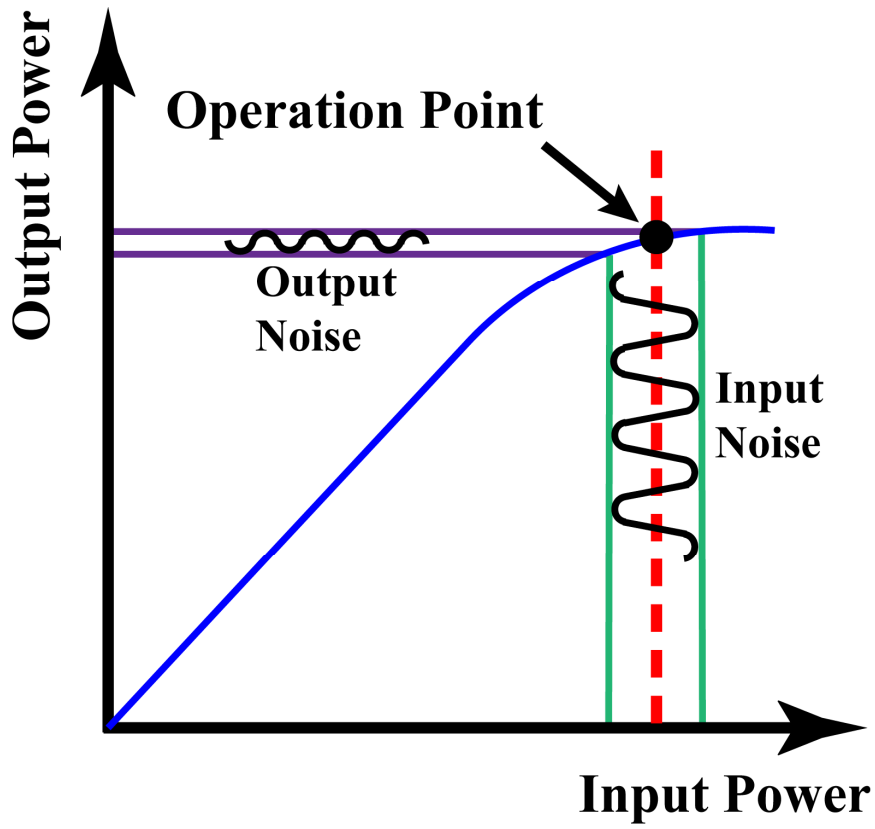

Figure 1-15: Illustration of intrinsic RIN suppression characteristic of a saturated device.

input. At the operating point, the amplifier's saturation causes the output to become a slow function of input power. If we consider the input power to now fluctuate (due to intensity noise), the resulting fluctuations on the output would be greatly attenuated. At the point where the slope is zero, the output noise can be effectively eliminated. It is important to note that this RIN suppression occurs for any saturated optical amplifier or for any system comprising a saturated amplifier (e.g. a laser) irrespective of its technology (fiber, SCOW, semiconductor, etc). However, this applies only if the gain medium can respond to the fluctuations. The corresponding cutoff frequencies are ~10 GHz for semiconductor and SCOW amplifiers and ~1 kHz for fiber amplifiers. The inability of fiber components to take advantage of this suppression mechanism beyond ~1 kHz makes their RIN (typically reaching a floor of ~-140 dBc/Hz near 100 kHz) too high for use in the OEO/COEO.

As can be seen from Table 1.2, the RIN is generally lowest for SCOW devices. In comparison to semiconductor technology, SCOW components offer higher power at similar levels of spontaneous emission which decreases the photodetected signal × spontaneous beat noise relative to signal × signal. In addition, SCOW lasers typically do not exhibit any signature of relaxation oscillations due to their long photon lifetime design [27]. For conventional semiconductor lasers, this relaxation resonance typically occurs between 5-10 GHz resulting in significant degradations to the overall high-frequency RIN performance. For fiber lasers, the relaxation oscillation occurs at ~100 kHz but becomes upconverted by the modulation/photodetection process into the operation band of the OEO (see Chapter 4 for more details). The unique advantages offered by the SCOW technology thus allow for excellent OEO/COEO phase noise at potentially any RF frequency of oscillation limited only by the bandwidth of the components. This wide operating range may become important when future frequency agile solutions become available.

One of the major goals of this work is to obtain an order of magnitude improvement in phase-noise compared to the OEO systems of Fig. 1-7. Based on the RIN of their Nd:YAG pump laser [11, 37], we can determine the required laser RIN in order to achieve these goals. The RIN of the Nd:YAG is -100 dBc/Hz at 10 Hz offset and decreases to a floor of -140 dBc/Hz at 10 kHz offset. At frequencies beyond its relaxation resonance (~200 kHz), the RIN drops towards its value limited by shot noise. To improve on OEO phase noise by an order of magnitude, our required laser RIN needs to be 10 dB lower. This effectively constrains the RIN to be lower than -110 dBc/Hz at 10 Hz offset frequency and lower than -150 dBc/Hz RIN at 10 kHz offset. In Chapter 4, we will show that these requirements are readily met by the SCOWECL. The final goal of this work would be to integrate the full functionality of the OEO onto a single chip of InP.

Chapter 2

Oscillator Phase Noise – White Noise

Oscillators are essential components enabling operation for a wide variety of systems. Their applications span multiple disciplines of science, and their use is ubiquitous at frequencies ranging from optical to microwave and below. A solid understanding of oscillator operation is critical for the modeling and design of future oscillator systems.

The most important property which characterizes oscillator performance is phase noise. Due to an oscillator's intrinsic negative feedback (maintaining gain = loss) and to various amplitude-limiting components in the cavity (e.g. the saturated amplifier), the low-frequency amplitude noise is typically greatly suppressed relative to phase noise. As the primary function of many oscillators is to generate a pure sinusoid, the phase noise acts to degrade operation by spreading the oscillator power across a range of frequencies.

Over the last several decades, significant research has been devoted towards understanding the problem of oscillator phase noise. The simplest theories represent the oscillator as a linear time-invariant (LTI) system and consider the oscillator's output as a resonant response to input noise [4, 38]. Although intuitive, these theories do not account for the randomness in the phase of noise upon each addition of noise to the oscillator field. Although intuitive, these theories do not account for the randomness in the phase of noise upon each addition of noise to the oscillator field. The relative phase between the signal field and the added noise results in separation of the noise perturbation into quadratures of amplitude and phase, forming the basis for linear time-variant (LTV) analysis as applied in [39, 40]. The linearization of the oscillator phase in [39, 40], however, introduces nonphysical artifacts of infinite spectral power at frequencies leading up to the carrier. In an alternative description of the oscillator through a rigorous stochastic differential equation, [41] and [42] apply Floquet theory to show the oscillator spectrum to be a Lorentzian for white-noise perturbation. The Lorentzian distribution [29], [41–45] establishes the power at the oscillation frequency to be finite, relieving predictions of infinite power [38, 39]. Although the approach of [41] and [42] is rigorous, its resulting solution is non-intuitive and difficult to

apply as it requires detailed analysis of the oscillator dynamics, e.g., the determination of the Floquet eigenvectors. Ideally, one desires a simple and intuitive functional description of oscillator phase-noise, similar to the empirical model proposed by Leeson [38], but based on physics fundamental to the behavior of an oscillator [41, 42]. Because of the many parallels that exist between electrical and optical oscillators, one would desire this description to be general so as to encompass the operation of oscillators across both disciplines.

In this chapter, we present a novel and general approach to the description of phase noise when the oscillator field is sinusoidal and perturbed by additive white-noise [46]. Our theory is intuitive and expands upon the method of vector addition used by Henry [45] to describe the linewidth of semiconductor lasers. This approach is consistent with the use of linear time-variant analysis but does not impose linearization of the oscillator's phase in the steady-state. To improve upon existing theories, we also introduce a concept of noise partitioning in order to treat the interaction of noise with the oscillating field. Our formulation is based on the observation that the continuum representation of noise outside the cavity becomes an inappropriate description of noise within the confines of the oscillator boundaries. The noise generated must instead be coupled into the modes of the resonant cavity, which together form the basis of the oscillator. The amount of noise coupling into each mode is modified by the density of modes, as has been well established in laser physics [29], [47–56]. We note that the restriction of our present analysis to white-noise perturbation prevents full application of the theory to oscillators which also exhibit noise of $1/f^{\alpha}$ characteristics. However, the foundations provided here should prove helpful for understanding oscillator behavior under noise perturbation of arbitrary form (Chapter 3). A central underlying theme for the work presented here is the unification in the understanding of phase noise for both electrical and optical oscillators. Towards that end, we show that our general theory of phase noise is consistent with well-established models of laser linewidth [29, 43, 45]. We also support our theory by measuring the phase noise of electrical oscillators and show excellent agreement over a wide range of operation. We conclude by comparing the theory to the measured phase noise of a hybrid optoelectronic oscillator [4, 37, 57, 58] to further demonstrate the generality of the theory.

2.1 Oscillator Phase Noise Theories

In the following sections, we present a few of the popular theories currently used for analyzing oscillator phase-noise. Our purpose is not to provide a review but rather to show the critical elements missing in each analysis. We believe that this information is not common knowledge in the literature on oscillators. This discussion will also provide the necessary introduction for our proposed unified theory of phase noise in Section 2.2.

2.1.1 LTI Theories of Oscillator Phase-Noise

In this section, we present a detailed discussion of LTI theories of phase noise, which currently find widespread usage due to their inherent simplicity [4, 38]. Our goal here is to show the foundations for LTI theory to be flawed, even though many of the model's predictions appear to correspond to measurement. This section will also serve to highlight the broad range of oscillators our theory is applicable to.

Figure 2-1 shows a block diagram of a generic oscillator operating by means of positive feedback. The amplifier noise ($N(\omega)$) is taken to be the system input that is delayed ($e^{-j\omega T}$),

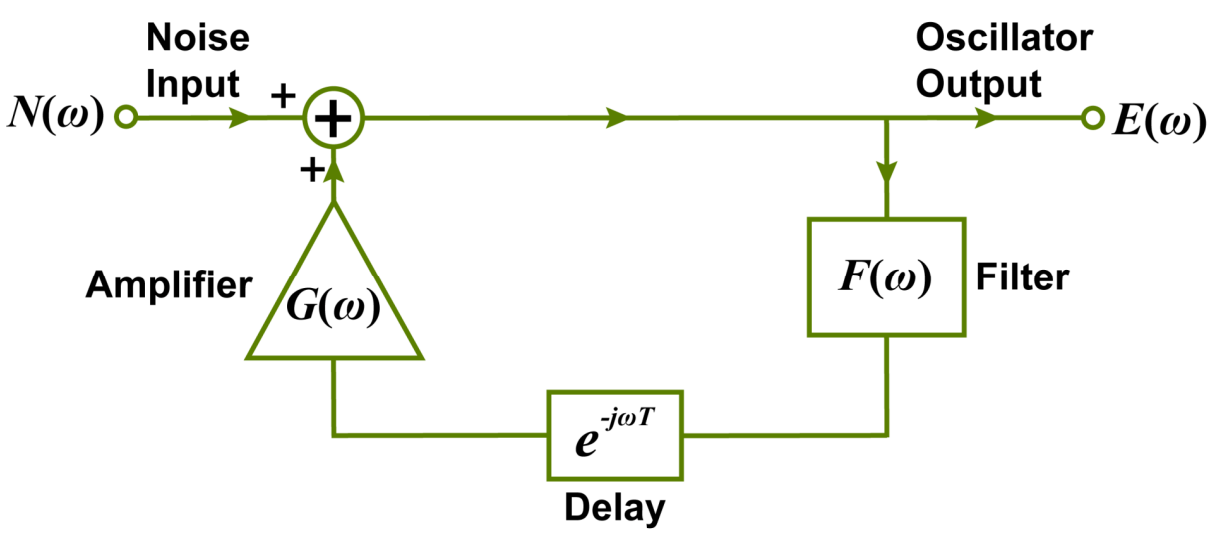

Figure 2-1: Block diagram illustration of phase noise in an oscillator consisting of an amplifier, delay line, and filter wrapped in a positive feedback circuit.

amplified (net gain $G(\omega)$), and filtered (transfer function $F(\omega)$) on each roundtrip of the oscillator. Note that the delay does not have to be purely a physical delay and in this case includes the group delay accumulated from signal propagation through the filter resonance. Despite its inherent simplicity, the system of Fig. 2-1 represents the general equivalent circuit for many types of oscillators. One example is a LC oscillator where the amplifier and system delay retain their usual definitions, and the LC resonator forms the equivalent filter.

We are interested in applying LTI analysis to the oscillator of Fig. 2-1. In addition to noise amplification, there is also reinjection of noise on every roundtrip with roundtrip time T. The system output can then be formulated as

$$E(\omega) = N(\omega) + N(\omega)G'(\omega)e^{-j\omega T} + N(\omega)G'(\omega)^2 e^{-j2\omega T} + \ldots = \frac{N(\omega)}{1 - G'(\omega)e^{-j\omega T}} \tag{2.1}$$

where $G'(\omega) = G(\omega)F(\omega)$ represents the cascaded amplitude response of the amplifier and filter. Equation (2.1) is the classic result derived from feedback analysis with the contributions of noise reinjection explicitly highlighted. To calculate the normalized spectrum, we multiply Eq. (2.1) by $E(\tilde{\omega})^*$, take the ensemble average, integrate over $\tilde{\omega}$ [29], and divide the result by the signal power (P_{sig}) yielding

$$\frac{S_E(\omega)}{P_{sig}} = \frac{S_N(\omega)}{P_{sig}} \frac{1}{1 + G'(\omega)^2 - 2G'(\omega)\cos(\omega T)} \tag{2.2}$$

In Eq. (2.2), $S_E(\omega)$ represents the spectral density of the output field, while $S_N(\omega)$ denotes the spectral density of the noise process itself. Under steady-state conditions, $G'(\omega)$ approaches the value of unity at the oscillation frequency. Equation (2.2) thus shows that modes are formed at the oscillator resonance frequencies ($\omega T = 2m\pi$) where m is a non-negative integer. Expanding Eq. (2.2) around a single resonance results in

$$\frac{S_E(\omega)}{P_{sig}} = \frac{S_N(\omega)}{P_{sig}} \frac{1}{\Delta\omega^2 T^2} \tag{2.3}$$

where we have taken $G'(\omega)=1$ for small $\Delta\omega$. Here, $\Delta\omega$ is the offset angular frequency around the carrier. Equation (2.3) is analogous to standard results from LTI models of phase noise [4, 38–40].

Many aspects of Eq. (2.3) are deceptively pleasing. For example, the oscillator spectrum is proportional to the strength of the noise relative to the signal power. This corresponds to intuition since one would expect worse phase-noise performance when the noise-to-signal ratio is larger. Equation (2.3) is also to a good approximation inversely proportional to the delay time squared, which agrees closely with results from experimental measurement. Note that the divergence of the spectrum at $\Delta\omega=0$ is primarily a result of specifying $G'(\omega)=1$. In a real oscillator, the net gain is always slightly below unity so that a constant power can be maintained in the presence of noise injection. With $G'(\omega)<1$ and expanding the cosine around the carrier, it can be seen that Eq. (2.2) assumes the form of a Lorentzian [4]. However, we wish to make clear this result represents only an approximation to Eq. (2.2), and thus LTI models of oscillator phase-noise do not predict Lorentzian behavior at higher offset frequencies. One consequence of this is that when $G'(\omega)\approx 1$, the lowest possible value of the spectrum (relative to carrier) predicted by Eq. (2.2) is one-fourth the noise-to-signal ratio ($S_N(\omega)/4P_{sig}$). This occurs when the total roundtrip phase shift is an odd multiple of π (i.e., $\omega T=\pi+2m\pi$).

As of this point, we have not constructed any clear argument indicative of flaws inherent to LTI treatments of phase noise. In the remainder of this section, we will discuss the critical error of LTI analysis, which is related to the assumption of time invariance. In particular, the timing (phase) of a noise event relative to the signal determines how the added noise power is split between amplitude and phase [39, 40]. Currently, Eq. (2.1) assumes *every* instance of noise injection to have a fixed phase relative to the signal. As a result, the distinction between noise and a deterministic signal becomes lost. This picture violates our understanding of noise as a random process. Note that the minimum spectrum value of $S_N(\omega)/4P_{sig}$ predicted by LTI analysis results from the destructive interference of noise. Once again, this interference cannot occur as the different instances of noise are incoherent with one another.

2.1.2 LTV Theories of Oscillator Phase-Noise

The limitations of time invariance for describing noise in oscillators have motivated some authors to search for linear time-varying (LTV) descriptions of phase-noise [39, 40]. We will again present a short review of this work while at the same time pointing out the key deficiencies of the theory.

The central principle behind LTV analysis is that the timing of a noise event relative to the signal determines the amount of noise that couples into amplitude or phase. This is best illustrated by Fig. 2-2, which shows the addition of noise that is both (a) in-phase and (b) out-of-phase to an oscillating signal. When the noise is in-phase, the peaks and valleys add constructively with the signal to generate a pure amplitude shift of the original signal. When the

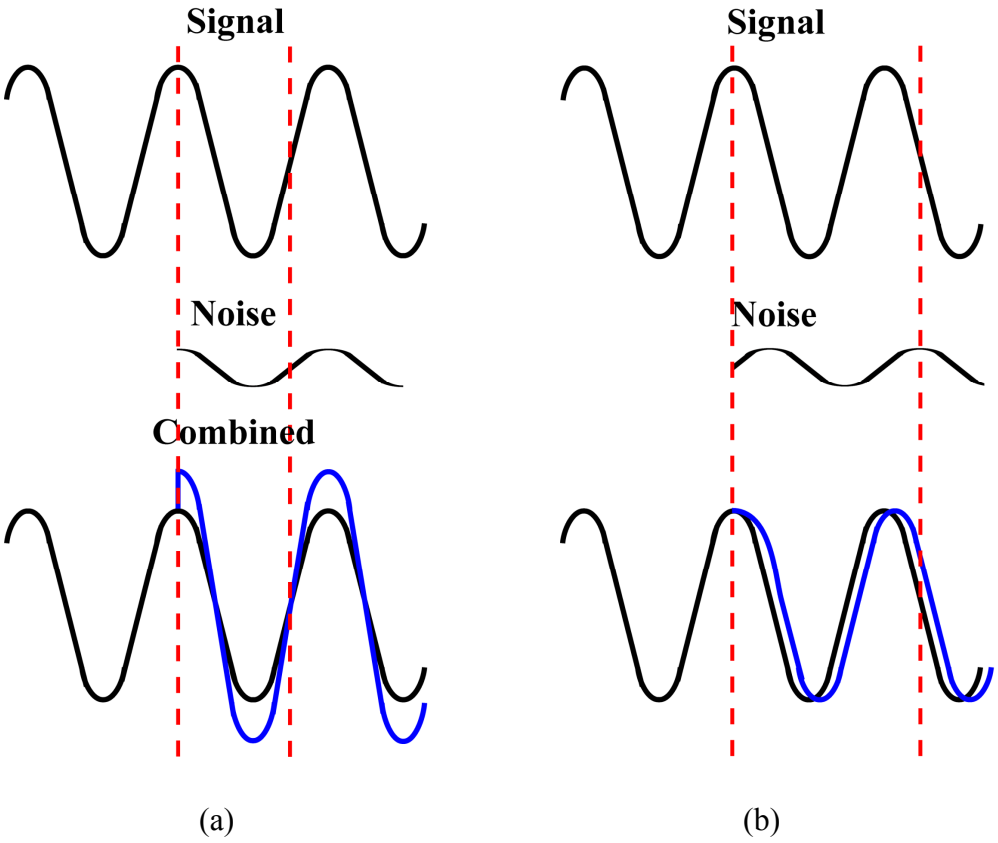

Figure 2-2: Illustration of noise that is added (a) in-phase and (b) out-of-phase to an oscillating signal. The relative phase between noise and signal results in a perturbation to amplitude, phase, or a combination of the two.

noise is out-of-phase, the superposition of noise with signal results primarily in a phase shift. Note that there is also a small amplitude-shift component in this case that we have neglected in the illustration of Fig. 2-2 (b). When the relative phase of the noise and signal is in between these two extremes, the result is a perturbation to both the amplitude and phase of oscillation. Each noise event permanently shifts the phase of the signal as there is no method of feedback in an oscillator to recover. The accumulated phase shift can then be described by [39]

$$\phi(t) = \frac{1}{q_{\max}} \int_{-\infty}^{t} \Gamma(\omega_0 \tau) i(\tau) d\tau \tag{2.4}$$

where $q_{\max}$ is the maximum charge displacement across a capacitor and $i(\tau)$ denotes the impulse of fluctuating noise. The ratio of $i(\tau)$ to $q_{\max}$ represents a quantity similar to the noise-to-signal ratio found in LTI theories of phase noise. $\Gamma(\omega_0 \tau)$ denotes the periodic phase sensitivity function of the oscillator to noise. Eq. (2.4) has the interpretation that the accumulated phase shift is found by summing over all the individual occurrences of noise multiplied by the oscillator's sensitivity to noise. As an example calculation, the authors of [39] consider a noise input of $i(\tau) = I_1 \cos\left[(\omega_0 + \Delta\omega)\tau\right]$. Expanding the periodic sensitivity function in terms of its Fourier components (c_n), the resulting phase shift can be expressed as

$$\phi(t) = \frac{I_1 c_1 \sin(\Delta\omega t)}{2 q_{\max} \Delta\omega} \tag{2.5}$$

There are three potential issues with Eq. (2.5). The first is that the phase of the noise input is not random relative to that of the oscillating signal. From this perspective, there is no difference between noise and a coherent tone at $\omega_0 + \Delta\omega$. The second issue is that the purpose of the integration in Eq. (2.4) is inappropriately accomplished by this choice of noise. Ideally, one would like to sum together all the individual occurrences of noise up until time t. However, through the definition of $i(\tau)$, the integral instead adds together the cosine contributions of the same noise instance. The final problem is that the treatment of noise at frequencies around the carrier is handled improperly. Note that Eq. (2.5) is designed to be applicable even when the frequencies of noise and signal are different ($\Delta\omega \neq 0$). In Fig. 2-2, this has the implication that

the noise and signal (at different frequencies) are being summed together to generate a net phase shift for the signal. However, this operation is invalid as the individual components of noise and signal are orthogonal in this case. In Section 2.2, we will show how to account for noise so that these issues are fundamentally resolved.

Continuing on, we are specifically interested in determining the spectrum of the oscillator's output. To begin, we use the relation between voltage and phase for small values of the phase fluctuation $[V(t)/V_0 = \cos(\omega_0 t + \phi(t)) = \cos(\omega_0 t) - \phi(t)\sin(\omega_0 t)]$. Note that we have also normalized to the signal voltage in anticipation of the forthcoming calculation of phase noise. Substituting in Eq. (2.5), it is clear that the two sinusoidal components mix together to produce sidebands spaced at $\pm\Delta\omega$ from the carrier. Converting to the frequency domain, multiplying by $V(\tilde{\omega})^* / V_0$, taking the ensemble average, and integrating over $\tilde{\omega}$, we find the oscillator's phase-noise spectrum to be

$$\frac{P(\Delta\omega)}{P_{sig}} = \left(\frac{I_1 c_1}{4 q_{\max} \Delta\omega} \right)^2 \tag{2.6}$$

Equation (2.6) is unbounded when $\Delta\omega = 0$ due to the linearization of phase during the definition of the oscillating voltage. The variance of the oscillator's phase shifts grow to infinity over time, and thus the approximation $\phi(t) << 1$ becomes invalid.

2.1.3 Time-Domain Theories of Oscillator Phase-Noise

In this section, we present a brief discussion of phase-noise theories that use time-domain stochastic differential equations to model the interaction of an oscillator and noise [41, 42]. These theories begin with a state-variable (x) whose time evolution can be described through

$$\frac{dx}{dt} = f(x) + B(x) b(t) \tag{2.7}$$

where $f(x)$ is a state-dependent forcing function that drives oscillations in x and $B(x)$ ($b(t)$) is the state-dependent (time-dependent) component of the noise perturbation. In the absence of noise, if we take x to represent the sinusoidal oscillator field, then we see that both dx/dt and

$f(x)$ are also periodic with the same oscillation frequency. These periodicities in time make the system amenable to analysis using Floquet theory. Insertion of the expected steady-state solution $x(t) = x^0(t+\alpha(t)) + \Delta x(t+\alpha(t))$ into Eq. (2.7) results in a differential equation for the accumulated timing-shift ($\alpha(t)$)

$$\frac{d\alpha(t)}{dt} = v_1^T(t+\alpha(t))B(x_s(t+\alpha(t)))b(t) \tag{2.8}$$

$x^0(t+\alpha(t))$ is the oscillator state in the absence of noise, and $\Delta x(t+\alpha(t))$ is a perturbation to the steady-steady solution in the form of an amplitude and timing shift. In Eq. (2.8), $v_1^T(t+\alpha(t))$ is a byproduct of Floquet analysis which represents the sensitivity of the oscillator's timing to noise events occurring at time t. Multiplying by dt on both sides, Eq. (2.8) has the interpretation that the accumulated shifts in timing are governed by the product of the noise occurring within dt and the oscillator's sensitivity function to noise [59]. This interpretation parallels the insights provided by the time-varying analysis of phase noise discussed in the previous section (Fig. 2-2).

Using Eq. (2.8), the authors of [41] derive a partial differential equation describing the probability density of $\alpha(t)$, known in literature as the Fokker-Planck equation. The Fokker-Planck equation can be transformed into an equation of its associated characteristic function, whose solution (over long time periods of perturbation) is a Gaussian random variable. This Gaussian characterizes the diffusion of phase (oscillator timing) as noise is injected into the cavity. The oscillator's phase-noise spectrum can then be determined from the autocorrelation of its field ($x(t)$), yielding the form of a Lorentzian. This Lorentzian establishes the power at the carrier frequency to be finite, in contrast to the LTI and LTV theories discussed in the previous sections. We refer the reader to [41, 42] for a full treatment using this method.

The mathematical rigor afforded by these time-domain phase-noise theories comes at a high cost of computational complexity. However, by itself, this is usually a fair price to pay for the analytical capabilities of a fully functional model of the oscillator. The major deficiency of these theories is instead that they currently cannot be used to make accurate phase-noise predictions. As we will see later, this results because the current knowledge base of oscillators is insufficient

to specify the noise fluctuation of Eq. (2.7), which was also a common theme in LTV analysis. Without a complete description of the injected noise, absolute levels of the oscillator phase-noise cannot be determined.

2.2 Unified Theory of Phase Noise

In the previous section, we highlighted the need for a consistent model of oscillator phase-noise. In particular, we emphasized that the conventional treatment of noise injection was incomplete in most of the major theories used today. In the following sections, we will show that this injected noise obeys a fundamental principle of partitioning such that the noise becomes distributed among the oscillator modes. We also supplement these concepts with our own model of phase noise, which expands upon techniques used by Henry to describe the linewidth of semiconductor lasers [45]. The end result will be a unified theory of phase noise applicable to electrical oscillators, optical oscillators, and beyond.

2.2.1 Phase-Noise Theory

We begin by considering the oscillator electric field $E(t)$ represented as a phasor in the complex plane (Fig. 2-3) [45]. Its initial magnitude is normalized such that $E_0^2 = P_0$, where P_0 is the intracavity power of the signal. The oscillator's phase starts at an arbitrary angle ϕ with respect to the real axis. The addition of a noise event, having magnitude E_n such that $E_n^2 = P_n$ and relative phase θ_i, results in perturbation of both the amplitude and phase of the original oscillating field. As the phase of the noise event is random relative to that of the field, θ_i is uniformly distributed between 0 and 2π. The amplitude of the total signal vector E_T is given by $E_T^2 = P_0 + \Delta P_i$ where ΔP_i is defined as the change in oscillation power induced by a noise event having relative phase θ_i. From Fig. 2-3, we can calculate the phase perturbation $\Delta\phi_i$ to be

$$\Delta\phi_i = E_n \frac{\sin(\theta_i)}{E_0} \tag{2.9}$$

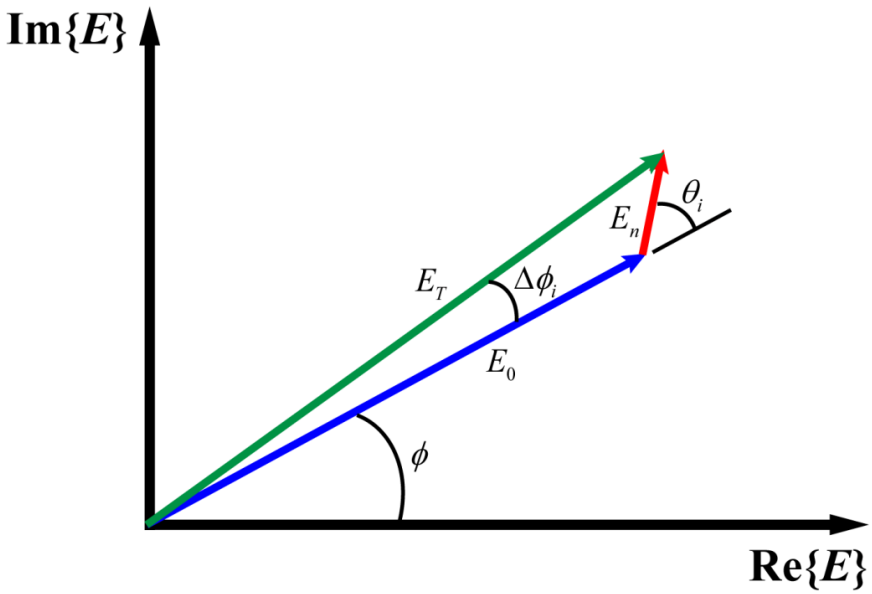

Figure 2-3: Vector-based description of an oscillator's field under noise perturbation.

where we have approximated $E_T \approx E_0$ and $\sin(\Delta\phi_i) \approx \Delta\phi_i$. The approximations state that the amplitude and phase shift induced by *a single* noise event results in only small perturbations of the oscillator's total amplitude and phase. This statement is intuitive and does not contradict the unbounded divergence in the variance of the total accumulated phase [42]. Using similar techniques, one can also formulate an expression for ΔP_i as

$$\Delta P_i = P_n + 2\sqrt{P_0 P_n}\cos(\theta_i) \tag{2.10}$$

Equations (2.9) and (2.10) describe the time-varying interaction of signal and noise [40, 41]. If the noise is in-phase with the oscillation field ($\theta_i = 0$), the noise appears only in the amplitude of the signal. If the noise is out-of-phase with the signal ($\theta_i = \pi/2$), the noise primarily appears as a phase shift. Note that the first term on the right hand side of Eq. (2.10) corresponds to the mean perturbation of the signal power (averaged over all θ_i) due to a single noise event. When also averaged over the strength of a noise event, this corresponds for a laser to the addition of one noise photon per optical mode [45]. For a general oscillator, P_n represents the noise power coupled into a single mode of the oscillator due to a single noise event. The fact that the axes

which govern pure phase shift and pure amplitude shift are oblique and not orthogonal has previously been shown in [60].

Using the Wiener-Khinchin theorem [61], one proceeds in calculating the phase-noise spectrum through the autocorrelation of the oscillating field (see Appendix A.1)

$$\left\langle E(t)^* E(t+\tau) \right\rangle \approx E_0^2 e^{j2\pi f_0 \tau} e^{-\left\langle \Delta\phi^2 \right\rangle / 2} \tag{2.11}$$

In Eq. (2.11), f_0 is the oscillation frequency, τ is the time delay over which noise events are observed, and $\left\langle \Delta\phi^2 \right\rangle$ is the second moment of the phase shift incurred over τ. As the phase shifts have zero mean, $\left\langle \Delta\phi^2 \right\rangle$ is also the variance of the total phase shift. Because the oscillating power is stabilized around its mean, we can use Eq. (2.9) to define $\Delta\phi$ induced by M noise events through

$$\Delta\phi = \sum_{i=1}^{M} E_n \frac{\sin(\theta_i)}{E_0} \tag{2.12}$$

Since each noise event is independent, the variance in phase shift can be shown to be

$$\left\langle \Delta\phi^2 \right\rangle = \frac{\overline{P}_n}{2P_0} M \tag{2.13}$$

where $\overline{P}_n = \left\langle P_n \right\rangle$ is the average strength of a noise event. The factor of 1/2 in Eq. (2.13) is due to equipartitioning of the noise such that half of the noise power is used for driving phase fluctuations [29].

As a starting point, one could potentially attempt to find E_n, P_n through the continuous spectrum of white noise. However, doing so, one quickly finds that it becomes necessary to vectorially add noise to the oscillating field (Fig. 2-3), even when their individual frequencies are different. This is resolved through the realization that the continuum representation of noise outside the cavity becomes inappropriate for describing noise within the confines of the oscillator boundaries. The noise must instead be distributed into the individual modes of the resonant system, which together form the basis of the oscillator. The average magnitude of the

noise event $\overline{P}_n$ is thereby found by determining the amount of noise coupled into the oscillating mode. For the case of lasers, quantum theory establishes the average magnitude of a spontaneous emission event to be the equivalent of one noise photon per cavity mode [29, 45, 62]. The corresponding rate of spontaneous photon emission into the cavity mode per unit volume is denoted as R'_{sp} [29, 45]. To progress further in our development, we require a similar fundamental relation but for the case of a general electromagnetic oscillator. In their laser analysis, the authors of [29] treat R'_{sp} by distributing the total spontaneous emission among the modes of the optical cavity. For the case of a white-noise spectrum, the noise is equally coupled into all the modes. As the properties of noise are identical in electromagnetic oscillators, one expects this approach to be applicable outside the description of a laser.

At this point, it is useful to make a few comments regarding application of this formalism to a general theory of oscillator phase noise. First, the modes of a general cavity are three dimensional in nature and are associated with various polarizations. Therefore, one must count the number of modes in all orthogonal directions and polarization states [29, 50, 53, 54]. For our purposes, we consider only a linear cavity supporting a single polarization, both for simplicity and for comparison to our measured results for electrical oscillators. Note that although our description above implicitly assumes a Fabry-Perot resonator, the developed phase-noise theory can be applied to any oscillator configuration. The concept of a mode is general to any three-dimensionally confined structure, which we will designate by the term 'cavity'. In the next section, we will measure electrical oscillators based on ring cavity geometries (i.e., microwave components connected in a closed loop). The ring geometry can be obtained from a Fabry-Perot by unfolding the Fabry-Perot at its reflection point. The electronic amplifier used in our oscillator only operates from 2-4 GHz and thus only couples noise to the fundamental TEM mode of a coaxial line. If necessary, one can readily extend our approach to cavities of higher dimensionality and number of polarization states. Second, the various noise sources considered are white only up to a certain cutoff frequency. In cases where the spectral width of the noise only encompasses a few cavity modes, the noise is approximately partitioned into only those modes. This is analogous to the concept of a thresholdless laser where all of the spontaneous emission is consumed by a single mode of the cavity [51, 52, 55, 56]. And third, as gain is required to achieve oscillation, it is unphysical to have an oscillator where the amplifier noise

and the oscillating cavity modes do not overlap. In systems where this overlap is small, both the gain and the emission of noise become inhibited [63].

For an oscillator supporting a single transverse mode having a single polarization state over the frequency range where noise is generated, the noise power is only distributed into the longitudinal modes of the cavity. When the cavity is large such that the noise spectrum encompasses many longitudinal modes, one can compute the noise power per mode $\overline{P}_n$ as

$$\overline{P}_n = \frac{N_{psd}}{T} \tag{2.14}$$

where N_{psd} is the power spectral density of the white-noise perturbation and T is the total roundtrip time delay of the cavity. Equation (2.14) is derived by integrating the white noise over a span Δf around the oscillating mode and subsequently dividing the result by the number of modes contained in Δf. This derivation thus implicitly assumes that the total noise power remains constant independent of the length of passive cavity. The conservation of power can be directly verified in the case of thermal noise. For thermal noise, each independent mode of the system acquires an average energy $k_B T_0$, and thus the average power delivered by each mode is $k_B T_0 / T$. Here, T_0 denotes the equilibrium temperature of the system. The density of modes per unit frequency in a one-dimensional cavity is given by T so that the number of modes in a frequency interval Δf can be expressed as $T\Delta f$. The total power delivered by all the modes within Δf is therefore $k_B T_0 \Delta f$, which agrees with conventional expressions for the integrated power spectral density of thermal noise. A similar line of reasoning starting with the laser rate equations can be used to show that the same conservation of power also applies to spontaneous emission. If we assume this property holds for noise in general, Eq. (2.14) then intuitively shows that a larger T results in a larger density of longitudinal modes and thus reduced noise power coupled into each mode. Note that this power conservation does not apply when the transverse dimensions of the cavity are increased.

For white noise, the occurrence of M noise events in Eq. (2.13) corresponds to an average rate of noise injection (R_{inj}) multiplied by an average observation time ($|\tau|$) [45]. We can combine all the noise sources encountered during a cavity roundtrip through vector addition and

treat the result as a single noise source acting on the signal of Fig. 2-3. The composite continues to satisfy Eq. (2.9) even if the total amplitude and phase shift are no longer small compared to that of the oscillating field (see Appendix A.2). The physics of the interaction are still governed by the phase and amplitude shifts of each individual noise event. Furthermore, as there is no distinction from one phase angle to the next, there can be no preference in direction of the resultant noise vector. The composite collection of noise thus obeys Eqs. (2.11)-(2.12) with $\theta_{i,tot}$ uniformly distributed between 0 and 2π. The total power ($\overline{P}_{n,tot}$) of the combined noise is

$$\overline{P}_{n,tot} = \frac{N_{psd,tot}}{T} \tag{2.15}$$

representing the addition in average power for each of the individual sources. $N_{psd,tot}$ is the power spectral density of the combined noise source that is injected once every cavity roundtrip. The corresponding rate of injection is therefore $R_{inj,tot} = 1/T$.

Incorporating the results of our previous discussion with Eqs. (2.13) and (2.15), we find

$$\left\langle \Delta\phi^2 \right\rangle = \frac{N_{psd,tot}}{2P_0T^2}\left|\tau\right| \tag{2.16}$$

Thus, the variance of the phase shift is linearly proportional to the observation time of noise events. This diffusion in phase is analogous to the random movement of particles governed by Brownian motion. Substituting Eq. (2.16) into Eq. (2.11) and taking the Fourier transform, we find

$$S(f) = P_0 \frac{1}{\pi} \frac{0.5\Delta f_{3dB}}{\left(f - f_0\right)^2 + \left(0.5\Delta f_{3dB}\right)^2} \tag{2.17}$$

where

$$\Delta f_{3dB} = \frac{N_{psd,tot}}{4\pi P_0 T^2} \tag{2.18}$$

Equation (2.18) is the main result of this analysis. It reveals that the oscillator full-width-at-half-power linewidth (Δf_{3dB}) is primarily dependent on the noise-to-signal ratio. To achieve low phase-noise, the perturbation should be made small in comparison to the signal so that each noise event only weakly disturbs the oscillator's phase (Fig. 2-3). Furthermore, the roundtrip time delay T should be made large so that the noise partitioned into each mode and its associated rate of injection decrease relative to the oscillating power. Dividing Eq. (2.17) by P_0, the corresponding normalized phase-noise spectrum is given by

$$L(f) = \frac{1}{\pi} \frac{0.5\Delta f_{3dB}}{(f - f_0)^2 + (0.5\Delta f_{3dB})^2} \tag{2.19}$$

The form of Eq. (2.19) is similar to that of Leeson's empirical equation for an oscillator perturbed by white noise [38]. At frequencies much larger than the linewidth ($f >> \Delta f_{3dB}$), the phase-noise spectrum decays at 20 dB/decade scaled by the noise-to-signal ratio. However, unlike LTI models of phase noise, the derivation of Eq. (2.19) makes clear the random nature of noise in its interaction with the oscillating field.

2.2.2 Unification with Laser Theory

In this section, we unify the concepts of oscillator phase noise across the electrical and optical domains. At optical frequencies, it is well established that the laser phase-noise follows a Lorentzian similar to Eq. (2.19) but with a modified linewidth appropriate to the description of a laser [29, 45]. Our aim here is to show that the framework offered by Eqs. (2.18) and (2.19) is consistent with conventional models of laser linewidth.

We begin by decomposing Eq. (2.18) into its fundamental components: a ratio of the noise to the signal multiplied by the rate at which noise is injected. Our previous analysis identifies the noise term as the total roundtrip noise that couples into a single mode (i.e., the oscillating mode) of the cavity ($N_{psd,tot}/T$). On the other hand, the signal term represents the total power accumulated in the oscillating mode (P_0). As we have grouped the noise into a combined total that is added every cavity roundtrip, the rate of noise injection is given by the inverse of the roundtrip delay ($1/T$).

These terms all have analogous, albeit slightly modified, interpretations in laser physics. For example, the signal power is described through N_p, which is defined as the photon density contained within the oscillating mode. Although not directly in power units, the photon density and the oscillating power are related through the group velocity of the medium along with several other factors [29, 45]. These factors will be cancelled by defining the noise in the numerator through photon density units. In these units, the total noise injected into the oscillating mode over a cavity roundtrip is given by $VR'_{sp}T/V_p$. Here, V is the active volume and V_p is the total photon volume (active + passive) including the effects of refractive index. Their ratio ($\Gamma = V/V_p$) is termed the confinement factor and represents the overlap of the optical mode with the active material. R'_{sp} is the rate of spontaneous photon emission (per unit active volume [29]) injected into a single mode. When multiplied by the active volume and the time period of a cavity roundtrip, $VR'_{sp}T$ represents the total noise injected into an oscillator mode per roundtrip. To convert to photon density units, the noise is divided by the photon volume. Note that since the total noise was defined over a cavity roundtrip, the corresponding rate of noise injection remains at $1/T$.

Inserting these terms into Eq. (2.18), the laser linewidth is found to be

$$\Delta f_{3dB,optical} = \frac{\Gamma R'_{sp}}{4\pi N_p} \tag{2.20}$$

which exactly matches the expressions derived from conventional laser theory [29, 45]. This equivalence unifies the understanding of phase noise for both electrical and optical oscillators.

2.3 Experimental Results of Oscillator Phase-Noise

In the following sections, we show experimental results of oscillator phase-noise when the injected noise is white. Note that at low enough offset frequencies, the spectrum of noise eventually changes to exhibit characteristics of $1/f^{\alpha}$. We will defer analysis of this operation regime to Chapter 3 and instead focus here only on the frequency range where white noise

dominates. Our discussions will be primarily centered on the phase noise of RF oscillators; however, we will also demonstrate the applicability of our developed phase-noise theory to a hybrid optoelectronic oscillator (OEO).

2.3.1 Comparisons to Measurement: Electrical Oscillator

To validate the theory of Section 2.2, we first compare Eq. (2.19) to the measured phase noise of an electrical oscillator whose configuration is provided in Fig. 2-4. The ring cavity oscillates at a frequency of 2.5 GHz using gain supplied by an Avantek 2-4 GHz AM-4080M RF amplifier (G = 25 dB at 6.9 V, small-signal noise figure NF_{ss} = 5.1 dB). The passive cavity consists of isolators at the RF amplifier input and output, an RF phase shifter for tuning the oscillation frequency, an RF filter for defining the center frequency, and a variable RF attenuator for control of intracavity loss. An output coupler is used to couple out most (90%) of the intracavity power, while the remainder (-10 dB) of the power is reused within the cavity to enable oscillation. Three different combinations of RF filters and delay were tested during our

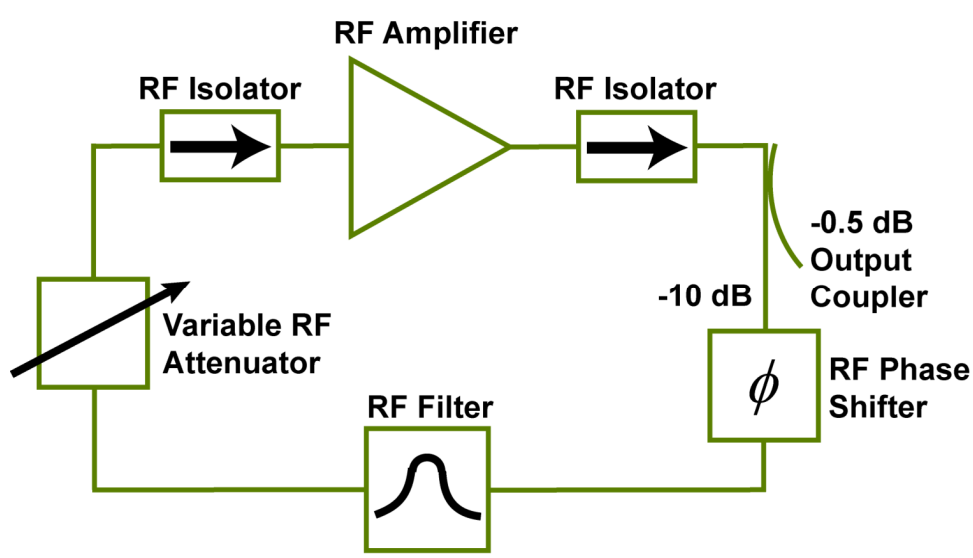

Figure 2-4: Circuit schematic of an RF oscillator operating at 2.5 GHz. The system delay is defined by various configurations of RF filters controlling the net group delay per cavity roundtrip. The RF signal is coupled out prior to filtering allowing for direct measurement of the noise added in each roundtrip.

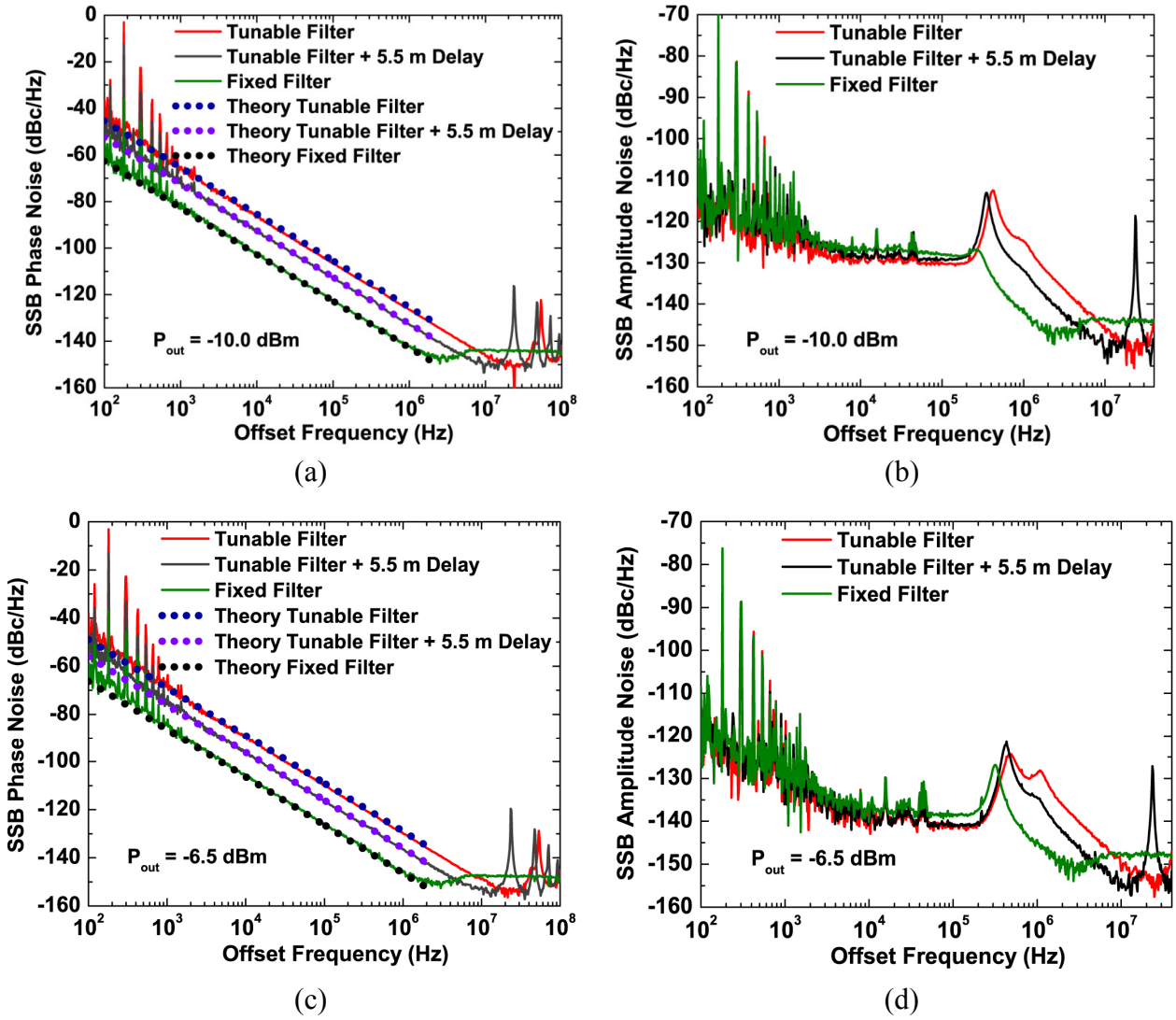

Figure 2-5: Measured RF oscillator phase-noise and amplitude-noise. (a) Measured phase-noise spectra and theory at -10.0 dBm RF power. (b) Amplitude-noise spectra at -10.0 dBm RF power. (c) Measured phase-noise spectra and theory at -6.5 dBm RF power. (d) Amplitude-noise spectra at -6.5 dBm RF power. The RF oscillator of Fig. 2-4 was tested with three filter configurations including 1) a tunable filter, 2) a tunable filter + 5.5 m delay, and 3) a fixed filter. The various filter configurations change the effective roundtrip delay through the associated resonances of the filters.

oscillator measurements: (i) tunable RF filter (halfwidth (*HW*) = 75 MHz at 2.5 GHz), (ii) tunable RF filter (*HW* = 75 MHz) with 5.5 m additional delay, and (iii) fixed RF filter (*HW* = 2.9 MHz). For each configuration, the center frequency was 2.5 GHz.

Figure 2-5 shows the oscillator's phase-noise and amplitude-noise spectra for the three different RF filter/delay configurations as measured by a commercial Agilent E5052B signal-source analyzer (SSA). These measurements were conducted at RF output powers of -10.0 dBm and -6.5 dBm and include ~4.4 dB of loss between the RF coupler output and the SSA (due to cabling and a variable attenuator for output control). The oscillator was operated at low powers in order to prevent flicker noise from dominating over white noise at low offset frequencies. The oscillator output power was controlled by varying the bias voltage of the RF amplifier (between 6.7 V and 6.9 V). In all of our measurements, the intracavity variable attenuator was adjusted so that the loss within the oscillator loop was kept constant. The primary effect of the different filters/delay configurations then is to introduce different time delays to the oscillating mode as a result of the group delay induced by the filter resonance. The phase noise decreases at 20 dB/decade as predicted for Lorentzian broadening due to white noise injection (see Eq. (2.19)). It is clear from Fig. 2-5 that the measured phase noise is greatly influenced by the RF filter/delay combination used. The corresponding amplitude noise is seen to be much lower in comparison. Note that 40 MHz is the maximum offset frequency of the SSA amplitude-noise measurement. The origin of the peaks near ~400 kHz in Figs. 2-5 (b) and (d) is currently unknown. However, the sidemodes of the oscillator can clearly be seen above 20 MHz in all of the spectra corresponding to the tunable filter. As expected, the sidemode spacing decreases for an increase in roundtrip delay. With the fixed filter, the filter bandwidth is narrow enough to reject all of the cavity sidemodes. In this case, the sidemode spacing was determined from the frequency translation of the oscillating mode corresponding to a 2π shift in cavity phase. The frequencies of the sidemodes were measured to be 53.5 MHz for the tunable filter, 23.6 MHz for the tunable filter + 5.5 m delay, and 7.3 MHz for the fixed filter.

The phase-noise spectrum can be calculated from Eqs. (2.18) and (2.19) once the oscillation power, injected noise power, and roundtrip time delay are known. The roundtrip delay (T) is directly found from the inverse of the measured sidemode spacing. Usually, knowledge of the amplifier's noise figure is required to estimate the noise added in a single roundtrip. However, in our case, $N_{psd,tot}$ can be directly measured from the noise beyond 10 MHz offset for the case of the fixed filter (Fig. 2-5). Because we have coupled out the power before filtering (Fig. 2-4), the noise power at large offset frequencies is exactly the white-noise power injected every cavity roundtrip. The narrow filter bandwidth prevents the accumulation of noise at these frequencies.

Equipartition can be verified as the injected noise is equal in both the amplitude- and phase-noise plots. The sum of both contributions yields a total noise ($N_{psd,tot}$) of -141.0 dBc/Hz at -10.0 dBm and -144.6 dBc/Hz at -6.5 dBm referenced to the carrier. The additive noise is invariant with signal power causing the relative ratio to decrease with increasing power. Note that our current theory does not apply for multiplicative noise (which scales proportionally to signal power) resulting from the upconversion of near-DC flicker noise. In principle, the measured noise and signal should be traced back to the input of the amplifier stage. However, as the ratio of noise to signal remains the same under attenuation, Eq. (2.18) can be evaluated directly from our measurements of the total noise (relative to carrier). Furthermore, since the same operating conditions (intracavity loss, RF power, and RF amplifier bias) were used for all three filter configurations, the total noise is constant at each RF power level. Note that the injected noise cannot otherwise be measured in the tunable filter configurations since the sidemodes are not completely rejected in Fig. 2-5. Using Eqs. (2.18) and (2.19) and the directly measured

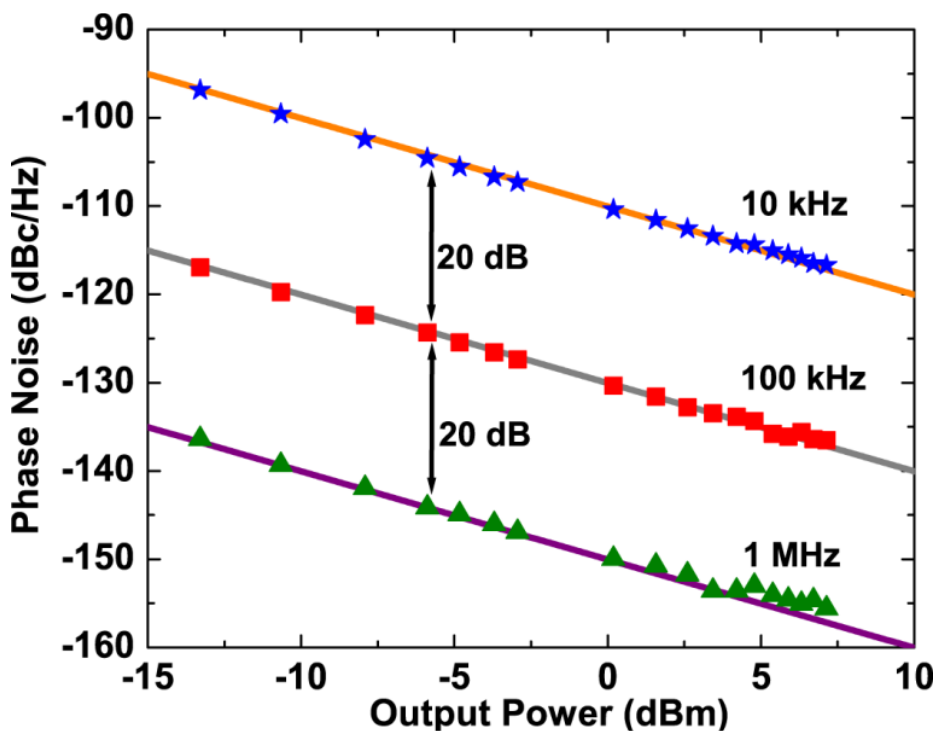

Figure 2-6: Measured and theoretical power dependence of oscillator phase-noise.

parameters (i.e., no fitting parameters), the oscillator phase noise was calculated for each of the cases and plotted (dotted line) against the measurement. The excellent agreement between theory and experiment verifies the dependence of phase noise on the square of the roundtrip time. The dependence of phase noise on the inverse of signal power can also be observed in Fig. 2-5 but is more clearly illustrated in Fig. 2-6.

For the measurements of Fig. 2-6, we use the same oscillator configuration as that of Fig. 2-4 but with an RF filter consisting of the cascade between the tunable and fixed filters. The sidemode spacing decreases to 6.8 MHz reflecting the additional phase delay through the filter cascades. The output power was varied between -13.3 dBm and 7.3 dBm through control of the RF amplifier bias voltage. Note that these measurements include ~4.4 dB of loss between oscillator output and the SSA. In Fig. 2-6, the measured phase noise is plotted against RF power for offset frequencies of 10 kHz, 100 kHz, and 1 MHz. Using the methods described previously, the phase noise was also calculated at these frequencies for operation at -13.3 dBm. The theory is then extrapolated to other RF powers using a $1/P_0$ dependence. This allows the comparison of experiment and theory over the entire range of oscillator power. As can be observed in Fig. 2-6, the agreement is excellent between the two. The inverse dependence of phase noise on signal power can be clearly seen with 20 dB separation in phase noise between each decade of offset frequency.

It is also possible to directly evaluate the phase noise using the noise figure (NF) of the RF amplifier along with knowledge of the input power. Typically, the measured small-signal noise figure (NF_{ss}) of the RF amplifier is dependent on the bias applied. For the measurement range of Fig. 2-6, NF_{ss} varies from 4.7 dB at 7.5 V bias (P_{out} = -13.3 dBm) to 3.6 dB at 13.8 V bias (P_{out} = 7.3 dBm) [see Fig. 2-7]. However, the NF required for evaluating the phase noise of Eqs. (2.18) and (2.19) is that under the large-signal operating conditions of the oscillator. Under these conditions, we find the NF to be approximately clamped at its value during the onset of oscillation, independent of applied bias. This is analogous to the clamping of a laser's spontaneous emission above threshold [29]. The large-signal NF extracted from all the cases tested in Fig. 2-6 is 5.1 dB. This agrees well with NF_{ss} = 4.8 dB independently measured at the oscillation threshold voltage of 7.4 V. Note, for the cases of Fig. 2-5, the extracted NF was

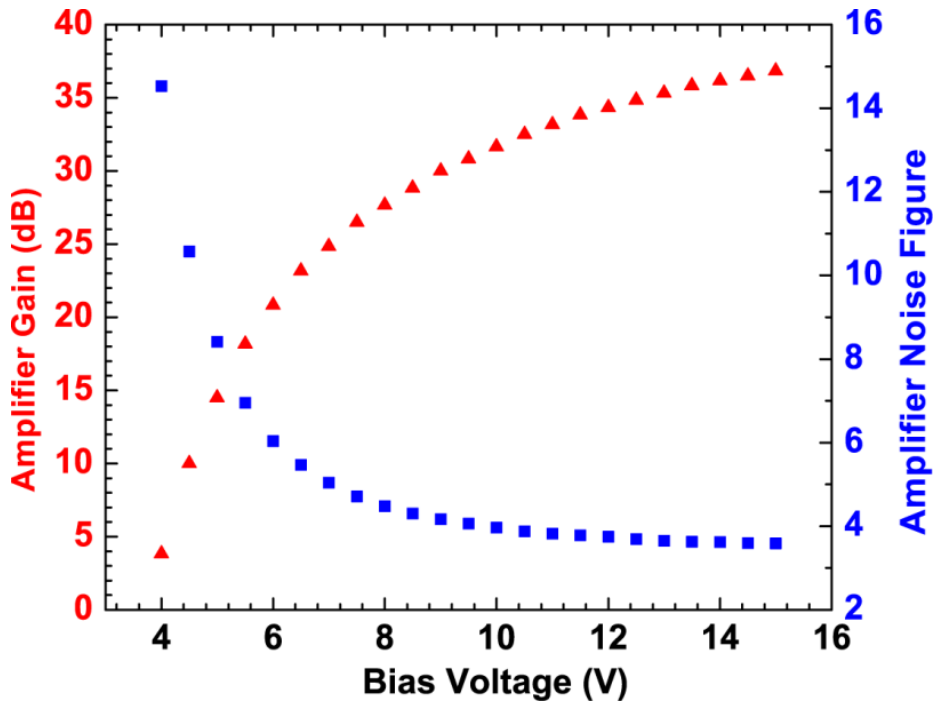

Figure 2-7: Measured RF amplifier small-signal gain and noise figure as a function of bias voltage

5.8 dB, and the corresponding NF_{ss} was independently measured to be 5.5 dB at an oscillation threshold of 6.4 V.

2.3.2 Comparisons to Measurement: Optoelectronic Oscillator

Since any electromagnetic oscillator can be represented in the form of an equivalent amplifier in a resonant cavity (Fig. 2-1), the theory of Eqs. (2.18) and (2.19) can in principle be applied to oscillators of arbitrary form. In this section, we apply the developed phase-noise theory to a hybrid optoelectronic oscillator (OEO) [4, 57, 58]. The OEO (Fig. 2-8) comprises both electrical and optical cavity elements, and amplification is achieved via microwave-photonic (MWP) gain [6].

Its optical cavity consists of a high-power low-noise slab-coupled optical waveguide external cavity laser (SCOWECL) [27, 28] (P = 250 mW at 3-A bias), a variable optical attenuator

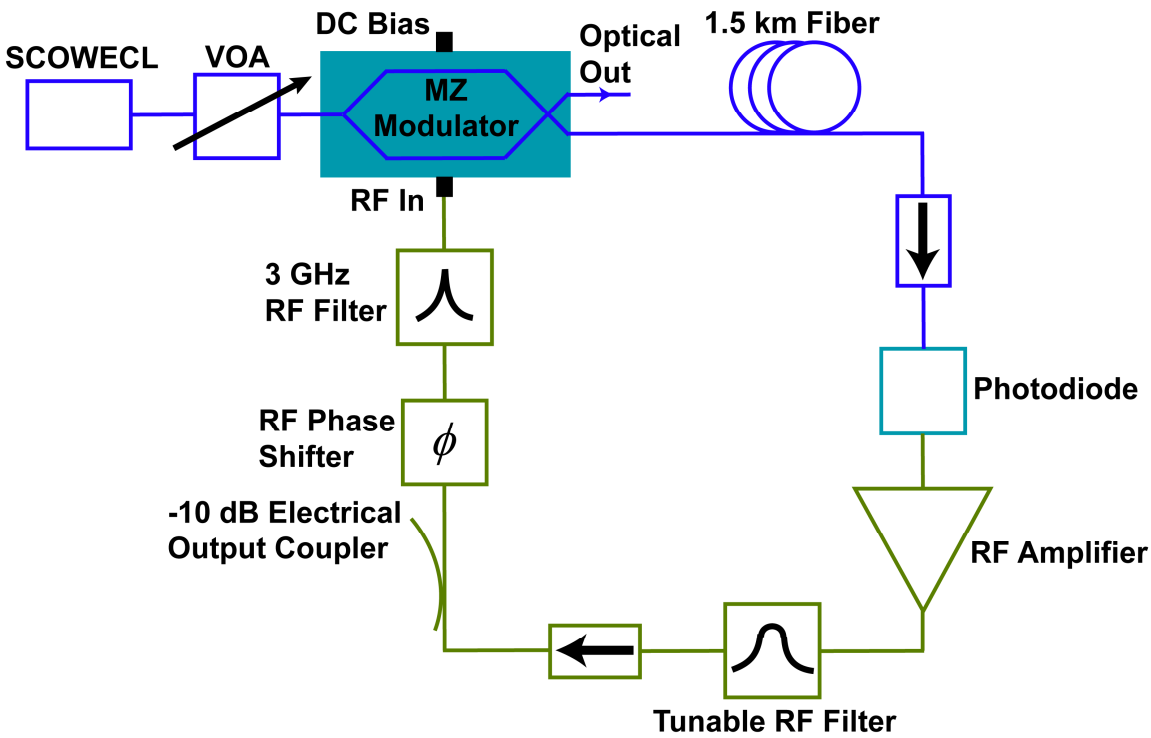

Figure 2-8: Configuration of an optoelectronic oscillator operating at 3.0 GHz. Microwave-photonic (MWP) gain is achieved by the combination of a high-power, low-noise slab-coupled optical waveguide external cavity laser (SCOWECL), Mach-Zehnder modulator (MZ Modulator) and photodiode.

(VOA), a Mach-Zehnder (MZ) modulator (BW = 15 GHz, V_π = 3.1 V at 3 GHz), a 1.5-km long spool of single-mode optical fiber, an optical isolator, and a commercial photodiode ($\Re$ = 0.8 A/W, BW = 12 GHz). In the electrical path, the photodiode output is amplified by a low flicker-noise AML26PNB2001 2-6 GHz RF amplifier (G = 23.4 dB, NF_{ss} = 5.7 dB) before passing through a tunable RF filter (f_{center} = 3.0 GHz, HW = 95 MHz at 3.0 GHz), an electrical isolator, an RF phase shifter, and a fixed 3.0 GHz RF filter (HW = 1.2 MHz). The optoelectronic loop is closed by feeding the electrical signal back as the input to the optical modulator. The cascade consisting of the SCOWECL, modulator, and photodiode provides heterodyne gain due to beat-note generation from modulator RF-in to photodiode RF-out. RF amplification was used as the MWP gain was not sufficient to overcome the losses of the system.

Oscillation begins from the amplification of noise incident on the modulator RF input port. The oscillation signal is accessed through a -10 dB RF coupler located after the RF isolator. As was done for the electrical ring oscillator case, the signal was coupled out prior to the 3 GHz RF filter (HW = 1.2 MHz) for measurement of the noise added in each cavity roundtrip. However, as we found the operation and measurement of the OEO to be sensitive to out-of-band noise, we included a second tunable filter (HW = 95 MHz) for stabilization of the OEO. The difference in filter bandwidths allows for a reasonably broad range where the injected noise may be measured. The SCOWECL was operated at 3-A bias for our measurements, while its output power was controlled using the VOA.

The OEO operates by modulation of the optical carrier with a coherent RF envelope. This RF envelope is photodetected, filtered, and reused as the input to the modulator. We may represent the cascade of the SCOWECL, MZ modulator, fiber delay, photodiode, and RF amplifier as an equivalent amplifier with an effective delay corresponding to 1.5 km of optical fiber (Fig. 2-1). This equivalent amplifier is placed within the RF loop of the OEO and filtered each roundtrip. The addition of incoherent noise (thermal noise, shot noise, laser relative intensity noise (RIN), and nonlinear fiber noise) causes perturbations of random phase to the coherent RF envelope [58]. This results in spectral broadening of the oscillation signal. It is straightforward to show that the noise is only partitioned into the longitudinal modes of an OEO. Since the MZ modulator was designed for a single polarization, only that polarization within the optical cavity may receive gain and thus noise injection from the MWP link. The use of single-mode fiber also prevents the excitation of higher-order transverse modes over the gain bandwidth of the laser. In the RF cavity, the bandwidth limitations of the modulator and photodiode (~10 GHz) prevent operation outside of the fundamental TEM mode of the coaxial line. Thus, the combined modes of the OEO are only described by the longitudinal indices of the cavity.

The modulation and photodetection processes in an OEO result in the mixing of noise near baseband with noise at microwave frequencies. Therefore, the laser RIN at low frequencies is upconverted into the frequency range of oscillation [58]. Typically the RIN at low frequencies dominates, which along with nonlinear fiber noise, result in the prevalence of colored noise in an OEO. However, we find that in cases where the SCOWECL is operating under typically undesirable mode-hopping conditions, the total noise is white and dominated by the high

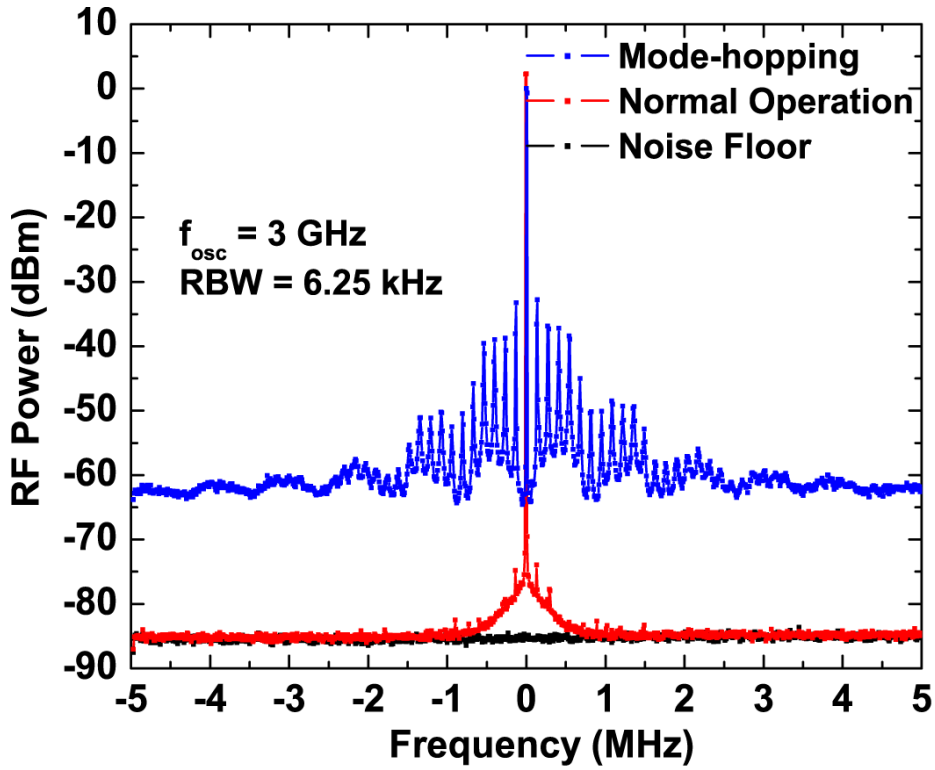

Figure 2-9: RF spectrum of the OEO corresponding to Fig. 2-8 when the laser is operated under mode-hopping conditions. The spectrum for normal operation is also provided.

frequency RIN of the laser. This can be verified in the RF spectrum of the 3 GHz OEO in Fig. 2-9.

Figure 2-10 shows the measured OEO phase noise when the SCOWECL is operated in mode-hopping regime. The operating photocurrent was 5.9 mA, and the output RF power (with cable losses) is ~0 dBm. The spectrum falls at 20 dB/decade characteristic of a Lorentzian. The sidemode spacing is 135 kHz corresponding to a fiber delay of 1.5 km. The noise injected in each roundtrip can be found from the spectrum at frequencies near 10 MHz offset. The total noise ($N_{psd,tot}$) resulting from both amplitude and phase contributions is -104 dBc/Hz relative to the carrier. Note that the sharp cutoff in phase noise near 90 MHz is due to the stopband of the tunable filter. Using these measured parameters in Eqs. (2.18) and (2.19), the theoretical OEO phase-noise was computed and graphed against the measurement results in Fig. 2-10. The

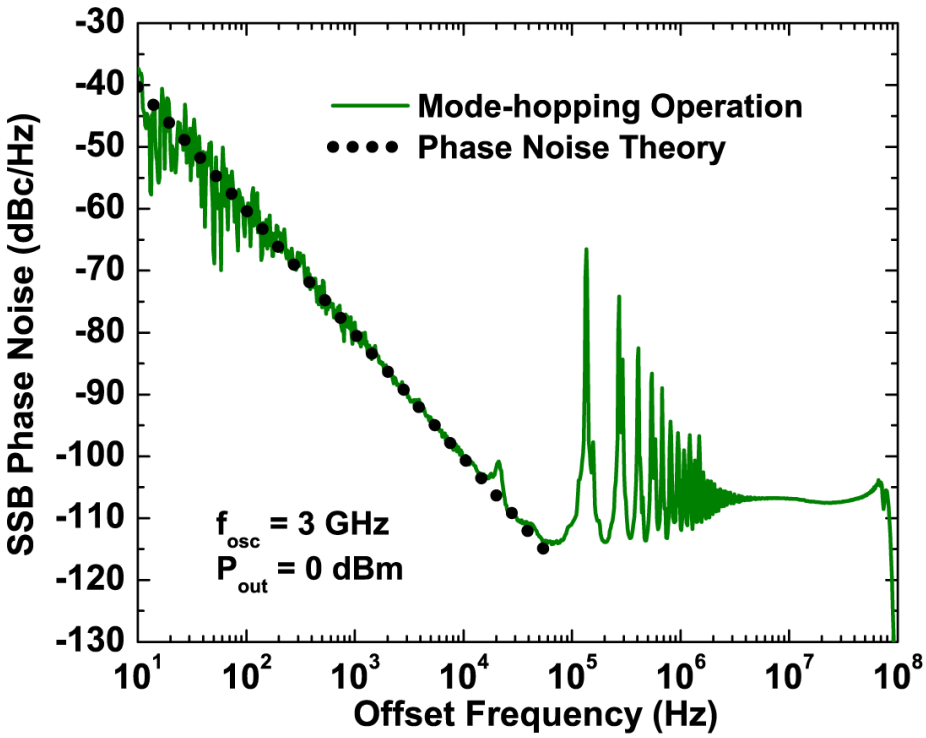

Figure 2-10: Phase-noise of the OEO corresponding to Fig. 2-8 operated under laser mode-hopping conditions. The white injected noise dominates resulting in a Lorentzian phase-noise spectrum.

agreement is once again excellent over the frequency range tested *with no fitting parameters*. We see that the phase noise of the OEO is comparable to that of the fixed-filter RF oscillator in Fig. 2-5 (a) despite having a 37 dB lower signal-to-noise ratio (SNR). The degradation in phase noise through SNR is balanced by the improvement in phase noise gained through using a longer roundtrip delay (54× compared to that of the fixed-filter oscillator cavity). This example illustrates the power of using delay to reduce phase noise. However, the lowest phase noise is achieved when both SNR and delay are maximized.

2.3.3 Discussion

Before concluding, we wish to address two potential points of confusion in our analysis. First, as the derivations of Eqs. (2.18) and (2.19) are based on noise perturbation, it is interesting to discuss the distinction between an oscillator and an amplifier. In an amplifier, one does not

expect to see Lorentzian broadening of the lineshape after signal amplification. Yet, the intuition offered by Fig. 2-3 does not appear to differentiate between the two systems. The key difference is that the modes of an amplifier form a continuum as there is no associated resonant cavity. A one-to-one mapping exists between the amplifier continuum and noise, and thus the noise becomes directly added to the spectrum at all frequencies. This direct summing of noise power with the oscillator spectrum is the basis for the concept of noise figure in both electrical [64] and optical amplifiers [65].

Second, although the validity of our phase-noise model was only specifically justified for the cases of electrical and optical oscillators, the scope of our approach is expected to be even more far-reaching. As long as the oscillator can be represented as an equivalent amplifier in a resonant configuration (Fig. 2-1), one needs only to partition the noise among the independent modes of the system. The addition of incoherent noise to a coherent oscillation signal results in phase diffusion and spectral broadening. With the appropriate definition of system parameters our theory should also prove applicable to mechanical oscillators as well as oscillators of other variety.

2.4 Conclusion

We have provided a general approach to the solution of oscillator phase noise when the oscillating field is sinusoidal and perturbed by additive white-noise. Our theory is intuitive and based on the partitioning of noise into the modes of the cavity. This partitioning is fundamental to any physical system whose basis becomes defined by the system boundaries. We have also unified our phase-noise theory with interpretations of linewidth fundamental to laser physics. For purposes of verification, we have measured the phase noise of RF oscillators with both roundtrip delay and intracavity power as free parameters. We have also constructed a hybrid optoelectronic oscillator whose operation is based on entirely different principles. In both cases, excellent agreement is found between calculated phase-noise spectra and those measured experimentally. The intuition offered by our approach will prove beneficial for extension to cases of $1/f^{\alpha}$ noise in Chapter 3.

Chapter 3

Oscillator Phase Noise – Flicker Noise

Noise is a problem common to all oscillator systems. We saw in Chapter 2 that the effects of noise on oscillators can be decomposed into perturbations of amplitude and phase, both of which act to degrade the spectral purity of the generated signal. In typical oscillators, the influence of phase noise is much larger than that of amplitude noise due to various amplitude-limiting mechanisms. These mechanisms include not only the oscillator's intrinsic negative feedback, which maintains loop gain equal to loop loss, but also the saturation of intracavity components (e.g., the amplifier). A complete understanding of oscillator phase noise is therefore essential for realizing future low-noise oscillator systems.

For the case of white noise, we showed in Chapter 2 that a common link existed between all oscillators based on the partitioning of noise among the modes of the oscillator [46]. In an open system, the noise appears white over a broad range of frequencies. However, within the confines of a resonant cavity, the noise is forced to couple only into the basis of the system [29, 45]. For white noise, the coupling of noise is equal into the local density of oscillator modes. With increasing intracavity delay, the number of modes increases but is counteracted by a decrease in power coupled into each mode. Note that we use the term 'cavity' throughout this manuscript to denote any general resonant configuration of the oscillator. For the oscillators that we will be analyzing later, the cavity geometry consists of a ring.

In this chapter, we extend our analysis of oscillator phase-noise to the case of low-frequency flicker noise. The case of flicker noise is particularly important as it is what ultimately limits the phase noise of high-performance oscillators, especially at low offset frequencies. In general, the problem of flicker noise is difficult to analyze as both its origin and spectral properties are not well defined. However, as we will show, its interpretation in oscillators becomes greatly simplified if one views the frequency upconversion of noise from the perspective of a gain perturbation.

Historically, both linear time-invariant (LTI) and linear time-varying (LTV) models have

been proposed to explain the phenomenon of oscillator phase-noise. Some of the deficiencies of these models have been previously described in Chapter 2 and thus will not be repeated here. Instead, our attention will be focused on theories which treat the effects of flicker noise on oscillators through integration over the frequency noise spectrum associated with the noise process [66–69]. This integral becomes unbounded unless restrictions of finite measurement time are taken into account [41, 66, 67, 69]. Here, we will take a similar approach paying careful attention to the effects of measurement. However, in contrast to previous theories, our formulation uses the noise coupled into the oscillating mode to uniquely specify the frequency noise spectrum corresponding to the noise perturbation. Knowledge of this noise is necessary as without it, only the shape of the oscillator's phase-noise spectrum can be determined and not its absolute magnitude.

The goal of this work is to provide a unified description of phase noise applicable to oscillators of both electrical and optical variety. Towards that end, we will show that only three fundamental parameters are necessary to specify the behavior of an oscillator: the spectrum of injected noise, the roundtrip time delay, and the oscillating power. We supplement our theory with measurements of phase noise in RF ring-cavity oscillators and show excellent agreement across multiple configurations and a wide range of operating conditions. Finally, we conclude with comparisons to the phase noise of a hybrid optoelectronic oscillator [4, 57, 58] to demonstrate the generality of the theory. As was the case in Chapter 2, our theory is applicable to any oscillator that can be represented through a gain element and delay wrapped in a positive feedback circuit. Note that the delay does not have to be purely a physical delay but can also include the group delay accumulated from signal propagation through a filter resonance. This encompasses a broad range of oscillators operating in both the electrical and optical domains. We will show that these oscillators are all united by a common technique of analyzing noise in the oscillator's basis. The concept of a basis is fundamental to every physical system and thus explains the widespread applicability of our phase-noise model.

3.1 Oscillator Spectrum Perturbed by Noise

In this section, we discuss the characteristics of the oscillator's spectrum under the influence of both white and flicker noise perturbation. Our goal is to provide intuition for understanding the phase-noise theory to be presented in Section 3.2. The examples here will consist of measurement results from three separate RF oscillators across a broad range of operation powers. We will show that the oscillator's behavior becomes strikingly different depending on its dominant noise mechanism (white or flicker noise).

Figure 3-1 shows the measured phase noise of the first RF oscillator (operating at 2.5 GHz) as a function of its RF power. The configuration of the oscillator will be presented in more detail during Section 3.3 (see Fig. 3-6) and consists of an RF amplifier, filter, and output coupler arranged within a resonant ring cavity. The amplifier used is an Advantek AM-4080M (BW = 2-4 GHz) which we will denote for the rest of this chapter by Amplifier 1. Note that the measured values of oscillator power are traced directly to the amplifier's output and controlled

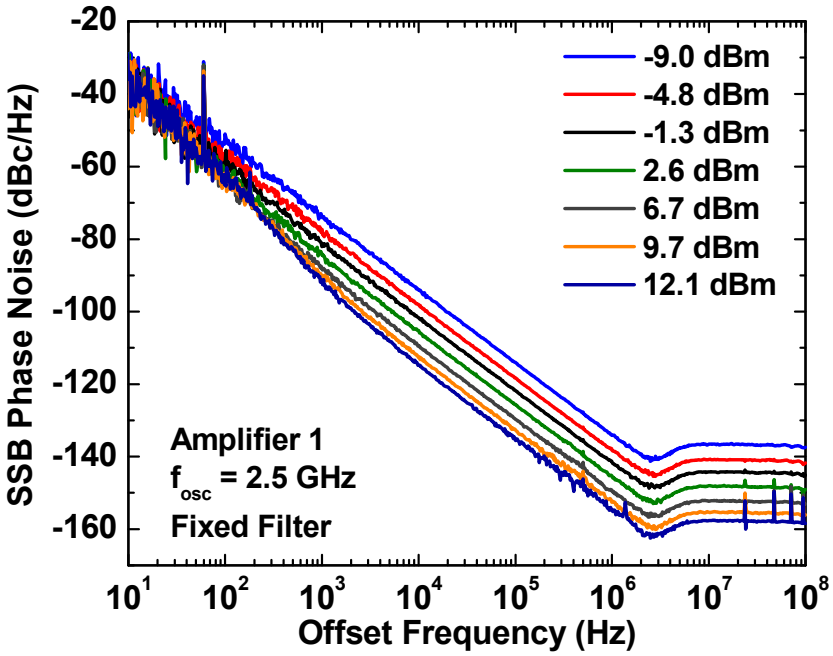

Figure 3-1: Measured phase noise of a 2.5 GHz fixed-filter oscillator as a function of RF output power. The system oscillates from gain supplied by Amplifier 1.

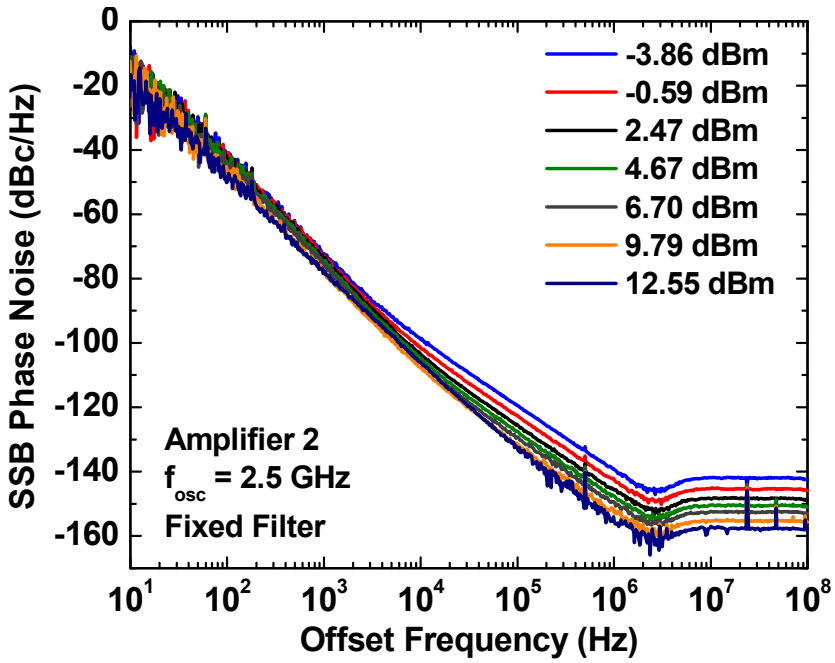

Figure 3-2: Measured phase noise of a 2.5 GHz fixed-filter oscillator as a function of RF output power. The system oscillates from gain supplied by Amplifier 2.

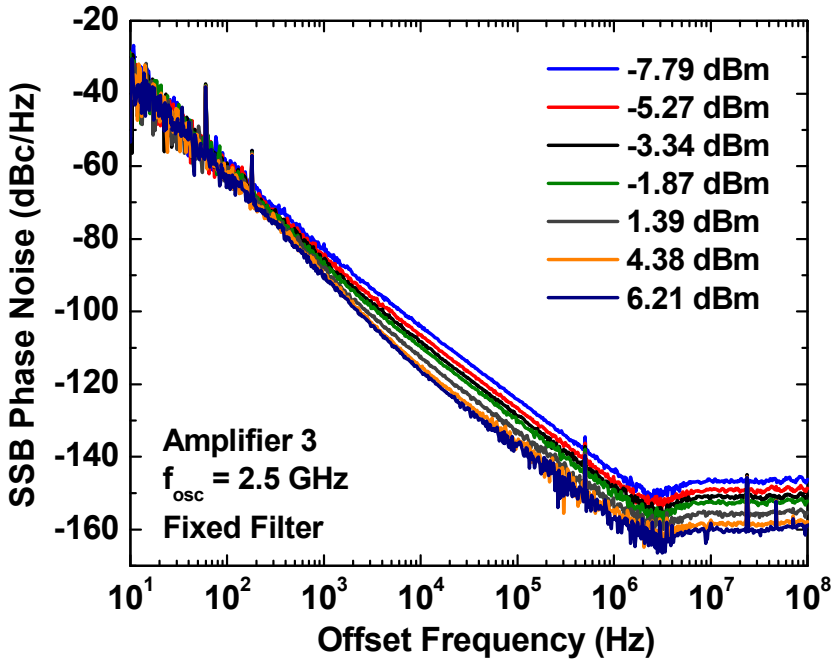

Figure 3-3: Measured phase noise of a 2.5 GHz fixed-filter oscillator as a function of RF output power. The system oscillates from gain supplied by Amplifier 3.

by varying the voltage bias supplied to the amplifier. The oscillator phase-noise measurement was performed using an Agilent E5052B Signal-Source Analyzer (SSA). Before discussing the characteristics of Fig. 3-1, we will first introduce the results of the phase-noise spectra for the other two oscillators (Figs. 3-2 and 3-3), which differ only by the RF amplifiers used. These RF amplifiers are the Miteq AFS4-02000800-45-10P (BW = 2-8 GHz) and the Miteq AM-3A-0520-0 (BW = 0.5-2 GHz), which we will designate as Amplifiers 2 and 3, respectively. Note that Amplifier 3 continues to supply gain at 2.5 GHz (although significantly reduced) despite its maximum specified operating frequency of 2 GHz.

Figures 3-1, 3-2, and 3-3 all show that the oscillator's behavior changes dramatically at low frequency offsets. It is at these frequencies that flicker ($1/f^{\alpha}$) noise begins to dominate over white noise. As we will see later, the flicker noise results from a multiplicative noise process, growing or shrinking with the level of the signal power. This means that the ratio of noise-to-signal (in the flicker noise regime) remains approximately constant. These properties can be observed in the phase-noise spectra of Figs. 3-1, 3-2, and 3-3. At higher frequency offsets, the noise becomes dominated by white noise, which is an additive noise process that is independent of signal level. For these frequencies, the noise-to-signal ratio varies inversely with the

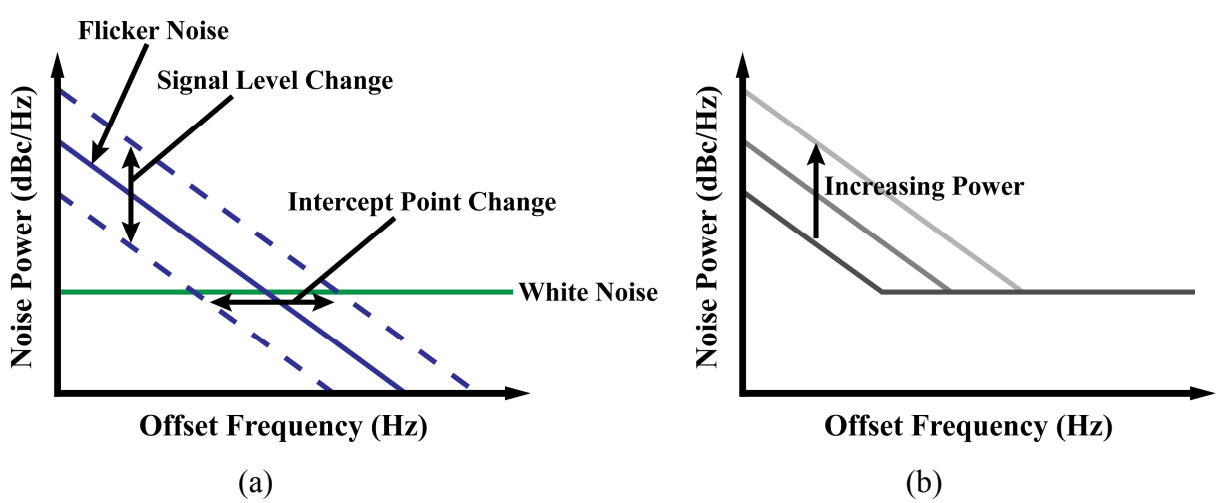

Figure 3-4: Illustration of the total noise power that results from a combination of both flicker and white noise. Since flicker noise is proportional to the signal power, a change in the signal level causes the intercept of flicker and white noise to shift (a). Thus, the spectrum of the total noise becomes dependent on the signal power (b).

oscillation power as was also observed in Chapter 2.

Figure 3-4 provides an intuitive depiction of our previous discussion on flicker and white noise. Note that the illustrations of Fig. 3-4 show the noise around a generic carrier, which may be at any arbitrary frequency. The process by which low-frequency flicker noise becomes upconverted onto the carrier will be discussed in detail in Section 3.2. Here, we instead note that the flicker noise is approximately proportional to signal level while the white noise is independent [70]. A change in the signal power therefore causes the intercept point of white and flicker noise to vary versus frequency. The total spectrum is given by the summation of both the white and flicker noise, which then also becomes a function of the signal power. Note that although this description in principle only applies to the spectrum of the noise process itself, these same characteristics can also be observed in the oscillator phase-noise spectra of Figs. 3-1, 3-2, and 3-3. In particular, the shift of the intercept point with signal power is prominent in the oscillator spectra of Fig. 3-1 for frequencies between 100 Hz and 1 kHz.

3.2 Unified Theory of Phase Noise

In Chapter 2, we presented a unified theory of oscillator phase-noise when the noise perturbation was characterized by a white-noise process. Although intuitive, this theory unfortunately does not fully apply to oscillators that are also affected by flicker noise. In the following sections, we will discuss how to modify our theory of Chapter 2 to account for noise whose spectral behavior is non-white. Essential to our treatment will be a discussion of how low-frequency flicker noise appears in the frequency band of the oscillating signal. We will also incorporate elements of noise partitioning in order to determine the noise coupled into the oscillating mode. By the end of this section, we will show how to predict the phase noise of any electromagnetic oscillator perturbed by noise of arbitrary form [71].

3.2.1 Description of an Oscillator Under Noise Perturbation

In this section, we formulate a description of oscillator phase noise by working with spectral densities of noise processes in the frequency domain [29]. The frequency domain allows us to

avoid ambiguities associated with the time representation of $1/f$ noise. Similar to [29, 45], our theory begins with a phasor description of the oscillator field under noise perturbation (Fig. 3-5). The initial field magnitude E_0 is normalized such that $E_0^2 = P_0$, where P_0 is the intracavity power of the signal. Without loss of generality, the oscillator's initial phase ϕ is taken to be 0. The addition of a noise event, having magnitude E_n such that $E_n^2 = P_n$ and relative phase θ_i, results in perturbation of both the amplitude and phase of the original oscillating field. If the phase of the noise event is random relative to that of the field, θ_i is uniformly distributed between 0 and 2π. The amplitude of the total signal vector (E_T) is given by

$$E_T^2 = P_0 + \Delta P_i \tag{3.1}$$

where ΔP_i is defined as the change in oscillation power induced by a noise event having relative phase θ_i. Alternatively, we can define E_T through the vector sum $E_T e^{j\Delta\phi_i} = E_0 + \Delta E_r + j\Delta E_{im}$. Multiplying by its complex conjugate, we find

$$E_T^2 \approx E_0^2 + 2E_0\Delta E_r \tag{3.2}$$

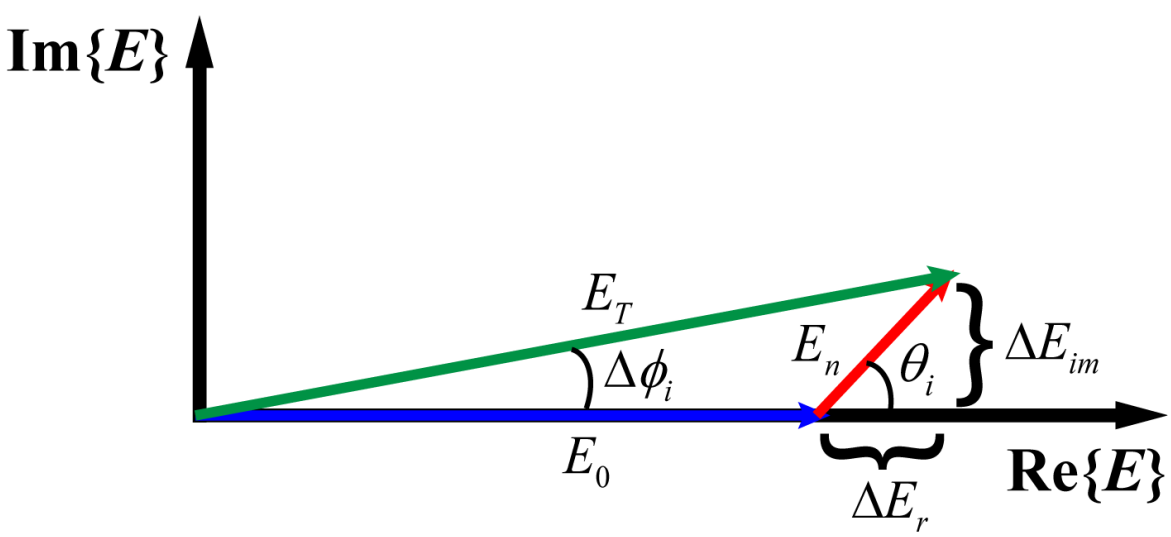

Figure 3-5: Vector-based diagram of oscillator field under noise perturbation.

where we have assumed $E_0 >> \Delta E_r, \Delta E_{im}$. The change in angle of the oscillating field ($\Delta\phi_i$) can similarly be found through

$$\Delta\phi_i \approx \Delta E_{im} / E_0 \tag{3.3}$$

where again we have assumed $E_0 >> \Delta E_r, \Delta E_{im}$. Note that these approximations represent the linearization of changes in power and phase due to a *single* noise event [46].

It is clear from Eqs. (3.1) and (3.2) that the fluctuation in power is related to the beating between the signal field and the in-phase component of the noise. We may change to units of fluctuation rates through the identification of $F_P(t)$ with ΔP_i and $F_r(t)$ with ΔE_r. $F_P(t)$ and $F_r(t)$ now represent the contribution rate of noise events to fluctuations of the oscillator power and in-phase field with their time dependencies made explicit. These quantities are equivalent to the force terms that describe noise perturbation in Langevin analysis [72]. The corresponding Langevin equations for $F_P(t)$ and $F_r(t)$ are given as

$$\begin{aligned} \frac{d\Delta P(t)}{dt} &= F_P(t) \\ \frac{d\Delta E_r(t)}{dt} &= F_r(t) \end{aligned} \tag{3.4}$$

$F_P(t)$ and $F_r(t)$ are related through

$$F_P(t) = 2\sqrt{P_0} F_r(t) \tag{3.5}$$

Similarly, defining $F_\phi(t)$ and $F_{im}(t)$ as the contribution rate of noise events to fluctuations of the oscillator phase and out-of-phase field, the corresponding Langevin equations are then given by [29]

$$\begin{aligned} \Delta\Omega(t) = \frac{d\Delta\phi(t)}{dt} &= F_\phi(t) \\ \frac{d\Delta E_{im}(t)}{dt} &= F_{im}(t) \end{aligned} \tag{3.6}$$

Here, $\Delta\Omega(t)$ represents the fluctuations in the instantaneous frequency of the oscillating field. From Eq. (3.3), $F_\phi(t)$ and $F_{im}(t)$ are related through

$$F_\phi(t) = \frac{F_{im}(t)}{\sqrt{P_0}} \tag{3.7}$$

Although Eqs. (3.4) and (3.6) are expected to be general across all noise processes, the Langevin analysis is typically only applied for the case of white noise. However, we note that any colored noise distribution can be built up from a collection of statistically-independent Ornstein-Uhlenbeck processes with varying damping rate [41]. If necessary, one can readily construct a system of Langevin equations to model the effects of flicker noise.

We may take the autocorrelation of Eqs. (3.5) and (3.7) obtaining $\left\langle F_P(t)^* F_P(t+\tau)\right\rangle$ and $\left\langle F_\phi(t)^* F_\phi(t+\tau)\right\rangle$, respectively. Here, τ represents the time delay of the correlation. After Fourier transformation into the frequency domain, the following relations between spectral densities can be defined

$$S_{F_P}(\omega) = 4P_0 S_{F_r}(\omega) \tag{3.8}$$

$$S_{F_\phi}(\omega) = \frac{S_{F_{im}}(\omega)}{P_0} \tag{3.9}$$

$S_{F_\phi}(\omega), S_{F_P}(\omega), S_{F_r}(\omega), S_{F_{im}}(\omega)$ in Eqs. (3.8) and (3.9) represent spectral densities corresponding to fluctuation rates of the oscillator phase, power, in-phase field, and out-of-phase field, respectively.

In order to proceed further, these spectral densities must be completely specified. To do so, we consider a generic representation of an oscillator in the geometry of a ring containing a localized region where amplification occurs. If we take the perspective of a signal travelling along the cavity, we would see that the signal undergoes amplification and noise injection with every pass through the amplifier. Within the confines of the oscillator boundaries, the noise is forced to emit only into the modes of the oscillator, which together form the oscillator's basis.

Previously in our analysis of white noise (Chapter 2), we showed that each mode received a fraction of the noise power according to the local density of modes. In one dimension and for a single polarization, the density of modes is given by the roundtrip delay of the cavity (T), so that the number of modes within a differential frequency interval Δf is equal to $T\Delta f$. The spectral density of the noise ($N_{psd,tot}(\omega)$) within Δf becomes distributed into these modes such that each mode receives a noise power of $N_{psd,tot}(\omega)/T$. In the limit where the spectral width of the noise only encompasses a few cavity modes, the majority of the noise couples into those modes [55, 56]. Note that this analysis can also be extended to cavities of higher dimensionality and polarization, but care must be taken when accounting for any spectral dependence of the mode density. Our previous discussion is also consistent with quantum mechanical formulations of thermal noise [73, 74] where each mode occupies an average energy $k_B T_0$, and thus the average power delivered by each mode is $k_B T_0/T$. This analysis was introduced earlier in Chapter 2 with T_0 representing the equilibrium temperature of the system.

We now return to Eq. (3.8) to first determine $S_{F_P}(\omega)$ for the case of white noise, later extending the analysis to colored noise. Examining Eq. (3.8), we see that $S_{F_P}(\omega)$ is inherently related to the beating between the in-phase component of noise $\left(N^r_{psd,tot}(\omega)/T\right)$ and the signal (P_0). Here, $N^r_{psd,tot}(\omega)$ is the power spectral density of the in-phase noise (assumed white) added in one roundtrip of the cavity. Dividing this noise by T yields the total in-phase noise partitioned into the oscillating mode over the course of the roundtrip. Note that as mentioned earlier, this analysis implicitly assumes a one-dimensional cavity operating in a single polarization state [45]. $N^r_{psd,tot}(\omega)$ is related to $N_{psd,tot}(\omega)$ by a factor of 2 [29]. This factor assumes that half the total noise contributes to in-phase fluctuations. The equal splitting of noise into amplitude and phase is a consequence of the randomness of noise such that the noise does not preferentially align along any particular field direction (Fig. 3-5). Combining these statements with Eq. (3.8), one can obtain the following form for $S_{F_P}(\omega)$

$$S_{F_P}(\omega) = \frac{4N^r_{psd,tot}(\omega)P_0}{T^2} \tag{3.10}$$

Note that Eq. (3.10) introduces one additional factor of T, which accounts for the injection of one roundtrip's worth of noise at a rate inverse to the roundtrip time. This factor of T is a consequence of defining noise fluctuations in terms of fluctuation rates. Although Eq. (3.10) was not a result of rigorous derivation, its form agrees with an analogous equation for lasers obtained independently through Langevin analysis [29]. Furthermore, we will see that Eq. (3.10) also leads to a final phase-noise spectrum equivalent to that derived in Chapter 2.

We wish now to extend Eq. (3.10) so that it may be applied to the case of colored noise. Our approach is to simply allow $N^r_{psd,tot}(\omega)$ to vary according to the shape of the noise process. We will see that this approach yields spectral densities of fluctuating variables that acquire the spectral shape of the noise process itself. However, it should be mentioned that some subtleties arise from our handling of colored noise in this manner. For example, one concern is whether the rest of Eq. (3.10) remains self-consistent within our interpretation of $N^r_{psd,tot}(\omega)$. In particular, we note that one of the factors of T in Eq. (3.10) accounts for the total amount of noise coupled into the oscillating mode per cavity roundtrip. For white noise, $N^r_{psd,tot}(\omega)/T$ is intuitive as it corresponds to the noise power spectral density partitioned into the local density of cavity modes [45]. We have not yet shown why this term remains unmodified for the case of flicker noise especially since its spectrum is no longer white. A secondary concern also exists pertaining to how low-frequency flicker noise couples into the oscillation at optical or RF frequencies. These topics will be delegated to Section 3.2.2.

To proceed further, we require the use of Eqs. (3.8)-(3.10) for determining $S_{F_\phi}(\omega)$. The first step of this procedure involves dividing Eq. (3.10) by $4P_0$ (as per Eq. (3.8)) to recover

$$S_{F_r}(\omega) = \frac{N^r_{psd,tot}(\omega)}{T^2} \tag{3.11}$$

Next, we relate $S_{F_{im}}(\omega)$ to $S_{F_r}(\omega)$. Note that if the noise is completely random, the in-phase and out-of-phase noise contributions are equal. This condition applies to conventional white noise but does not necessarily apply to all noise processes. In order to provide a general relation between $S_{F_{im}}(\omega)$ and $S_{F_r}(\omega)$, we define a factor X such that $S_{F_{im}}(\omega) = XS_{F_r}(\omega)$. X is equal to 1 for white noise but may be a different factor if the total noise power splits unevenly between

amplitude and phase. We combine the factor of X with $N^{r}_{psd,tot}(\omega)$ in Eq. (3.11) to recover $N^{im}_{psd,tot}(\omega)$ in the definition of $S_{F_{im}}(\omega)$. Finally, after dividing by P_0 (as per Eq. (3.9)), we obtain

$$S_{F_\phi}(\omega) = \frac{N^{im}_{psd,tot}(\omega)}{P_0 T^2} \tag{3.12}$$

3.2.2 Flicker Noise in Oscillators

Equation (3.12) can be used to determine the spectral density of frequency fluctuations and subsequently to calculate the phase-noise spectrum of the oscillator. However, before doing so, let us first examine the topic of flicker noise and address how it affects the modes of the oscillator. Critical to this discussion is the method by which flicker noise evolves from an inherently near-DC phenomenon into a noise source at RF or optical frequencies.

To begin, consider the scenario where an ideal signal passes through an amplifier so that the output consists of a scaled version of the input signal but degraded by noise. Our focus will be on flicker noise since the system behavior under additive white noise has already been analyzed in Chapter 2. Following [70], we see that the flicker noise at RF frequencies results from a frequency upconversion process, as the noise is not present in the absence of a carrier. However, in contrast to [70], we believe the flicker noise upconversion to be intrinsic to the operation of the gain medium itself. That is, an amplifier functions by converting DC voltage/current into gain at frequencies extending to the bandwidth of the amplifier. Near-DC noise entering the amplifier (generated by the voltage/current source, defects [75], etc) results in perturbation of the amplifier gain and therefore affects all signals being amplified. As the amplification process is multiplicative, the resulting RF flicker noise will be proportional to the output signal level.

This can be more concretely seen from the amplifier input-output relations given as

$$E_{out}(t) = \left[G + \Delta G(t)\right] E_{in}(t) \tag{3.13}$$

where G denotes the amplifier's field gain. $\Delta G(t)$ represents a time-dependent perturbation to the gain, which we attribute to be due to low-frequency flicker noise, and $E_{in}(t)$ ($E_{out}(t)$) represents the amplifier's time-dependent input (output) field. Note that in Eq. (3.13), we have ignored the contribution from white noise, which would introduce an additive noise term to the amplified input. This viewpoint of gain is general to any amplifier system. If a near-DC gain fluctuation ($\Delta G(t)$) is introduced, it is clear that this fluctuation propagates to the amplifier output through multiplication by E_{in}. Thus, even if the magnitude of $\Delta G(t)$ remains constant, the observed output noise power will rise or fall with the input signal level. Note that $\Delta G(t)$ may be introduced from flicker-noise fluctuations in the power supply or from defects/traps within the amplifier. As any signal within the bandwidth of the amplifier experiences gain, those signals all feel the effect of the noise perturbation. However, the upconverted noise for each mode ultimately depends on the strength of that particular mode (Eq. (3.13)). Since the strength of the oscillating mode is much larger than that of the sidemodes, the flicker noise predominantly resides around the oscillating mode.

The preceding discussion describes the process by which flicker noise upconverts into the frequency band of oscillation. In the white noise case, the noise provides a direct kick to the system, and the strength of the kick couples equally into each of the available oscillator modes. In the flicker noise case, the noise provides a perturbation to the gain, which then becomes upconverted and is coupled into the oscillator modes. However, we have not yet shown how to determine the amount of flicker noise coupled into each mode. Quantifying the noise into the oscillating mode is especially difficult due to the $1/f^{\alpha}$ spectral dependence of flicker noise. For example, integration over the $1/f$ spectral density would yield an unbounded amount of added noise power. One can potentially circumvent this issue by defining cutoff frequencies for the noise process. However, after integration, one is then left with cumbersome logarithmic quantities dependent on the chosen integration limits. In the end, the noise coupled into the oscillating mode must reproduce a second factor of $1/T$ to be consistent with Eqs. (3.10)-(3.12). We will show in Section 3.3 that this $1/T^2$ dependence is *necessary* to yield agreement with experimental observation.

One possible resolution to this issue can be seen from Eq. (3.11) by equating $S_{F_r}(\omega)$ to the Fourier transform of $\left\langle F_r(t)^* F_r(t+\tau)\right\rangle$ where τ is the time delay of the correlation. As noted earlier, one factor of T accounts for the rate at which the integrated roundtrip noise is added into the cavity. We established that Eq. (3.11) is valid for white noise, and it is clear that for this case the correlation $\left\langle F_r(t)^* F_r(t+\tau)\right\rangle$ must be proportional to $\delta(\tau)$ to recover the spectral properties of the noise [29]. The remaining terms ($N^r_{psd,tot}/T$) of the correlation yield the strength of the total in-phase noise partitioned into the available oscillator modes.

Let us now examine the case of flicker noise using the same approach as before but letting $N^r_{psd,tot}(\omega)$ vary over frequency. Here, we assume the flicker noise process to be stationary, modeled from an ensemble of statistically independent random processes [41]. The Fourier transform of the correlation $\left\langle F_r(t)^* F_r(t+\tau)\right\rangle$ provides the desired $1/f^{\alpha}$ shape of the flicker noise spectrum. The remaining terms ($N^r_{psd,tot}/T$) of the correlation again appear to yield a partitioning of noise similar to the case of white noise. This analysis suggests that the underlying processes of flicker noise are also distributed into the local density of cavity modes, whereas the color of the spectrum is introduced from the correlation between noise events.

3.2.3 Oscillator Phase-Noise Spectrum

Having established a useful interpretation for the partitioning of flicker noise, we are now ready to continue with our treatment of oscillator phase-noise. Our starting point is the Langevin equation for fluctuations in the instantaneous frequency ($\Delta\Omega(t)$) defined through Eq. (3.6). Note that we have not included any terms governing the coupling of amplitude and phase [29, 45] in Eq. (3.6). Should the need arise, one can readily define an equivalent "linewidth enhancement factor" for any oscillator system. The autocorrelation of Eq. (3.6) can be found through $\left\langle \Delta\Omega(t)^* \Delta\Omega(t+\tau)\right\rangle$. Subsequent application of the Fourier transform yields

$$S_{\Delta\Omega}(\omega) = S_{F_\phi}(\omega) = \frac{N^{im}_{psd,tot}(\omega)}{P_0 T^2} \tag{3.14}$$

where $S_{\Delta\Omega}(\omega)$ is defined as the spectral density of frequency fluctuations. It is clear that $S_{\Delta\Omega}(\omega)$ follows the same spectral dependence as that exhibited by the noise process itself. With $S_{\Delta\Omega}(\omega)$ defined, one can then determine the variance in the oscillator's phase fluctuations to be [29, 66–69, 76].

$$\left\langle \Delta\phi^2(\tau) \right\rangle = \frac{2}{\pi} \int_{-\infty}^{\infty} S_{\Delta\Omega}(\omega) \frac{\sin^2(\omega\tau/2)}{\omega^2} d\omega \tag{3.15}$$

Equation (3.15) provides the result necessary for obtaining the oscillator's phase-noise spectrum. To show this, we apply the Wiener-Khinchin theorem beginning with the autocorrelation function of the electric field. As we saw in Chapter 2, when the oscillator's amplitude noise is negligible compared to its phase noise, this autocorrelation becomes

$$\left\langle E(t)^* E(t+\tau) \right\rangle \approx E_0^2 e^{j2\pi f_0 \tau} e^{-\left\langle \Delta\phi^2(\tau) \right\rangle / 2} \tag{3.16}$$

where f_0 is the frequency of oscillation. Note that Eq. (3.16) assumes that the phase fluctuations are Gaussian distributed (via the Central Limit Theorem) [46]. The Fourier transform of Eq. (3.16) yields the desired phase-noise spectrum of the oscillator centered at its oscillation frequency. Division by $P_0 = E_0^2$ is also required in order to normalize the spectrum to the carrier power.

We now apply Eqs. (3.14)-(3.16) to the calculation of phase noise for an oscillator perturbed by both white and $1/f$ noise. The sum of both noise contributions can be compactly represented through

$$S_{\Delta\Omega}(\omega) = \frac{1}{P_0 T^2} \left(N_0^{im} + \frac{N_1^{im}}{|\omega|} \right) \tag{3.17}$$

where N_0^{im} is the strength of the phase component of white noise at any particular frequency and N_1^{im} is the strength of the phase component to $1/f$ noise at 1 rad/s. Note that N_1^{im} differs from the usual $1/f$ flicker-noise coefficient by a factor of 2π since we have represented the noise in

angular frequency units. The individual contributions of white and $1/f$ noise are separable and can be independently evaluated in Eq. (3.15). For white noise, we find

$$\left\langle \Delta\phi^2(\tau) \right\rangle_W = \frac{N_0^{im}|\tau|}{P_0 T^2} \tag{3.18}$$

With the identification of $N_0^{im} = N_{psd,tot}/2$, Eq. (3.18) is identical to Eq. (2.16) of Chapter 2 whose derivation makes use of a vector-based approach to phase noise.

The same process used to determine Eq. (3.18) can in principle be applied to the case of $1/f$ noise. Doing so, one finds that the integral of Eq. (3.15) diverges to infinity when integrating through $\omega = 0$. This divergence is a direct consequence of the large increase in noise power as the frequency approaches the carrier. However, in real (physical) systems, the measurement time is always restricted, and the bandwidth is always finite. These conditions present bounds on both the minimum and maximum frequencies that effectively contribute to the measurement. Some discussion is warranted regarding how these bounds are implemented within the framework of Eq. (3.15).

For this discussion, we consider a thought experiment taking the perspective of the measurement system whose purpose is to determine the phase noise of an oscillator. Our first task is to obtain a finite-length sample of the oscillator field. The field we measure consists of a periodic signal embedded in random fluctuations due to noise. We next take the field's autocorrelation as per Eq. (3.16) so that the spectrum may be computed from its Fourier transform. It is clear that if the noise fluctuations of interest occur slower than the time allotted to our field sampling, then these fluctuations are effectively *invisible* to the measurement. This introduces a low-frequency limit, below which the noise contributions become approximately zero to the integral of Eq. (3.15). Note that the original statement of Eq. (3.15) has the interpretation that all frequencies of $S_{\Delta\Omega}(\omega)$ contribute to the observed phase noise. A similar line of reasoning also follows for the high-frequency limit where it is now the measurement bandwidth that renders higher frequencies of noise to zero. However, since the integrand in Eq. (3.15) consists of decaying functions with frequency, we choose instead to keep $\pm\infty$ as the high-frequency limit with negligible loss to accuracy. This choice simplifies the number of variable definitions necessary to the setup of the integral.

We may now evaluate Eq. (3.15) for $1/f$ noise with the help of a lower frequency cutoff (ω_c). With this bound in place, the previous issues of divergence are circumvented. Note that in defining ω_c, we have introduced an abrupt cutoff in the frequencies that contribute to measurable phase fluctuations. Should the need arise, a more gradual rolloff can readily be used. The integral for $1/f$ noise can be calculated by first recognizing that the integrand is even and subsequently introducing ω_c as the lower frequency limit. This integration yields

$$\left\langle \Delta\phi^2(\tau) \right\rangle_{1/f} = \frac{N_1^{im}\tau^2}{\pi P_0 T^2}\left(\frac{\sin^2(\omega_c\tau/2)}{2(\omega_c\tau/2)^2} + \frac{\sin(\omega_c\tau)}{\omega_c\tau} - Ci(\omega_c|\tau|) \right) \tag{3.19}$$

where $Ci(\omega_c|\tau|)$ represents the cosine integral of its argument. To maintain self-consistency with our chosen cutoff frequency, τ must be restricted so that $\omega_c|\tau| < 2\pi$. This condition expresses the fact that although we have accounted for ω_c introduced by the finite length of our sampled field, we have not limited the time delay of our autocorrelation function (Eq. (3.16)). Clearly, $|\tau|$ must be less than the duration of the field ($2\pi/\omega_c$) for the overlap of the fields to be meaningful. Having established $\omega_c|\tau| < 2\pi$, we ideally would like to proceed further and simplify Eq. (3.19) using $\omega_c|\tau| << 1$. However, as it stands, it appears that some error would be incurred in making this approximation when $\omega_c|\tau|$ is close to 2π. In actuality, this error is negligible for a wide variety of cases. Substitution of Eq. (3.19) into Eq. (3.16) shows that the exponential of the autocorrelation becomes a strong function of τ. We are specifically interested in showing this exponential to be negligible in the range of large τ. This becomes true for typical values of ω_c ~ 1 rad/s and under typical levels of $1/f$ noise injection. For these cases, we may approximate Eq. (3.19) using $\omega_c|\tau| << 1$ to obtain

$$\left\langle \Delta\phi^2(\tau) \right\rangle_{1/f} = \frac{N_1^{im}\tau^2}{\pi P_0 T^2}\left(\frac{3}{2} - \gamma - \ln(\omega_c|\tau|) \right) \tag{3.20}$$

where $\gamma \approx 0.5772$ is the Euler-Mascheroni constant. In Section 3.3, we will show examples where we justify this approximation for use in calculating the phase noise of an oscillator. Furthermore, we will also apply Eqs. (3.14)-(3.16) to noise exhibiting $1/f^{\alpha}$ dependence with values of α other than 0 or 1. Note that approximating $\omega_c|\tau| << 1$ introduces a sign reversal from positive to negative in Eq. (3.20) when $\omega_c|\tau| \sim 2.5$. Beyond these limits $\langle \Delta\phi^2(\tau) \rangle_{1/f}$ must be set to infinity in order to prevent this artifact from distorting the computations of Eq. (3.16).

To evaluate the total phase-noise spectrum, we combine Eqs. (3.18) and (3.20) in Eq. (3.16) and take the Fourier transform of the result. We also normalize to the carrier power through division by P_0. The combined spectrum consists of the convolution between the individual phase-noise contributions due to white and $1/f$ noise. The white-noise contribution leads to a Lorentzian, while the spectrum due to $1/f$ noise must be evaluated numerically. It is clear from Eqs. (3.18)-(3.20) that the phase variance is dependent on the ratio of noise to signal and on the square of the roundtrip delay. To reduce phase noise, the noise should be minimized relative to the oscillating signal. This can be easily achieved for white noise through an increase in intracavity power. However, this method becomes ineffective for the case of flicker noise whose noise is approximately proportional to signal power. Note that in Eqs. (3.19) and (3.20), the noise and signal terms are not independent. For these cases, the roundtrip delay must be increased in order to gain significant reductions in phase noise.

3.2.4 Modeling Procedure: Oscillator Phase-Noise

In this section, we provide a step-by-step prescription detailing how to apply our developed theory to the modeling of oscillator phase-noise. The overarching goal is to determine the oscillator's phase-noise spectrum from the Fourier transform of Eq. (3.16). Note that normalization by $P_0 = E_0^2$ is also required to maintain consistency with traditional definitions of phase noise. Equation (3.16) depends critically on $\langle \Delta\phi^2(\tau) \rangle$, which can be derived from Eqs. (3.14) and (3.15) once the appropriate variables (i.e., the noise-to-signal ratio and the roundtrip delay) are specified. $\langle \Delta\phi^2(\tau) \rangle$ can also be directly calculated from Eq. (3.18) for the

case of white noise and from Eqs. (3.19) and (3.20) for $1/f$ noise. Below, we summarize the steps required for the modeling of oscillator phase-noise.

First, the total phase-noise spectrum injected into the oscillator in one roundtrip of the cavity is measured. This noise can be due to the amplifier alone or to multiple components within the oscillator cavity. In the next section, we will quantify this noise from measurements of the residual noise added in a single roundtrip. This process also allows the determination of the corresponding signal power under oscillation. Note that the individual components of the cavity should be operated (i.e., current and voltage) and also driven (i.e., the signal input) under their appropriate oscillating conditions. The ratio of the noise spectrum to the signal power specifies half of the unknown variables in Eq. (3.14).

Second, the time delay of the system in the vicinity of the oscillating mode is measured. This specifies the rest of the unknown parameters in Eq. (3.14). The roundtrip delay can be found from the frequency translation of the mode corresponding to a 2π shift in phase. An alternative method is to directly probe the S21 response of the system and to subsequently determine the group delay from the slope of the unwrapped phase. For the measurements that we will be conducting in the next section, we measure the roundtrip delay from the frequency separation between cavity sidemodes.

And third, once Eq. (3.14) is specified, the calculation of Eq. (3.15) is applied to determine $\langle \Delta\phi^2(\tau) \rangle$ subject to the appropriate cutoff frequency. Using $\langle \Delta\phi^2(\tau) \rangle$ in Eq. (3.16), normalizing the result by P_0, and subsequently numerically evaluating the Fourier transform yields the desired oscillator phase-noise spectrum.

3.3 Experimental Results of Oscillator Phase-Noise

In the following sections, we show experimental results of oscillator phase-noise when the perturbation consists of both injected white and $1/f^{\alpha}$ noise. The total injected noise spectrum is given by the superposition of the individual noise sources (as per Fig. 3-4). This fact will be evident in our measurements of the noise that is added in each cavity roundtrip. Using these measurements of the injected noise, we show that the phase noise of an oscillator can be

precisely predicted across a variety of operating conditions. Although our investigations will be primarily focused on RF oscillators, the developed phase-noise theory is expected to be general and applicable to oscillators operating in any domain (optical, RF, mechanical, etc). As a demonstration of this point, we will show excellent agreement between our model and experiment for the case of a hybrid optoelectronic oscillator.

3.3.1 Comparisons to Measurement: Electrical Oscillator

In this section, we will compare the phase-noise theory of Eqs. (3.14)-(3.16) to phase-noise measurements of three different RF ring-cavity oscillators operating at 2.5 GHz. These oscillators all share the same generic ring architecture of Fig. 3-6 but differ in the type of RF amplifier used. RF isolation was employed at the input and output of each amplifier to allow only for unidirectional oscillation. The output of the amplifier was then sent to an output coupler where the majority (90%) of the RF power was coupled out of the cavity. The remainder (10%) of the power was recirculated within the cavity to drive self-oscillation. The other intracavity elements of the oscillator include an RF filter for defining the oscillator operating frequency, an RF phase shifter for tuning the oscillation frequency, and a variable RF attenuator for controlling

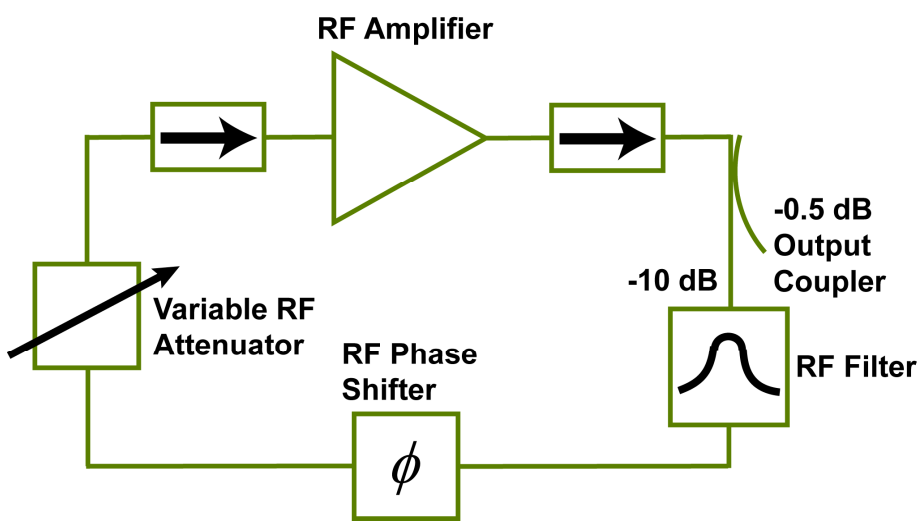

Figure 3-6: Generic system diagram employed for three RF oscillators comprising different types of RF amplifiers. The system delay is defined by various configurations of RF filters controlling the net group delay per cavity roundtrip. The RF signal is coupled out prior to filtering allowing for direct measurement of the noise added in each roundtrip.

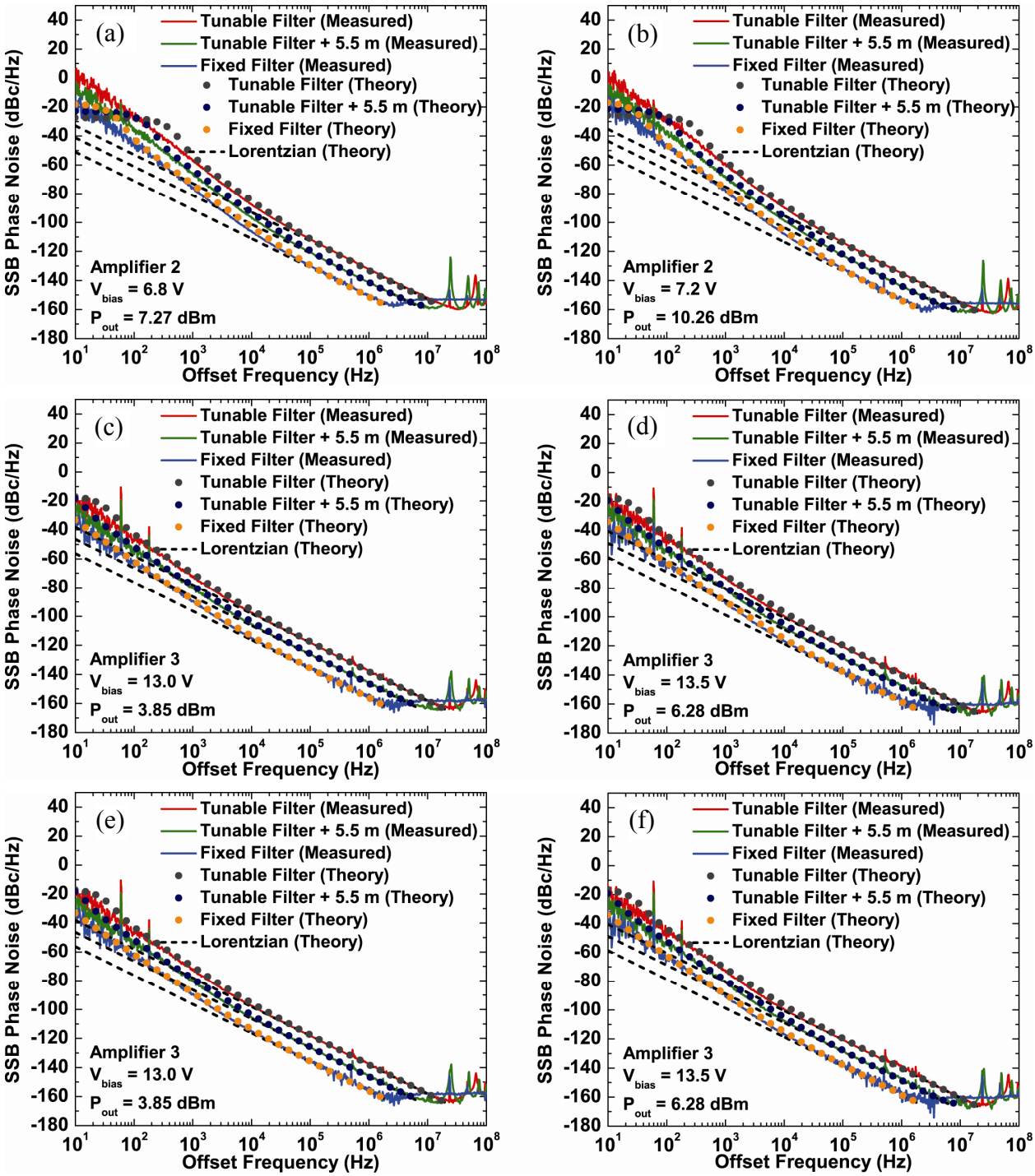

Fig. 3-7. Measured (solid lines) and theoretical (solid circles) RF oscillator phase-noise for three different types of amplifiers. (a) Phase noise for Amplifier 1 at 9.12 dBm RF power. (b) Phase noise for Amplifier 1 at 11.17 dBm RF power. (c) Phase noise for Amplifier 2 at 7.27 dBm RF power. (d) Phase noise for Amplifier 2 at 10.26 dBm RF power. (e) Phase noise for Amplifier 3 at 3.85 dBm RF power. (f) Phase noise for Amplifier 3 at 6.28 dBm RF power. The RF oscillator of Fig. 3-6 was tested with three filter configurations including 1) a tunable filter, 2) a tunable filter + 5.5 m delay, and 3) a fixed filter. The Lorentzian phase noise predictions (dashed line) are also shown.

the operating point of the oscillator. We wish to emphasize that the signal is coupled out directly after the amplifier prior to any RF filtering (Fig. 3-6). As we saw in Chapter 2, this allows us to directly measure the noise power added by the amplifier in each roundtrip of the cavity before this noise is rejected by the filter. Note that there is no accumulation of noise power at frequencies outside the filter passband as the noise is rejected before the completion of each cavity roundtrip.

For each RF amplifier used, we measured the oscillator phase-noise under three different configurations of the RF filter. These configurations consist of: (i) a tunable RF filter (halfwidth (*HW*) = 75 MHz at 2.5 GHz), (ii) a tunable RF filter (*HW* = 75 MHz) with 5.5 m additional delay, and (iii) a fixed RF filter (*HW* = 2.9 MHz). For each configuration, the center frequency was 2.5 GHz. By altering the RF filter configuration, we are able to adjust the group delay (and thus roundtrip time) induced by the resonance of the filter.

The results of the phase-noise measured by an Agilent E5052B signal-source analyzer (SSA) are shown in Fig. 3-7. Note that the measurements for each amplifier were performed at two separate operating conditions controlled by the bias voltage of the amplifier. At each operating point, the amplifier voltage, intracavity loss, and output power were maintained constant over all three filter configurations tested. The primary effect of the different filter configurations is then to vary the roundtrip delay experienced by the oscillating mode of the cavity. The three amplifiers used for our measurements are as follows: Amplifier 1 – Advantek AM-4080M 2-4 GHz (Figs. 3-7 (a) and (b)), Amplifier 2 – Miteq AFS4-02000800-45-10P 2-8 GHz (Figs. 3-7 (c) and (d)), and Amplifier 3 – Miteq AM-3A-0520-0 0.5-2 GHz (Figs. 3-7 (e) and (f)). Note that these are the same three amplifiers as that used in Figs. 3-1 to 3-3. We will first describe our measured phase-noise results for these oscillators and neglect for the moment the phase noise predicted by theory.

It is apparent from Fig. 3-7 that all of the measured phase-noise spectra exhibit Lorentzian characteristics (20 dB/decade) at high offset frequencies but vary at a faster rate for frequencies closer to the carrier. This increase in phase-noise slope signifies the influence of flicker noise, as we hinted at in Section 3.1. The inverse roundtrip delay associated with each filter configuration was estimated through the free-spectral-range corresponding to the sidemode spacing of the cavity. For the configurations comprising a tunable filter and a tunable filter + 5.5 m delay, these inverse roundtrip times are 62.8 MHz and 24.2 MHz, respectively and remain approximately

invariant across all three amplifiers. In the case of the fixed filter, the sidemodes cannot be observed as the RF filter is sufficiently narrow (HW = 2.9 MHz) to prevent power from accumulating at the sidemode frequencies. For these cases, the sidemode spacing can instead be estimated using the techniques described in Section 3.2.4 or by simply detuning the phase shifter until the sidemode appears relative to the oscillating mode. With these methods, the sidemode frequency was found to be approximately 7.7 MHz for all three oscillators that employ the fixed filter.

From the sidemode frequency, or equivalently the inverse roundtrip time, one can verify the scaling dependence of oscillator phase noise on T. The phase-noise scaling was previously found to be $1/T^2$ for white noise in Chapter 2, and this same dependence can also be observed in the measurements of Fig 3-7. Taking as an example the Lorentzian contribution to Fig. 3-7 (a),

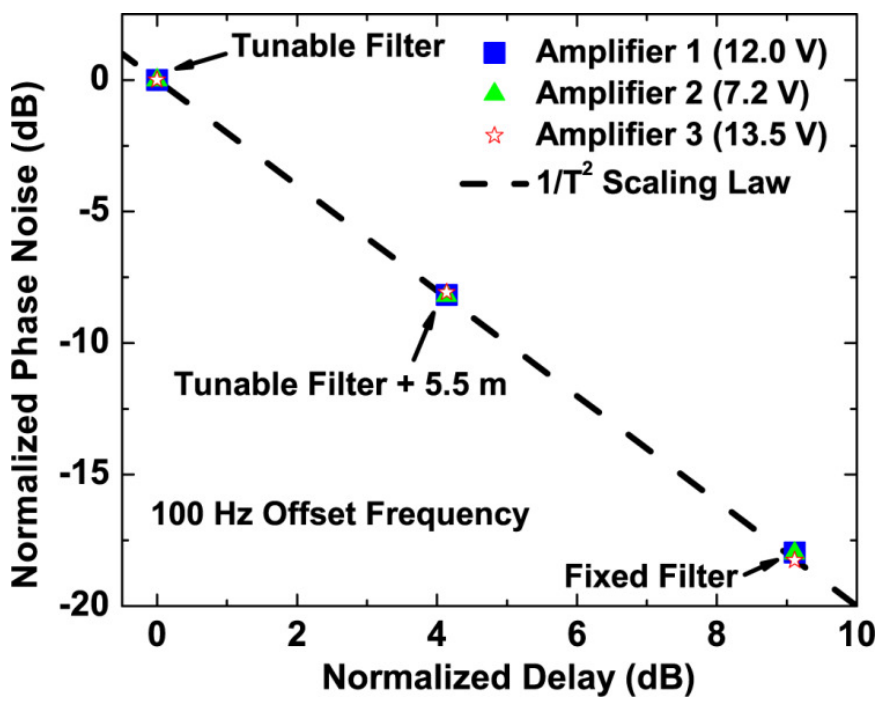

Figure 3-8: Measured normalized phase noise at 100 Hz offset frequency as a function of the normalized delay for Amplifier 1 (12.0 V), Amplifier 2 (7.2 V), and Amplifier 3 (13.5 V). The phase noise is plotted for the tunable filter, tunable filter + 5.5 m, and fixed filter configurations, normalized to the tunable filter case. The delay is similarly normalized to the delay of the tunable filter. The ideal $1/T^2$ dependency of phase noise on delay (dashed line) is also provided.

the measured phase-noise values at 1 MHz offset are -134.1 dBc/Hz for the tunable filter, -142.5 dBc/Hz for the tunable filter + 5.5 m, and -152.4 dBc/Hz for the fixed filter. Note that $1/T^2$ corresponds to a difference of 8.3 dB between the configurations of the tunable filter and tunable filter + 5.5 m and corresponds to a difference of 10 dB between the tunable filter + 5.5 m and the fixed filter.

These scaling relations also apply to the portions of the phase-noise spectrum due to flicker noise, as can be seen in all the measurements of Fig. 3-7. The corresponding results are consolidated in Fig. 3-8 for an offset frequency of 100 Hz from the carrier. In Fig. 3-8, the normalized phase noise is plotted as a function of the normalized delay for Amplifier 1 (12.0 V), Amplifier 2 (7.2 V), and Amplifier 3 (13.5 V). The delay is controlled by the configuration of the oscillator (tunable filter, tunable filter + 5.5 m delay, or fixed filter). Both the plotted phase noise and delay are normalized to their respective values for the tunable filter case. Ideally, one expects a 2 dB decrease in phase noise for every 1 dB increase in delay corresponding to a $1/T^2$ scaling dependence. We see that the measured results agree well with these predictions. This $1/T^2$ dependence also agrees with the form of Eqs. (3.10)-(3.12) presented in Section 3.2.

An inverse relation also exists between phase noise and the corresponding signal power of the oscillator. This relationship can in principle be deciphered from Fig. 3-7 but is most easily seen in the measurements of Figs. 3-1, 3-2, and 3-3. Let us focus for now on Fig. 3-1, which (as described in Section 3.1) shows the phase noise of a fixed filter oscillator as a function of the measured output power. The system uses the ring-cavity configuration of Fig. 3-6 and oscillates from gain supplied by Amplifier 1. The output power was varied through the bias voltage supplied to the amplifier. As noted earlier, the measured values of RF power represent directly the powers at the output of the amplifier. Similar to the fixed filter cases of Figs. 3-7 (a) and (b), the sidemodes of Fig. 3-1 also cannot be observed in the phase-noise spectrum. In its place is the broadband white-noise added by the amplifier in a single roundtrip of the cavity. The filter prevents power from accumulating at frequencies beyond its passband. It is clear from Fig. 3-1 that the added white-noise floor decreases in direct proportion to the output power. In actuality, the added white noise remains approximately constant, and it is the normalization relative to carrier power that causes the noise floor to decrease with RF power. The observed clamping of the added white noise above threshold is analogous to the clamping of spontaneous emission in a

laser [29, 46]. A similar dependence on carrier power can also be seen in the Lorentzian contribution to the spectrum at higher offset frequencies. The Lorentzian phase-noise is inversely related to signal power, as was both theoretically and experimentally shown in Chapter 2.

The properties of the Lorentzian phase noise are noticeably different from the noise characteristics at lower offset frequencies. At these offsets, upconverted flicker noise dominates over white noise, and the shape of the phase-noise spectrum changes to reflect this behavior. As noted in Section 3.1, the phase noise at lower offsets appears somewhat constant and no longer depends inversely on carrier power. These results support our interpretation of flicker noise as a perturbation to the amplifier gain. A fluctuation in the gain propagates into all the modes of the oscillator supported by the gain. However, as this process is multiplicative (Eq. (3.13)), the upconverted noise that appears around a particular mode becomes approximately proportional to the strength of the mode. The end result is that the ratio of noise-to-signal remains relatively constant since the noise follows any increase or decrease in carrier power. Combining the properties of white and flicker noise then, we expect that their crossover point can be controlled through the RF power. This behavior is apparent in Figs. 3-1, 3-2, and 3-3 and can also be observed directly in noise measurements of the amplifier itself [70].

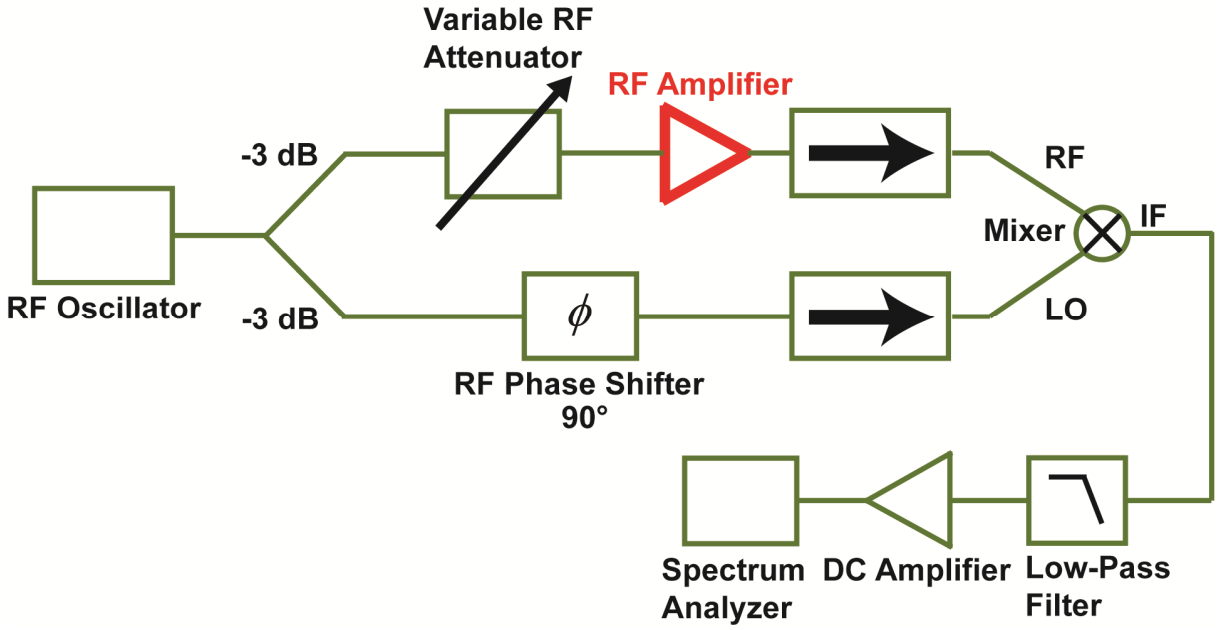

Figure 3-9: Diagram of the system used to measure the residual phase-noise added by an RF amplifier.

Next, we compare our theoretical predictions of oscillator phase-noise to the measurements of Fig. 3-7. For this comparison, Eq. (3.14) requires the phase-noise spectral density added in a single cavity roundtrip to be specified relative to the oscillation power ($N_{psd,tot}^{im}(\omega)/P_0$). This quantity can be determined through a residual noise measurement of the amplifier phase noise (Fig. 3-9). In this measurement, a 2.5 GHz RF oscillator signal is equally split along two paths. The RF path probes the RF amplifier under test with an amount of power controllable by the variable RF attenuator. The LO path passes through an RF phase shifter maintaining quadrature between both arms. These two paths are combined in a double balanced mixer thereby generating a downconverted IF signal that is subsequently low-pass filtered to remove mixing harmonics. The resulting signal is then amplified (40 dB) and detected on an Agilent E4440A spectrum analyzer. The common-mode phase noise of the RF oscillator is rejected by the mixing process if the LO and RF paths are balanced in length. Similarly, the amplitude noise (of both the oscillator and the amplifier) is also suppressed by the saturated amplifier/mixer. The system of Fig. 3-9 then in principle measures only the added phase noise of the amplifier at its bias point of operation. In practice, the effects of amplitude noise and oscillator phase-noise are not completely suppressed and can both cause distortion to the results.

Ground loops represent another source of unwanted noise that can influence the results of the residual phase-noise measurement. The ground-loop noise usually manifests itself as spurs at harmonics of the line frequency (60 Hz) but can also in addition appear as noise at other frequencies within the spectrum. Its impact can be minimized by using battery power supplies whenever possible instead of directly drawing power from the line.

Fig. 3-10 shows the measured residual phase-noise for Amplifiers 1, 2, and 3 under the operating conditions (bias voltage and input RF power) used in Fig. 3-7. These measurements are calibrated by determining the system transfer function due to broadband noise injection. The resulting phase noise is normalized to the signal power for each of the cases in Fig. 3-10. It is clear that the phase noise measured all exhibit a similar general form. The low-frequency noise shows characteristics of $1/f^{\alpha}$, while the high-frequency noise flattens into a broadband floor of white noise. The spurs at harmonics of 60 Hz are due to what remains of the power-line noise, while the feature near 5.5 kHz is due to unintentional noise present in the measurement system (ground loops, etc). In addition to these measured results, Fig. 3-10 also provides the asymptotic

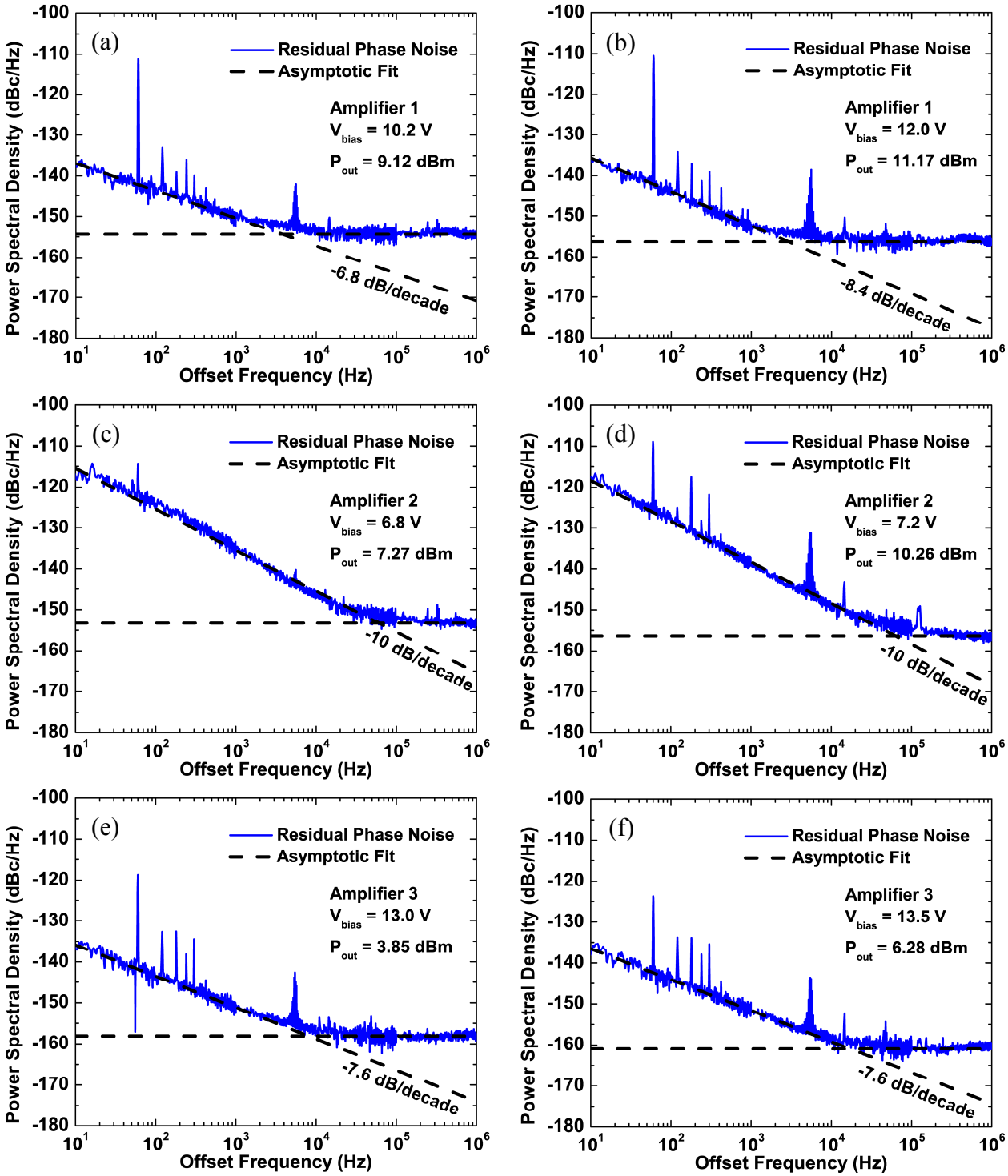

Fig. 3-10. Measured phase-noise (solid line) with asymptotic fits (dashed line) for three different types of RF amplifiers. (a) Amplifier 1 phase noise with 9.12 dBm output RF power. (b) Amplifier 1 phase noise with 11.17 dBm output RF power. (c) Amplifier 2 phase noise with 7.27 dBm output RF power. (d) Amplifier 2 phase noise with 10.26 dBm output RF power. (e) Amplifier 3 phase noise with 3.85 dBm output RF power. (f) Amplifier 3 phase noise with 6.28 dBm output RF power. The phase-noise slope is also indicated for each case.

fits to the low- and high-frequency noise spectra. For the case of Amplifier 2, we use a slope of -10 dB/decade even though the actual noise shape varies at a slightly faster rate. This choice of flicker slope introduces a small error but allows for simpler noise calculations using Eq. (3.20) as we will see later. A summary of our results is provided in Table 3-1.

As expected, the additive white phase-noise of each amplifier decreases in direct proportion to its corresponding carrier power. This is a consequence of the normalization such that the noise power appears lower relative to the signal. Since the operating conditions were made constant between the oscillator measurements of Fig. 3-7 and the amplifier measurements of Fig. 3-10, the white phase-noise levels between the two are directly comparable. Note that the values of the oscillator white phase-noise must be obtained from the fixed filter cases since the sidemodes are not completely extinguished using the tunable filter. The properties of flicker noise are harder to predict since the noise upconversion process depends on the characteristics of the amplifier (Eq. (3.13)). However in general, the ratio of noise to signal remains relatively constant over most of the frequency range since the upconversion process is multiplicative. For example, Table 3-1 shows that the flicker noise of Amplifier 1 extrapolated to 1 Hz offset is -130.1 dBc/Hz for P_{out} = 2.42 dBm and is -127.3 dBm for P_{out} = 4.47 dBm. Although this value has increased by 2.8 dB over a ~2 dB difference in power, the slope has also increased from -6.8 dB/decade to -8.4 dB/decade. The net result is that the noise at many of the intermediate

Table 3-1: Summary of RF amplifier residual phase-noise measurements corresponding to Amplifiers 1, 2, and 3.

	P_{out}	V_{bias}	$1/f^{\alpha}$ at 1 Hz	White Noise	$1/f^{\alpha}$ Slope
Amplifier 1	9.12 dBm	10.2 V	-130.1 dBc/Hz	-154.4 dBc/Hz	-6.8 dB/decade
	11.17 dBm	12.0 V	-127.3 dBc/Hz	-156.3 dBc/Hz	-8.4 dB/decade
Amplifier 2	7.27 dBm	6.8 V	-105.5 dBc/Hz	-153.3 dBc/Hz	-10 dB/decade
	10.26 dBm	7.2 V	-108.3 dBc/Hz	-156.4 dBc/Hz	-10 dB/decade
Amplifier 3	3.85 dBm	13.0 V	-128.3 dBc/Hz	-158.1 dBc/Hz	-7.6 dB/decade
	6.28 dBm	13.5 V	-129.0 dBc/Hz	-161.0 dBc/Hz	-7.6 dB/decade

frequencies does not change significantly in strength. It is interesting to note that Amplifier 2 exhibits the largest flicker noise (by ~20 dB), whereas the flicker noise of Amplifier 1 and 3 are similar. These properties can also be seen in the phase noise of the oscillators (Fig. 3-7) associated with Amplifiers 1, 2, and 3.

We now use the measured noise properties of Amplifiers 1, 2, and 3 to predict the phase noise of their corresponding oscillators in Fig. 3-7. Most of this analysis follows from our discussions of Eqs. (3.14)-(3.20). We will however mention a few of the important points in these calculations. First, the analysis of $1/f^{\alpha}$ noise for non-integer α follows similarly from Eqs. (3.14)-(3.16). When $0 \le \alpha < 1$, the integral from zero to infinity converges, and the effects of finite measurement time can usually be ignored to good approximation. Second, the flicker noise coefficient used in Eq. (3.14) is expressed in units of angular frequency. For $1/f^{\alpha}$ noise, the conversion from linear frequency to angular frequency results in a factor of $(2\pi)^{\alpha}$. And third, as discussed earlier, Eq. (3.20) for $1/f$ noise is only applicable when the autocorrelation of Eq. (3.16) vanishes in the large τ limit. In order to apply Eq. (3.20) to Amplifier 2 then, we would need to justify that this condition is satisfied. Let us do so by first revisiting the more general Eq. (3.19) and specifically evaluate the coefficient $C = N_1^{im}/\pi P_0 T^2$. Using $1/T$ = 7.7 MHz and N_1^{im}/P_0 = (2.82×10^{-11}) $\times 2\pi$ (Table 3-1: Amplifier 2 at 6.8 V), we find C to be ~3340 1/s^2. Furthermore, for τ ranging from 0 to 12.9 s corresponding to the SSA measurement time, we find that ω_c = $2\pi/12.9$ rad/s. With these values, it is clear that Eq. (3.19) evaluates to be much greater than unity (and thus Eq. (3.16) becomes negligible) in the limit of large τ. The use of Eq. (3.20) can be similarly justified for the remaining operating points of $1/T$ and N_1^{im}/P_0 corresponding to Amplifier 2. Note that τ = 12.9 s corresponds to a lower frequency limit of 1 Hz offset for measurements in the SSA. This value coincides with our measurements in Fig. 3-7 even though the displayed frequency range has been limited to 10 Hz offset for ease of comparison to Fig. 3-10.

Fig. 3-7 shows both the calculated and measured phase noise for oscillators employing the three different RF amplifiers discussed previously. In the theoretical curves of Fig. 3-7, we have also included the Lorentzian prediction of phase noise (dashed line) due solely to white noise. These contributions were calculated using the theory of Chapter 2, or equivalently, by combining

Eq. (3.18) with Eq. (3.16), normalizing by P_0, and taking the Fourier transform. The parameters used for this calculation consist of the measured noise-to-signal ratios of Table 3-1 and the estimated values of roundtrip delay discussed previously. By comparing the Lorentzian curves to measurement, we see that the high frequency behavior of oscillator phase-noise is accurately captured, whereas large differences are observed at low frequency offsets. These inadequacies at low frequencies are resolved by accounting for the effects of flicker noise using the full theory of oscillator phase-noise (solid circles). As is apparent in Fig. 3-7, the agreement of the full theory with measurement is excellent over most of the frequency range. However, deviations are still present below 100 Hz for Amplifiers 1 and 3 and below 1 kHz for Amplifier 2. These deviations arise from discrepancies in the definition of phase noise (described next) rather than from any source of errors in our prediction.

Currently, there are two definitions of phase noise used throughout literature: (1) $S_E(\omega)$ - the spectral density of the field and (2) $S_\phi(\omega)$ - the spectral density of the phase. $S_E(\omega)$ is the quantity calculated from Eqs. (3.14)-(3.16) as we have taken an autocorrelation in the oscillator field. On the other hand, measurements of phase noise effectively find $S_\phi(\omega)$ instead. This can be shown by calculating the mixer output voltage (IF) corresponding to the measurement and subsequently determining the spectrum of the result (see Appendix B.1). $S_E(\omega)$ and $S_\phi(\omega)$ are approximately equal at higher offset frequencies but deviate from each other at frequencies close to the carrier. In particular, $S_E(\omega)$ clips at low frequencies attesting that the oscillator spectrum is bounded. This behavior is clearly visible in Figs. 3-7 (c) and (d) but can also be seen in the other measurements of Fig. 3-7. Note that $S_\phi(\omega)$ is unbounded at low frequencies reaching measured values of 25 dBc/Hz at 1 Hz offset (not shown) for Amplifier 2. As expected, these values cannot correspond to physical measures of the oscillator field spectrum as they would imply the noise power integrated over 1 Hz would be larger than the total power available to the carrier. Combined with the fact that real systems typically work with periodic functions of phase rather than any direct phase variable, we regard $S_E(\omega)$ to be more fundamental than $S_\phi(\omega)$.

3.3.2 Comparisons to Measurement: Optoelectronic Oscillator

In this section, we apply Eqs. (3.14)-(3.16) to a hybrid optoelectronic oscillator (OEO) in order to demonstrate the generality of the theory. The OEO (Fig. 3-11) comprises both optical and electrical cavity elements, and net gain is achieved via a combination of microwave-photonic (MWP) gain [6] and RF amplification. The OEO is driven by a high-power low-noise slab-coupled optical waveguide external cavity laser (SCOWECL) [27, 28] (P = 150 mW at 2-A bias) whose power is controlled by a variable optical attenuator (VOA). The other elements of the optical cavity consist of a Mach-Zehnder (MZ) modulator (BW = 15 GHz, V_π = 3.1 V at 3 GHz), an optical isolator, and a commercial photodiode ($\Re$ = 0.8 A/W, BW = 12 GHz). Typically, an OEO would also employ a long optical fiber delay for the goal of obtaining low phase-noise. We have excluded this element within our cavity as the phase noise becomes too low to measure compared to the SSA noise floor. In the electrical path, the photodiode output is

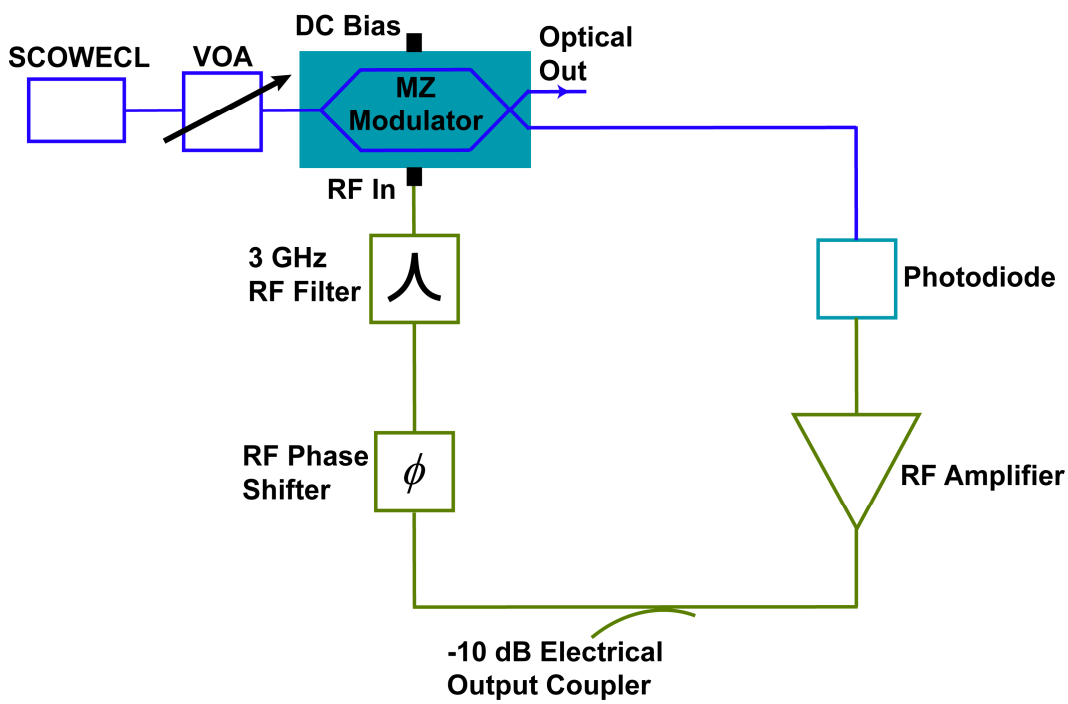

Figure 3-11: Configuration of an optoelectronic oscillator (OEO) operating at 3.0 GHz. Microwave-photonic (MWP) gain is achieved by the high-power, low-noise slab-coupled optical waveguide external cavity laser (SCOWECL), Mach-Zehnder modulator (MZ Modulator) and photodiode.

amplified by a low flicker-noise AML26PNB2001 2-6 GHz RF amplifier (G = 23.4 dB, small-signal NF = 5.7 dB) and coupled out through a -10 dB RF tap. The remainder of the power (90%) is recirculated within the cavity first to an RF phase shifter and subsequently to a 3 GHz RF filter (HW = 1.2 MHz). The optoelectronic loop is closed by feeding the RF signal back as input drive to the MZ modulator. Oscillation begins from the amplification of noise incident on the modulator RF input port. Similar to the RF oscillator cases discussed in the previous section, the noise is coupled out before passing through the filter. This allows the white noise of a single roundtrip to be directly measured from the oscillator output [46].

The MWP gain in an OEO results from a two-step process where the CW (pump) laser source is first modulated by an RF input generating sidebands around the optical carrier. The RF information is later recovered after photodetection from the heterodyning of the sidebands with the carrier. For a given frequency, net gain is achieved if the signal amplitude increases from RF in to RF out. This process can be described through [4, 77]

$$V_{out} = V_{supply} \frac{J_1\left(\pi V_{in}/V_\pi\right)}{V_{in}} V_{in} \tag{3.21}$$

where V_{out} $\left(V_{in}\right)$ is the amplitude of the sinusoidal output (input) voltage and V_π is the MZ modulator half-wave switching voltage. $V_{supply} = P_O \sin\left(\Gamma_0\right)\alpha\Re R$ consists of a product between the optical power supplied by the laser (P_O), the sine of the MZ modulator bias angle ($\sin\Gamma_0$), the optical attenuation accumulated from signal propagation to the photodiode (α), the photodiode responsivity ($\Re$), and the photodiode load resistance (R).

Equation (3.21) expresses that the MWP voltage gain from V_{in} to V_{out} is dependent on the supplied voltage (V_{supply}) and a saturation parameter ($J_1\left(\pi V_{in}/V_\pi\right)/V_{in}$). If $V_{in} << V_\pi$, this saturation parameter evaluates to a constant $\pi/2V_\pi$. However, for larger values of V_{in}, the gain quickly compresses below its small signal value. It is clear that Eq. (3.21) exhibits a similar functional form compared to the gain model introduced in Eq. (3.13) with $\Delta G(t)$ representing noise on the supply voltage. A low-frequency relative intensity noise (RIN) fluctuation of the SCOWECL source becomes directly upconverted into a fluctuation on the carrier. This process occurs in conjunction with the additive white noise that directly perturbs the OEO.

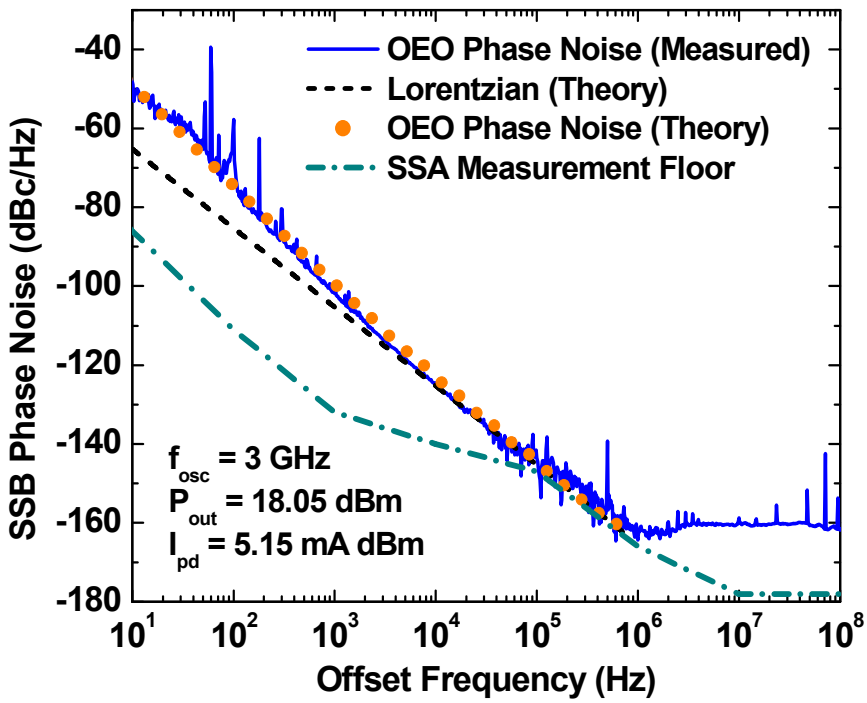

Figure 3-12: Measured (solid line) and theoretical phase noise (solid circles) of an OEO corresponding to the configuration of Fig. 3-11. The SSA measurement noise floor (dash-dot line) and Lorentzian theory (dashed line) are also provided.

Here, we are interested in comparing measurements of the OEO phase-noise to predictions obtained from Eqs. (3.14)-(3.16). Figure 3-12 shows the measured 3 GHz OEO phase-noise along with the noise floor of the SSA measurement. The SCOWECL was operated at 2 A bias, while the intracavity attenuation was adjusted to maintain 5.15 mA photocurrent. The OEO phase-noise shows characteristics corresponding to a Lorentzian (20 dB/decade) at high frequencies but falls off at a faster rate at low frequencies. These phase-noise properties are indicative of a transition from white noise to flicker noise in the spectrum of injected noise. The SSA noise floor also suggests that the measured phase noise between 100 kHz and 1 MHz is slightly high due to influence from the noise of the measurement system. As was found for the fixed filter cases of the RF oscillator, the cavity sidemodes are again rejected here by the narrow passband of the 3 GHz filter. Separate measurements of the sidemode frequency spacing, however, determine its value to be near 3.6 MHz.

In order to calculate the OEO phase-noise, we require knowledge of the injected noise in a single roundtrip of the cavity. The added noise is the combined total from contributions of the MWP link and also from that of the RF amplifier. We may treat their combination as an equivalent amplifier providing gain from RF in to RF out. The phase noise of the combined amplifier can be probed using the system of Fig. 3-13 in an analogous manner to a conventional amplifier (Fig. 3-9). For this measurement, the individual components of the amplifier are driven under their respective OEO operating conditions. This yields 14.3 dBm RF input into the MZ modulator and 18.1 dBm RF output after the RF amplifier. The measured phase noise of the combined amplifier is shown in Fig. 3-14. We have also provided the noise floor of the measurement, which can be seen to slightly increase the noise at low offset frequencies. The phase noise extrapolated to 1 Hz offset is found to be -138.4 dBc/Hz with a slope of -5.8 dB/decade. This noise level is lower than that of conventional RF amplifiers (Fig. 3-10) due to the use of low-noise components in the MWP link and also to the use of a low flicker-noise RF amplifier. The white phase-noise floor of the combined amplifier is -161 dBc/Hz and matches the level of white noise found in Fig. 3-12. Note that both the noise feature near 5.5 kHz and the spurs at 60 Hz harmonics can again be observed in the measurements of Fig. 3-14.

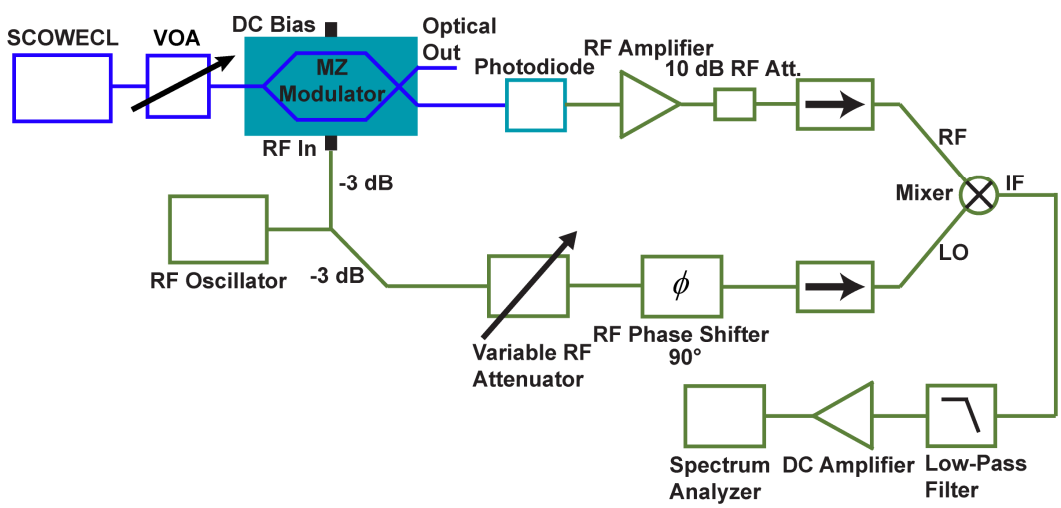

Figure 3-13: Schematic of a system that measures the residual phase-noise of an OEO. The system is similar to that of Fig. 3-9 but measures the phase noise of the combined amplifier (MWP link + RF amplifier).

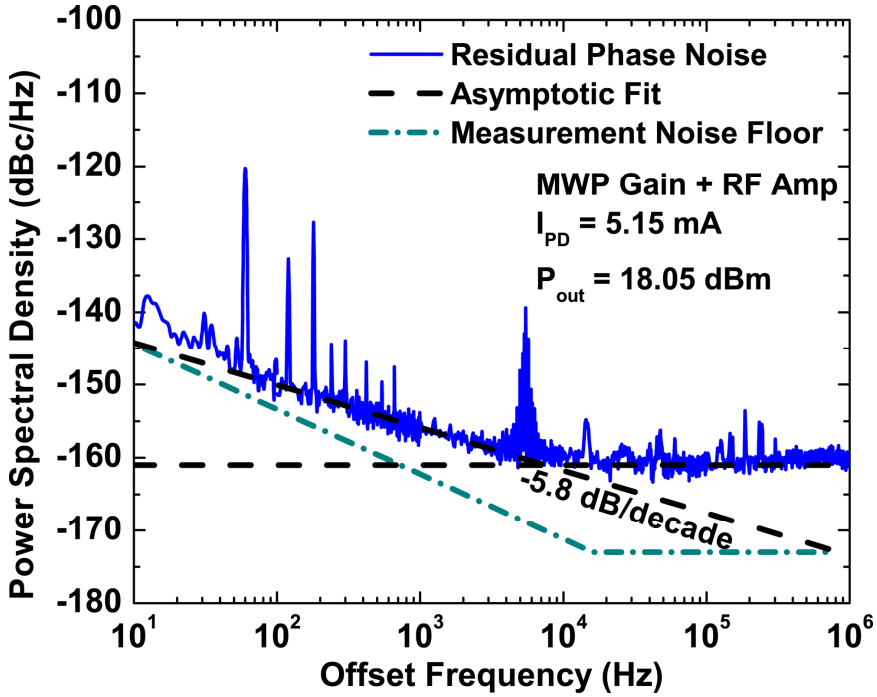

Figure 3-14: Measured residual phase-noise of an OEO system consisting of a MWP link + RF amplifier. In addition to the OEO residual noise (solid line), the asymptotic fit (dashed line) and measurement noise floor (dash-dot line) are also provided.

Using the measured amplifier noise characteristics, we can now predict the phase noise of the OEO. These calculations closely mirror that of the RF oscillator in Figs. 3-7 and 3-10. Thus, we will only present their results which are illustrated in Fig. 3-12. When only white noise is taken into account, the spectrum is a Lorentzian (dashed line) and agrees well with the measured OEO phase-noise at higher offset frequencies. At low frequencies where the influence of flicker noise begins to dominate, the agreement quickly degrades. On the other hand, the full theory (solid circles) accurately captures the effects of both white and flicker noise and therefore shows excellent agreement to measurement. The OEO phase-noise is lower than that corresponding to the RF oscillators of Fig. 3-7 even with no intentionally added optical delay. With a factor of 10-100 increase in delay, the phase noise can be improved by 20-40 dB. Using optical fiber, this can all be achieved suffering only small penalties in loss.

3.4 Conclusion

We have presented a general theory of oscillator phase-noise when the perturbation is driven by sources of white and flicker noise. The upconversion of low-frequency noise is treated from the perspective of a gain perturbation which then couples into the modes of the oscillator. We apply the theory to several cases of RF oscillators varying between their RF amplifiers used and the configuration of their RF filter. The phase noise of each oscillator was also tested at two separate operating points in oscillation power. With knowledge of the oscillation power, roundtrip delay, and corresponding injected noise spectrum, the oscillator phase-noise was predicted to excellent accuracy. The theory was also applied to a hybrid optoelectronic oscillator as a demonstration to its generality. Excellent agreement was again found in this case. Although only electromagnetic oscillators were tested in this work, the theory can be extended to oscillators of other varieties.

Chapter 4

Slab-Coupled Optical Waveguide Optoelectronic Oscillators (SCOW-OEOs)

Introduced in Chapter 1, the optoelectronic oscillator (OEO) describes an oscillator system that uses microwave-photonic (MWP) down-conversion to generate a stable RF signal with low phase-noise [4, 5]. Potentially any RF frequency can be synthesized as long as the components of the optical cavity (e.g., modulator, photodetector) have the bandwidth required for operation. Unlike conventional electronic oscillators, the phase-noise of an OEO does not theoretically degrade at higher frequencies since the loss of optical fiber is constant for any RF frequency that can be generated. We saw in Chapters 2 and 3 that the phase noise of an oscillator fundamentally depends only on the delay time and on the spectral density of the injected noise relative to the signal power. The primary noise mechanisms which affect the OEO are thermal noise, shot noise, laser relative intensity noise (RIN), and noise resulting from optical fiber nonlinearities.

The phase noise of an OEO can be made low because the delay line used in the optical path can be made long with almost negligible increases in roundtrip loss. The noise coupled into the oscillating mode is reduced as the density of cavity modes increases. The overall reduction of phase noise depends on the square of the delay-length, thus allowing the spectral purity of the OEO (free-running) to rival that of the best microwave oscillators [11, 37, 78]. However, due to nonlinearities in the transport of optical signals over fiber, the scaling laws of delay usually break down at higher optical powers and longer delay lengths. These nonlinearities will be addressed in Section 4.2. In addition to the issue of fiber noise, a long fiber delay causes the mode frequency spacing to decrease below the limit where the sidemodes can be rejected by an RF filter. For 1 km of delay, the sidemode spacing is 200 kHz, which is less than the bandwidth of typical filters at RF frequencies. In Chapter 5, we will show how the problem of cavity sidemodes can be almost completely eliminated by the judicious setting of the OEO operating conditions.

Previous reports have shown that the OEO is capable of phase-noise as low as -160 dBc/Hz at 10-kHz offset oscillating at 10-GHz center frequency [11, 37]. This level of performance comes at the cost of large sidemode spurs due to the many sidemodes (>100 for a 16-km fiber delay) that compete for gain within the bandwidth of the RF filter. Typically, RF amplification is employed in an OEO to provide the gain necessary to oscillate. However, this is not always true as some OEOs have demonstrated oscillation using only the microwave-photonic (MWP) gain provided by a modulated optical source. In these cases, optical amplification has still been required and incorporated either internally to the OEO cavity [79] or externally to the laser source [78, 80]. The use of an optical amplifier is undesirable as it increases both the noise and power consumption of the OEO. In this work, we demonstrate a 3-GHz high-performance amplifier-free slab-coupled optical waveguide optoelectronic oscillator (SCOW-OEO) [58]. The operating frequency of 3 GHz was set by the availability of narrow bandwidth dielectric bandpass filters manufactured by K&L Microwave. The OEO uses a high-power low-noise slab-coupled optical waveguide (SCOW) laser source [27, 28] and photodiode [34] to enable oscillation solely from gain intrinsic to the MWP link. No optical or RF amplifiers were used within the configuration of our system. We find that the SCOW-OEO demonstrates excellent phase-noise performance, even with only 1.5 km of delay length, due to the use of high-power, low-noise SCOW components.

4.1 SCOW-OEO System and Operation

A schematic of the SCOW-OEO system [58] is shown in Fig. 4-1. The system consists of a high-power low-noise slab-coupled optical waveguide external cavity laser (SCOWECL) (P_O = 300 mW at 4 A) [27, 28] and a high-power variable-confinement slab-coupled optical waveguide photodiode (VC-SCOWPD) (BW = 3.5 GHz, I_{sat} = 38 mA, $\Re$ = 1 A/W) [34]. The SCOWECL is modulated by a Mach-Zehnder (MZ) modulator (BW = 15 GHz, V_π = 3.1 V at 3 GHz, $Loss$ = 2.2 dB), and the resulting signal is sent to the VC-SCOWPD after passing through a fiber stretcher and a 1.5-km fiber delay-line. The photodiode down-converts the optical signal

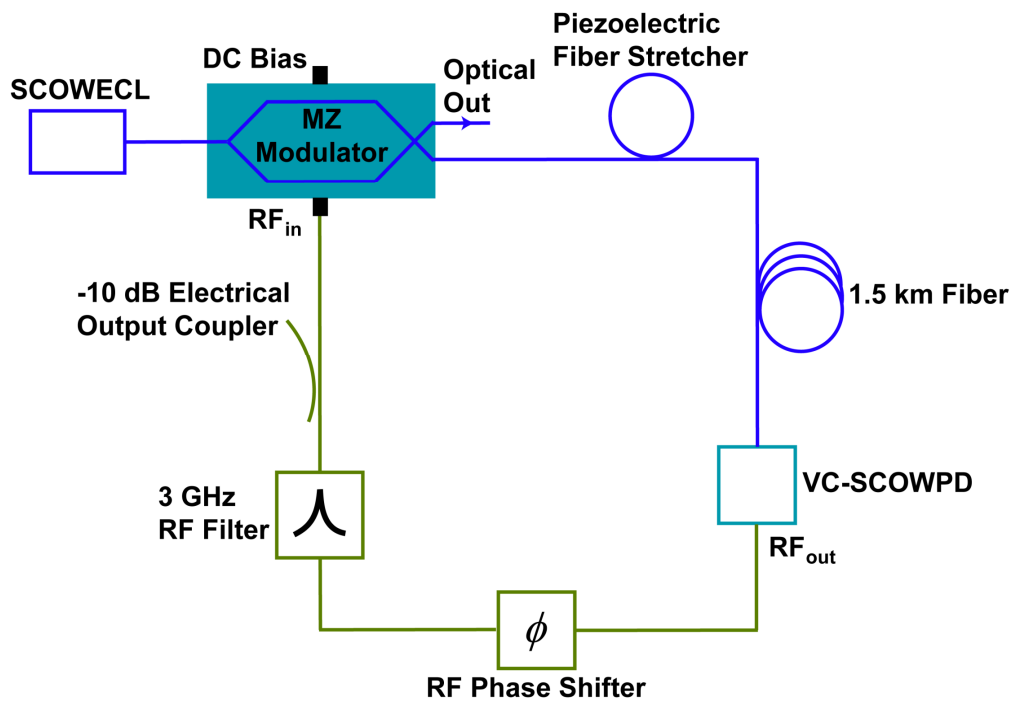

Figure 4-1: Schematic of a 1.5 km cavity length SCOW-OEO system that oscillates due to MWP gain supplied by the SCOWECL, Mach-Zehnder (MZ) modulator, and VC-SCOWPD. Oscillation was achieved at 3 GHz without the use of RF amplification.

into an RF photocurrent at the beat frequency of the optical modulation. This RF signal is sent to an RF phase shifter and an RF filter (f_{center} = 3 GHz, BW = 2.5 MHz) before being coupled out of a -10 dB RF coupler. The majority of the RF power is reused to drive the RF input port of the modulator to obtain self oscillation. The SCOWECL, modulator, fiber delay, and photodiode form an intensity modulated direct-detection (IMDD) link allowing signal amplification from modulator RF_{in} to photodiode RF_{out}. The piezoelectric fiber stretcher serves as a low-loss (*Loss* = 0.5 dB) phase modulator for suppression of fiber nonlinearities (stimulated Brillouin scattering (SBS) and double-backscattered interferometric noise) [37, 78]. The fiber stretcher was operated at resonance by driving it with a 60-kHz sinusoid having a peak-to-peak voltage of 30 V. The RF filter defines the center frequency of oscillation and filters unwanted sidemodes, while the RF phase shifter allows for static fine-tuning around this operating point. It is important to note that the SCOW-OEO does not employ any optical or RF amplification and thus oscillates solely from MWP gain [6].

OEO oscillation begins from noise entering the RF input port of the modulator. This noise is a combination of thermal noise, shot noise, and laser RIN or noise from nonlinear optical fiber scattering. The incident noise causes a tiny modulation of the optical carrier, which is converted to an RF signal after the photodetection process. If the RF signal after one roundtrip exceeds the original noise input into the modulator, the OEO achieves net gain and can therefore oscillate. The signal continues to receive amplification with each roundtrip until saturation occurs. Usually, the saturation mechanism results from the modulator exceeding its linear range of operation but can also occur from compression of other components (e.g., photodiode or RF amplifier when present). For the SCOW-OEO, the dominant amplitude-limiting mechanism occurs through saturation of the modulator response. In steady-state, the gain saturates to approximately the level of the net intracavity loss. For more details regarding the operation of an OEO, we refer the reader to Section 1.2 and Ref. [4].

4.1.1 SCOW-OEO Threshold Analysis

In this section, we present an analysis of the threshold condition for the SCOW-OEO. The threshold is found from the point where the net gain (gain – loss) compensates for the losses in the cavity. Our analysis makes use of Eq. (1.7), simulating the net gain as a function of the DC photocurrent for multiple levels of modulator V_π. We assume a load resistance of R = 50 Ω, perfect modulator extinction, and that the modulator is biased at quadrature ($\Gamma = \pi/2$). We also square the voltage gain calculated via Eq. (1.7) to determine the power gain. Note that this is the net power gain under small-signal conditions as the gain saturates to nearly 1 (0 dB) during oscillation. The results are shown in Fig. 4-2 for V_π between 1.5 V and 5.0 V in intervals of 0.5 V.

It is clear from Fig. 4-2 that the gain increases as the V_π of the modulator decreases. This is intuitive as the modulator V_π controls the amount of voltage required for a sinusoidal swing of the optical power. The condition for the onset of oscillation (net gain = 0 dB) is highlighted by the dashed horizontal line. Positive values of gain in Fig. 4-2 indicate that excess gain is available in the system to compensate for loss, whereas negative gain indicates

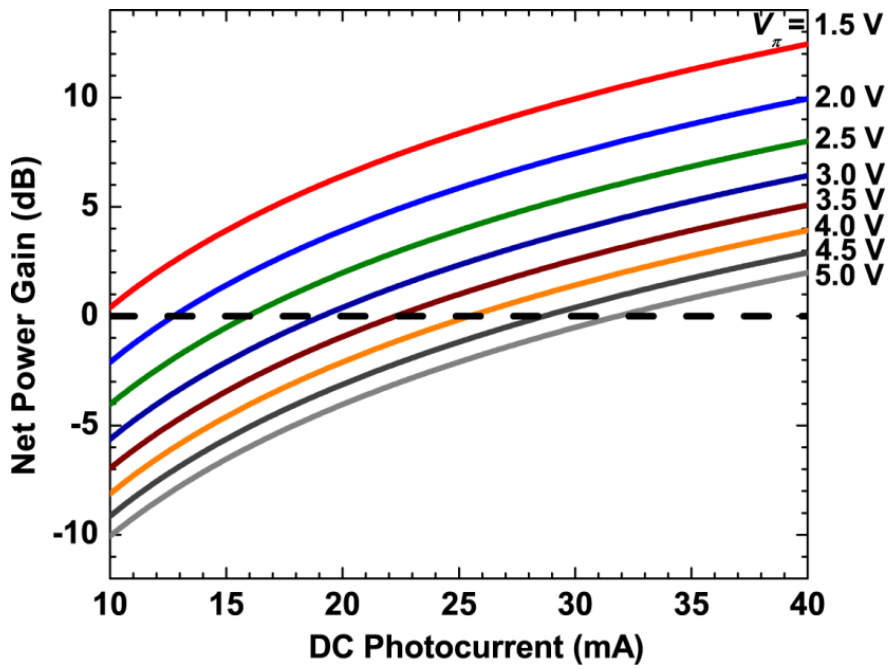

Figure 4-2: Simulation of an OEO's small-signal net power gain (gain – loss) as a function of photocurrent for V_π between 1.5 V and 5.0 V. The threshold condition is determined when the net gain becomes greater than 0 dB (dashed line).

that gain must be supplied to reach oscillation. Therefore modulators with higher V_π require more photocurrent to reach threshold. Low V_π modulators can have V_π below 2 V. However, the modulator's insertion loss, extinction ratio, and power handling are all also important and must be collectively optimized to achieve the best OEO performance. In addition, linearity is beneficial as it is desirable for most of the modulation power to be located in the first harmonic. Higher order harmonics do not disturb operation however, as they are rejected by the RF filter and the bandwidths of the photodiode and modulator. Note that low V_π is not always desirable as the output voltage becomes limited by the railing of the modulator V_π. Thus, OEOs with excess gain may benefit in performance from increasing V_π.

In our SCOW-OEO system with V_π = 3.1 V (at 3 GHz), we expect threshold to occur at I_{ph} ~ 20 mA under ideal zero-loss operation. The RF loss in the SCOW-OEO cavity is ~4.9 dB corresponding to an actual threshold photocurrent of ~35 mA when the modulator is biased at

quadrature. One technique for reducing the threshold current of the OEO is to low-bias the modulator. This method is particularly useful when one wants to limit the optical power launched through the fiber delay and incident on the photodiode. Low-biasing an electro-optic MZ modulator shifts power away from the DC and odd order harmonics towards the even order harmonics. However, the zeroth order (DC) harmonic reduces at a faster rate than the first order harmonic so that the overall RF power will be larger when comparing operation across a fixed DC photocurrent. This means that a low-biased MWP link operating at 25 mA will yield a larger OEO gain than a quadrature-biased MWP link operating at 25 mA.

As mentioned earlier, low-biasing the modulator's operation has many important advantages for an OEO. As long as the system can still oscillate, the optical power can be kept low so that undesirable fiber nonlinearities can be minimized. Furthermore, low-biasing reduces the optical power handling required of the photodiode. This is useful as typical wideband (> 10 GHz) photodiodes cannot handle more than ~20 mA of photocurrent before the device response begins to saturate. Even the VC-SCOWPDs have saturation photocurrents presently near ~40-50 mA, as we will see later. In the operation of our SCOW-OEO, we employ low-biasing of the modulator to take advantage of these properties.

4.1.2 SCOW-OEO System and Environmental Isolation

Previously, we showed a schematic of the SCOW-OEO comprising both optical and electrical cavity components (Fig. 4-1). Here, we connect this illustration to a physical system. Fig. 4-3 shows a photograph of the SCOW-OEO resting on an air-floated optical table. Various strategies are employed to further isolate the SCOW-OEO from environmental perturbations. Of these strategies, we find the most benefit by simply using rubber blocks to dampen the vibrations of the system. The rubber blocks are placed beneath optical breadboards, which serve as stabilized platforms for the components of the SCOW-OEO. In Fig. 4-3, two vibration-isolated platforms can be observed. One platform stabilizes both the SCOWECL and VC-SCOWPD while a second stabilizes the passive routing fibers and polarization controllers. The use of vibration-damping blocks reduces the SCOW-OEO phase-noise by >30 dB (not shown) for frequencies close to the carrier.

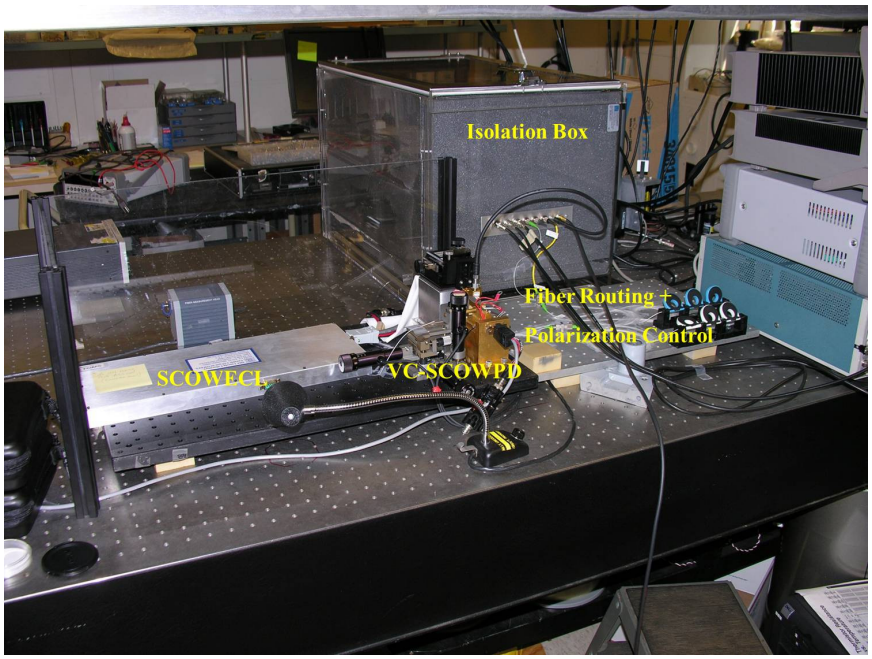

Figure 4-3: SCOW-OEO system resting on an optical table and employing passive vibration control. Rubber blocks are used to isolate the SCOWECL, VC-SCOWPD, and passive optical fiber from environmental perturbations.

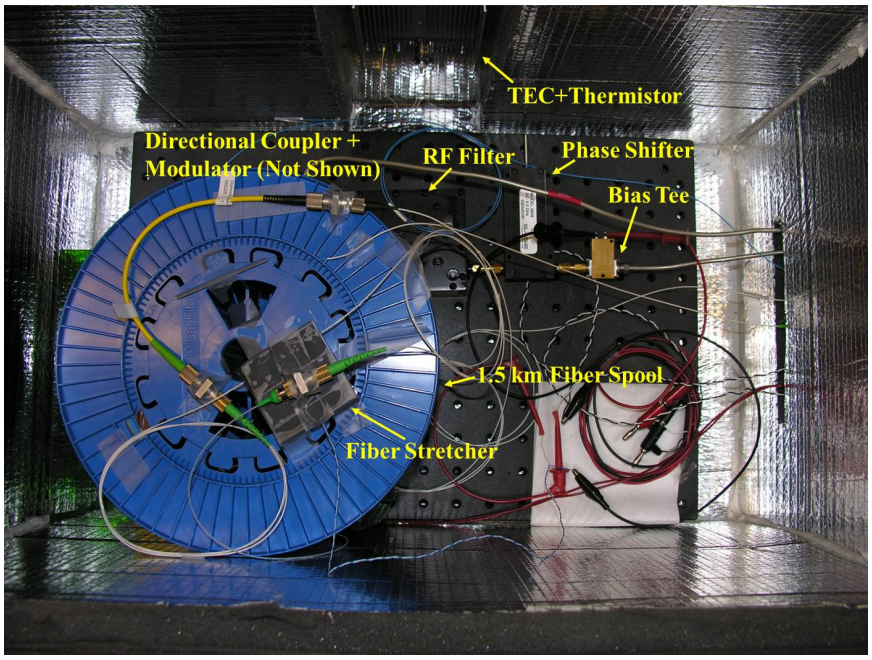

Figure 4-4: SCOW-OEO isolation box for temperature and environmental stabilization of a 1.5-km fiber spool. This box is also shared by many other passive optical and RF cavity elements.

In addition to these blocks, we also employ a temperature-controlled isolation box as a housing unit for the long optical fiber delay. Figure 4-4 shows a photograph of the components within the isolation box. The output of the SCOWECL passes through a polarization controller, enters one of the input ports, and connects to a $LiNbO_3$ amplitude modulator (not visible). One output of the modulator is routed outside to a power monitor. The other output is sent through a fiber stretcher (phase modulator) and into the 1.5-km fiber spool. The output of the optical fiber is then directed outside of the box for photodetection by the VC-SCOWPD. The electrical signal is rerouted back inside the box through a bias tee, RF phase shifter, 3 GHz RF filter, -10 dB RF directional coupler (not visible), and finally into the RF port of the amplitude modulator. The design of the SCOW-OEO system keeps the active units outside so that the passive elements within the isolation box may be temperature controlled with relative ease. Note that acoustic dampening foam is used on the surrounding walls of the box enclosure and that rubber blocks (not visible) are employed to further stabilize the passive components against environmental perturbation.

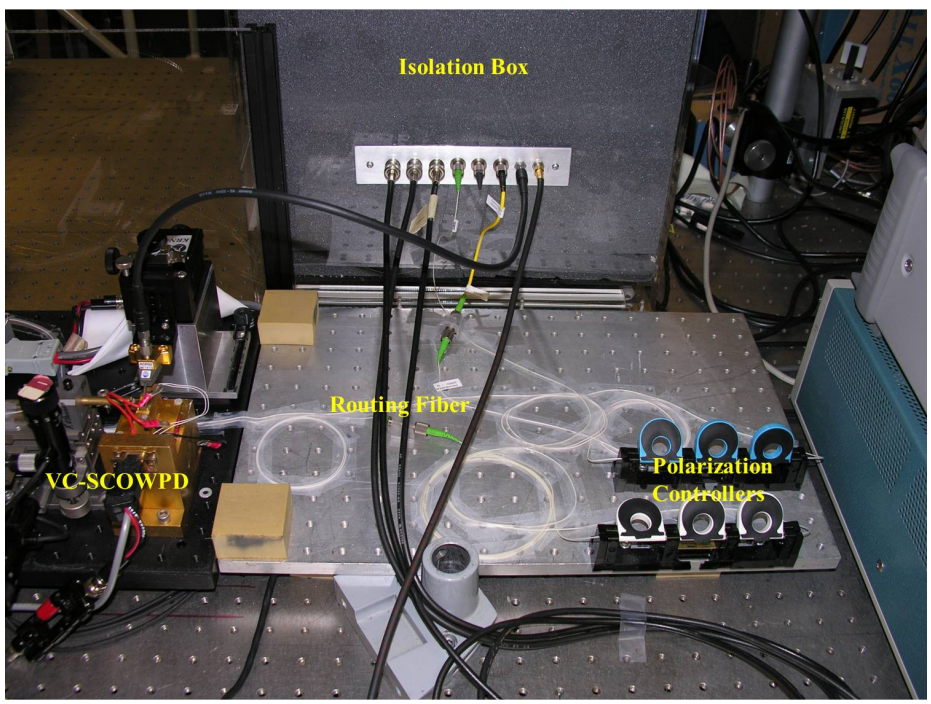

Figure 4-5: Fiber and electrical cable routing assembly for SCOW-OEO system. The front panel of the isolation box provides the connections between the active and passive components of the OEO.

Figure 4-5 shows a zoomed-in picture of the fiber and electrical cable routing assembly. The SCOWECL output is transmitted through one of the polarization controllers before entering the modulator via the front panel of the isolation box. The output of the fiber delay exits through this panel and is sent through another polarization controller before photodetection by the VC-SCOWPD. The RF cables serve to couple RF power into and out of the unit, while the BNC cables are used to enable voltage drives for the modulator, fiber stretcher, and bias tee.

4.2 SCOW-OEO Components and Noise

Commonly, the phase-noise spectrum of high-performance OEOs degrades significantly from amplitude-to-phase (AM-PM) noise conversion during the photodetection process [37]. This process is analogous to the linewidth enhancement factor of semiconductor lasers [45]. The photodiode must be biased at the null in the AM-PM conversion slope in order to suppress these effects. Lower performance OEOs are often limited by RF amplifier flicker noise instead. While the AM-PM process is important, we wish to make clear that even without any AM-PM conversion, intensity noise still becomes the ultimate limit to OEO phase-noise. This is true because the injection of incoherent intensity noise on top of a coherent modulation signal perturbs the phase of the oscillation and results in broadening of the phase-noise spectrum (see Chapters 2 and 3). For this reason, it is essential for a high-performance OEO that all intensity-noise processes are reduced as much as possible. In the following sections, we will describe measurements of the RIN and AM-PM conversion noise for the SCOWECL and VC-SCOWPD used in the SCOW-OEO system. We will also present an assessment of the stimulated Brillouin scattering induced by large optical powers propagating over fiber.

4.2.1 SCOWECL Relative Intensity Noise

The limiting performance of an OEO is determined by the RIN of the pump laser. Note that the laser's phase-noise or linewidth does not play a role here since all phase information of the optical carrier is lost during the square-law photodetection process. The RIN spectrum of the

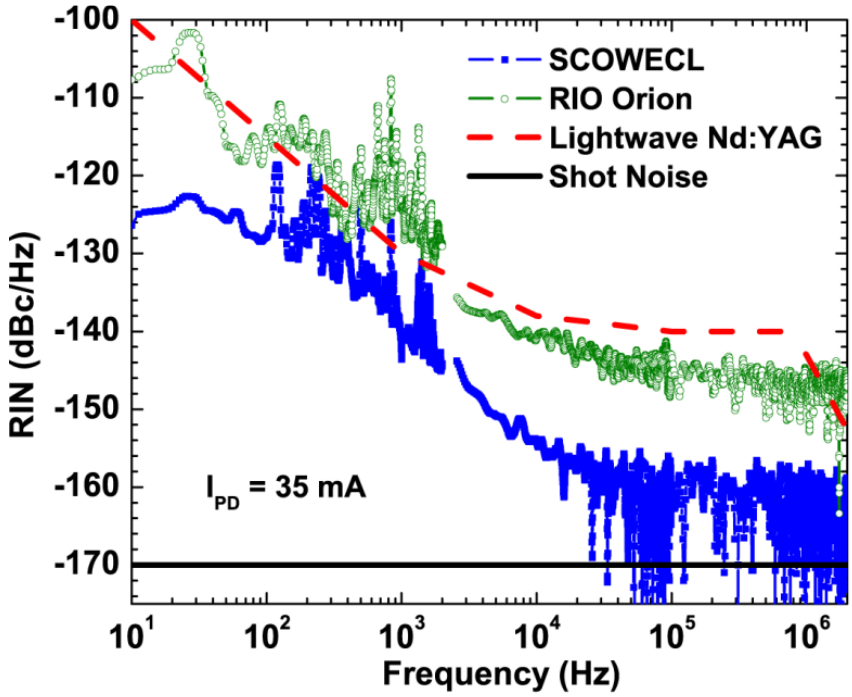

Figure 4-6: Measured RIN of a SCOWECL (solid squares) and commercial ECL (open circles) at low-frequencies (10 Hz – 2 MHz) with the corresponding shot-noise floor indicated (solid line). The reported RIN of a Lightwave Electronics Nd:YAG laser (dashed line) is also provided for comparison.

SCOWECL was determined by directly photodetecting its continuous wave (CW) optical power and measuring the resulting electrical noise signal on an Agilent 89410A vector signal analyzer. Ideally, the CW optical power should yield only a DC photocurrent with no extraneous contributions of power at any other frequency. However, due to the SCOWECL's RIN, the photodetected spectrum contains noise power at frequencies offset from DC. Figure 4-6 shows the measured low-frequency RIN of the SCOWECL and of a commercial RIO Orion high-performance external cavity laser (ECL). Both measurements were taken using the same experimental setup and calibrated using the RIN transfer standard method [81]. The RIN was measured in three separate intervals 10 Hz – 2 kHz (resolution bandwidth (RBW) = 10 Hz), 10 Hz – 100 kHz (RBW = 1 kHz), and 10 Hz – 2 MHz (RBW = 10 kHz). Points at frequencies close to the RBW of each measurement were discarded due to corruption from near-DC noise. In Fig. 4-6, we have also provided the RIN of a Lightwave Electronics Nd:YAG laser (obtained from Ref. [37]) for comparison. Note that the relaxation resonance peak of the Nd:YAG laser is

not shown here but can be found in Fig. 4 of Ref. [37]. The SCOWECL RIN is 10-15 dB below both the commercial ECL RIN and the Nd:YAG laser RIN throughout the measurement range (0-2 MHz) and also compares favorably against other semiconductor, fiber, and solid state lasers. We believe most of the peaks in the measured RIN spectra at low frequencies (100 Hz – 1 kHz) to be due to 60 Hz harmonics and technical noise.

Although we have thus far only discussed the low-frequency RIN of the SCOWECL, we wish to emphasize that the RIN at both low and high frequencies are important to an OEO. Oscillation starts through RIN at the oscillation frequency, and eventually causes the generation of sidebands through optical modulation of the carrier. The sideband generation process results in the upconversion of low frequency RIN into the frequency band of the oscillation signal. The RIN around the carrier therefore becomes a weighted average of the RIN at low and high frequencies. Typically, low-frequency RIN dominates over high-frequency RIN, and the spectrum of injected noise follows the spectrum of the laser's low-frequency RIN. Figure 4-7

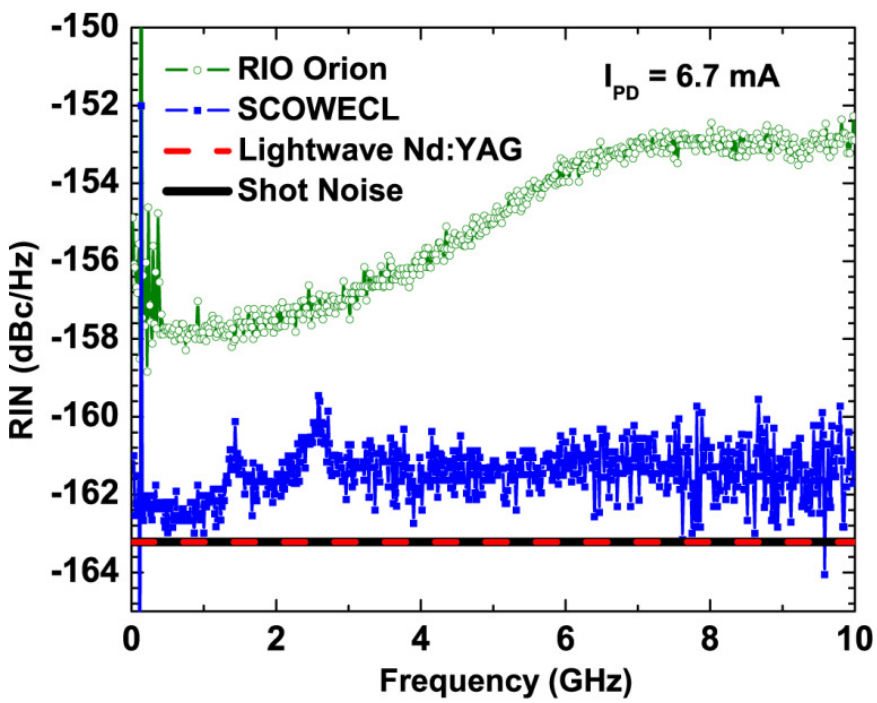

Figure 4-7: Measured RIN of a SCOWECL (solid squares) and commercial ECL (open circles) at high-frequencies (10 Hz – 10 GHz) with the corresponding shot-noise floor indicated (solid line). The RIN of a Lightwave Electronics Nd:YAG laser (dashed line), which is assumed to be shot-noise limited at high frequencies, is also provided for comparison.

shows the measured high-frequency RIN for the SCOWECL and the commercial ECL from 10 Hz to 10 GHz. The expected RIN of the Lightwave Electronics Nd:YAG laser, which is assumed to be shot-noise limited, is also provided for comparison. Again, the SCOWECL high-frequency RIN is lower than the commercial ECL RIN, but only by 4-8 dB for noise below 10 GHz offset frequency. The commercial ECL exhibits a relaxation resonance peak between 6-10 GHz that increases its RIN to -153 dBc/Hz. For many semiconductor lasers, this resonance peak is even larger and can significantly increase the average injected RIN of the OEO. As can be seen in Fig. 4-7, the SCOWECL RIN spectrum is nearly shot-noise limited throughout the measurement range and thus exhibits similar high-frequency RIN to that of the Nd:YAG laser. Note that the shot-noise level is higher in Fig. 4-7 compared to Fig. 4-6 since a photodiode having higher bandwidth and lower saturation current was used for the high-frequency measurements. The SCOWECL relaxation resonance is also not visible above the shot-noise floor. The resonance is damped by the long photon lifetime due to the SCOWECL's exceptionally low intracavity optical loss.

4.2.2 VC-SCOWPD AM and PM Noise

In this section, we describe our measurements of the VC-SCOWPD's noise contribution to the SCOW-OEO phase-noise. The VC-SCOWPD used in the OEO was 1-mm long with ~1 A/W responsivity and 3.5 GHz bandwidth. As mentioned earlier, the photodetection process results in AM-PM noise conversion that broadens the phase-noise spectrum of the RF signal. The measured VC-SCOWPD amplitude response (open circles) and phase response (solid squares) are shown in Fig. 4-8 for DC photocurrents between 1-46 mA. These results were obtained through S21 measurements of the photodiode using an Agilent N5230C lightwave component analyzer (LCA). The measurement applies a 5 dBm RF tone to an internal modulator and outputs a modulated optical signal for probing the VC-SCOWPD. The optical signal is externally amplified by a high-power erbium-doped fiber amplifier (EDFA) and subsequently attenuated using a variable optical attenuator for control of the optical power incident on the photodiode.

The DC photocurrent is a parameter that sets the operating point of the OEO since it is inherently related to the average optical power of an IMDD link. Intensity noise on top of the optical signal causes a fluctuation in this operating point, which leads to a fluctuation in the

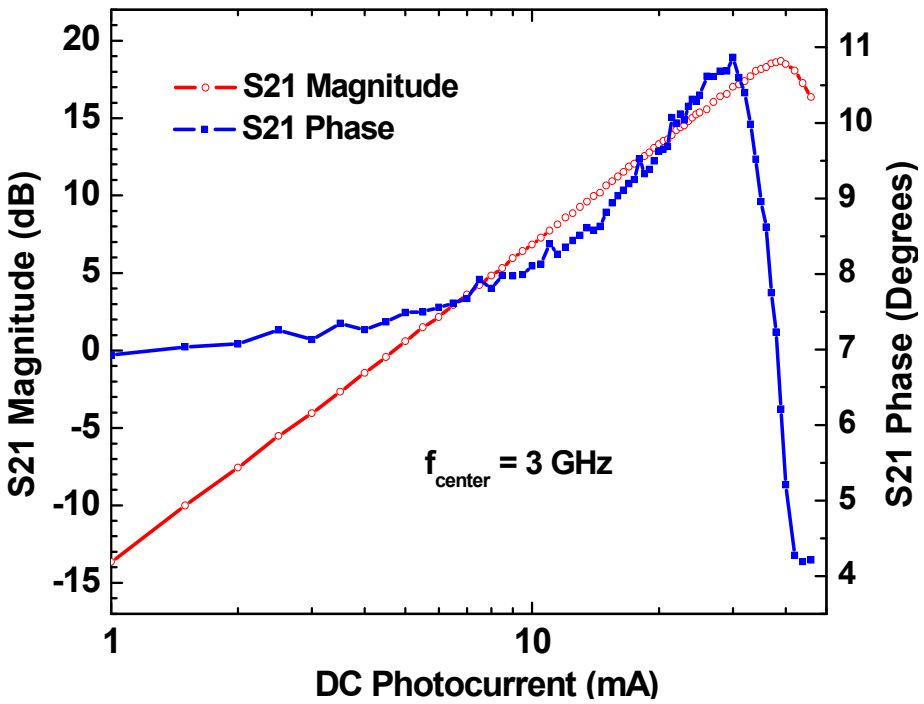

Figure 4-8: Measured dependence of the VC-SCOWPD phase (solid squares) and amplitude (open circles) on DC photocurrent at 3 GHz operation and -3.5 V DC bias.

output RF signal. Both the amplitude and phase of the RF output are affected, but in nonlinear ways due to the complicated behavior of carrier transport in the photodiode at higher photocurrent levels. Ideally, the phase response should be flat for OEO operation so that an intensity noise fluctuation causes nearly zero change in the RF output response. As can be observed in Fig. 4-8, the flat regions of phase response are located at low photocurrents (1-4 mA) and at a small window between 26-29 mA. It is essential for the SCOW-OEO to be operated at these points for the lowest phase-noise performance. In a similar vein, it is also beneficial for the amplitude response of the VC-SCOWPD to be operated at a region of zero slope. This allows for intensity fluctuations to become attenuated during the downconversion to RF, thus resulting in decreased OEO amplitude-noise. The zero-slope region of the amplitude response occurs near 38 mA for the measured VC-SCOWPD. It is ideal if both regions of zero-slope are collocated at a single photocurrent operation point. However, our measured VC-SCOWPD does not exhibit these characteristics for the applied reverse bias of -3.5 V.

4.2.3 Discovery Semiconductor DSC50S AM and PM Noise

In this section, we apply the S21 magnitude and phase measurement to a commercial Discovery Semiconductor DSC50S high-power photodiode (BW = 13 GHz, $\Re$ = 1 A/W). Note that this photodiode includes an internal 50 Ω termination, which effectively doubles its bandwidth at the cost of 6 dB in electrical power. The measured magnitude and phase responses are shown in Fig. 4-9 for DC photocurrents in the range of 1-28 mA. As before, intensity fluctuations in the optical power can result in fluctuations of these quantities around their steady-state values. The photocurrent at which the amplitude response of the DSC50S is flat corresponds to ~21 mA. It makes sense that this saturation value is less than that of the VC-SCOWPD due to the improved capabilities of the VC-SCOWPD to handle higher power. The phase response of the DSC50S is generally flat below 10 mA but includes a sudden spike near ~8 mA. This spike will be important in Section 4.3 when we discuss the performance of OEOs that make use of this photodiode.

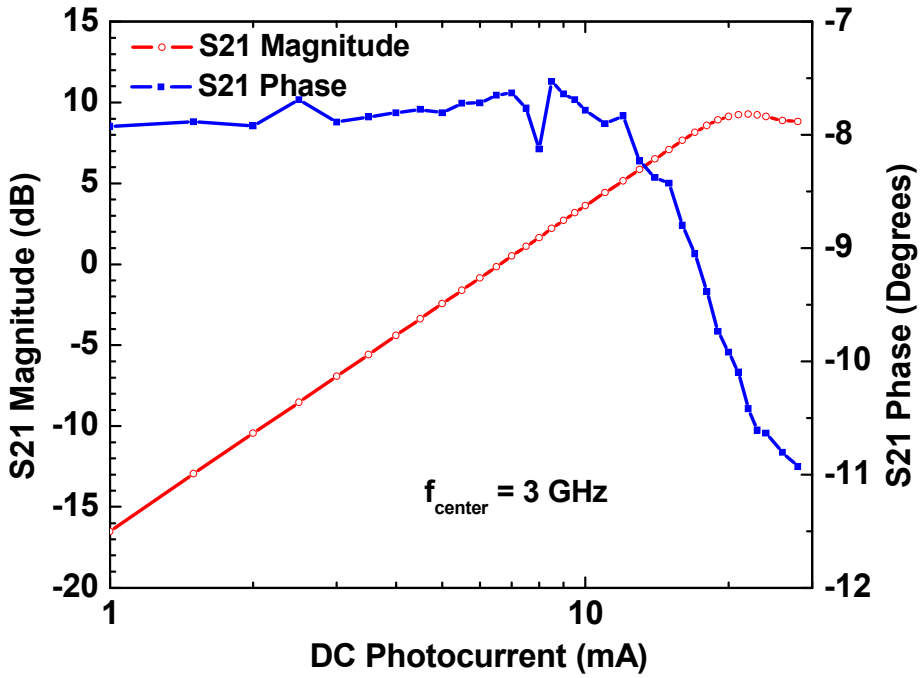

Figure 4-9: Measured dependence of the DSC50S phase (solid squares) and amplitude (open circles) on DC photocurrent for operation at 3 GHz and -9.0 V DC bias.

4.2.4 Stimulated Brillouin Scattering (SBS) Noise

An understanding of stimulated Brillouin scattering (SBS) is important for the SCOW-OEO as the scattering threshold is inversely proportional to the product of the fiber length and propagating optical power. SBS is well-understood and results from the optical signal scattering off time-dependent density variations (acoustic waves). At low optical powers, this process occurs spontaneously from the interaction with random acoustic phonon modes within the fiber medium. The interference of the forward propagating and backscattered waves generates an additional density variation via the electrostriction process which can further scatter light. This process becomes stimulated at high optical powers when the scattered light is coherently reinforced by the developed density grating. For the long fiber delays and high optical powers necessary to the operation of the SCOW-OEO, this scattering threshold may be easily reached. SBS is a noisy process that randomly reflects the incident light and thus significantly increases the RIN of the optical carrier. It is extremely important to suppress this effect in OEOs so that

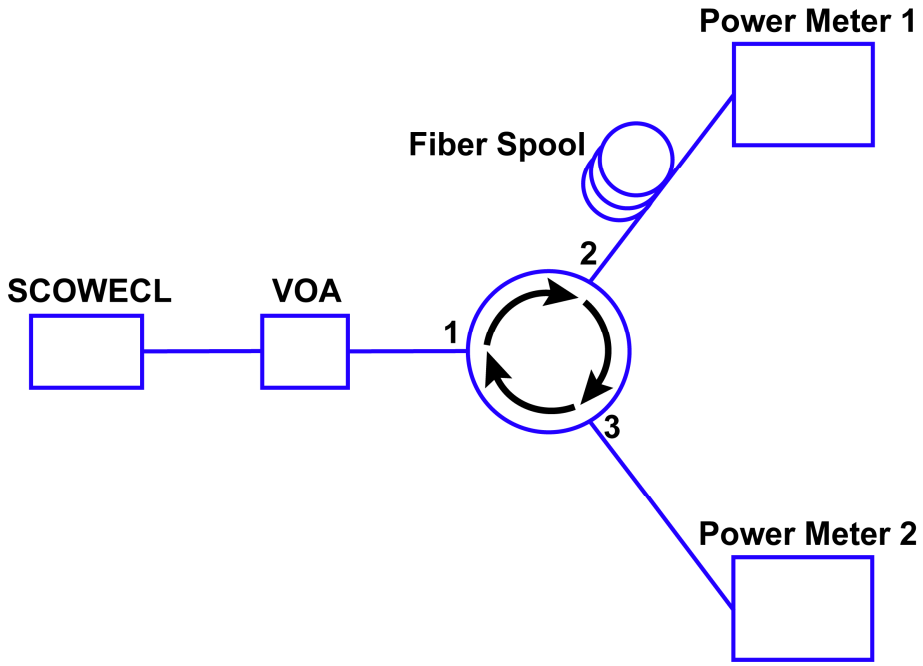

Figure 4-10: Diagram of the measurement technique used to determine transmitted and backreflected signals from a spool of optical fiber. The variable optical attenuator (VOA) is used for control over the SCOWECL power.

low phase-noise can be achieved [37, 78]. Using the setup of Fig. 4-10, we characterized the SBS threshold across several varieties of optical fiber by detection of the backreflected signal.

The system of Fig. 4-10 is straightforward to analyze. The SCOWECL power is controlled by a variable optical attenuator (VOA) and sent through port 1 of a circulator. The power is subsequently routed to port 2 and passes through a fiber spool under test of varying length. The light passing through the fiber spool is detected by an optical power meter, while the backscattered light is rerouted to port 3 and into a second power meter. The use of two power meters allows for simultaneous detection of both the forward-propagating and backscattered light as a function of the incident optical power (controlled by the VOA). The input power to the fiber spool was varied between 0.67 mW and 67 mW for this measurement. The crosstalk between ports 1 and 3 was measured to be -54 dB, and thus port 3 is sensitive down to ~300 nW of backscattered power at 0.67 mW.

Figure 4-11 shows the measured backscatter relative to the input signal for several different fiber lengths and types (Corning Single Mode Fiber (SMF), Corning Large Effective Area Fiber

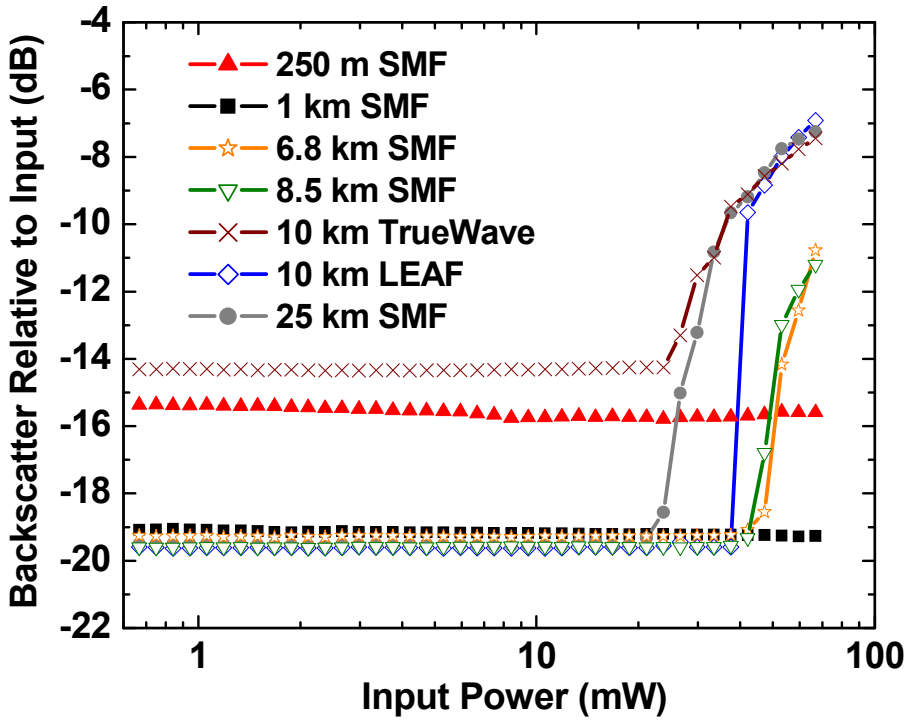

Figure 4-11: Measured backscatter relative to the signal input for various fiber types and lengths. Input powers between 0.67 mW and 67 mW were used in this measurement.

(LEAF), and Lucent TrueWave fiber). We do not show plots of the transmission here as it becomes difficult to see small differences in signal loss due to the presence of the large residual carrier. From Fig. 4-11, we see that the backreflected powers are in the range of 6.7 μW for an input of 0.67 mW, well above the limit set by the crosstalk of the circulator. Furthermore, the backreflection relative to the input is generally constant at low input powers, suggesting that the reflected power is scaling proportional to the signal level. This is due to residual reflections at the connectors between fiber interfaces rather than to any source of nonlinear fiber scattering. Above ~20 mW, the backscattered signal quickly rises after reaching the threshold of the SBS process. These thresholds vary from fiber-to-fiber but decrease when the fiber lengths become longer. Note that the 250 m and 1 km SMF fibers do not reach their SBS thresholds for optical powers up to 67 mW. The measurements also show that LEAF fiber is capable of handling approximately 1.5× the power that TrueWave fibers can handle. Although no direct comparison of LEAF and SMF fiber is available, the Brillouin scattering measurements for 8.5 km SMF and 10 km LEAF suggest that their scattering thresholds may be similar. Figure 4-11 is misleading to some degree as it suggests that noise is absent below the SBS threshold. However, we want to emphasize that even below this threshold, the SBS noise may be significant compared to the other noise processes of the system [82]. One effective way to reduce the influence of SBS is to phase modulate the optical carrier. This technique spreads the optical field across a wide distribution of frequencies beyond the coherence of a single SBS resonance. We will see both the benefits and undesired consequences of phase modulation in our experimental measurements in the next section.

4.3 SCOW-OEO Experimental Measurements

In the following sections, we describe the experimental demonstration of a 3-GHz SCOW-OEO operating without the use of any RF or optical amplification. This system is characterized through an array of phase-noise measurements and RF spectrum measurements. The aim is to assess both the spectral purity of the SCOW-OEO and also its sidemode suppression. Interestingly, we find that the sidemodes of our amplifier-free system are at the level of noise on a spectrum analyzer measurement (>88 dB down from the carrier). These low sidemode spurs

are achieved without the use of dual-loop [12] or injection-locked [83, 84] configurations, which would otherwise increase the complexity or degrade the performance of our oscillator. Comparisons to SCOW-OEO topologies that use RF amplification will also be made when possible. We observe that the use of amplification (RF or optical) within the OEO cavity appears to significantly increase the level of the measured sidemodes.

4.3.1 SCOW-OEO Phase-Noise Measurements

In this section, we detail our measurements assessing the phase-noise performance of the 3-GHz SCOW-OEO whose configuration is shown in Fig. 4-1. These measurements were obtained by direct detection of the signal out of the -10 dB OEO output port using a commercial Agilent E5052B signal-source analyzer (SSA). The results of the high-performance RF-amplifier-free SCOW-OEO system are shown in Fig. 4-12 along with the noise-floor of the SSA system. The phase-noise is instrument noise-floor limited throughout almost the entire

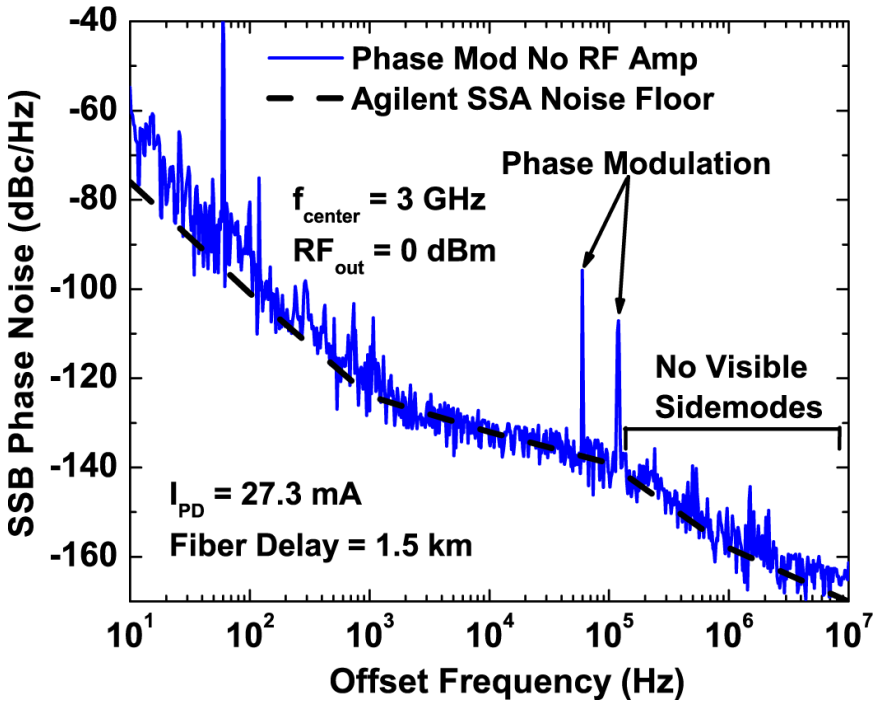

Figure 4-12: Measured phase noise of a 3 GHz SCOW-OEO operating at 27.3 mA and using 1.5-km delay. The phase modulation peaks at 60 kHz and 120 kHz can be observed, while the sidemodes at 135 kHz are below the measurement noise floor (dashed line)

measurement range. Only at low frequencies (<100 Hz) does the OEO phase-noise rise above the measurement-limit of the SSA. Our measured sidemodes (at harmonics of 135 kHz corresponding to 1.5 km optical delay) are <-140 dBc/Hz. We thus achieve large sidemode suppression in our SCOW-OEO, even when multiple modes can oscillate within the 2.5-MHz bandwidth of the RF filter. We will show in Chapter 5 that this is due to the saturation properties of MWP gain resulting in the sidemodes experiencing less gain than the main oscillating mode of the cavity. We experimentally optimized the SCOW-OEO's photocurrent for operation around 27.3 mA. This agrees well with the minimum AM-PM conversion point for our photodiode as observed in Fig. 4-8. Finally, the RF output power taken from the -10 dB output coupler was measured to be 0 dBm. This corresponds to an intracavity RF power of ~10 dBm.

It is interesting at this point to ask how the SCOW-OEO phase-noise behaves when the operating conditions are not optimal. Some possible variations include not operating at the photodiode's AM-PM conversion null, not using phase modulation, and employing RF

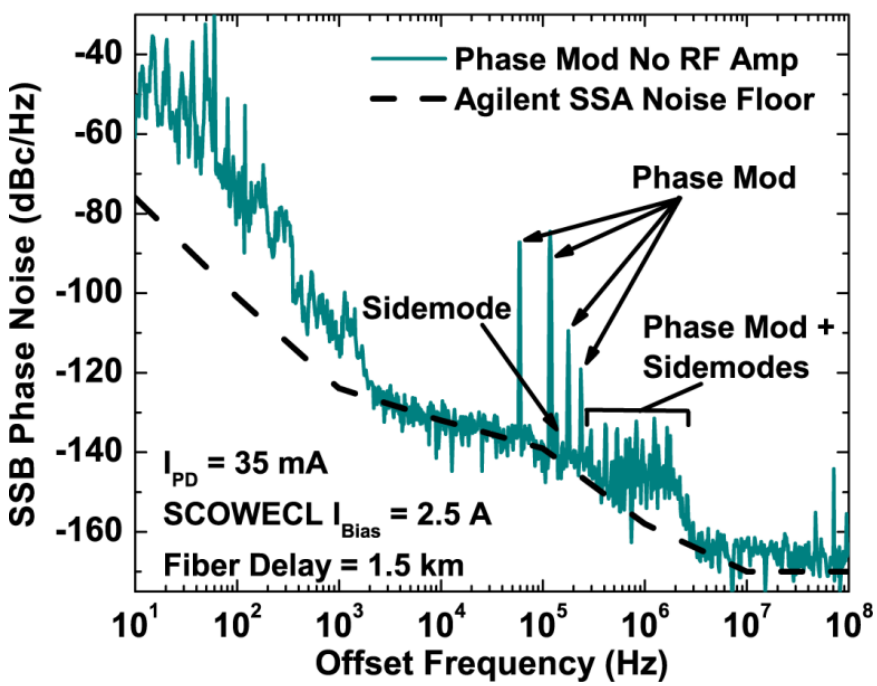

Figure 4-13: Measured phase noise of a 3 GHz SCOW-OEO operating at 35 mA and using 1.5 km delay. Both the phase modulation peaks at 60 kHz and 120 kHz and the sidemodes at 135 kHz harmonics can be observed. The SSA noise floor (dashed line) is also provided.

amplification within the cavity. We will explore each of these scenarios in turn, starting with the influence of AM-PM noise processes. Our goal here is to change the SCOW-OEO's steady-state operation to a point beyond the AM-PM null of Fig. 4-8. This can be achieved by operating at a DC photocurrent beyond 30 mA. Figure 4-13 shows the measured SCOW-OEO phase-noise at 35 mA obtained by changing the DC bias supplied to the modulator (and thus changing the power splitting between the modulator arms). Ideally, one would like the SCOWECL bias current to remain constant at 3 A for an accurate comparison of this measurement to that of Fig. 4-12. However, at the time Fig. 4-13 was taken, the SCOWECL was operated at 2.5 A. Even then, supporting measurements (not shown) confirm that the SCOWECL RIN does not change much (<5 dB) with this shift in operating point. Furthermore, later experimental trials with the SCOWECL biased at 3 A verify the results of Fig. 4-13 but were not captured at the time of measurement. The measured phase noise of Fig. 4-13 is noticeably worse (~20 dB) compared to that found in Fig. 4-12. In addition, both the phase modulation and sidemode spurs also increase significantly. This example illustrates the necessity of operating an OEO at the point where the AM-PM conversion becomes minimized.

We now discuss the importance of phase modulation to the performance of an OEO. In Fig. 4-12, there are two visible spurs located at 60 kHz and 120 kHz that result from the applied phase modulation internal to the OEO cavity. This phase modulation is necessary to suppress the effects of fiber nonlinearities and interferometric noise. As we indicated earlier, SBS is the dominant fiber nonlinearity at kilometer lengths and milliwatt levels of optical power. Even below its threshold, the fluctuations caused by SBS can still dominate the low-frequency noise of an optical link [82]. The suppression of SBS through phase modulation is well-known and significantly reduces phase-noise in high-performance OEOs [37, 78]. A second phenonmenon that degrades the system noise at low offset frequencies is interferometric noise resulting from double-backscattered optical signals [85, 86]. Reflections of the signal can theoretically occur at any interface of the optical cavity. We find these reflections to be most significant at the facet of the photodiode. The other reflection interface is created by scattering processes in the optical fiber. The presence of interferometric noise in our OEO link was discovered when we found improvements to phase noise even when the phase modulation is applied *after* the fiber delay. This noise process acts to convert phase fluctuations between a signal and its delayed counterpart

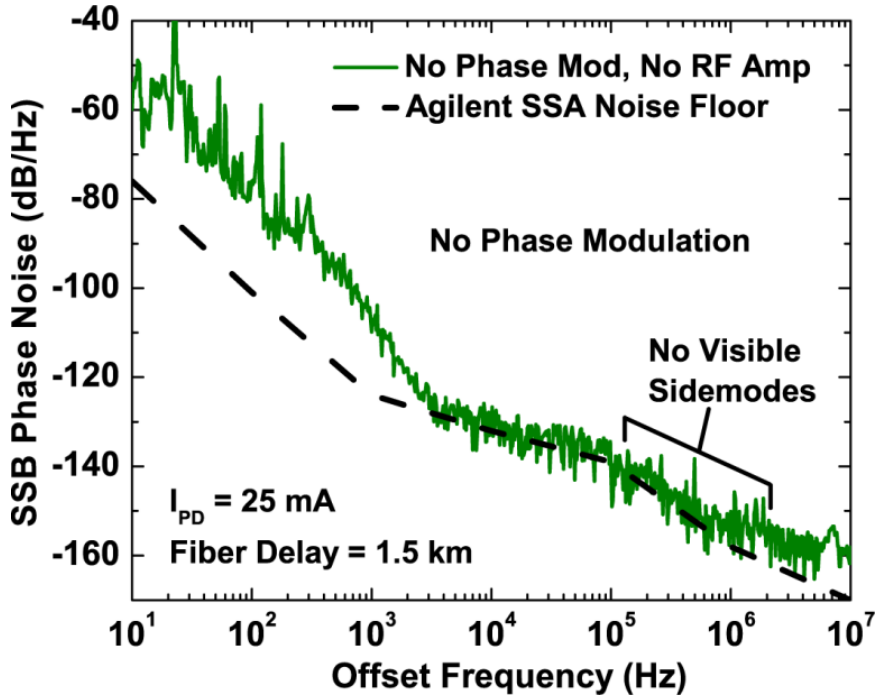

Figure 4-14: Measured phase noise of a 3-GHz SCOW-OEO operating without the use of phase modulation. No sidemodes are visible above the measurement noise floor (dashed line) in the spectrum.

into intensity fluctuations on a photodiode. Phase modulation reduces the interferometric noise present in the main oscillating mode since it causes a spreading of this noise power into the modulation sidebands [86]. In addition to phase modulation, optical isolation at the photodiode interface may be used to greatly suppress the influence of this noise process.

Figure 4-14 shows the measured SCOW-OEO phase-noise without phase modulation (and without an optical isolator at the photodiode interface). The photocurrent was maintained at 25 mA for this measurement, which is near the ideal operating point of the SCOW-OEO (Fig 4-8). It can be observed that the phase noise is no longer limited by measurement at low offset frequencies. Comparing Fig. 4-14 to Fig. 4-12, we see that the phase noise degrades by ~20 dB when phase modulation is not employed. As mentioned earlier, this degradation is due to noise introduced by effects of SBS and interference due to double-backscattered light. The phase-noise degradation at higher offset frequencies (>3 kHz) cannot be evaluated due to the limitation of the measurement noise-floor. Note that the sidemodes of Fig. 4-14 also cannot be seen above this floor.

Next, we are interested in evaluating the SCOW-OEO phase-noise when RF amplification is introduced into the system, after the photodetection step. Figure 4-15 shows this measurement for an RF amplifier (Miteq JS4-00102600-60-8P-4K) exhibiting 28-dB gain and 4 dB noise figure (*NF*). Aside from introducing the amplifier, no other component modifications were made to the system. With the amplifier, oscillation is possible at a few milliamps photocurrent as excess gain is available to the system. Our final operation point was chosen to be 16 mA for the VC-SCOWPD controlled by the modulator DC bias. We ideally would prefer to operate near 27.3 mA but were careful not to drive the amplifier too hard into saturation. We later realized that this operating point yielded higher AM-PM noise as per Fig. 4-18. However, during our testing, we verified that the OEO with RF amplification achieved similar performance across many different current ranges. This suggests that the RF amplifier's noise dominates over all other noise sources in the system. The impact of the RF amplifier noise can be observed in Fig. 4-15 where we find a degradation of ~20 dB in the SCOW-OEO's low-frequency phase-

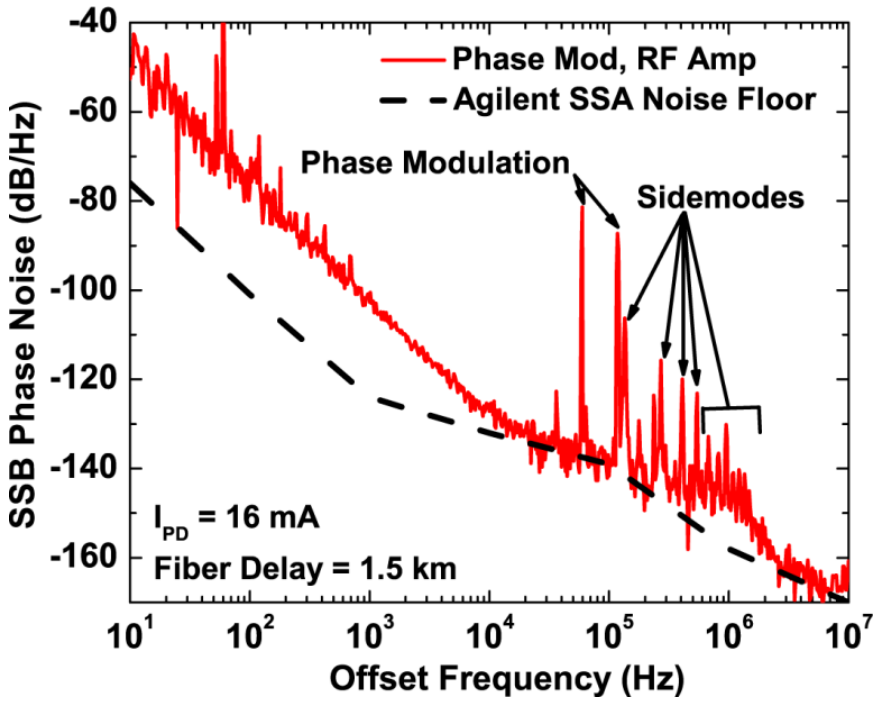

Figure 4-15: Measured phase noise of a 3-GHz SCOW-OEO operating with the use of RF amplification. The phase modulation and sidemode spurs are noticeably visible in the spectrum. The measurement noise floor (dashed line) is also provided.

noise. This large degradation occurs despite a *NF* of only 4 dB. The amplifier's *NF* is primarily a characterization of its white noise level far from the frequency of the carrier. However, as seen from Chapter 3, the upconverted flicker noise is the dominant contribution to oscillator phase-noise for low offset frequencies. Therefore, an amplifier's *NF* usually gives little indication of its behavior in an oscillator configuration. It is interesting to note that the sidemodes at harmonics of 135 kHz are now noticeably visible when an RF amplifier is used in the cavity. The first sidemode spur reaches a level of -106 dBc/Hz, while the later spurs decrease gradually to the level of noise. At ~1.5 MHz, the influence of the RF filter brings the phase-noise spectrum down to the measurement floor.

Figure 4-12 showed the performance of the SCOW-OEO under optimum operating conditions. Unfortunately, the phase noise was found to be below the limitations of our measurement system. We are thus motivated to seek ways to improve upon the resolution of Fig. 4-12. To accomplish these goals, we make use of the Agilent SSA's functionality to perform cross correlation between two measurement channels. Ideally, this cross correlation would not have been necessary since only the autocorrelation of a single channel is required to calculate the spectrum of an oscillator. However, because of noise that is added during the measurement process (e.g., amplifier noise, phase noise of the reference oscillator, etc.), the resolution of this measurement becomes limited. The cross correlation technique provides a way to circumvent these limitations. The fundamental idea of this technique is to split the signal of the oscillator under test between two measurement channels. Each channel has its own reference oscillator, mixer, and amplifiers that allow for analysis of the incoming field. A cross-correlation operation is performed between the individual fields and averaged to generate the phase-noise spectrum of the oscillator. If the individual paths were completely equal, this cross correlation would be equivalent to an autocorrelation. The signal is identical between both channels; however, the generated noise due to amplifiers, the reference oscillator, etc is uncorrelated. Upon averaging, these uncorrelated sources diminish towards zero. This has the effect of reducing the measurement noise floor by $5\log_{10} M$ dB where M is the number of averages.

In the following, we use the SSA's cross-correlation capability to improve the sensitivity of our phase-noise measurements. This function comes with the unfortunate consequence of increasing measurement time by a factor of M. The measurement time of Fig. 4-12 was 3.3 s

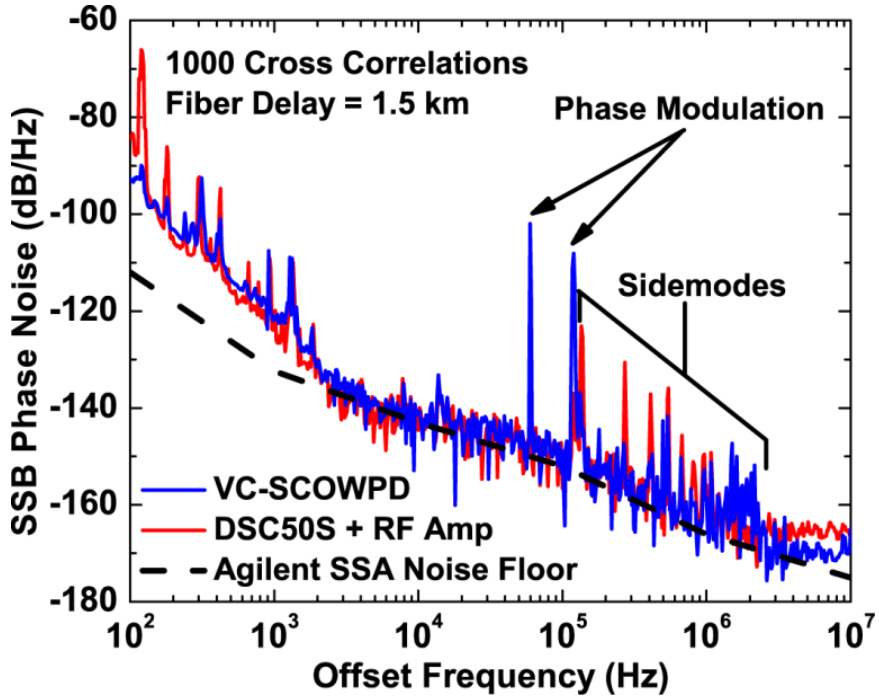

Figure 4-16: Measured 3-GHz SCOW-OEO phase-noise for two configurations: one comprising a VC-SCOWPD and another comprising a DSC50S + low-noise RF amplifier. Cross-correlation averaging (1000x) was employed to reduce the noise-floor (dashed line) of the measurement system.

and would thus increase to 55 minutes with 1000 averages. To prevent overly long averaging times, we reduce the span of our measurement to cut off at a large offset of 100 Hz. In this case, each measurement requires only 0.41 s, and 1000 averages would then take ~7 minutes to complete. The number of cross-correlations that can be practically applied is limited by the drift of our intensity modulator. Even at 7 minutes, the drift of our modulator is large enough to yield significant deviations (i.e., a few milliamps) in our operating point.

Figure 4-16 shows the phase noise of the SCOW-OEO for two different configurations. One configuration uses a VC-SCOWPD for its detection link and is identical to the system of Fig. 4-12. The other configuration uses a DSC50S photodiode along with an AML26PNC1002 low flicker-noise RF amplifier (G = 11 dB, P_{sat} = 22 dBm). The DC photocurrent was maintained at 27.3 mA for the VC-SCOWPD system and at 7 mA for the DSC50S + low noise RF amplifier link. Similar to the VC-SCOWPD current of 27.3 mA, the DSC50S operation at

7 mA was experimentally optimized as we found large degradation in phase noise when the photocurrent was increased beyond this point. This phase-noise degradation agrees well with measurements of the AM-PM response for the DSC50S (Fig. 4-9). Under oscillating conditions, the measured RF output powers are -1.2 dBm and -5 dBm (including cable loss) for the VC-SCOWPD and DSC50S + low-noise RF amplifier systems, respectively. Phase modulation was employed for both measurements in order to suppress noise contributions from SBS and double-backscattered light. The measured phase-noise is comparable for both systems in the range of 100 Hz to 2 kHz. Above 2 kHz, both systems reach the SSA measurement-limit. Note that the measurements are noise-floor limited even in the range 3 MHz – 10 MHz (RF filter bandwidth ~ 2.5 MHz). The observed difference at high offset-frequency (3-10 MHz) results from the sensitivity of the SSA's minimum level of noise-floor to RF input power. This sensitivity likely arises due to the additive white-noise of the RF amplifiers used in measuring phase noise. As we saw in Chapters 2 and 3, the additive white-noise is constant, and thus the noise relative to signal decreases for larger input powers.

The measured phase-noise performance is similar for both OEOs since the laser used is the same and because the RF amplifier noise (which degraded operation in Fig. 4-15) is no longer a limitation. Averaging over drift and noise spikes during the 7-minute measurement causes the phase-noise to increase slightly above the values found in Fig. 4-12. The sidemodes, however, are clearly still larger for the system using RF amplification, as was also found to be the case in Fig. 4-15. The RF amplifier also adds additional size/weight and considerably raises total power consumption (>3 W).

In Fig. 4-16, the first two phase-modulation spurs are clearly visible at offset frequencies of 60 and 120 kHz. Similarly, the first sidemode is also visible for each of the systems at 135 kHz. The first sidemode reaches levels of -123 dBc/Hz and -137 dBc/Hz for the DSC50S + RF amplifier and VC-SCOWPD systems, respectively. For the SCOW-OEO operated with RF amplification, the subsequent sidemodes are also present, but gradually decay with offset frequency. The second and third sidemodes, for instance, are at levels of -131 dBc/Hz and -137 dBc/Hz, respectively. Note that the SSA resolution bandwidth is constant (3.1 kHz) from 100 kHz to 780 kHz. In the amplifier-free VC-SCOWPD system, these sidemodes cannot be clearly distinguished above the noise-floor (~-160 dBc/Hz). As noted earlier, the low sidemodes are due to the saturation properties of MWP gain in an IMDD link [77]. For certain offset

frequencies, the residual harmonics from phase modulation mix with the sidemodes to generate spurs in the phase-noise spectrum. For example, the spur near 535 kHz results from an interaction between the 9th phase modulation harmonic and the 4th sidemode peak.

Based on the results of Fig. 4-15 and Fig. 4-16, we can conclude that RF amplification results in increased sidemode levels during the operation of the OEO. The physics of this process is currently not well understood as it appears that the RF amplifier affects only the sidemodes and not overall phase noise. Measurements with other high-performance RF amplifiers have yielded the same results. Furthermore, the observed sidemode enhancement is not limited to electrical means, as we have found intracavity optical amplification (Fig. 4-17) to behave similarly. In Fig. 4-17, we attenuate the SCOWECL signal and use an intracavity commercial Covega semiconductor optical amplifier (SOA) (model BOA1004P, G = 27 dB, NF = 7.5 dB, P_{sat} = 15 dBm) to provide additional gain necessary for self-oscillation. This SOA is introduced after the fiber delay and before the VC-SCOWPD in the OEO link. The VC-SCOWPD is operated at

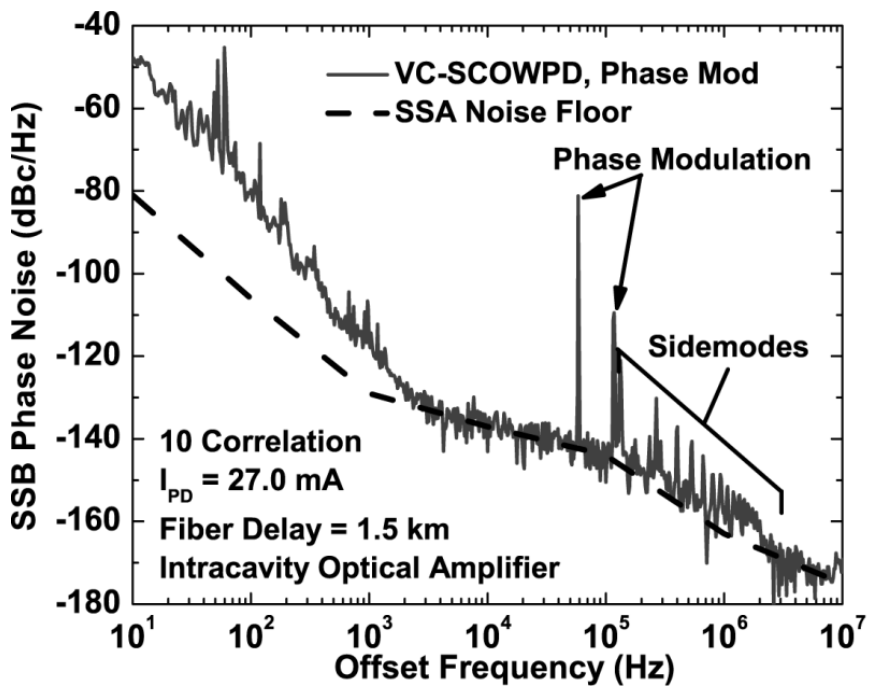

Figure 4-17: Measured 3-GHz SCOW-OEO phase-noise comprising an intracavity Covega semiconductor optical amplifier. Cross-correlation averaging (10x) was employed to reduce the noise-floor (dashed line) of the measurement system.

27 mA to maintain similar conditions to that of Fig. 4-12. Comparing Fig. 4-17 to Fig. 4-12, we see that the SCOW-OEO phase-noise at low offset frequencies degrades (by ~20 dB) due to the added noise of the amplifier. In addition, the cavity sidemodes are now clearly visible at harmonics of 135 kHz with the first spur at a level of -121 dBc/Hz. We should note that the added sidemode power for both the optical and RF amplifier cases appears primarily in the oscillator's phase response. In contrast, we find little influence of amplification on the sidemodes when we measure the oscillator's amplitude-noise spectrum. Again, the physics of this process is currently not well understood. However, we see that in the cases where amplification is used, the sidemodes all gradually decrease in magnitude as the offset frequency increases (Figs. 4-15, 4-16, and 4-17). On the other hand, the sidemodes of Fig. 4-13 (due to AM-PM conversion) are relatively constant throughout the spectrum. The characteristic shape of the sidemodes under amplification gives evidence of a low-frequency flicker noise process.

4.3.2 SCOW-OEO RF Spectrum Measurements

In this section, we discuss measurements of the SCOW-OEO's spectrum captured by an RF spectrum analyzer. The main utility of this measurement is that it provides information on the total integrated power of the sidemodes. This is in contrast to our measurements of the previous section which determine the sidemode power normalized to an arbitrary resolution bandwidth. Figure 4-18 shows the RF spectra of the SCOW-OEO measured under a variety of operating conditions. The conditions tested were with/without RF amplification (Miteq JS4-00102600-60-8P-4K) and phase modulation, at the corresponding operating points of Figs. 4-12, 4-14, and 4-15. The resulting spectra are displayed over offset frequencies close to the carrier (-2.5 kHz to 2.5 kHz) with their peak magnitudes normalized to 0 dBm. Note that the resolution bandwidth was maintained at 100 Hz.

The measurements of Fig. 4.18 confirm our findings of the SCOW-OEO phase-noise in Figs. 4-12, 4-14, and 4-15. The noise level is at its maximum when the SCOW-OEO is operated without phase modulation and with RF amplification. Furthermore, the noise levels are similar between the case employing phase modulation and RF amplification and the case using neither phase modulation nor RF amplification. Finally, the noise level of the SCOW-OEO is lowest when only phase modulation is used. Near zero offset frequency, the resolution bandwidth integrates over the oscillating signal and prevents the ability to resolve differences in noise.

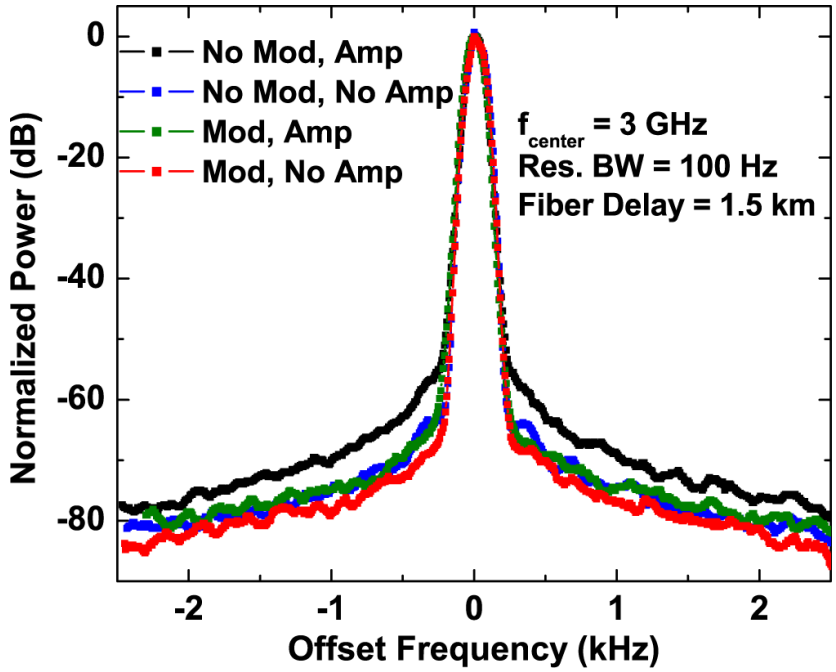

Figure 4-18: Measured 3-GHz SCOW-OEO RF spectrum with/without RF amplification and phase modulation. The frequency ranged tested was +/- 2.5 kHz centered around the carrier with a resolution bandwidth of 100 Hz.

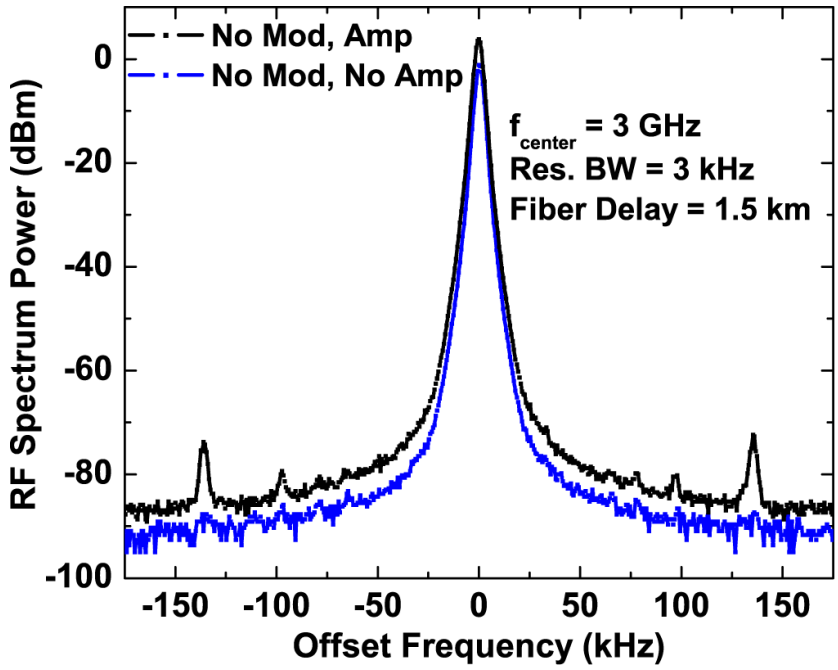

Figure 4-19: Measured 3-GHz SCOW-OEO RF spectrum with/without RF amplification. The frequency ranged tested was +/- 175 kHz centered around the carrier with a resolution bandwidth of 3 kHz.

Figure 4-19 shows the RF spectrum of the SCOW-OEO (without normalization) for larger offset frequencies between -175 kHz to 175 kHz using a resolution bandwidth of 3 kHz. For this experiment, the SCOW-OEO was operated with and without RF amplification. Phase modulation was not employed during either measurement. The RF power (including cable losses) out of the -10 dB RF coupler was found to be 3.8 dBm and -1.2 dBm with and without RF amplification, respectively. In Fig. 4-19, we subtracted out the spectrum analyzer noise floor so that the sidemodes could be made more apparent. The sidemodes are clearly visible at ±135 kHz offset when an RF amplifier is used in the system. The measured sidemode level of -72.3 dBm results in a sidemode suppression of ~76 dB. For the amplifier-free SCOW-OEO system, the sidemodes cannot be seen above the level of noise. In this case, the sidemode suppression is measured to be >88 dB.

4.3.3 Discussion

As a sanity check, let us take the values of the first sidemode in Figs. 4-15 and 4-16 and compare them to our measurements with the spectrum analyzer. The SCOW-OEO using RF amplification has a sidemode level of -106 dBc/Hz, which yields -71 dBc (relative to the carrier) after integrating over the SSA resolution bandwidth (3.1 kHz). We see that the calculated sidemode suppression is near what we measured on the spectrum analyzer (76 dB). The last 5 dB difference may be due to fluctuations in the sidemode levels from trial to trial. Although we have not added in the contributions of amplitude noise to our sidemodes, we have already noted earlier that these contributions are much smaller for the optical or RF amplifier cases. The SCOW-OEO of Fig. 4-16 (without an RF amplifier) has a first sidemode at -137 dBc/Hz, which yields an integrated sidemode power of -102 dBc. The contribution of amplitude noise here (if assumed equal to the phase contribution) will at most increase this estimate by 3 dB. Thus, it is clear that our reported >88 dB sidemode suppression of Fig. 4-19 greatly underestimates the actual SCOW-OEO sidemode suppression.

As a second sanity check, let us compare the calculations/measurements of Chapter 3 to the measurement results of the SCOW-OEO phase-noise in this chapter. In particular, Fig. 3-12 shows the phase-noise for an RF amplifier based SCOW-OEO with the SCOWECL operated at a slightly lower bias level. Even with the additional amplifier and the shift in SCOWECL bias, we expect that the total RIN of the two systems to be comparable. The RF amplifier exhibits low

flicker-noise, and thus only contributes a relatively small amount to the total noise added in a single roundtrip. Furthermore, the SCOWECL RIN does not change much (< 5 dB) with bias. Therefore, we can take the measured phase noise of Fig. 3-12 (which is visible above the noise floor) and scale it by the ratio of squared delays to obtain an estimate of the SCOW-OEO phase-noise at 1.5 km. In Fig. 3-12, the phase noise was measured to be -50 dBc/Hz and -101.6 dBc/Hz at 10 Hz and 1 kHz offset frequency, respectively. At 1.5 km, these values are decreased by 28.5 dB. With these corrections, we see that the resulting phase noise is in agreement with the measurements and noise floor of Fig. 4-12.

As our SCOW-OEO can operate without RF amplification, it is useful to discuss its performance characteristics for potential scaling to longer delays and higher frequencies. The SCOW-OEO exhibits a threshold of 20 mA, and we operate our system at 27.3 mA photocurrent. The net small-signal power gain is 1.2 dB after accounting for MWP amplification and RF cavity loss. This can be verified from Fig. 4 of Ref. [4] with a modulator V_π of 3.1 V and an oscillating voltage of 1 V input into the modulator. The combined loss for the components of the RF cavity excluding the photodiode is 2.8 dB. The bandwidth of the VC-SCOWPD (3.5 GHz) imposes an extra 2.1 dB of loss for operation at 3 GHz. This suggests the MWP link power gain to be 6.1 dB total. The net gain of the MWP link is 4.0 dB operating at 3 GHz after accounting for losses due to finite photodiode bandwidth. One can potentially increase the fiber delay from 1.5 km to 15 km for 20 dB improvement in SCOW-OEO phase-noise. However, the loss incurred through the additional delay is ~3.0 dB at 1550 nm (attenuation = 0.2 dB/km), and thus the photocurrent needs to be approximately doubled (~27 mA to ~54 mA) in order to drive oscillation. The required photocurrent is within reach of the VC-SCOWPD technology. However, suppression of nonlinear fiber noise would be necessary for the benefits of delay to be fully realized. Currently the bandwidth of the VC-SCOWPD limits operation of the SCOW-OEO to a few GHz. Higher bandwidth VC-SCOWPDs (10-12 GHz) have been demonstrated with slightly reduced responsivity (0.7 A/W) and lower current handling capabilities (~30 mA) [34]. Traveling-wave electrode structures are required to extend the VC-SCOWPD technology beyond these operation regimes [35].

4.4 Conclusion

We have demonstrated a 3-GHz amplifier-free slab-coupled optical waveguide optoelectronic oscillator (SCOW-OEO) with low phase-noise (<-120 dBc/Hz at 1 kHz offset) and ultralow sidemode levels. These sidemodes are indistinguishable from noise on a spectrum analyzer measurement (>88 dB down from carrier). This performance was achieved with 1.5 km of optical delay and through the use of high-power low-noise SCOW lasers and photodiodes. We have also evaluated the effect of RF amplification on the phase-noise of the SCOW-OEO. The OEO's operation is significantly degraded by amplifier noise except in the cases when the highest performance amplifiers are used. We found that the sidemode suppression, however, always degrades with amplification, even with the use of low flicker noise amplifiers.

In Chapter 1, our goal for the SCOW-OEO was to improve on the phase-noise of state-of-the-art OEOs (Fig. 1-7) by an order of magnitude. This would require phase-noise levels of -80 dBc/Hz at 10 Hz offset frequency and of -155 dBc/Hz at 1 kHz offset. To achieve these goals, our strategy was to use a low-RIN SCOWECL pump laser. The RIN requirements were -110 dBc/Hz at 10 Hz offset and -150 dBc/Hz at 10 kHz offset. It can be verified from Fig. 4-6 that these RIN levels are well within the capabilities of current SCOWECL technology. However, even with the SCOWECL in place, Figs. 4-12 and 4-16 show that the performance of the SCOW-OEO lags behind the targets set for phase noise. The main performance loss is from using 1.5 km instead of 16 km of fiber delay. This delay difference transforms into a 20.6 dB difference in phase noise. If we account for this factor in Fig. 4-12, it is clear that our measured results are within reach of the desired goal. Currently, fiber nonlinearities and interference effects prevent the use of longer delays in the SCOW-OEO system. Once these limitations are overcome, the full capabilities of the OEO can then be realized.

Chapter 5

Super-Homogeneous Gain in Microwave-Photonic Links

It is well known that an intensity-modulated direct-detection (IMDD) microwave photonic (MWP) link can achieve net electrical gain when the optical carrier power is large enough to compensate for inefficiencies in electrical-to-optical and optical-to-electrical conversion [6, 87]. Figure 5-1 shows an example of an IMDD link capable of providing electrical amplification of a RF input signal V_{in}. The modulator imprints the RF tone onto the envelope of an optical carrier and the photodiode recovers the electrical signal through detection of the beat note. The amplitude of the resulting voltage V_{out} depends on the optical power incident on the photodiode, the photodiode responsivity ($\Re$), the RF load resistance (R), and also the ratio of V_{in} to the modulator half-wave switching voltage (V_{π}). Net electrical gain is achieved when $|V_{out}/V_{in}| > 1$. This principle of MWP gain has been used in many aspects of microwave-photonics, including analog fiber-optic interconnects [6] and optoelectronic oscillators (OEOs) [4, 5]. Under small-

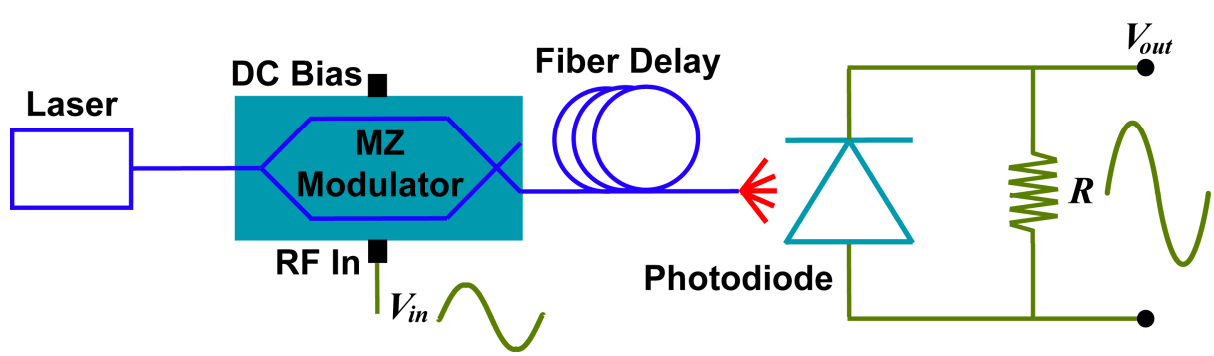

Figure 5-1: Microwave-Photonic (MWP) amplification of V_{in} by signal transmission over an intensity modulated direct detection (IMDD) optical link.

signal conditions, often encountered in simple analog links, the MWP gain is approximately independent of the input microwave signal amplitude. However, under the large-signal conditions encountered in OEOs, the gain varies as a function of input signal amplitude due to the saturation properties of the intensity modulator and photodiode. In this analysis, we will assume the photodiode to be linear and focus primarily on the saturation properties of the modulator. When multiple microwave signals are transmitted through a link, a phenomenon similar to cross-gain modulation can occur with each signal not only depleting its own gain, but also the gain of the others [88, 89].

Previous demonstrations of OEOs have shown excellent phase-noise performance up until the offset-frequency range where sidemodes begin to dominate the spectrum [11, 37, 78]. Many techniques, such as the use of dual-loop [12, 80] and dual injection-locked configurations [83, 84], have been proposed to suppress the oscillation of these sidemodes. While these approaches help to reduce spur levels, it has been shown that sidemode suppression ratios (SMSRs) >50 dB can still be obtained even in the most basic single-loop OEO systems [11, 58, 78, 90, 91]. In fact, we showed in Chapter 4 that the slab-coupled optical waveguide

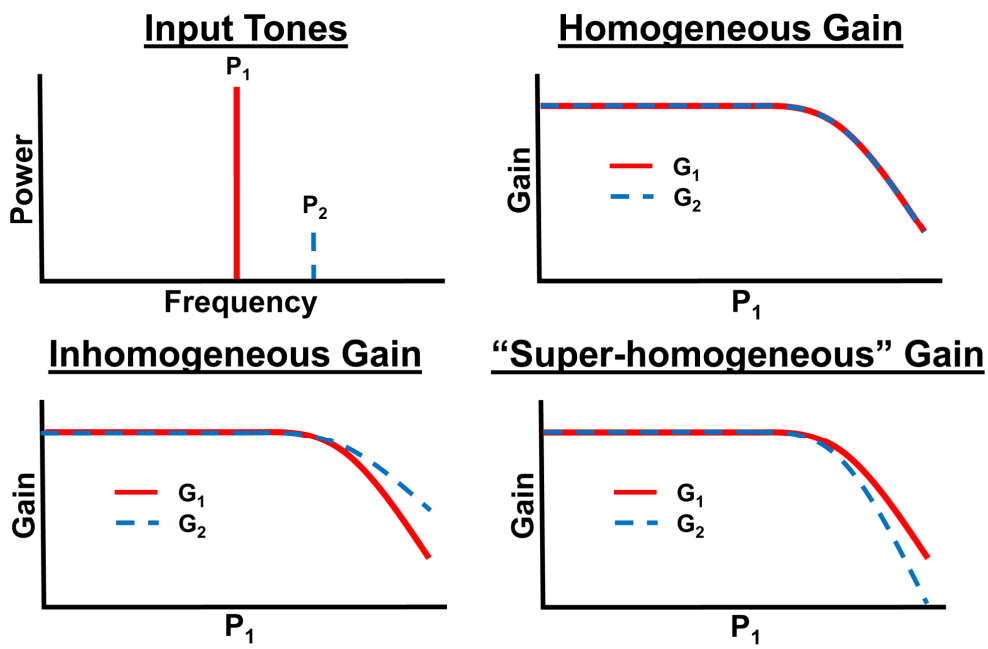

Figure 5-2: Illustration of homogeneous, inhomogeneous, and superhomogeneous gain saturation for two input tones (one small, one large).

(SCOW)-OEO exhibited SMSRs in excess of 88 dB limited by the noise floor of our measurement. The goal of this chapter is to explain how these large SMSRs can be achieved despite the presence of many (10-1000) sidemodes capable of oscillating within the passband of the OEO. In particular, we will show that the saturation behavior of MWP gain is such that smaller signals saturate more rapidly than larger signals [77]. We refer to this type of saturation as "super-homogeneous". This behavior is distinctly different from traditional gain mediums which may be homogeneous (all signals saturate at the same rate) or inhomogeneous (larger signals saturate faster). An illustration of these saturation properties is shown in Fig. 5-2. The attenuation of secondary tones is particularly useful in an OEO as the sidemodes of the oscillator can be considered as unwanted noise transmitted with a primary oscillating signal. Using the model of MWP gain developed here, we simulate the steady-state operation of a high-performance SCOW-OEO system. We compare our simulation with experiment and show excellent agreement across several performance parameters, including the OEO's sidemode levels. The unique properties of MWP gain can result in large SMSRs (>110 dB), even when the filters used in the OEO support multiple cavity modes.

5.1 Super-Homogeneous Gain

In this section, we present a theoretical treatment of the gain in a MWP link. Commonly, this gain is only analyzed for a single modulation tone. Similar to any other gain medium, the MWP gain saturates when the tone becomes sufficiently large. This saturation is a necessary condition to maintain power conservation in the system. In our analysis here, we will keep track of one additional tone, which can be thought of as a sidemode in an OEO. We will show that the saturation properties for this sidemode greatly differ from that of the main tone, yielding characteristics that are super-homogeneous (i.e., the sidemode saturates faster). We conclude with experimental evidence and a discussion of the fundamental physics behind this process.

5.1.1 Theory of Two-Tone MWP Gain

Here, we are interested in determining the behavior of MWP gain in the presence of a large oscillating mode and a secondary smaller sidemode. We begin by analyzing the transfer-function of a Mach-Zehnder modulator derived from the Bessel-expansion for two input tones [88]. The results of this expansion are well known, and the output photodetected voltage $V(t)$ can be expressed in terms of the amplitudes and frequencies of the sinusoidal inputs through

$$V(t) = \frac{P_0 \Re R}{2}\left\{1 - \cos\left[\Gamma_0 + \frac{\pi}{V_\pi}\left(v_1 \sin(\omega_1 t) + v_2 \sin(\omega_2 t)\right)\right]\right\} \tag{5.1}$$

with

$$\cos\left[\Gamma_0 + \frac{\pi}{V_\pi}\left(v_1 \sin(\omega_1 t) + v_2 \sin(\omega_2 t)\right)\right] = \sum_{n,m^3 0}\begin{cases} \cos\Gamma_0 J_0\left(\frac{\pi v_1}{V_\pi}\right) J_0\left(\frac{\pi v_2}{V_\pi}\right) & n = m = 0 \\ (\pm 1)^n\, 2\cos\Gamma_0 J_n\left(\frac{\pi v_1}{V_\pi}\right) J_m\left(\frac{\pi v_2}{V_\pi}\right)\cos(n\omega_1 \pm m\omega_2)t & n+m \text{ even} \\ -(\pm 1)^{n+1}\, 2\sin\Gamma_0 J_n\left(\frac{\pi v_1}{V_\pi}\right) J_m\left(\frac{\pi v_2}{V_\pi}\right)\sin(n\omega_1 \pm m\omega_2)t & n+m \text{ odd} \end{cases} \tag{5.2}$$

Here, P_o is the average optical signal power at the output of the modulator, $\Re$ is the photodiode responsivity, R is the load resistance, Γ_0 is the bias point of the modulator, V_π is the modulator half-wave switching voltage, and v_1 (v_2) and ω_1 (ω_2) are the amplitudes and frequencies of the first (second) input tones, respectively.

We are specifically interested in the situation comprising a strong tone (v_1) and a weak tone (v_2) (Fig. 5-3) corresponding to the main oscillating signal and a sidemode of an OEO. From Eq. (5.2), we see that one contribution to the voltage at ω_2 comes from the gain of first-order interactions obtained by substitution of ($n = 0,\ m = 1$). There are also higher-order interactions of

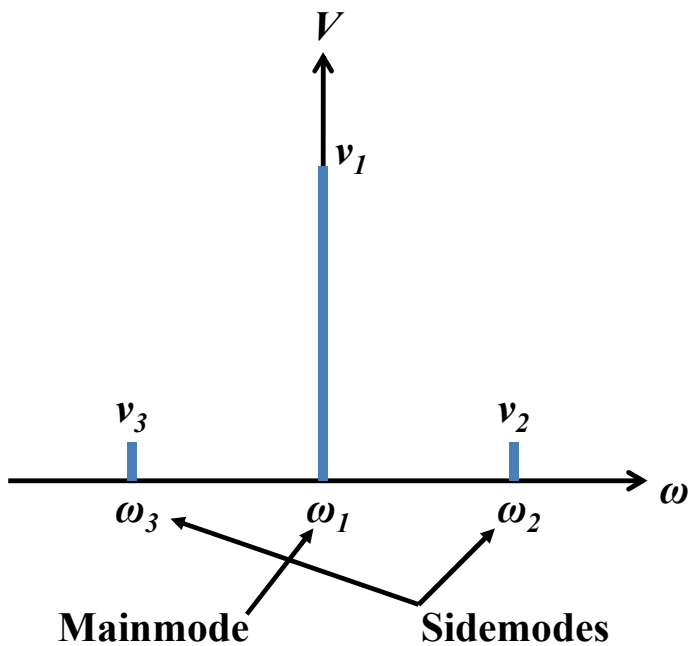

Figure 5-3: Illustration of the two-tone interaction between a mainmode and a sidemode of an OEO. The amplitudes of the tones v_1, v_2, v_3 and their corresponding frequencies $\omega_1, \omega_2, \omega_3$ are also indicated.

ω_1 with a third tone (ω_3) such that $2\omega_1 - \omega_3 = \omega_2$ ($n = 2,\ m = 1$). In principle, Eq. (5.2) must be modified to account for the interaction of multiple tones. However, it is readily shown that these multiple tones would simply result in additional Bessel factors in each of the expansions. For the case of the $2\omega_1 - \omega_3 = \omega_2$ interaction, the factors are $J_2\left(\pi v_1/V_\pi\right) J_0\left(\pi v_2/V_\pi\right) J_1\left(\pi v_3/V_\pi\right)$. When there is only one large signal (v_1) with many smaller tones as in an OEO, the factor of $J_0\left(\pi v_2/V_\pi\right)$ is approximately unity yielding again an interaction of two tones. With appropriate microwave filtering, interactions of ω_1 with frequencies near DC or with higher harmonics of the modulation signal can also be ignored. Aside from the cases of ($n = 0,\ m = 1$) and ($n = 2,\ m = 1$), all other interactions are negligibly small due to higher-order interactions of small signals. Furthermore, for a symmetric spectrum, the signal level at ω_3 is the same as that at ω_2. This condition approximately applies to the OEO (corresponding to the sidemodes to the left and right of the oscillating tone) and also applies to the case of signal modulation in the presence of

background noise. The cross-coupling of the gain maintains symmetry between the two halves of the spectrum. Finally, we note that the voltage contribution to the signal at ω_1 comes primarily from ($n=1,\ m=0$). All other terms are negligibly small in comparison.

In general, the contributions to $V(\omega_2)$ from the Bessel expansions with ($n=0,\ m=1$) and ($n=2,\ m=1$) must be incoherently summed when the signals at ω_2 and ω_3 share a random phase relation. This random phase relation is typical for describing noise and clearly applies to the case of noise transmitted alongside a modulated carrier. As will be seen later, the sidemodes of an OEO are also each phase incoherent and behave similar to noise, even when the OEO is oscillating above threshold. The lack of sidemode coherence is due to the super-homogeneous nature of MWP gain, which results in the sidemodes suffering net attenuation with each cavity roundtrip. This topic will be discussed in detail next.

Based on our previous discussion, we can identify the signal contributions at ω_1 and ω_2 to be

$$\begin{aligned} V(\omega_1 t) &= P_0 \Re R \sin\Gamma_0 J_1\left(\frac{\pi v_1}{V_\pi}\right) J_0\left(\frac{\pi v_2}{V_\pi}\right) \sin(\omega_1 t) \\ V(\omega_2 t) &= P_0 \Re R \sin\Gamma_0 J_1\left(\frac{\pi v_2}{V_\pi}\right) \sqrt{J_0^2\left(\frac{\pi v_1}{V_\pi}\right) + J_2^2\left(\frac{\pi v_1}{V_\pi}\right)} \sin(\omega_2 t) \end{aligned} \tag{5.3}$$

The form of Eq. (5.3) reveals saturation by cross-gain modulation as the voltages are reduced by the presence of secondary signals. Note that Eq. (5.3) is applicable to an approximately symmetric spectrum with at most one dominant modulated tone. For an OEO, the assumption of a symmetrical spectrum only breaks down when the difference between $\omega_2 - \omega_1$ and $\omega_1 - \omega_3$ is larger than the linewidth of a sidemode. This may occur in rare cases of extreme mode pulling or chromatic dispersion. However, even in these situations, a spectrum analyzer measurement performs its own incoherent addition process when the resolution bandwidth is larger than the asymmetry between ω_2 and ω_3. For asymmetries beyond these two extremes, one can proceed by modifying Eq. (5.3) to separately account for each voltage contribution.

The voltage gains are found by normalizing the outputs at ω_1 and ω_2 in Eq. (5.3) to their respective inputs. These gains are determined to be

$$
\begin{aligned}
G(\omega_1 t) &= \frac{P_0 \Re R}{v_1} \sin\Gamma_0 J_1\left(\frac{\pi v_1}{V_\pi}\right) J_0\left(\frac{\pi v_2}{V_\pi}\right) \\
G(\omega_2 t) &= \frac{P_0 \Re R}{v_2} \sin\Gamma_0 J_1\left(\frac{\pi v_2}{V_\pi}\right) \sqrt{J_0^2\left(\frac{\pi v_1}{V_\pi}\right) + J_2^2\left(\frac{\pi v_1}{V_\pi}\right)}
\end{aligned}
\tag{5.4}
$$

The functional form of Eq. (5.4) is relatively complex as it depends on the power contained in both the mainmode and sidemode. However, if we once again assume the sidemodes to be small (relative to V_π/π), we can rewrite Eq. (5.4) as

$$
\begin{aligned}
G(\omega_1 t) &= \frac{P_0 \Re R}{v_1} \sin\Gamma_0 J_1\left(\frac{\pi v_1}{V_\pi}\right) \\
G(\omega_2 t) &= \frac{P_0 \Re R \pi}{2V_\pi} \sin\Gamma_0 \sqrt{J_0^2\left(\frac{\pi v_1}{V_\pi}\right) + J_2^2\left(\frac{\pi v_1}{V_\pi}\right)}
\end{aligned}
\tag{5.5}
$$

where we have simplified the Bessel expansions using $J_0(\pi v_2/V_\pi) \approx 1$ and $J_2(\pi v_2/V_\pi)/v_2 \approx \pi/2V_\pi$. Note that the voltage gain $G(\omega_2 t)$ in Eq. (5.5) does not contain any phase information as coherence is lost by the incoherent addition process. Should one of the terms in $G(\omega_2 t)$ dominate over the other, the phase information of the gain cannot be recovered from Eq. (5.5). One must instead use Eq. (5.2) to discern the phase contributed by the dominant term to $G(\omega_2 t)$.

5.1.2 Super-Homogeneous Gain Measurement Results

Figure 5-4 shows the voltage gain (normalized to $P_0 \Re R \sin\Gamma_0$) of the large and small signals (Eq. (5.5)) as a function of the large signal input voltage. Note that the choice of V_π also affects the magnitude of the voltage gain but does not affect the overall shape of the graph. For plotting purposes, we have chosen a value of V_π that normalizes Fig. 5-4 to unity. We again wish to emphasize that phase information is lost for the gain of the smaller signal due to the incoherent addition of Eq. (5.5). We use voltage units in Fig. 5-4 primarily because they are the most natural for describing the functionality of the modulator-photodetector link. For $\pi v_1/V_\pi << 1$, the gains

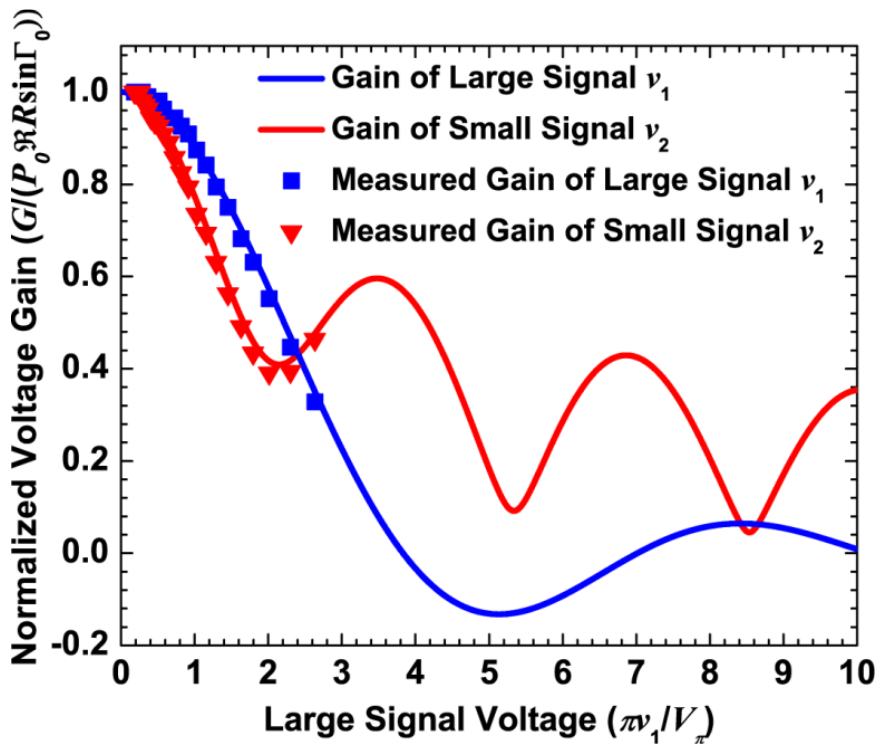

Figure 5-4: Simulated (solid line) and experimentally measured (solid squares/triangles) voltage gain for two tones amplified over an IMDD link. The gain is normalized to a peak value of 1 and plotted versus the voltage of the larger signal.

of the two tones are approximately equal as the distinction between tones 1 and 2 becomes indiscernible when they both have low amplitude. As $\pi v_1/V_\pi$ increases, Fig. 5-4 remarkably shows that the MWP gain is super-homogeneous with the gain of the larger signal saturating at a slower rate than the gain of the smaller signal. We note that this is distinctly different from conventional homogeneous gain where the gain saturation induced by the larger signal is the same for both signals [92]. The gain difference between the two tones continues until the primary tone reaches a value of $\pi v_1/V_\pi \approx 2.4$, at which point the secondary tone experiences larger gain. The saturation characteristics of the two tones result solely from the nonlinear response of the Mach-Zehnder modulation transfer function. The lost voltage (and power) between the two signals is accounted for by the higher order Bessel harmonics such that the sum of the contributions from all frequencies must yield the total voltage of Eq. (5.1) at any instant of time. In Fig. 5-4, the voltage gain coefficient of the smaller tone reaches a local minimum at

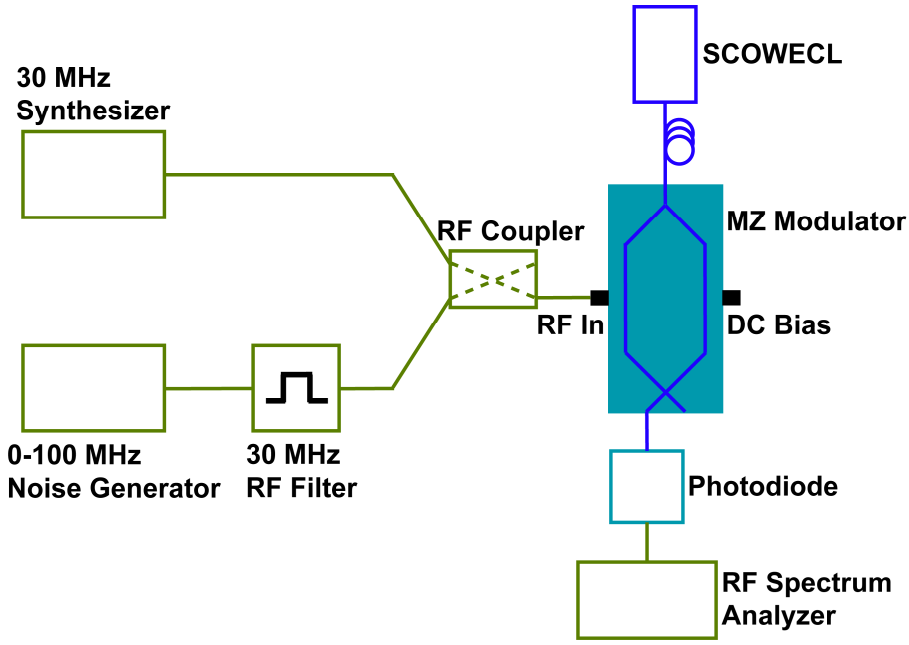

Figure 5-5: Experimental setup for measuring the MWP gain saturation of an IMDD link. Here, the noise acts as the small tone and the synthesizer acts as the large tone.

$\pi v_1/V_\pi \approx 2.1$. There are also additional local minima for higher values of v_1 but with significantly reduced gain for the primary signal.

Figure 5-4 also shows measurements of the MWP gain saturation for both the small and large tones. The experiment setup used for this measurement is illustrated in Fig. 5-5. The output of a noise generator (100 Hz – 100 MHz) was filtered by a bandpass filter (f_{center} = 30 MHz, BW = 2 MHz) and combined with an Agilent E8241A synthesizer. The output was applied to a Mach Zehnder (MZ) modulator (V_π ~ 3.5 V at 30 MHz) to drive intensity modulation of a high-power CW slab-coupled optical waveguide external cavity laser (SCOWECL) [27, 28]. The optical signal was then detected by a commercial Discovery photodiode (DSC20H) before subsequent analysis on an RF spectrum analyzer. The RF signal out of the synthesizer was varied between 0 dBm and +23 dBm while the photodetected outputs at 30 MHz (large tone) and 31 MHz (small tone) were monitored for the saturation measurement. The measured normalized gain compression for both the small and large signals agree very well with the simulated gains for v_1

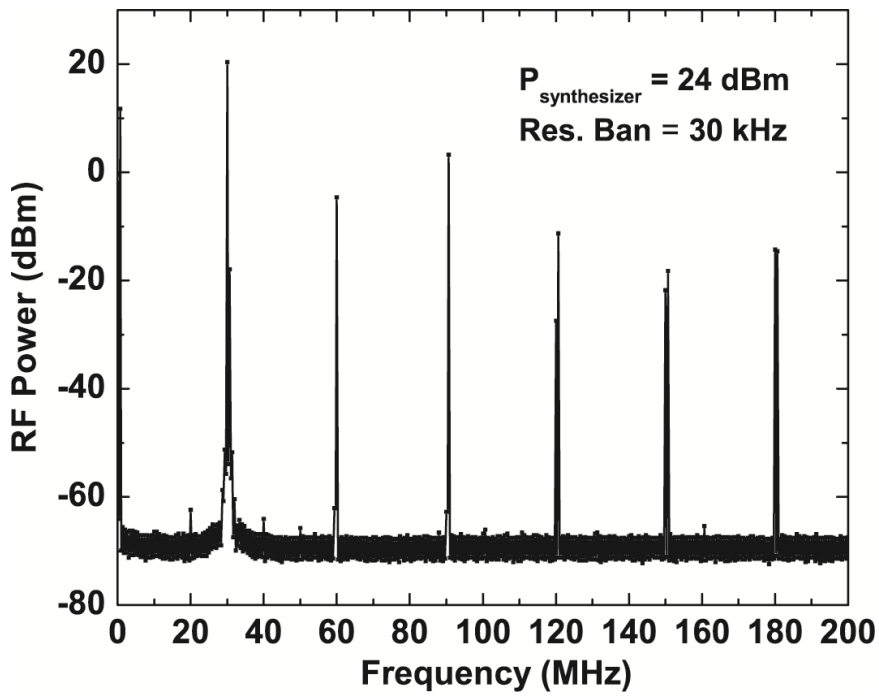

Figure 5-6: Illustration of Agilent E8241A synthesizer spurs at harmonic multiples of 30 MHz. The synthesizer power was set to 24 dBm for this measurement.

and ν_2, respectively. The crossing point in gain between the two tones is clearly visible in the measurement and will be important for our discussion in Section 5.2.

Note that one must be cautious to prevent the occurrence of extraneous signals during this measurement. These spurs can mix with the signals currently present to generate unwanted intermodulation products at 30 MHz and (more importantly) at 31 MHz. An example of this is shown in Fig. 5-6 for the Agilent synthesizer of Fig. 5-4. The synthesizer power was set to 24 dBm, which is 1 dB beyond the range plotted in Fig. 5-3. The synthesizer power is most likely internally amplified, and the spurs of Fig. 5-6 are the mixing products of the amplifier's nonlinear saturated response. We are interested in determining how these spurs impact the measurement of Fig. 5-4 and are thus motivated to search for extraneous contributions at 31 MHz. One contribution is from the interaction of the spur at 60 MHz and the noise at 29 MHz generating a difference frequency of 31 MHz. A few other combinations are for example 90 MHz – 2×29.5 MHz, 120 MHz – 60 MHz – 29 MHz, 150 MHz – 90 MHz – 29 MHz, 180 MHz – 120 MHz – 29 MHz, 180 MHz – 2×60 MHz – 29 MHz, etc. Note that these spurs

continue to ~1 GHz. The net result is an inaccuracy of this measurement when the synthesizer is operated at high RF powers (>24 dBm).

One way to potentially get around this problem is by filtering the output of the synthesizer. The RF filter of Fig. 5-5 can for example be shared by both the noise generator and synthesizer after their signals have been combined. We have verified experimentally that this method works and can extend the operation of the synthesizer to its maximum capability of +25 dBm. However, the additional RF filter introduces 4-dB loss to the synthesizer output and has the net effect of reducing the range of voltages that can be applied to the modulator.

5.1.3 Discussion – Super-Homogeneous Gain

It is useful at this point to discuss why one might expect the MWP gain to be super-homogeneous. We note that this behavior is currently not known to be exhibited by any other gain medium over a broad range of frequencies. We begin by examining Eqs. (5.1)-(5.5) with a change of perspective into the frequency domain. The saturation of the larger signal occurs as a result of the modulation response generating field components at the harmonics of the modulation frequency. This is also the traditional sense of MWP saturation with the modulation signal swinging beyond the quasi-linear regime of the sinusoidal response. However, the gain saturation of the smaller signal is caused by an entirely different mechanism as the smaller signal is well within the linear range of the modulator. Ignoring the $J_2\left(\pi v_1/V_\pi\right)J_1\left(\pi v_2/V_\pi\right)$ term, which is small at relatively low v_1, the saturation of the smaller signal is due to the depletion of the field component at the carrier by the presence of the larger signal. As the field at the carrier frequency is shared by the beat-note of both tones, the MWP gain of the smaller tone becomes compressed. The fact that both saturation mechanisms only depend on the larger signal makes sense in light of Eq. (5.5). Both the small and large tones are compressed by the shift in power from the carrier to higher harmonics of ω_1. However, because all the harmonics of ω_1 contribute to the gain of the larger tone via beat-note generation of nearest neighbor harmonics, the gain of the larger signal saturates at a relatively slow rate. In contrast, the signal powers at harmonics of ω_1 beyond the carrier do not contribute (to first order) to the gain of the smaller signal. The only field component that contributes to gain is at the carrier frequency, which decreases rapidly to

supply power to all the higher harmonics of ω_1. Compared to the larger signal then, we expect the gain of the smaller signal to initially decrease at a faster rate. Mathematically, the comparison between the saturation rates of the large and small tones becomes a comparison of $J_1(\pi v_1/V_\pi)/v_1$ to $\pi J_0(\pi v_1/V_\pi)/2V_\pi$ (for relatively low values of v_1).

5.2 SCOW-OEO Simulation and Experimental Results

In this section, we apply the super-homogeneous gain model of Eq. (5.4) to the simulation of a SCOW-OEO. Our simulation strategy at a given DC power of the pump laser is to iterate the response of the OEO until the system establishes steady state. Starting from an input of noise, we keep track of the power after each roundtrip of the cavity. This process is performed across a range of DC powers to achieve a full characterization of the SCOW-OEO. We will compare our simulation results of RF power and sidemode suppression to experimental measurements of the SCOW-OEO. By the end, it will be demonstrated that large SMSRs can be obtained even when many modes are allowed to exist within the cavity.

5.2.1 SCOW-OEO Parameters and Experimental Configuration

Figure 5-7 shows a schematic of the SCOW-OEO system that we simulated the performance of. The experimental demonstration of this SCOW-OEO was discussed earlier in Chapter 4 and also in [58]. The SCOW-OEO cavity includes a high-power, low-noise SCOWECL pump laser and a high-current variable confinement (VC) SCOW photodiode to enable oscillation without the need for additional RF amplification. The laser, Mach-Zehnder (MZ) modulator, phase modulator (fiber stretcher), fiber delay, and photodiode form the IMDD link for MWP gain. The phase modulator, driven by a 60-kHz sinusoid, is used for suppression of fiber nonlinearities (stimulated Brillouin scattering and double-backscattered-interferometric noise) during signal propagation through the delay [37, 86]. The signal at the input of the modulator is amplified by the IMDD link and filtered during one roundtrip of the cavity. If the gain is large enough to compensate for the loop losses, the OEO will oscillate at the center frequency determined by the RF filter. Note that the starting point of this oscillation process is noise.

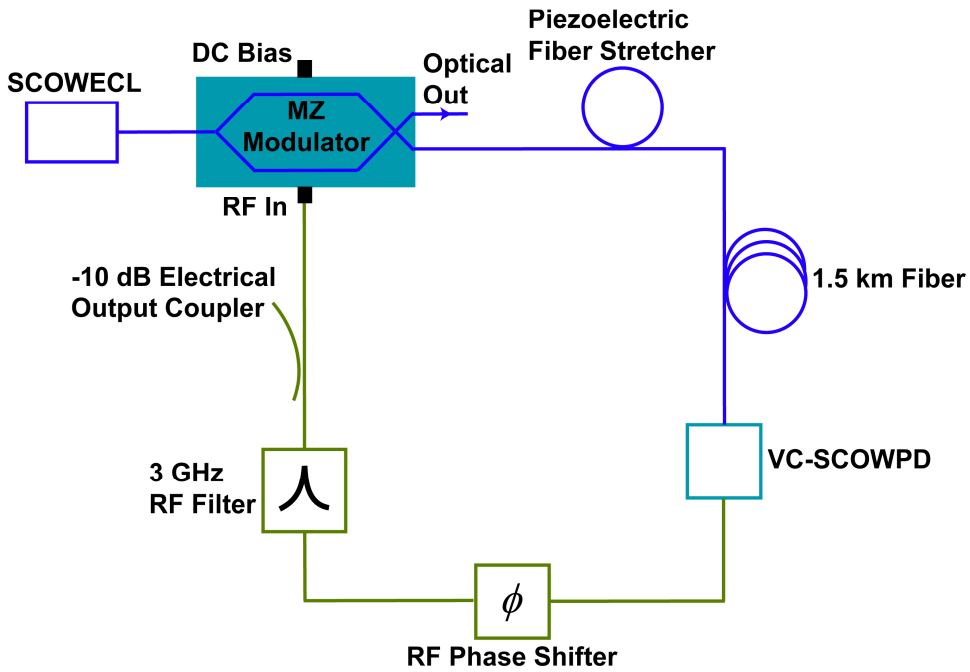

Figure 5-7: Configuration of the SCOW-OEO comprising a high-power, low-noise SCOWECL pump laser and a high-current variable confinement (VC)-SCOW photodiode.

The simulation is performed by iterating over successive roundtrips of the OEO, each time updating the signal voltage. Beginning from noise whose contributions include thermal noise, shot noise, and laser RIN, we use Eq. (5.4) to calculate the voltage amplified by one pass through the MWP link. Next, we incoherently add noise to the resulting voltage and iterate the process over 1000 roundtrips of the cavity. In each iteration, we monitor the intracavity power and gain of both the mainmode and sidemode. Mathematically, the power in the mainmode or sidemode after the *N*th roundtrip ($P_{RF,N}$) can be expressed as

$$P_{RF,N} = P_{RF,N-1}G + P_{Noise} \tag{5.6}$$

Here $P_{RF,N-1}$ is the power of the previous roundtrip, G is the equivalent MWP power gain (Eq. (5.4)) for the mainmode or sidemode, and P_{Noise} is the added contribution due to thermal noise, shot noise, and laser RIN. The measured losses of the RF loop were included as direct

Table 5-1: Summary of measured SCOW-OEO parameters used in the simulation

Parameter	Value
RF Loss (α_{RF})	4.9 dB
Responsivity ($\Re$)	1 A/W
Modulator V_{π}	3.1 V
Characteristic Impedance (R)	50 Ω
Modulator Bias Point (Γ_0)	58º
Relative Intensity Noise (RIN)	-160 dBc/Hz
Optical Loss After Modulator (α_{op})	1.5 dB

losses to the voltage gain and injected noise. Table 5-1 summarizes the experimentally measured parameters used in the OEO simulation. It should be emphasized that no fitting parameters were used for the simulation of the SCOW-OEO. In the first iteration only, we introduce a ~1 dB noise spike between the noise at frequencies ω_1 and ω_2. As will be shown later, this difference in injected noise is enough to cause the system to evolve to a state where the larger signal dominates.

In general, noise processes are referenced to a 1-Hz bandwidth and must be scaled appropriately to determine the absolute noise coupled into a single oscillator mode. We saw in Chapters 2 and 3 that the strength of white noise divides equally into all the available modes. However, for the purposes of simulation, it does not matter what scaling factor is chosen as the convergence of the simulation only depends on the parameters of Table 5-1. The steady-state behavior of the oscillating mode is independent of input conditions as long as both input tones are initially small, and one tone starts larger than the other (by means of noise fluctuation). The input tones continue to receive gain (or loss) from the system until the modulation Bessel-function response saturates. For ease of simulation, we use a 1-Hz noise bandwidth. The simulation quickly converges to steady-state within ~1000 iterations.

5.2.2 SCOW-OEO Steady-State Simulation

The simulation procedure of Eq. (5.6) can be applied to determine both the RF power and RF gain as a function of the DC photocurrent. Note that the actual value of the DC photocurrent

depends on the saturation of the MWP link (Eqs. (5.1), (5.2) with $n = 0,\ m = 0$). For this simulation, we thus pick the value of the supplied optical power and iterate to determine the system's photocurrent.

Figure 5-8 shows the RF power of both the mainmode and sidemode in steady-state graphed as a function of the DC photocurrent. Starting with just a small difference in noise during the first iteration, the system evolves such that the stronger (mainmode) tone receives all of the signal power above threshold. Below threshold, the mainmode and sidemode (weaker tone) RF powers are similar. The simulation reaches oscillation threshold at 19 mA, which matches our experimentally observed threshold photocurrent of ~20 mA. Beyond threshold, the simulated RF power is 9.3 mW at 27.3 mA photocurrent operation. Experimentally, we measure 1 mW output from a -10 dB coupler when the SCOW-OEO was operated at 27.3 mA. This corresponds to ~9 mW intracavity power after accounting for output losses and therefore agrees very well with our simulated RF power.

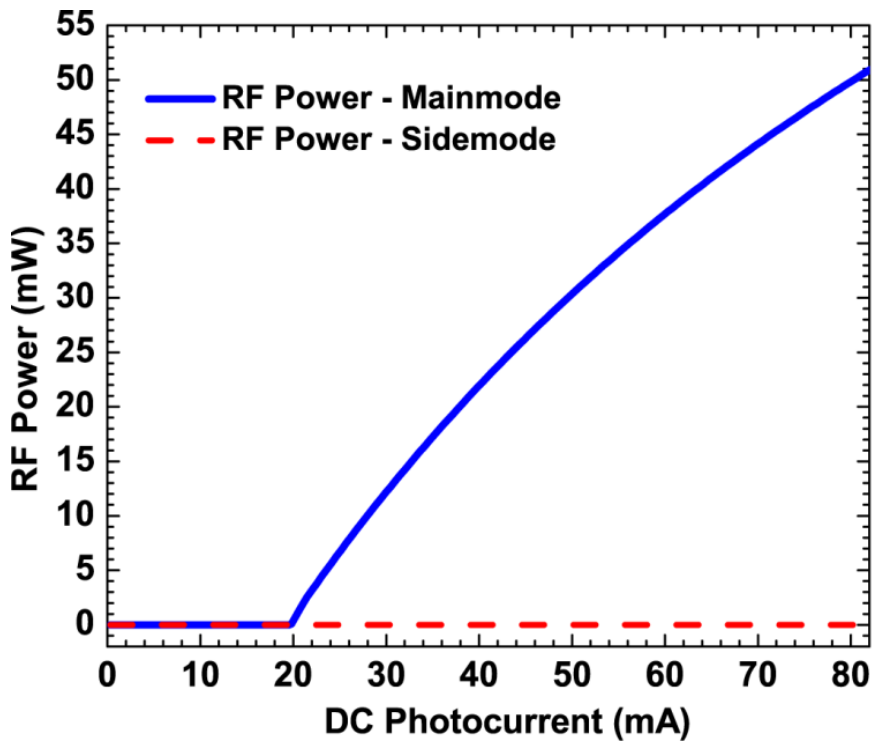

Figure 5-8: Simulation of SCOW-OEO RF power versus DC photocurrent using the parameters of Table 5-1.

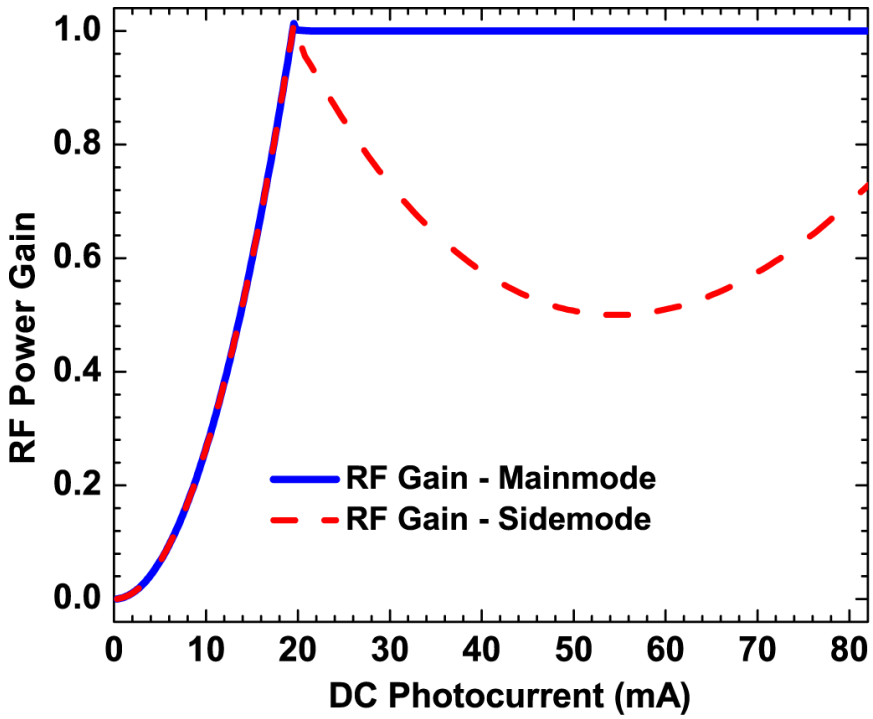

Figure 5-9: Simulation of SCOW-OEO RF power gain versus DC photocurrent using the parameters of Table 5-1.

Figure 5-9 shows the mainmode and sidemode power gains as a function of the DC photocurrent. Here, we graph the gain of RF power (instead of voltage) as an aid for the discussion of sidemode suppression provided next. Below threshold, the gains of the mainmode and sidemode are similar as both tones are small signal and nearly indistinguishable in Eq. (5.3). Once the mainmode reaches a gain of 1, the system oscillates and builds up power into the mainmode. As power continues to increase with photocurrent, the sidemode gain decreases according to the behavior determined in Fig. 5-4 for a single roundtrip. Figure 5-9 shows that a large gain differential can be achieved resulting solely from the super-homogeneous gain of the MWP link. At 27.3 mA operation, we simulate the gain ratio of the SCOW-OEO to be 0.79. The sidemode gain begins to increase again past 54 mA due to the inherent nonlinearity of the modulator Bessel transfer function. Eventually beyond 80 mA, the sidemode gain becomes larger than the mainmode gain causing multi-mode operation of the OEO.

5.2.3 SCOW-OEO Sidemode Simulation and Experimental Results

Our steady-state simulation of the SCOW-OEO can also in principle be applied to the determination of the SMSR, or the ratio between the sidemode and mainmode powers. Here however, the choice of noise bandwidth influences the result as the steady-state power of the sidemode tone depends on its initial conditions. The reason for this is because the sidemode tone operates below threshold, and thus becomes attenuated with each roundtrip of the cavity. The steady-state sidemode RF power is thus the power accumulated from its last few roundtrips within the OEO cavity. This power is expected to be proportional to the level of the injected noise during each iteration, and therefore the SMSR varies with these input conditions. Instead of calculating the total ratio of sidemode and mainmode powers, we first simulate the sidemode ratio per Hertz bandwidth (Fig. 5-10). We later calculate the total mode power by integrating the sidemode suppression over the linewidth of the mode. The fact that this method works appears at first to contradict our claims in Chapters 2 and 3 where the total noise should instead be

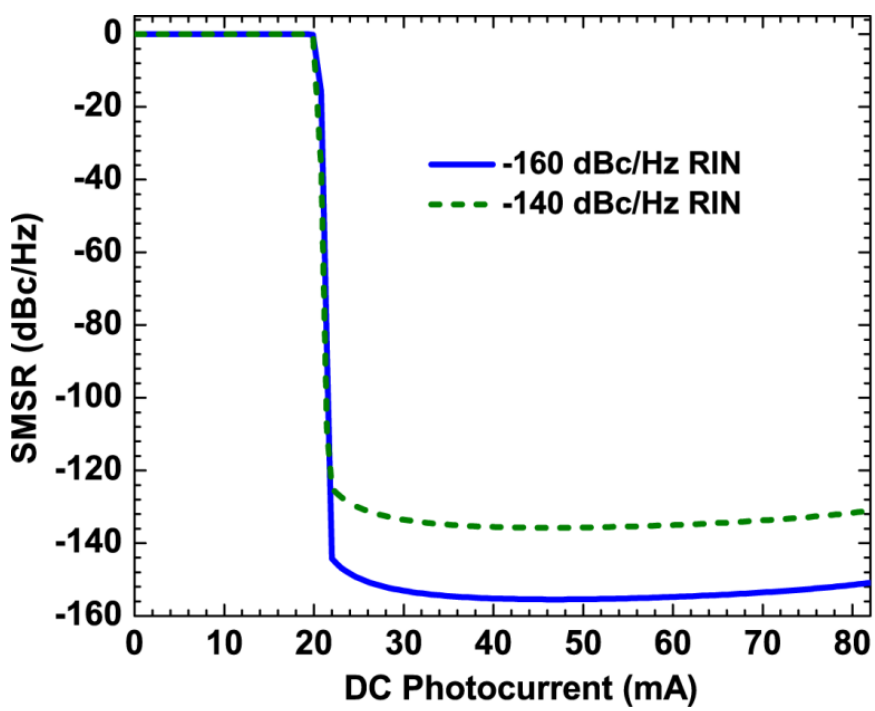

Figure 5-10: Simulation of SCOW-OEO SMSR versus DC photocurrent using the parameters of Table 5-1.

partitioned into the oscillator's modes. We will show later that these different viewpoints are not inconsistent with one another when the sidemodes are greatly attenuated compared to the mainmode.

Figure 5-10 indicates that the sidemode ratio is 0 dBc/Hz below threshold. This is expected as the mainmode and sidemode levels are similar before the OEO can oscillate. At 27.3 mA, the sidemode ratio is simulated to be -152 dBc/Hz (solid line). The RIN used for this simulation was -160 dBc/Hz, which is equal to the measured SCOWECL white-noise RIN for offset frequencies (100 kHz – 1 MHz) [58]. Injection of shot noise and thermal noise were also separately accounted for in the simulation but only become important at low photocurrent values (<10 mA). The linewidth (Δf) of a sidemode can be calculated from the cavity quality factor through [61]

$$\Delta f = \frac{\delta_c}{2\pi T_{rt}}$$
$$\delta_c = \ln\left(\frac{1}{g_{rt}}\right) \tag{5.7}$$

where T_{rt} (7.4 μs) is the roundtrip time and g_{rt} is the power gain of a sidemode per roundtrip. Since g_{rt} is limited to be <1, the linewidth of the cavity modes will be finite. Using g_{rt} = 0.79, we find Δf ~ 5.1 kHz. Multiplying the sidemode ratio by the 5.1 kHz linewidth, we calculate the total sidemode power relative to the mainmode to be -115 dBc.

We mentioned earlier that this technique of determining the sidemode levels is consistent with the noise partitioning model of Chapters 2 and 3. This is only true because the sidemodes are greatly attenuated relative to the mainmode so that their corresponding spurs are near the level of noise. We justify our statements using Fig. 5-11, which shows the amplitude-noise spectrum of the SCOW-OEO system measured using an Agilent E5052B signal-source analyzer (SSA). From noise partitioning, we know that a fraction of the total noise is coupled into each of the modes of an oscillator. We saw in Chapters 2 and 3 that if these modes suffer net attenuation, their corresponding linewidths broaden and thus the power density of each mode approaches the level of broadband noise injected with every cavity roundtrip. For the case of white noise, the spectrum flattens to a constant independent of frequency. The situation is similar to the SCOW-

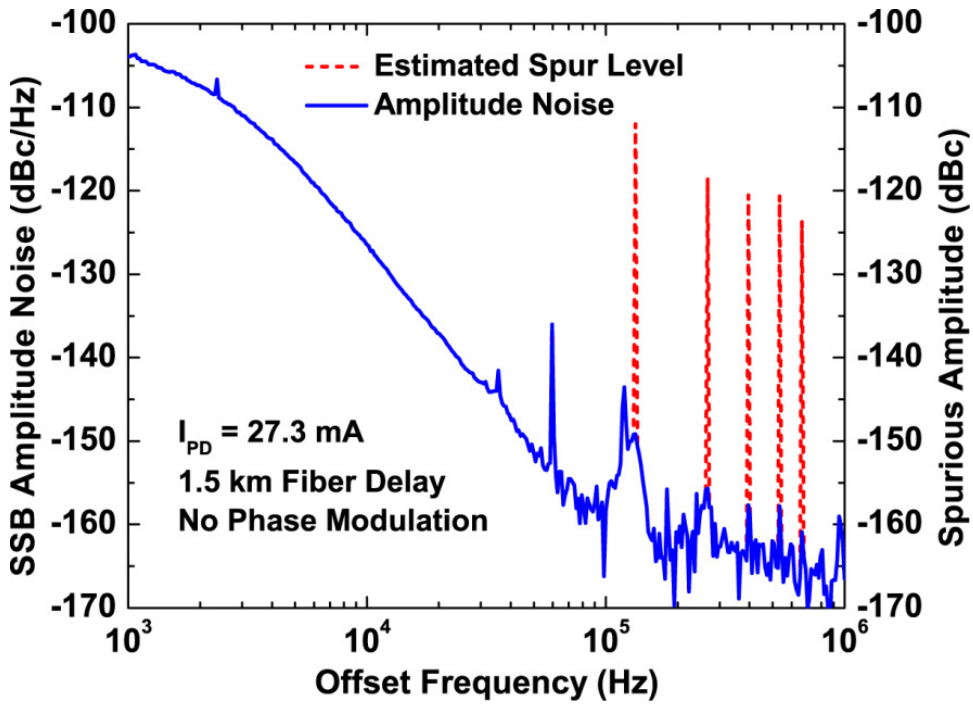

Figure 5-11: Measured SCOW-OEO amplitude-noise spectrum with estimated sidemode spur levels indicated.

OEO here where all of the sidemodes are attenuated (-1 dB *every roundtrip*) by the super-homogeneous gain of the system. However, note that Fig. 5-11 is difficult to analyze beyond 100 kHz as the actual noise is slightly below the resolution limit of the SSA. What we measure instead is the noise floor of the SSA plus a contribution due to the SCOW-OEO noise, with sidemode spurs intermittently spaced throughout the spectrum. However, because of the large sidemode attenuation and low sidemode levels (Fig. 5-11), we make the argument that our system represents a perturbation from the ideal case of perfect sidemode attenuation. That is, most of the spectrum is flat at the level of the injected noise except for a small amount of power accumulated at the sidemode resonance frequencies. The power stored within the sidemode is approximately the level of noise accumulated over all the cavity roundtrips multiplied by the spectral extent of the sidemode. This is identical to the calculation we performed in Eq. (5.7) and Fig. 5-10. Note that we assume the total power of the sidemode is sufficiently low that it does not perturb the levels of noise elsewhere.

We now return to discuss the measurement results of Fig. 5-11. Phase modulation is commonly applied to OEOs to suppress nonlinear noise processes due to signal propagation over optical fiber. Phase modulation was not applied here to prevent confusion between spurious tones and sidemodes. In the offset frequency range 100 kHz – 780 kHz, the resolution bandwidth (RBW) setting is 3.1 kHz. Since the RBW is similar to the linewidth of a sidemode, the calculated sidemode ratio can be directly compared to the measured spur levels (in dBc/Hz) without suffering too much accuracy loss integrating over noise. For the purposes of this comparison, we assume the power in the sidemode is evenly divided between amplitude and phase. We thus subtract 3 dB from our simulated sidemode ratio (Fig. 5-10) for comparison to the measured sidemodes in the amplitude-noise spectrum (Fig. 5-11). This value (-155 dBc/Hz) agrees well with the baseline sidemode levels (solid line) measured at harmonics of ~135 kHz. In Fig. 5-11, the spurious detection function of the SSA was also used to detect the ratio of total sidemode power relative to the mainmode. We calibrated this measurement against spurs from an external source as the SSA could not directly detect the sidemode peaks. The dashed lines indicate the estimated amplitude-noise level of the OEO sidemodes and agree with the simulated value (-118 dBc) after accounting for the 3-dB phase-noise contribution. In principle, the sidemode levels can also be determined from a measurement of the SCOW-OEO's phase-noise spectrum. However, these sidemodes are at the level of the noise-floor for the SSA's phase-noise measurement as we saw in Chapter 4.

Note that our simulation of sidemode ratio in Fig. 5-10 did not assume any RF filter bandwidth to reject the sidemodes. The low sidemode levels achieved are solely due to the gain differential introduced by the nonlinear modulation properties of MWP gain. With further increase of photocurrent, we find that the sidemode ratio decreases towards the level of the injected noise (normalized to the noise bandwidth). That is, as the gain difference between mainmode and sidemode increases further, the contribution to the sidemode power approaches the limit set by the injected noise for a single roundtrip. Figure 5-10 also shows the simulated sidemode ratio with a RIN noise injection level of -140 dBc/Hz. This represents the RIN performance of conventional semiconductor, fiber, and solid state lasers at ~100 kHz offset frequency [37]. In Fig. 5-10, the sidemode ratio degrades by 20 dB, corresponding to the 20 dB increase in noise injection. The increase of sidemode levels in direct proportion to the noise injection level is expected in light of our previous discussion on the impact of noise bandwidth.

To provide further intuition, we note that the simulation process (below threshold) of multiplying by the gain and adding noise with each iteration step resembles the propagation of amplified spontaneous emission (ASE) through an optical amplifier. The total ASE at the output of the amplifier can be integrated, and the resulting expression is also directly proportional to the amplifier's spontaneous emission noise injection [23]. Finally, the dependence of the sidemodes on RIN can also be seen in Figs. 4 and 6 of Ref. [37]. The low RIN of the SCOW lasers is the primary reason why the SCOW-OEO exhibits much lower sidemode levels compared to typical OEOs. However, we found the removal of the RF amplifier to also be beneficial for sidemode reduction as we saw in Chapter 4.

It is tempting to apply Eq. (5.3) to the case when the OEO is operated in deep-saturation (DC photocurrent > 90 mA). At these limits, the sidemode gain becomes larger than the mainmode gain, and the assumption of one large signal oscillating in the presence of multiple smaller signals breaks down. One can potentially obtain corrections to the gain response by expanding Eq. (5.3) to include third-order Bessel interactions between the modes of the OEO (second-order

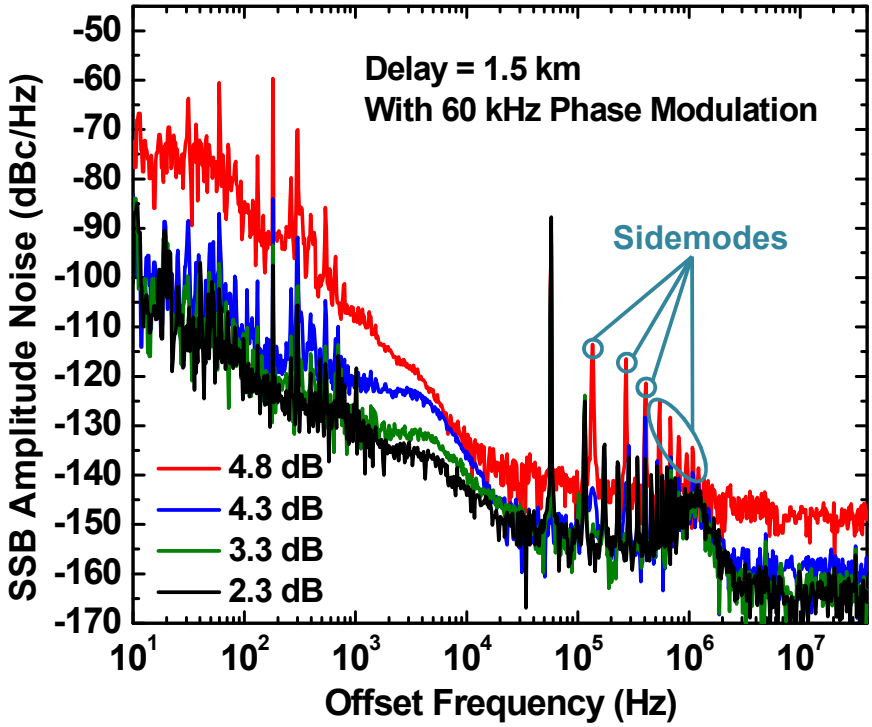

Figure 5-12: Measured SCOW-OEO amplitude-noise spectrum under varying optical attenuation (4.8 dB – 2.3 dB).

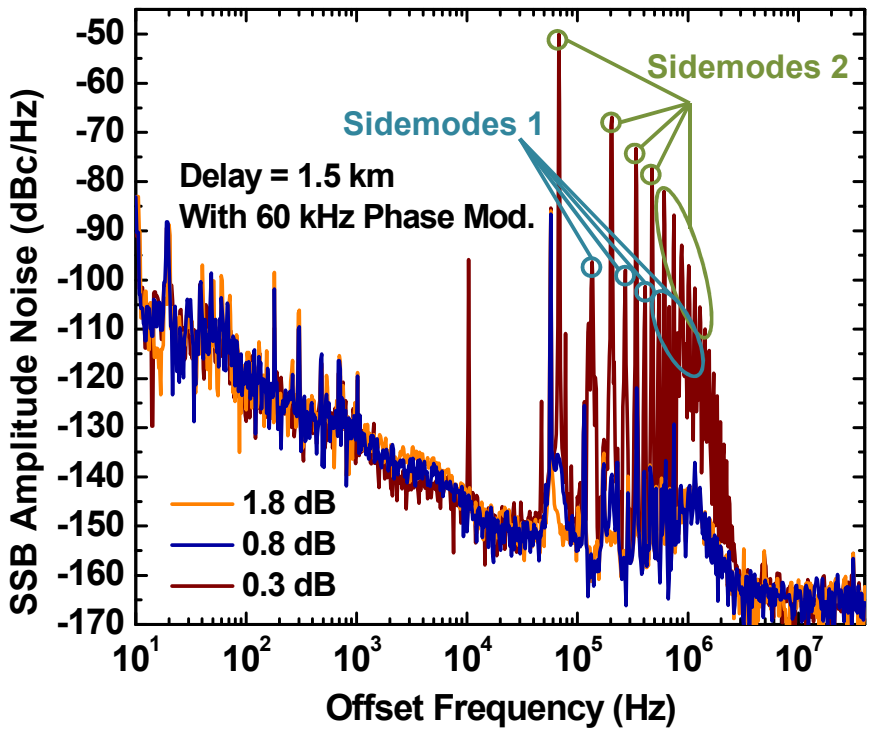

Figure 5-13: Measured SCOW-OEO amplitude-noise spectrum under varying optical attenuation (1.8 dB – 0.3 dB).

interactions are small due to the RF filter). Doing so, we find that the sidemodes increase rapidly towards the level of the mainmode in the deep-saturation limit. Higher-order Bessel interactions are required in order to simulate the behavior of the OEO beyond these extremes.

The behavior of the OEO in the high saturation limit can be experimentally determined by increasing the gain through use of RF amplification in the cavity (Figs. 5-12 and 5-13). For our SCOW-OEO system, we use an AML26PNA1811 low-flicker-noise amplifier with $G \sim 23$ dB and $P_{sat} \sim 25$ dBm. We also use a variable optical attenuator following the laser to control the total MWP gain within the OEO cavity. The optical attenuation is varied between 4.8 dB and 0.3 dB for the measurement in Figs. 5-12 and 5-13. At 4.8-dB attenuation, the OEO operates just above threshold and exhibits significantly larger amplitude noise compared to the rest of the cases. However, over much of the frequency range (>30 kHz), we expect the baseline noise-floor to be measurement-limited. The SSA measurement noise-floor depends on the input RF signal level and is near its sensitivity limit when the OEO oscillates just above threshold. This can be

seen above 2 MHz where no rollover in the amplitude-noise is observed, even past the RF filter cutoff. The first sidemode spur is located at 135 kHz offset at a level of -114 dB/Hz and is clearly above the system noise-floor. The other sidemodes can also be observed but are difficult to isolate from the 60-kHz phase-modulation spurs.

As the attenuation is decreased, the sidemode levels can be observed to decrease (relative to the mainmode) at all frequencies within the spectrum. This improvement in SMSR is due to "super-homogeneous" saturation of MWP gain in the SCOW-OEO. At ~2.3 dB attenuation, the sidemodes decrease to the level of noise (-155 dBc/Hz) and are masked in the amplitude-noise spectrum. This continues until the attenuation reaches 0.8 dB, at which point the sidemodes begin to grow. Interestingly, the sidemodes are located at offset frequencies of 67.5 kHz, 202.5 kHz, 337.5 kHz, etc and appear to be shifted by half the free spectral range (FSR) relative to the mainmode. Upon reaching 0.3 dB attenuation, the sidemodes experience exponential growth and increase towards the level of the oscillating signal. At this attenuation level, the condition $\pi v_1 / V_\pi \approx 2.4$ is satisfied, and the sidemode gain becomes equal to the mainmode gain. From the total detected RF power (~9.0 dBm accounting for loss) output from the 10-dB coupler, we find $\pi v_1 / V_\pi \approx 2.67$, which agrees with the theoretically predicted value. It appears that two distinct sets of sidemodes form, starting at 67.5 kHz and 135 kHz offset frequency and periodic at intervals of the FSR (135 kHz). However, the modes located at harmonics of 135 kHz are created by difference frequency generation due to the 67.5 kHz sidemodes after modulation. This can be verified through evaluation of how the modes scale with optical attenuation or by simple observation of the power level difference between each set of modes. Any multiple of 135 kHz can be generated between any two sidemodes as the modes are spaced by the FSR of the cavity. Similarly, the signal at ~10 kHz is created by the difference frequency between the first sidemode (67.5 kHz) and the phase modulation tone (57.5 kHz).

It is interesting to discuss the origin of the phase shift, which results in sidemodes located half an FSR closer to the oscillating signal. As one FSR corresponds to 2π phase, the total phase shift experienced by each sidemode is π. This π phase shift can be interpreted from the voltage gain expressions of Eq. (5.4). The gain was determined by an incoherent addition of voltage between sidemodes located at identical frequency offsets from the oscillating mode. The phase information of the voltage signal is lost after this incoherent addition, and the voltage gain

becomes just an expression related to the power gain. However, at the point where $\pi v_1/V_\pi \approx 2.4$ is reached, $J_0(\pi v_1/V_\pi)$ is over two orders of magnitude lower than $J_2(\pi v_1/V_\pi)$ and thus can be ignored in the expression for gain in Eq. (5.4). The remaining contribution of $J_2(\pi v_1/V_\pi)J_1(\pi v_2/V_\pi)$ to the sidemode gain is always opposite in sign to the voltage gain of the primary mode ($J_1(\pi v_1/V_\pi)J_0(\pi v_2/V_\pi)$), as can be seen in Eq. (5.2). This introduces an extra π phase shift in the gain of the sidemodes relative to the gain of the mainmode. Since the roundtrip phase shift of a sidemode must be a multiple of 2π to maintain self-coherence, the significance of the π phase shift is to shift the sidemodes half an FSR closer to the oscillating mode.

Before concluding, we wish to discuss the role RF amplification plays in the measurements of Figs. 5-12 and 5-13. In particular, we showed in Chapter 4 that the use of any amplifier (RF or optical) greatly increases the level of the sidemodes. It was mentioned that this increase in sidemodes is primarily observed in the phase response of the OEO. Thus, the amplitude-noise measurements of Figs. 5-12 and 5-13 are largely unaffected. For completeness, we show the

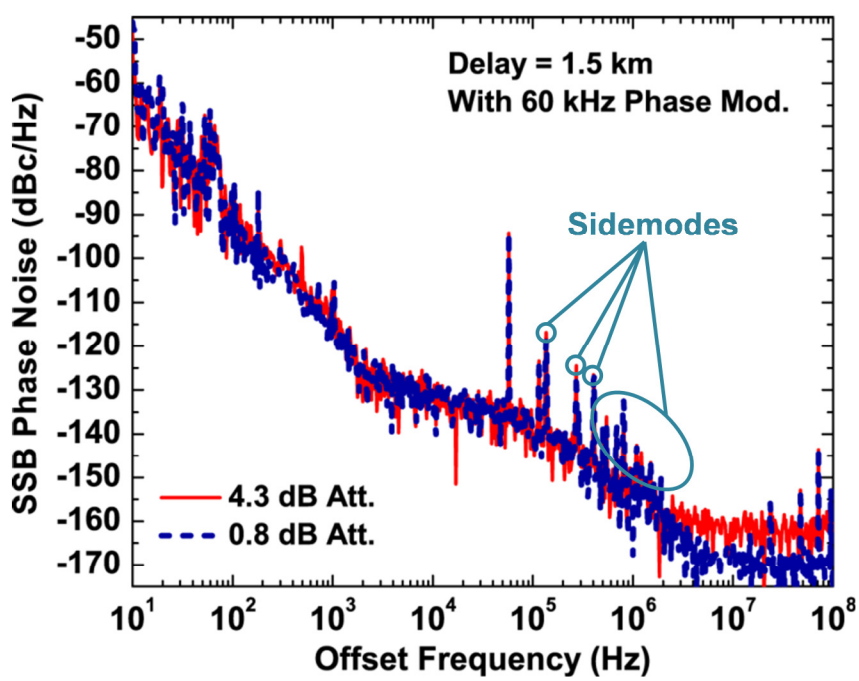

Figure 5-14: Measured SCOW-OEO phase-noise spectrum for 4.3 dB (solid line) and 0.8 dB (dashed line) optical attenuation.

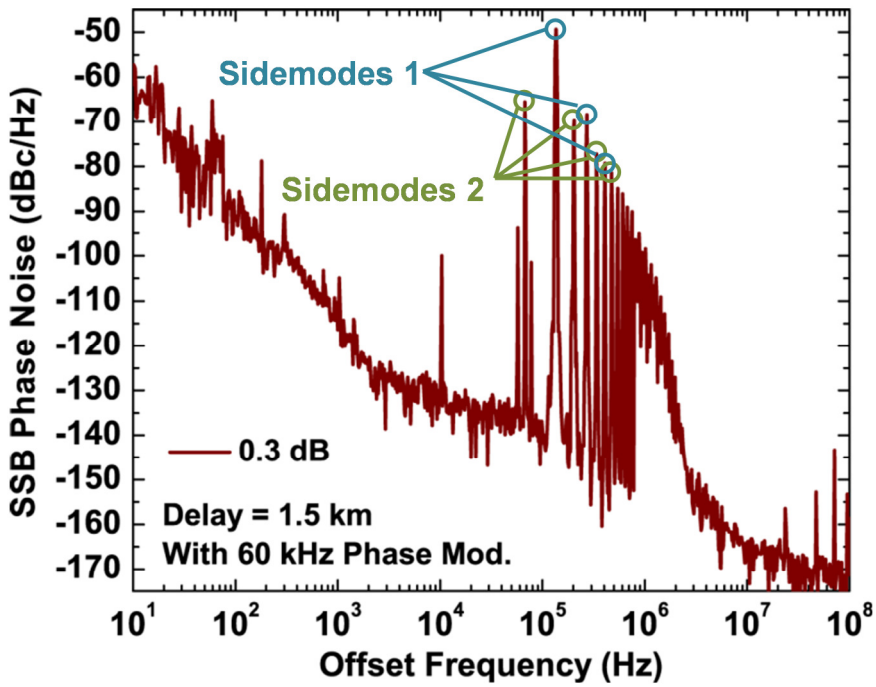

Figure 5-15: Measured SCOW-OEO phase-noise spectrum for 0.3 dB optical attenuation.

measured phase-noise spectrum of the SCOW-OEO to illustrate this point. Figure 5-14 shows the SCOW-OEO phase-noise comparing the cases of 4.3 dB and 0.8 dB optical attenuation. We see that not only is the difference in the relative sidemode levels between these two cases imperceptible now, but the sidemodes are now also much larger than in Figs. 5-12 and 5-13. Figure 5-15 shows the SCOW-OEO phase-noise with 0.3 dB optical attenuation. At this attenuation level, the voltage increases beyond $\pi v_1 / V_\pi \approx 2.4$ resulting in exponential growth of the sidemodes. We again observe two sets of spurs each periodic at 135 kHz and separated from one another by half the FSR of the OEO cavity. Comparing Fig. 5-15 to Fig. 5-13, we find the spurs to be similar in magnitude specifically for the 67.5 kHz set (labeled Sidemodes 2 in Fig. 5-15). On the other hand, the spurs corresponding to the 135 kHz set (Sidemodes 1) are much larger in the phase measurement than in the amplitude measurement. As mentioned previously, we currently do not have any explanation for the complex behavior of the OEO sidemodes exhibited in Figs. 5-14 and 5-15.

5.3 Nonlinear Filtering Using MWP Links

Section 5.1 illustrated the super-homogeneous properties of gain for two signals transmitter over a MWP link. Here, we exploit the properties of MWP gain to achieve the opposite effect: the suppression of a larger tone relative to the strength of a smaller tone. We will show that when the voltage of the larger signal reaches a specific magnitude, its gain becomes identically zero. In contrast, the gain of the smaller signal remains finite thus allowing only the smaller signal to survive the transmission over this link. This suppression applies not only to the peak of the signal but also to its surrounding phase-noise sidebands, potentially uncovering the presence of smaller signals which would otherwise be buried below the noise of a larger tone. Moreover, the nulling of the larger tone applies regardless of the frequency separation between the transmitted signals and thus is not subject to the bandwidth limitations of conventional filters. The nonlinearity of the modulation-photodetection response which enables these unique properties of MWP gain also serves as the major disadvantage of this approach. As we will see in Sections 5.3.1 and 5.4, the presence of the larger tone generates higher-order harmonics of the input and also results in intermodulation products between the input tones. However, we expect the unique capabilities of the MWP gain to outweigh the penalties incurred through the generation of these unwanted spurs.

5.3.1 Theory of Two-Tone Gain Over a MWP Link

Our goal in this section is to develop the theory for the gain of two RF signals transmitted over a MWP link. By the end, we will show that the larger signal along with its associated phase fluctuations can both be nulled by the unusual characteristics exhibited by the MWP gain. Much of this analysis follows from Section 5.1. The main difference here is that the input spectrum we consider is no longer symmetric about the larger tone, and so we no longer need to include the intermodulation term as a contribution to the ω_2 output in Eqs. (5.3)-(5.5). Instead, the larger input at ω_1 mixes with the smaller input at ω_2 to generate a spur at $\omega_3 = 2\omega_1 - \omega_2$. In general, there are multiple other possible combinations of the third-order product, but only one more of which generates an unwanted spur within the band of ω_1 and ω_2. Note that this statement implicitly assumes ω_1 and ω_2 to be near each other in frequency. With one large tone (v_1) and

one small tone (v_2), the dominant contributions to the voltage at the output of the link are given as

$$
\begin{aligned}
V(\omega_1 t) &= P_0 \Re R \sin\Gamma_0 J_1\left(\frac{\pi v_1}{V_\pi}\right) J_0\left(\frac{\pi v_2}{V_\pi}\right)\sin(\omega_1 t) \\
V(\omega_2 t) &= P_0 \Re R \sin\Gamma_0 J_0\left(\frac{\pi v_1}{V_\pi}\right) J_1\left(\frac{\pi v_2}{V_\pi}\right)\sin(\omega_2 t) \\
V(\omega_3 t) &= -P_0 \Re R \sin\Gamma_0 J_2\left(\frac{\pi v_1}{V_\pi}\right) J_1\left(\frac{\pi v_2}{V_\pi}\right)\sin(\omega_3 t)
\end{aligned}
\tag{5.8}
$$

A diagram of the voltage inputs at ω_1 and ω_2 along with the intermodulation output at ω_3 is illustrated in Fig. 5-16.

Through division by the inputs at ω_1 or ω_2, Eq. (5.8) can be transformed into expressions describing the voltage gain over the MWP link. In general, the link gain depends on the amplitude levels of both input tones. However, under the conditions that $\pi v_2 / V_\pi << 1$, the

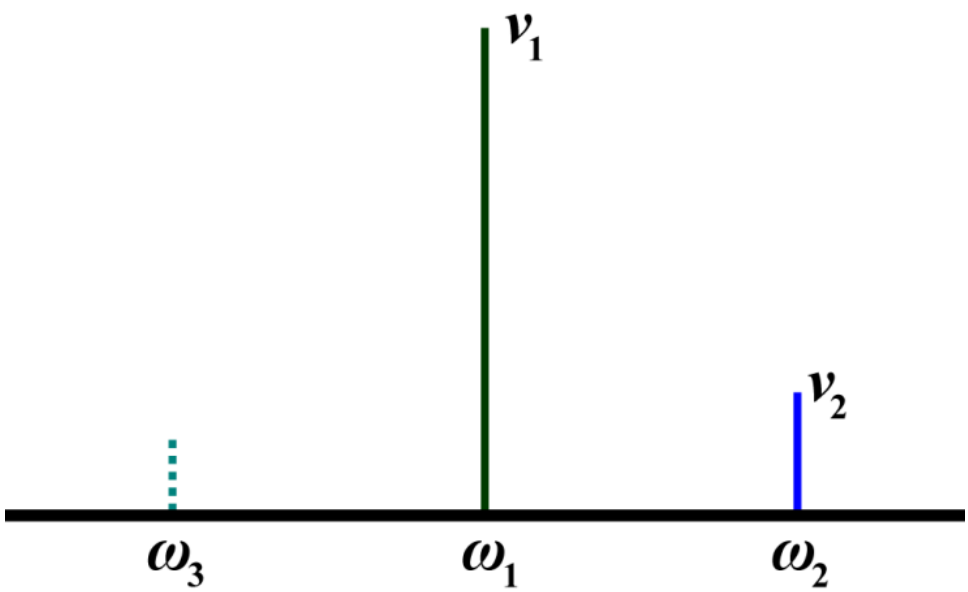

Figure 5-16: Diagram of two input tones, one large tone at ω_1 and one small tone at ω_2, generating an intermodulation output at ω_3.

voltage gains ($G(\omega_i t)$) for i=1, 2, and 3 can be simplified to

$$
\begin{aligned}
G(\omega_1 t) &= \frac{P_0 \Re R \sin\Gamma_0}{v_1} J_1\left(\frac{\pi v_1}{V_\pi}\right) \\
G(\omega_2 t) &= \frac{\pi P_0 \Re R \sin\Gamma_0}{2V_\pi} J_0\left(\frac{\pi v_1}{V_\pi}\right) \\
G(\omega_3 t) &= -\frac{\pi P_0 \Re R \sin\Gamma_0}{2V_\pi} J_2\left(\frac{\pi v_1}{V_\pi}\right)
\end{aligned}
\tag{5.9}
$$

Note that for the voltage component at ω_3, no direct gain exists since the inputs to the link were applied at the frequencies of ω_1 and ω_2. In Eq. (5.9), we instead determine $G(\omega_3 t)$ through normalization of Eq. (5.8) by the strength of the smaller tone. $G(\omega_3 t)$ thus represents the gain

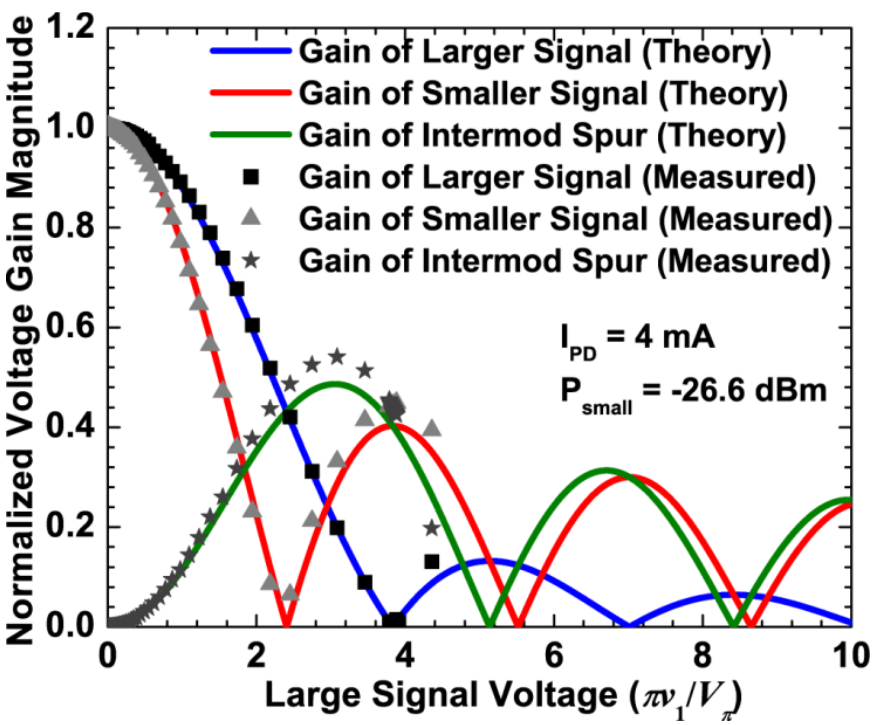

Figure 5-17: Measured and simulated values of the normalized voltage gain magnitudes corresponding to the larger signal, smaller signal, and intermodulation spur for $0 < \pi v_1 / V_\pi < 10$. The input power of the smaller tone was -26.6 dBm, while the photocurrent was maintained near 4 mA over the course of the measurement.

from an input at ω_2 to an output at ω_3 resulting from a third-order intermodulation product of the link.

From Eq. (5.9), it is clear that the gain saturation induced by v_1 is asymmetric for the inputs at ω_1 and ω_2. This can be more concretely seen in Fig. 5-17, with the magnitude of all three voltage gains plotted as a function of $\pi v_1/V_\pi$. Note that by taking the magnitude of the voltage, the phase information of the voltage gain is lost in Fig. 5-17. The gains at ω_1 and ω_2 are also normalized to achieve the value of unity when $v_1 \to 0$. For uniformity, this normalization factor was also applied to $G(\omega_3 t)$. Both $G(\omega_1 t)$ and $G(\omega_2 t)$ start at the same maximum value initially but undergo saturation behavior of different forms as v_1 increases. The MWP gain is super-homogeneous under certain ranges of v_1 as was found to be the case in Fig. 5-4. $G(\omega_3 t)$, on the

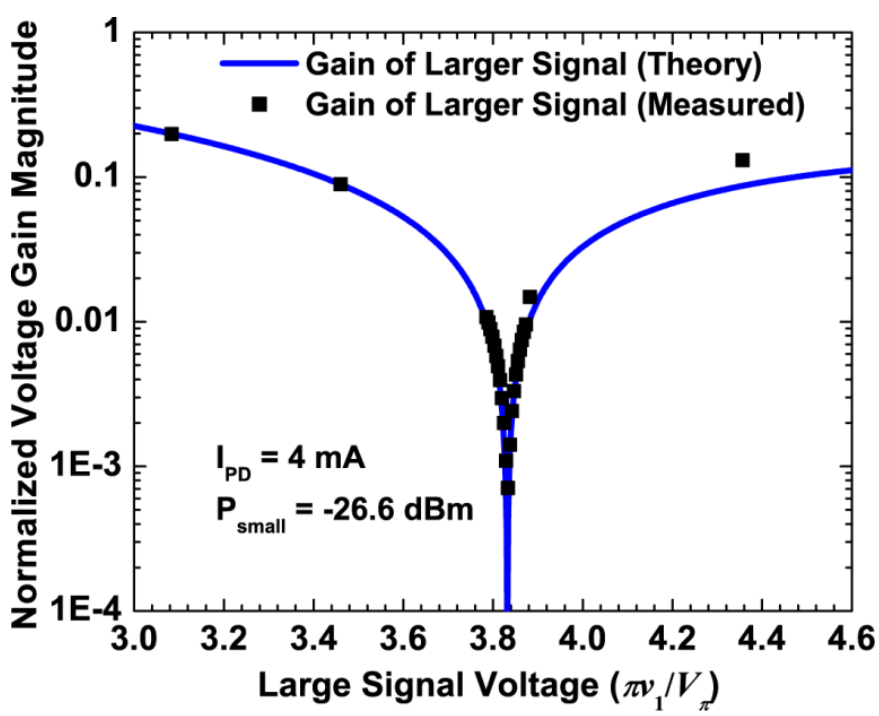

Figure 5-18: Measured and simulated values of the normalized voltage gain magnitudes corresponding to the larger signal, smaller signal, and intermodulation spur for $3.0 < \pi v_1/V_\pi < 4.6$. The input power of the smaller tone was -26.6 dBm, while the photocurrent was maintained near 4 mA over the course of the measurement.

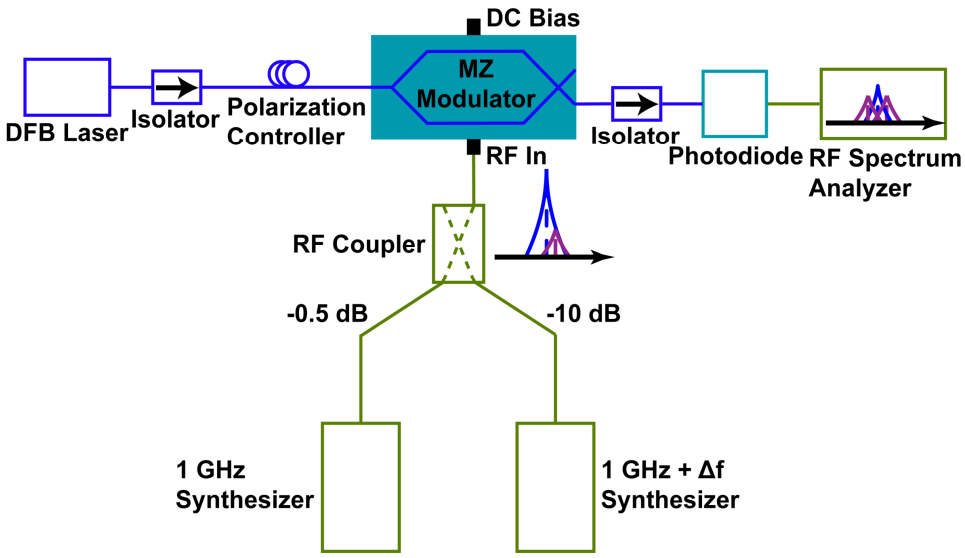

Figure 5-19: Diagram of the setup used to measure the gain of the larger signal, smaller signal, and intermodulation spur transmitted over a MWP link. The 1 GHz synthesizer serves as the larger input tone, while the 1 GHz + Δf synthesizer serves as the smaller input tone. The MWP link consists of a distributed feedback (DFB) laser, optical isolators, polarization controller, Mach-Zehnder (MZ) modulator, and photodiode.

other hand, starts at the value of zero when $v_1 = 0$. This is to be expected since the spur generated at ω_3 depends on the intermodulation product of the input tones. As v_1 increases, $G(\omega_3 t)$ grows initially but then decreases upon reaching $\pi v_1 / V_\pi = 3.05$. In the vicinity of $\pi v_1 / V_\pi = 3.83$, it can be observed that the gain of the larger tone approaches zero, while the gain of the smaller tone and of the intermodulation spur remains finite. A clearer depiction of this nulling behavior can be observed in the gain of the larger tone plotted on a logarithmic axis in Fig. 5-18.

The unusual saturation behavior of the MWP gain can be experimentally verified using the measurement setup of Fig. 5-19. The setup configuration consists of two synthesizers, one at 1 GHz (model Agilent E8241A) representing the larger tone and one at 1 GHz + Δf (model HP 8665B) representing the smaller tone. During the measurement, Δf was fixed at 30 kHz. The outputs of both synthesizers are combined on a 10 dB coupler and sent into the RF port of the MZ modulator. In the optical path, the output of a JDS Uniphase distributed feedback (DFB)

laser is sent through an optical isolator and polarization controller before being modulated by the RF inputs. The modulated waveform is next sent through another isolator before photodetection and subsequent processing by an RF spectrum analyzer (model E4440A). For the measurement of the MWP gain, the RF power of the larger signal was swept between -30 dBm and +23 dBm, while the RF power of the smaller signal was maintained at -15 dBm. Accounting for the effects of the 10 dB coupler and for the loss of the cables, the RF power incident on the modulator was -26.6 dBm for the smaller signal.

Figure 5-17 shows the results of the measurement normalized to a small-signal gain of unity. As was the case in Fig. 5-4, excellent agreement is again observed between the theoretical and measured values of MWP gain across all three tones. A V_π of 2.66 V can be extracted from the measurements of Fig. 5-17, which coincides with V_π~2.4 V specified by the manufacturer at the operating frequency of 1 GHz. In addition, the nulling behavior of the larger signal is clearly visible in the fine scan of Fig. 5-18. Note that spacing of the data points in the vicinity of the null corresponds to a 0.01 dB change of the larger signal's RF power. The attenuation of the larger tone comes at the price of generating an intermodulation spur whose strength will be equal to that of the smaller tone at the output of the MWP link.

Our previous discussion highlights the unique capabilities of the MWP gain, indicating the possibility of completely suppressing the larger signal while leaving the smaller signal intact. Moreover, this suppression is independent of the frequencies of the larger and smaller tones, limited only by the bandwidth restrictions of the modulator and photodiode. However, we have not yet discussed the behavior of this nulling in the presence of amplitude or phase modulation carried along with the larger tone. We address this topic next with the help of Eqs. (5.1) and (5.2). The results of this discussion can also be extended from the deterministic case of modulation to the case of random fluctuations in amplitude and phase.

5.3.2 Nulling Behavior Under Amplitude Modulation

We observed in Fig. 5-18 that the suppression of the larger signal depends critically on the signal's amplitude level at the input to the MWP link. In particular, at the specific point where $\pi v_1/V_\pi = 3.83$, the Bessel response $J_1(\pi v_1/V_\pi)$ becomes identically zero. It is therefore intuitive that this nulling behavior becomes inhibited in the presence of amplitude modulation where the

signal level varies as a function of time. We justify this statement now assuming amplitude modulation of the larger tone such that the total input to the link can be represented as

$$\begin{aligned} V_{in}(t) &= v_1\left[1+m\cos(\omega_{AM}t)\right]\sin(\omega_1 t)+v_2\sin(\omega_2 t) \\ &= v_1\sin(\omega_1 t)+v_2\sin(\omega_2 t)+\frac{v_1 m}{2}\sin\left((\omega_1+\omega_{AM})t\right)+\frac{v_1 m}{2}\sin\left((\omega_1-\omega_{AM})t\right) \end{aligned} \tag{5.10}$$

where m denotes the modulation index, ω_{AM} denotes the frequency of amplitude modulation, and the rest of the variables retain their original definitions. After expanding the first term of Eq. (5.10), it is clear that the AM modulation consists of the two original inputs at ω_1 and ω_2 but also introduces two additional sidebands spaced at a frequency ω_{AM} apart from ω_1. These sidebands effectively behave as supplementary inputs to the MWP link thus generating additional Bessel factors in the modulation-photodetection response. We can trace the contributions of all four tones to the output of the link for the frequencies of ω_1, ω_2, $\omega_3 = 2\omega_1 - \omega_2$, and $\omega_{AM}^{\pm} = \omega_1 \pm \omega_{AM}$.

For ω_1, two of the contributions can be identified as $1\times\omega_1 + 0\times\omega_2 + 0\times\omega_{AM}^{+} + 0\times\omega_{AM}^{-}$ and $-1\times\omega_1 + 0\times\omega_2 + 1\times\omega_{AM}^{+} + 1\times\omega_{AM}^{-}$ but are both zero at $\pi v_1/V_\pi = 3.83$ due to the interaction of $J_1(\pi v_1/V_\pi)$. The first non-zero contribution results from $3\times\omega_1 + 0\times\omega_2 - 1\times\omega_{AM}^{+} - 1\times\omega_{AM}^{-}$ thus signifying that the output of the MWP link can no longer be perfectly suppressed under amplitude modulation. Similarly, the modulation sideband at $\omega_{AM}^{\pm}$ receives contributions from $0\times\omega_1 + 0\times\omega_2 + 1\times\omega_{AM}^{\pm}$ and $2\times\omega_1 + 0\times\omega_2 - 1\times\omega_{AM}^{\mp}$, both of which are non-zero at $\pi v_1/V_\pi = 3.83$. We note that the only contribution to ω_2 is that due to $0\times\omega_1 + 1\times\omega_2 + 0\times\omega_{AM}^{+} + 0\times\omega_{AM}^{-}$, while the dominant contribution to ω_3 results from $2\times\omega_1 - 1\times\omega_2 + 0\times\omega_{AM}^{+} + 0\times\omega_{AM}^{-}$. Additional combinations of the input tones also exist but will not be discussed further here.

5.3.3 Nulling Behavior Under Phase Modulation

The situation with phase modulation is dramatically different from that of amplitude modulation. With phase modulation, the signal amplitude remains fixed so that the condition $J_1(\pi v_1/V_\pi)$ can be continuously maintained. The phase jumps primarily result in shifts of the instantaneous frequency, which have little impact on the behavior of the MWP link. This can be shown by considering the case where the larger tone exhibits a variable phase ($\phi(t)$) so that the total RF input can be expressed as

$$V_{in}(t) = v_1 \sin(\omega_1 t + \phi(t)) + v_2 \sin(\omega_2 t) \tag{5.11}$$

Using Eq. (5.11) in Eq. (5.1), we see that the net effect on Eq. (5.2) is a replacement of $\omega_1 t$ with $\omega_1 t + \phi(t)$. For a constant $\phi(t)$, this replacement generates only a phase shift in the outputs of the MWP link. When $\phi(t)$ is an oscillatory function as in the case of phase modulation, the inherent nonlinearities result in additional Bessel factors that multiply the expansion of Eq. (5.2).

If we assume $\phi(t)$ to be of the form $\phi_0 \cos(\omega_{PM} t)$, we can identify the MWP outputs at ω_1, ω_2, $\omega_3 = 2\omega_1 - \omega_2$, and $\omega_{PM}^{\pm} = \omega_1 \pm \omega_{PM}$ to be

$$\begin{aligned}
V(\omega_1 t) &= P_0 \Re R \sin\Gamma_0 J_1\left(\frac{\pi v_1}{V_\pi}\right) J_0\left(\frac{\pi v_2}{V_\pi}\right) J_0(\phi_0) \sin(\omega_1 t) \\
V(\omega_2 t) &= P_0 \Re R \sin\Gamma_0 J_0\left(\frac{\pi v_1}{V_\pi}\right) J_1\left(\frac{\pi v_2}{V_\pi}\right) \sin(\omega_2 t) \\
V(\omega_3 t) &= -P_0 \Re R \sin\Gamma_0 J_2\left(\frac{\pi v_1}{V_\pi}\right) J_1\left(\frac{\pi v_2}{V_\pi}\right) J_0(2\phi_0) \sin(\omega_3 t) \\
V(\omega_{PM}^{\pm} t) &= P_0 \Re R \sin\Gamma_0 J_1\left(\frac{\pi v_1}{V_\pi}\right) J_0\left(\frac{\pi v_2}{V_\pi}\right) J_1(\phi_0) \cos(\omega_{PM}^{\pm} t)
\end{aligned} \tag{5.12}$$

where ϕ_0 represents the strength of the phase modulation and ω_{PM} represents the modulation frequency. In contrast to the amplitude modulation case, Eq. (5.12) shows that both the strong tone ($V(\omega_1 t)$) and its modulation harmonics ($V(\omega_{PM}^{\pm} t)$) can be completely suppressed when

$\pi v_1/V_\pi$ reaches 3.83. Note that the Bessel functions of ϕ_0 indicate the depletion of the larger tone by phase modulation, redistributing the power into the modulation harmonics. This depletion applies also to the voltage contribution at ω_3, supplying power to the modulation sidebands around ω_3 (not evaluated in Eq. (5.12)). Equation (5.12) further shows that the MWP output at ω_2 is unaffected by phase modulation (compare to Eq. (5.8)), which corresponds to intuition when the modulation is viewed as an instantaneous frequency fluctuation of the larger tone.

5.4 Experimental Verification of MWP Filtering

In Section 5.3, we showed that both the larger tone and its corresponding phase-modulation sidebands become suppressed when transmitted at the point of $\pi v_1/V_\pi = 3.83$ over a MWP link. In contrast, this suppression was inhibited for the case of amplitude modulation. These properties can be verified from the experimental findings of Figs. 5-20 and 5-21 gathered using the measurement setup of Fig. 5-19. For this measurement, we switch the two signal generators of Fig. 5-19, making use of the HP 8665B's capabilities of amplitude and frequency modulation. However, due to the signal generator's limitations of output power, RF amplification (Mini-Circuits ZHL-42W) was also required to reach operation at $\pi v_1/V_\pi = 3.83$. The photocurrent was maintained at 4 mA throughout the amplitude and frequency modulation measurements.

Figure 5-20 shows the case when the larger signal is frequency modulated at a rate of 1 kHz. The modulation sidebands offset from ω_1 by harmonics of 1 kHz are clearly visible in the spectrum of the modulator's RF input. Also visible is the secondary tone applied at 1 GHz + 3.5 kHz with an amplitude level of -26.3 dBm. Note that the case of frequency modulation (FM) is analogous to the case of phase modulation analyzed in Section 5-3 with the modulation strength controllable by the allowable range of instantaneous frequency deviations. During our measurements, this maximum frequency deviation was set to 100 Hz for a 1 GHz carrier. In the same figure, the spectrum of the MWP link output is shown corresponding to three different

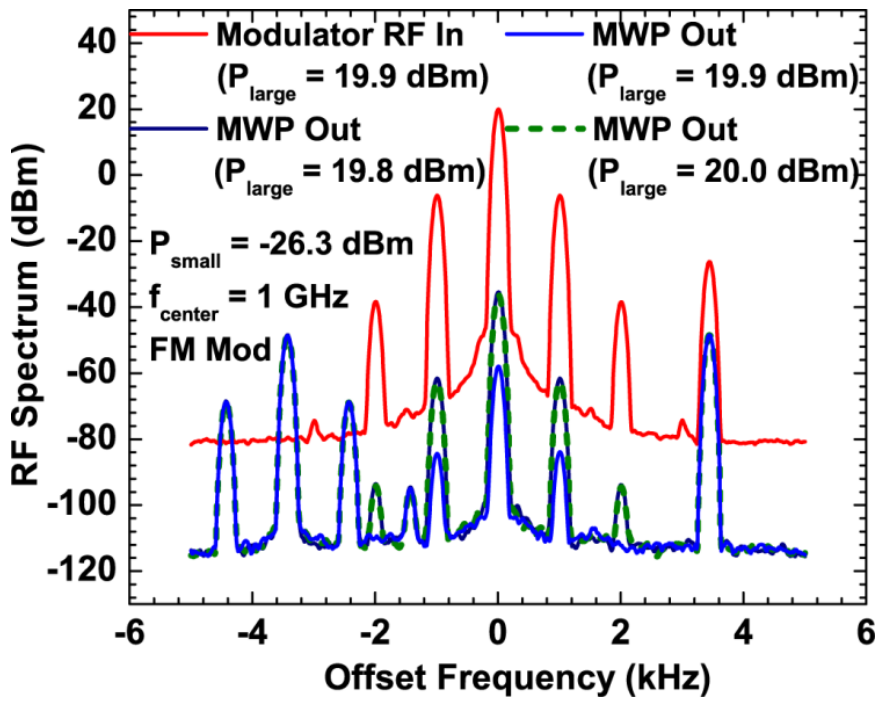

Figure 5-20: MWP link operation under small-signal frequency modulation of a larger tone in the presence of a secondary tone. The total modulator input corresponding to P_{large} = 19.9 dBm and P_{small} = -26.3 dBm is provided for reference. A comparison of the MWP outputs for P_{large} ranging from 19.8 dBm to 20.0 dBm is also shown. At P_{large} = 19.9 dBm, the suppression of the larger tone is at its maximum.

values of the larger signal power spaced 0.1 dB apart. The suppression is maximum for an RF signal input of 19.9 dBm.

From Fig. 5-20, the attenuation of the larger signal compared to the net loss of the smaller signal yields a relative suppression ratio of 55.8 dB. Note that the observed loss of the smaller signal can be compensated with an increase in optical power. It is clear that the measured suppression applies not only to the main peak at ω_1 but also to the modulation sidebands surrounding ω_1. However, the level of suppression changes significantly with the RF power of the larger signal. For a 0.1 dB fluctuation of RF power around the 19.9 dBm optimum, the suppression of the larger tone degrades by 22 dB. These observations match the sensitivity of the null in the MWP gain measurements of Fig. 5-18. In Fig. 5-20, the intermodulation spur at

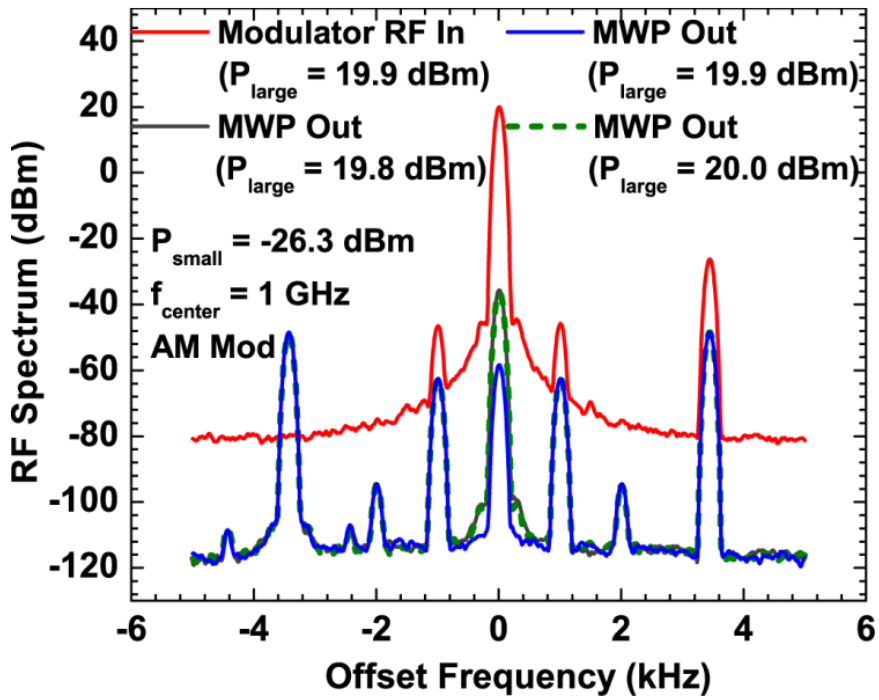

Figure 5-21: MWP link operation under small-signal amplitude modulation of a larger tone in the presence of a secondary tone. The total modulator input corresponding to P_{large} = 19.9 dBm and P_{small} = -26.3 dBm is provided for reference. A comparison of the MWP outputs for P_{large} ranging from 19.8 dBm to 20.0 dBm is also shown. At P_{large} = 19.9 dBm, the suppression of the larger tone is at its maximum.

$\omega_3 = 2\omega_1 - \omega_2$ can also be seen near an offset frequency of -3.5 kHz. The FM modulation applied to the larger tone results in a set of modulation sidebands centered around ω_3 (not evaluated in Eq. (5.12)).

Figure 5-21 shows the behavior of the MWP link when the larger tone undergoes amplitude modulation (AM) at a 1-kHz rate. Again, the modulation sidebands offset from ω_1 by 1 kHz can be seen in the spectrum of the modulator's RF input. The suppression of the larger signal at ω_1 is determined to be 56.1 dB relative to the attenuation of the smaller signal. In Section 5-3, we found the contribution of the AM modulation sidebands to spoil the larger signal's suppression at ω_1. However, this effect is relatively small in Fig. 5-21 due to the low modulation depth of 0.1%

employed during the measurements. The measured suppression is similar to that found in Fig. 5-20, which we believe to be limited by the polarization dependence of the modulator. In contrast, the AM modulation sidebands of Fig. 5-21 are insensitive to the nulling of the larger signal. A 0.1 dB fluctuation of RF power around the optimum point yields a 22 dB change in suppression at ω_1 but makes little difference on the levels of the modulation sidebands. This behavior agrees with our analysis of Section 5-3. Finally, the intermodulation product of the larger and smaller signals generates a peak at -3.5 kHz offset frequency, while the intermodulation product between the modulation sidebands and the smaller signal generates secondary spurs centered around the -3.5 kHz peak.

In Figs. 5-20 and 5-21, we investigated the effects of frequency and amplitude modulation when the depth of modulation was maintained at relatively low levels. Figures 5-22 and 5-23, show a similar set of measurements, but for the case when the modulation depth is larger. In

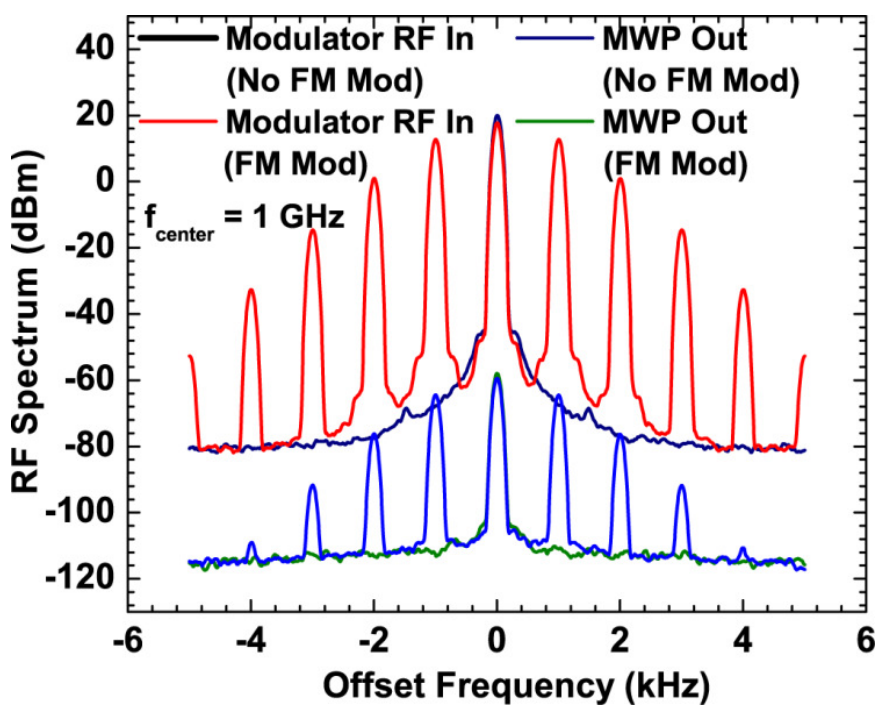

Figure 5-22: MWP link operation under large-signal frequency modulation (FM) of an RF tone. The modulator RF input is provided corresponding to an applied RF power of P_{large} = 19.9 dBm. The MWP link input and output when the FM modulation is turned off is also provided for reference.

these measurements, we also turn off the application of the smaller tone to prevent confusion from extraneous spurs generated by third-order mixing products. The photocurrent was maintained at 4 mA over the course of the measurements.

Figure 5-22 shows the case of FM modulation at a rate of 1 kHz but with an instantaneous frequency fluctuation of 1 kHz (10× larger than in Fig. 5-20). As expected, the modulation harmonics increase in strength and number over the 10 kHz span. Also shown is the same input but with the FM modulation turned off. In both cases, the RF power of the large applied tone is 19.9 dBm. Both inputs operate at the point of maximum suppression even though the power contained within the central lobe of the FM modulated tone is slightly less than that without FM modulation. In the FM modulated case, the instantaneous frequency fluctuations of the applied tone spreads the power to other frequencies within the spectrum thereby reducing the power contained within the central lobe. However, fundamentally, there is still only one tone applied to

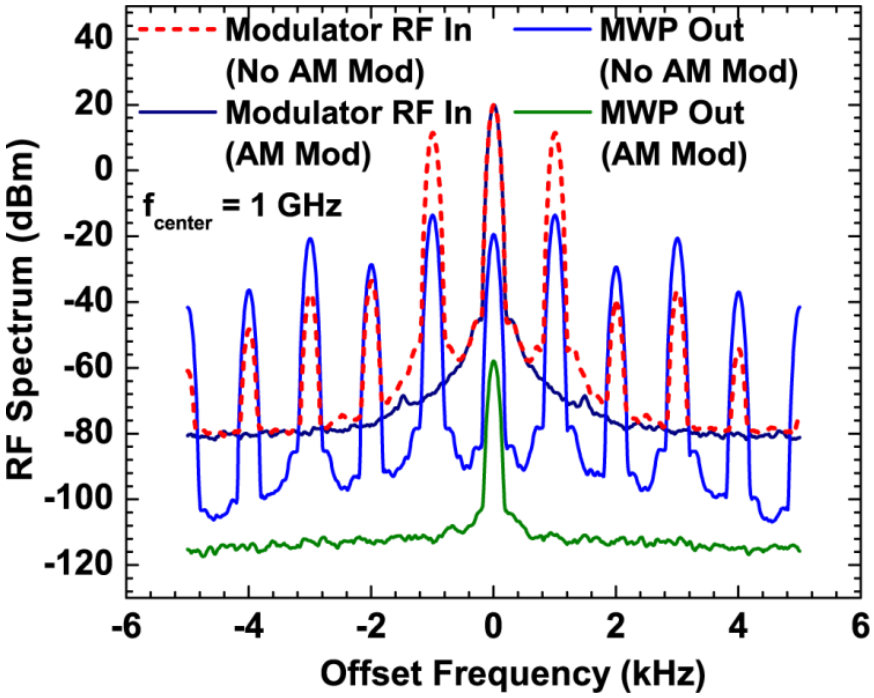

Figure 5-23: MWP link operation under large-signal amplitude modulation (AM) of an RF tone. The modulator RF input is provided corresponding to an applied RF power of P_{large} = 19.9 dBm. The MWP link input and output when the AM modulation is turned off is also provided for reference.

the link at all times, and thus it is the integrated voltage over the spectrum that determines when $\pi v_1 / V_\pi = 3.83$ is reached. Comparing the suppression achieved in Figs. 5-20 and 5-22, it can be verified that no loss of suppression is observed at larger FM modulation depths.

Figure 5-23 shows the case of AM modulation at a rate of 1 kHz and with a modulation depth of 75%. At the input to the modulator, the AM modulation spurs at 1 kHz again increase in amplitude. The harmonics beyond 1 kHz frequency are likely due to imperfections of the AM modulation process resulting in residual effects of phase modulation. Once again, we provide as a reference the applied RF tone with the AM modulation turned off. It can be verified that no loss of power is present in the central lobe. Both inputs are operated at the point of optimum suppression, but the maximum nulling is only achieved when the AM modulation is absent. The AM modulation spurs do not receive any suppression and also spoil the suppression of the larger tone, as predicted in Section 5-3. Due to the strength of the AM modulation tones, the

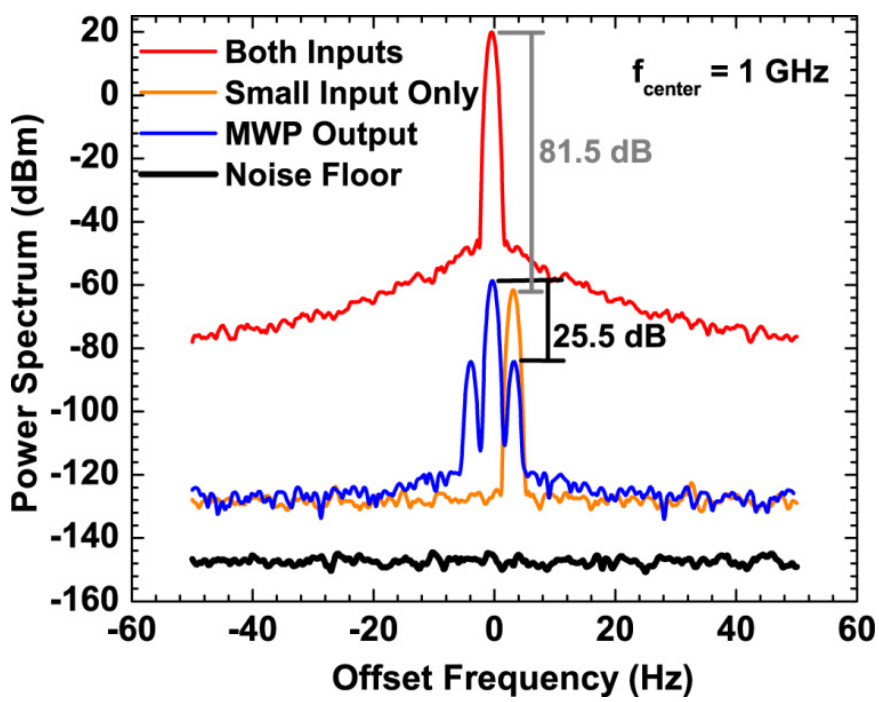

Figure 5-24: Phase-noise suppression of a 1-GHz larger signal (P_{large} = 19.9 dBm) in the presence of a smaller signal (P_{small} = -61.6 dBm) spaced 3.5 Hz away. The smaller signal normally hidden underneath the phase noise of the larger tone is uncovered after transmission over the MWP link. The noise floor of the measurement is provided for reference.

nonlinearities of the modulator generate a spectrum of intermodulation products at the output of the MWP link.

The unusual suppression properties of a MWP link apply not only to the case of deterministic modulation but also to the case when the fluctuations are random and due to the noise of the transmitted signal. In Figs. 5-24 and 5-25, we verify the phase-noise suppression of a larger tone in the presence of a smaller applied tone(s). We again use the measurement setup of Fig. 5-19 with the larger tone at 1 GHz and the smaller tone slightly offset from 1 GHz. Figure 5-24 shows this measurement for an offset of 3.5 Hz and with a 81.5 dB difference in strength between the two inputs (P_{large} = 19.9 dBm, P_{small} = -61.6 dBm). The spectrum with both inputs gives the appearance of a single tone as the phase noise of the larger tone masks the presence of the smaller input. Note that the resolution bandwidth of 1 Hz for this measurement yields a large spike in power when integrated over the RF carrier. If the larger input is switched off, the smaller tone becomes visible in the resulting spectrum at a point 13 dB below the previous limitations of phase noise. This example illustrates the unique capabilities available to MWP systems. Conventional filters would not only experience difficulty in extracting the information of the smaller signal beneath the noise but would also have trouble obtaining the bandwidth required to filter out only the larger signal. However, upon passing both inputs through a MWP link with the larger signal operated at $\pi v_1 / V_\pi = 3.83$, one can selectively suppress the larger signal by 56 dB relative to the smaller signal (Fig. 5-24). This suppression is independent of the frequency spacing between the individual tones. The signature of the smaller tone can now be clearly identified in the MWP output of Fig. 5-24 along with the remnant of the larger signal and the generated third-order intermodulation spur.

Figure 5-25 shows a similar measurement but with the smaller signal (P_{small} = -76.6 dBm) located at an offset of 35 Hz from the 1 GHz carrier. The smaller signal is also amplitude modulated at a frequency of 10 Hz with a modulation depth of 100%. At the input to the modulator, the smaller tone and its modulation sidebands are masked by the phase noise of the larger tone. However, after transmission over the MWP link, the larger signal receives a relative suppression of 55.4 dB, thus uncovering the presence of the hidden signals. This suppression reveals a lower floor which results from a combination of the larger signal's amplitude noise, the noise of the MWP link, and the noise of the larger signal's internal amplification stages. The

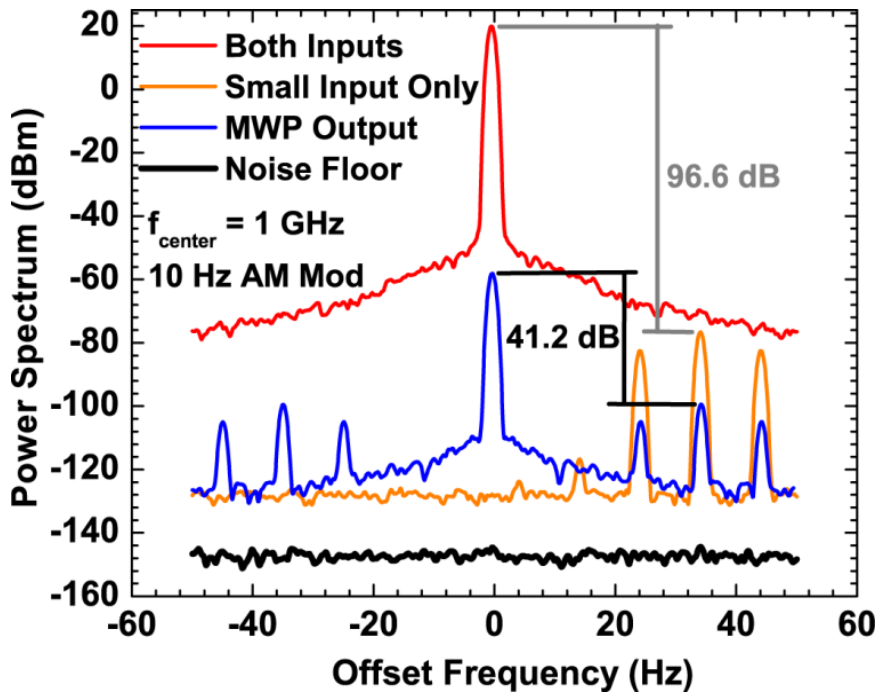

Figure 5-25: Phase-noise suppression of a 1-GHz larger signal (P_{large} = 19.9 dBm) in the presence of a 10-Hz amplitude-modulated smaller signal (P_{small} = -76.6 dBm) spaced 35 Hz away. The smaller signal normally hidden underneath the phase noise of the larger tone is uncovered after transmission over the MWP link. The noise floor of the measurement is provided for reference.

nonlinearities of the MWP link again result in intermodulation spurs generated on the opposite side of the spectrum. Note that the smaller signals transmitted over the MWP link and their corresponding intermodulation products are approximately equal in amplitude, as was also the case in Fig. 5-24. This behavior agrees with the predictions of Fig. 5-17 at the operating point of $\pi v_1 / V_\pi = 3.83$.

The signal suppression capabilities of a MWP link are independent of the frequency spacing between the larger and smaller tones. Figures 5-24 and 5-25 show this to be true for frequency separations below 100 Hz. We now show measurement results of this suppression when the input tones are separated by 300 kHz (Fig. 5-26). The large signal is operated at the point of optimum suppression (P_{large} = 19.9 dBm), while the RF power of the smaller signal is P_{small} = -26.6 dBm.

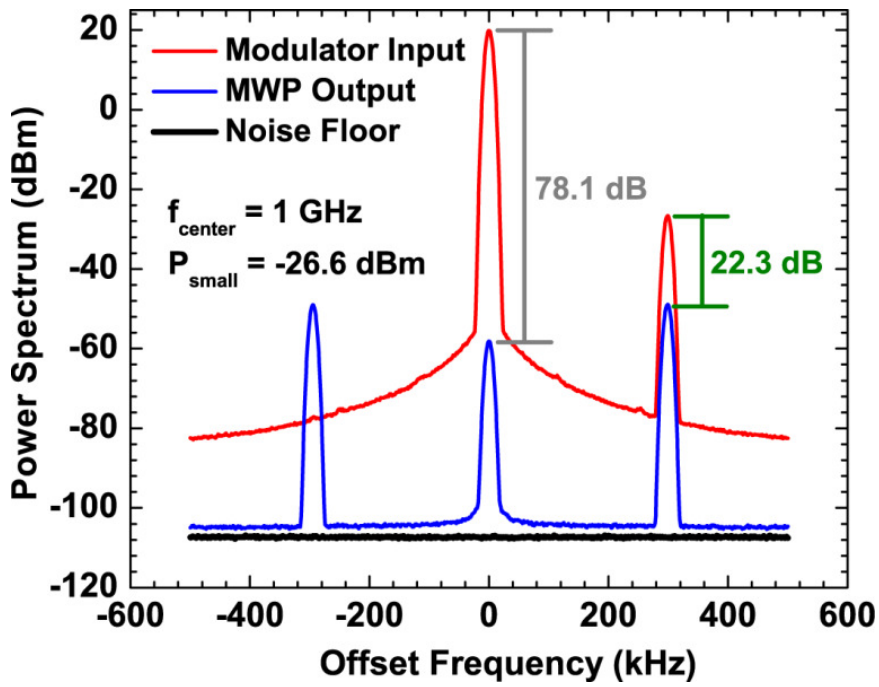

Figure 5-26: Suppression of a 1-GHz larger signal (P_{large} = 19.9 dBm) in the presence of a smaller signal (P_{small} = -76.6 dBm) spaced 300 kHz away. The noise floor of the measurement is provided for reference.

The measured suppression is 55.8 dB, which is nearly identical to the suppression achieved in Figs. 5-24 and 5-25.

We are now interested in exploring the behavior of the MWP link with the input RF power of the smaller signal as a variable parameter. This measurement is shown in Fig. 5-27 for P_{small} ranging from -29.6 dBm to 6.4 dBm in 12 dB increments applied at a frequency of 1 GHz + 30 kHz. As usual, the frequency of the larger tone is 1 GHz, and its RF power is fixed at 19.9 dBm to allow for operation at the point of maximum suppression. The photocurrent of the MWP link was maintained near 4 mA over the course of the measurement.

At the lowest power settings tested in Fig. 5-27 (P_{small} = -29.6 dBm), the two RF inputs mix together ($\omega_3 = 2\omega_1 - \omega_2$) to generate an intermodulation spur at an offset of -30 kHz. As expected from our earlier discussions, the level of the intermodulation spur is approximately equal to that of the transmitted smaller tone. No other spurs appear to be visible above the level of noise

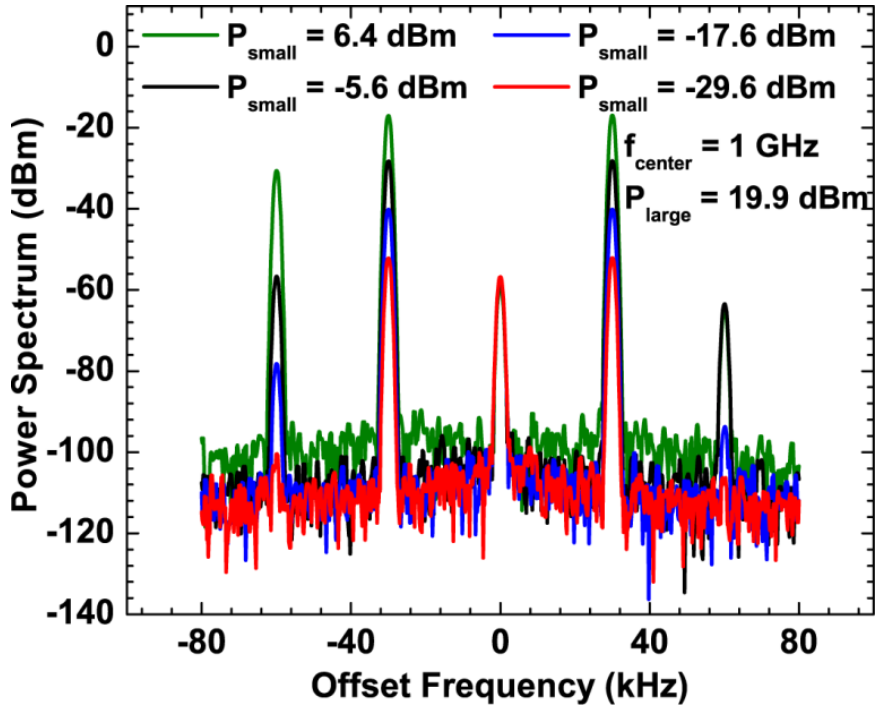

Figure 5-27: Output behavior for two RF tones transmitted over a MWP link. The larger tone is applied at 1 GHz with a RF power fixed at 19.9 dBm, while the smaller tone is applied at 1 GHz + 30 kHz with its power varied between -29.6 dBm and 6.4 dBm.

within the band of ω_1 and ω_2. Note that due to the nonlinearities induced by the larger tone, additional spurs will also be generated at harmonics of ω_1 but can be readily removed through the use of narrowband RF filtering. When the level of P_{small} increases to -17.6 dBm, higher-order intermodulation products begin to appear in the spectrum. The spur at -60 kHz results from $3\omega_1 - 2\omega_2$ interactions, while the spur at 60 kHz consists of contributions from $2\omega_2 - \omega_1$. The intermodulation tones continue to increase in strength as P_{small} approaches 6.4 dBm. The rate of increase for the -60 kHz spur is approximately double that of the -30 kHz spur, giving indication to a higher-order interaction. Note that the $2\omega_2 - \omega_1$ spur at 60 kHz is ideally zero due to the contribution of $J_1(\pi v_1/V_\pi)$ at $\pi v_1/V_\pi = 3.83$. However, because this suppression is incomplete, a residual spur can still be observed in the spectra of Fig. 5-27. We also wish to point out that the 60 kHz spur for the P_{small} = 6.4 dBm case is hidden behind the P_{small} = -5.6 dBm measurement.

5.5 Conclusion

We have shown that the microwave-photonic (MWP) gain is "super-homogeneous" such that a stronger signal saturates the gain of a weaker signal more than the saturation of its own gain. This concept has been applied to the simulation of an optoelectronic oscillator to determine its steady-state operation. Without any fitting parameters, the simulation agrees well with experimental measurements of the SCOW-OEO's steady-state operation. We show theoretically and experimentally that excellent sidemode suppression ratios of >110 dBc can be achieved despite the presence of multiple modes within the OEO cavity. However, the same nonlinear microwave photonic gain properties that result in large OEO sidemode suppressions also cause multi-mode operation when the oscillation signal becomes too large. At these limits, the sidemodes undergo a frequency shift of half the free spectral range relative to the mainmode oscillation.

We have also shown that the properties of gain over a MWP link can be exploited to realize functionality beyond the capabilities of conventional systems. The MWP gain is non-uniform across the transmitted signals of the link and can be strategically manipulated to selectively suppress one input in the presence of the others. In Sections 5.3 and 5.4, we demonstrated this suppression for a larger transmitted tone while leaving intact a smaller tone simultaneously applied to the link. We showed that this suppression is independent of the frequency spacing between the inputs and holds true even for the power contained within the phase fluctuations of the larger tone. Through careful amplitude control, we achieved a relative attenuation of 55 dB for a 1 GHz larger signal, uncovering the presence of a smaller signal located 3.5 Hz away. We also studied the behavior of the link for cases when the larger tone is amplitude or phase modulated. The nonlinearities of the modulation-photodetection process which enable these unique capabilities also generate unwanted harmonics and intermodulation spurs at the output of the link. Therefore, we expect the techniques presented here to be most applicable to cases where these spurs either do not disrupt the functionality of the system or can be later removed. These unique properties of the MWP gain may find other practical applications in the design of optoelectronic systems.

Chapter 6

Slab-Coupled Optical Waveguide Coupled Optoelectronic Oscillators (SCOW-COEOs)

The coupled optoelectronic oscillator (COEO) [7] is a system based on the regenerative modelocked laser (RML) architecture [10, 93] that is capable of generating both an optical pulse train and a low phase-noise microwave tone. The conversion from optical to microwave occurs through the beating of adjacent comb-lines during photodetection. With a long optical delay (~100–300 m), the phase-noise of the generated signal can be lower than that achieved by traditional electronic microwave oscillators [94].

Previous work on COEOs using semiconductor optical gain have shown excellent phase noise of -115 dBc/Hz at 1-kHz offset frequency operating at a carrier of 10 GHz [11]. Although the pulsewidths were not directly reported in Ref. [11], later reports revealed the COEO pulses to be highly asymmetric with widths of 22 ps [9]. Reported COEOs using erbium-doped fiber amplifier (EDFA) gain have also achieved low phase-noise (<-115 dBc/Hz at 1 kHz) and narrow pulsewidth (2 ps) at an oscillation frequency of 9.4 GHz [95]. In this paper, we demonstrate a 10-GHz high-performance slab-coupled optical waveguide COEO (SCOW-COEO) comprising a novel high-power, low-noise semiconductor gain medium. Previous SCOW-COEO work has shown the gain medium to be suitable for generation of a stable microwave signal at 10.24 GHz with optical pulsewidths of 17 ps [96]. In this work, we expand on the previous results and show that low phase-noise can be achieved with greatly suppressed sidemode oscillation (>70 dB). Here, we use the term sidemode to refer to the spurious oscillation modes of both the optical and optoelectronic cavities.

In all of the COEO demonstrations to date, RF amplifiers have been used within the cavity in order to sustain optoelectronic oscillation. The RF amplifier adds noise and increases the system's size, weight, and power (SWaP) performance. In this chapter, we describe the operation of an RF-amplifier-free SCOW-COEO oscillating on MWP gain. Our focus will be on the phase-noise performance of the COEO system where we will be providing a detailed investigation into

its noise properties. The findings of this study allow us to identify the key parameters important for low phase-noise performance. Finally, we conclude with measurements of the RF spectrum and optical pulse train coupled out of the electrical and optical cavities. Comparisons to a similar system operated with RF amplification will also be provided when applicable.

6.1 SCOW-COEO System and Operation

In this section, we describe the configuration of a 10-GHz RF-amplifier-free SCOW-COEO system and present the details of its operation. The COEO is unlike conventional oscillators in that its operation is governed by the simultaneous oscillation of two coupled cavities. The interaction of both cavities can be exploited to yield many desirable system properties, as we shall see in the sections to follow. Despite the complexities of the COEO, we will show that its behavior can be analyzed using principles commonly applied to conventional oscillators. At the core of the SCOW-COEO is a slab-coupled optical waveguide amplifier (SCOWA), which provides the gain necessary to self-oscillate without RF amplification. The noise of the SCOWA is essential to the performance of the SCOW-COEO, and we will present an assessment of its noise properties here.

6.1.1 SCOW-COEO Configuration

The COEO belongs to a class of oscillators based on a coupled-cavity system whose oscillation is dependent on the interaction between an optical and an optoelectronic cavity [7, 8]. A schematic of the RF-amplifier-free SCOW-COEO is illustrated in Fig. 6-1. The optical cavity configuration of the SCOW-COEO resembles that of a modelocked laser with a SCOWA serving as the active gain medium [21, 28]. The SCOWA used in our experiments exhibited saturation output power P_{sat} ~ 400 mW and small-signal gain G ~ 30 dB at 5-A bias [28]. Most (80%) of the SCOWA's output power is recirculated within the optical cavity of which 1% is later coupled out as useful optical output. An isolator was used to maintain uni-directional propagation of the optical power. After the isolator, the signal passes through a $LiNbO_3$ intensity modulator (V_π ~

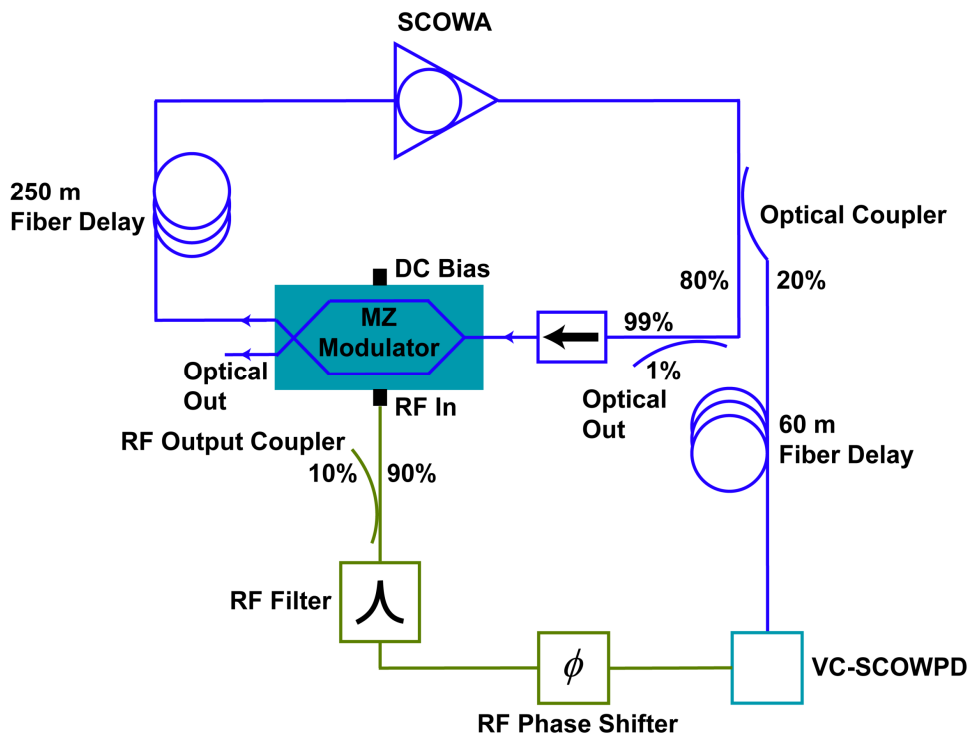

Figure 6-1: Schematic of the RF amplifier-free SCOW-COEO configuration exhibiting a total delay of ~310 m.

3.0 V at 10 GHz) and finally through a 250-m SMF fiber delay line. Due to the large intracavity circulating power (>250 mW average) allowed by the SCOWA, 2 mW optical power can be coupled out with only a 1% output coupler. In the optoelectronic cavity, the amplified and delayed signal from the 20% coupler passes through a 60-m SMF fiber delay and is incident on a photodiode. The 60-m delay is used for stabilization of the cavity and will be explained in more detail later. In our RF-amplifier-free SCOW-COEO, we used a high-power (I_{sat} = 40mA, BW = 14 GHz) variable confinement SCOW photodiode (VC-SCOWPD) for generation of the microwave signal [34]. The signal is first sent through a phase shifter for fine control of the oscillation frequency and then through a 10-GHz RF filter (BW = 10 MHz). The filter sets the oscillation frequency of the COEO and rejects unwanted frequencies beyond its passband. Finally, 10% of the signal is coupled out as useful RF output, while the remainder is fed back into the modulator to induce self-oscillation. Although not explicitly shown, polarization

controllers are included before the modulator, SCOWA, and photodiode for optimizing the functionality of polarization-sensitive components. The similarities of the COEO configuration to that of the regenerative modelocked laser were already discussed in Chapter 1.

The COEO operates by amplifying noise through successive roundtrips of the cavity until a large steady-state signal is developed. In the first iteration, thermal noise, shot noise, and spontaneous-spontaneous beat noise within the passband of the filter become incident on the modulator RF port and induce a small modulation of the amplifier's spontaneous emission. By itself, this process generally undergoes net MWP loss with each roundtrip as the spontaneous emission power is too small to generate a large beat-signal. However, when the optical cavity can also oscillate, the optical power stored within the longitudinal modes can now generate a large microwave signal at the beat frequencies between the cavity modes. If the net MWP gain is larger than unity, the beat frequencies falling within the filter passband induce larger and larger modulation of the optical signal until modelocking occurs. In steady-state, the COEO produces pulses in the optical output and a low-noise single-frequency tone through the filtered RF output.

In general, many modes can oscillate within the bandwidth of the RF filter. For example, in our case with ~250 m optical cavity fiber delay, ~12 modes can oscillate within the 10 MHz filter passband. The growth of a single mode and suppression of sidemodes occurs by the Vernier interaction between modes of the optical and optoelectronic cavity as was discussed in Chapter 1. The lengths of these two cavities are slightly offset such that only one set of modes within the filter passband can simultaneously satisfy both resonance conditions. Any frequency that satisfies the resonance of only one cavity will be greatly attenuated through the filter response of the second cavity. As such, large suppression of the sidemodes can be achieved without any additional requirement of complexity or cost. The 60 m of optical fiber in Fig. 1 then was optimized for the purpose of offsetting the resonance frequencies of the optoelectronic cavity from that of the optical cavity. The effects of this Vernier interaction will be evident in our measurements of Section 6.2.

Note that it is unclear the role that super-homogeneous gain saturation plays in the operation of a COEO. The super-homogeneous gain of a MWP link in Chapter 5 was derived for modulation of a CW laser signal. Upon photodetection, the sidemode tones saturate at a faster rate than the mainmode. Here, the situation changes to the modulation of an optical pulse. On a single roundtrip, the effects giving rise to pulse narrowing counteract the effects of pulse

broadening so that steady-state is reached. However, in this case, it becomes unclear how saturation affects the mainmode and sidemodes relative to each other. In Section 6.2, we will see that in general, the sidemodes of a COEO are slightly larger than that of the OEO suggesting that effects of super-homogeneous gain saturation may be minimal.

6.1.2 SCOW-COEO Equivalent Circuit

The coupled-cavity configuration of the COEO makes it difficult to analyze its operation. The goal of this section is to introduce an equivalent but simpler representation of Fig. 6-1. In particular, we will view the COEO from the perspective of a single-cavity oscillator but treat its optical cavity similar to a conventional intracavity filter (Fig, 6-2). That is, the modulator's RF port serves as the input to the filter, while the photodetector port serves as its output. The filter has an associated delay and, in this case, also provides net gain (G) from input to output. Similar to any other intracavity filter, the oscillating mode of the combined optoelectronic cavity must also be a valid mode of the equivalent filter. Note that the output of the filter is in general

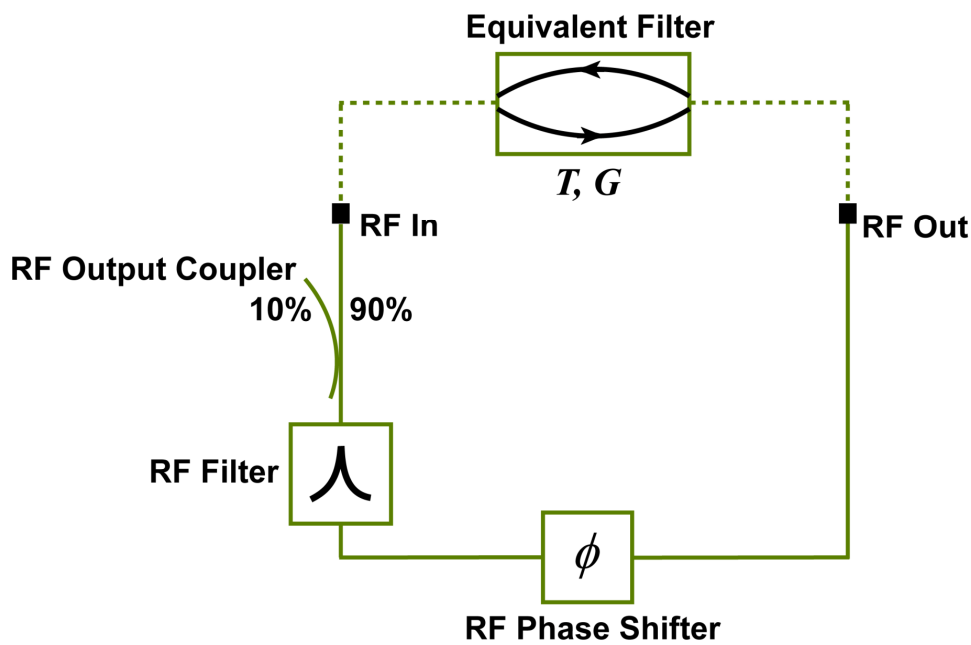

Figure 6-2: Equivalent circuit of the SCOW-COEO in Fig. 6-1 where the optical cavity has been replaced by an equivalent filter with delay T and net gain G .

nonlinear yielding components at harmonics of the input. We may combine the RF filter of Fig. 6-2 with this equivalent filter to define an effective configuration that is linear from input to output. The entire COEO system then reduces to that of a conventional oscillator but with an oscillating mode that must be coherent across three different cavities. It is this addition of one extra cavity that allows the COEO to achieve highly single-mode behavior.

6.1.3 Noise Measurements of the SCOWA

In this section, we present an assessment of the noise properties of the SCOWA used in the COEO system. The noise figure (*NF*) of a SCOWA has been previously measured in Refs. [22, 23] operating under small-signal conditions. Here, our goal is to measure the noise under conditions where the amplifier is saturated. Our strategy is to first measure the relative intensity noise (RIN) of a seed laser and subsequently to measure the RIN of the same laser amplified by the SCOWA. The RIN degradation provides a measure of the noise added by the SCOWA. For comparison purposes, we perform this measurement across two different seed lasers and across two different optical amplifiers. One of the lasers is a slab-coupled optical waveguide external cavity laser (SCOWECL), while the other is a commercial RIO Orion semiconductor external cavity laser (SECL). Of the two amplifiers tested, one is the SCOWA used in the COEO system, while the other is a commercial IPG Photonics 2-W erbium-doped fiber amplifier (EDFA) with a specified *NF* of 5 dB.

Figure 6-3 shows the results of the amplifier noise measurement for offset frequencies up to 10 GHz. The SCOWECL was operated at 4-A bias for its measurements corresponding to an optical output power of 330 mW. This optical power was then later attenuated down to 10 mW prior to photodetection or optical amplification. The SECL on the other hand was maintained at an output power of 10 mW and thus did not require any additional optical attenuation. For the cases employing optical amplification, the amplifier output power was controlled (via the bias current) to be 400 mW. It is clear that the SCOWA is operated in compression as its small-signal gain was measured to be near ~30 dB. However, we cannot make any definitive comments regarding the saturation of the EDFA as its gain has not been previously measured. Prior to photodetection, the amplifier output was attenuated down to the level of 10 mW. The corresponding photocurrent for all of these cases was 7 mA.

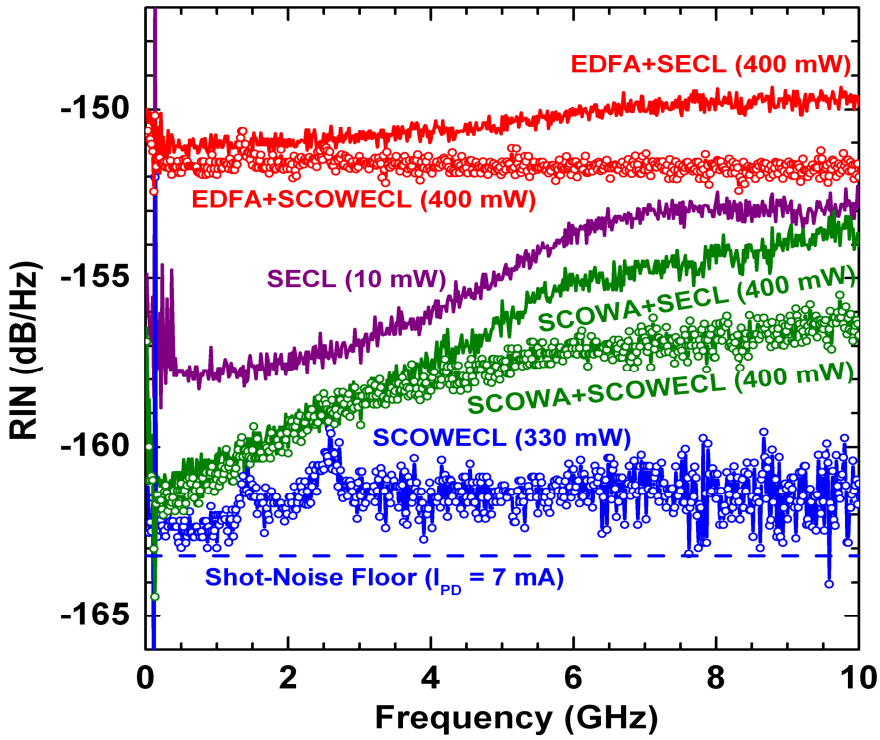

Figure 6-3: Relative intensity noise of a SCOWECL and a commercial SECL for three cases of operation: unamplified, amplified by a SCOWA, and amplified by a commercial EDFA. The shot-noise floor (dashed line) corresponding to 7 mA photocurrent is also provided.

From the measurement results of Fig. 6-3, it is observed that the SCOWECL RIN is near the limit of shot noise and exhibits no evidence of a relaxation oscillation resonance. In contrast, the RIN of the SECL is ~5 dB larger than shot noise at low frequencies and increases even more at higher frequencies due to relaxation oscillations. Note that these same measurements were presented earlier in Chapter 4 during our discussion of the OEO pump. We now wish to evaluate the RIN degradation due to the use of optical amplification. We first examine the case of the SCOWA and specifically with the SECL as the seed. It is clear from Fig. 6-3, that the RIN of the SECL + SCOWA is lower than that of the SECL by itself. Moreover, this improvement in RIN appears to increase at lower frequencies. As we have discussed in Chapter 1, this phenomenon is due to the saturation of the SCOWA, which acts to attenuate effects of intensity fluctuations. The RIN becomes suppressed at frequencies below the inverse carrier lifetime (<10 GHz) with the largest benefits gained at the lowest frequencies. Eventually beyond 10 GHz, we expect the RIN

of the combined SECL + SCOWA to recover to a value above that measured for the SECL operating alone. When the SCOWECL is used as the seed, the RIN of the amplified output is no longer lower than that of the SCOWECL source. The reason is because the SCOWECL noise is near its fundamental limit, and thus the added noise of the SCOWA becomes dominant. From Fig. 6-3, we see that the RIN of the SCOWECL + SCOWA is only slightly lower than the RIN of the SECL + SCOWA, despite the large RIN difference in the seed lasers. We have already mentioned one contributing factor to this, which is due to the RIN suppression of the SECL. The second factor is that the RIN of the SECL starts at a higher value so that the addition of SCOWA noise has a diminished effect on the overall RIN.

We are now interested in comparing the performance of the SCOWA to a commercial high-power EDFA. The total RIN of the SECL + EDFA is clearly worse than in the case of the SCOWA. Note that regardless of its saturation state, the EDFA does not provide noise suppression for its seed laser at these frequencies. The carrier lifetime of the EDFA is typically in the millisecond range, which translates to a cutoff frequency between 100 Hz – 1 kHz. The shape of the total RIN with the SECL is intuitive as the EDFA noise is nearly white (flat). The increase in noise at higher frequencies is due to the added noise of the SECL's relaxation oscillation resonance. For the case of the SCOWECL + EDFA, the RIN becomes flat over the range of frequencies tested. As the SCOWECL RIN is near the level of shot noise, the RIN degradation from the addition of the EDFA provides an approximate measure of its *NF*. For the measurement conditions here, the estimated EDFA *NF* is 9 dB.

6.2 SCOW-COEO Measurement Results and Discussion

Here we discuss measurement results of our SCOW-COEO organized into three separate subsections. The first subsection details a comparison of the phase noise, RF spectra, optical spectra, and optical pulse properties between two SCOW-COEO systems. One system uses a high power VC-SCOWPD to enable oscillation without RF amplification, while the other system employs a commercial photodiode and RF amplifier. The second subsection presents a series of experimental measurements with the purpose of analyzing the fundamental limitations of phase noise in a COEO. In the third subsection, we describe our procedure for optimizing the oscillator.

This will also serve to highlight the abnormal behavior that can result if the COEO is improperly designed.

6.2.1 Comparison of SCOW-COEO Systems

We measured the phase-noise of the 10-GHz RF-amplifier-free SCOW-COEO in Fig. 6-1 using a commercial Agilent E5052B signal-source analyzer (SSA) and E5053A microwave downconverter. Figure 6-4 shows the results of this measurement along with the phase-noise of a SCOW-COEO constructed using a commercial Discovery Semiconductors DSC50S photodiode. As the commercial photodiode does not provide sufficient current to achieve net MWP gain, a commercial low phase-noise RF amplifier (AML612PNA1211 G = 14 dB, P_{sat} = 28 dBm) was used to sustain oscillation. Aside from the photodiode and RF amplifier, both systems are otherwise identical. One-thousand (1000) cross-correlations were used in the measurement to reduce the SSA phase-noise floor (dashed line). The floor was estimated from the frequencies

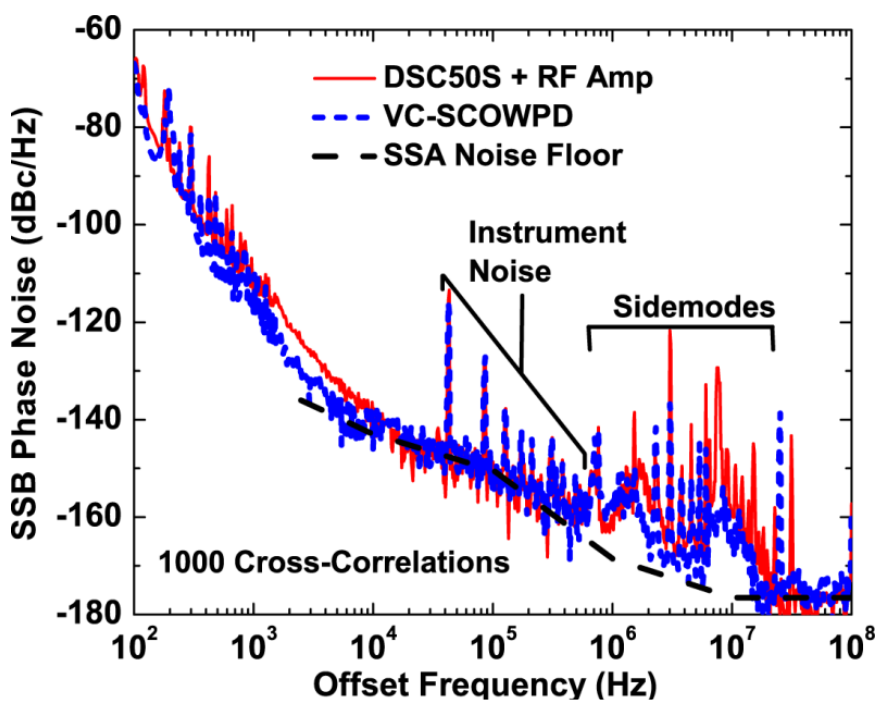

Figure 6-4: Measured phase-noise of a VC-SCOWPD SCOW-COEO system (blue dashed-line) and of a DSC50S + RF amplifier SCOW-COEO system (red line). The phase-noise floor (black dashed line) is also provided.

where cross-correlation averaging improves the phase-noise. The operation photocurrent was 36.2 mA using the VC-SCOWPD configuration and 16.1 mA using the DSC50S + RF amplifier configuration. This corresponds to a SCOWA bias between 1.5-2.0 A. In both cases, the SCOW-COEO is noise-floor limited throughout most of the offset frequency range beyond 15 kHz. For frequencies between 5-15 kHz, only the RF-amplifier-free SCOW-COEO remains measurement limited.

The intracavity powers for each system can be calculated from their respective photocurrents. With 36.2 mA of photocurrent on the VC-SCOWPD and 0.7 A/W responsivity (and using a 80:20 coupling ratio), the average intracavity optical power is ~260 mW. However, with 16.1 mA of photocurrent on the DSC50S and 0.8 A/W responsivity, the intracavity optical power decreases to ~100 mW. The improvement in phase-noise afforded by using a high-power system is reflected in Fig. 6-4. The phase-noise is <-115 dBc/Hz and <-110 dBc/Hz at 1 kHz offset for the VC-SCOWPD and DSC50S + RF amplifier systems, respectively. As we will show later, this improvement in phase-noise is due to a decrease in RIN as the circulating power is increased in the optical cavity. Because COEO oscillation starts from intensity fluctuations, the level of RIN directly impacts the phase-noise of the system, similar to the case of an optoelectronic oscillator (as we saw in Chapters 2 and 3). One additional disadvantage of the DSC50S system is that it requires the use of RF amplification to achieve the necessary gain to oscillate. Although the RF amplifier phase-noise does not limit the measurement here, ~10 W electrical power is required to sustain its operation. Therefore, the removal of the RF amplifier offers significant benefits in SWaP performance.

The sidemodes also improve from <-120 dBc/Hz to <-135 dBc/Hz using the VC-SCOWPD system. These sidemodes occur at harmonics of ~710 kHz corresponding to an effective delay of 280 m. In general, the sidemode levels are slightly larger than that exhibited by the OEO systems measured in Chapters 4 and 5. Note that the spurs at harmonics of 43 kHz and the spur near 20-30 MHz are introduced by the SSA and microwave downconverter. The reduction of sidemode levels results from increased saturation of the semiconductor gain medium. It is well known that saturation of an optical amplifier suppresses the intensity noise at frequencies below the inverse of the gain medium's carrier lifetime [36]. We also experimentally verified the RIN suppression of the saturated SCOWA in Section 6.1. Above the inverse carrier lifetime, the carriers cannot respond to the intensity fluctuations, and therefore the amplifier completely

passes high frequency noise to the output. The beat frequencies at the mode spacing of 710 kHz are too fast for the response times of solid-state or fiber gain media (~ 1 kHz) but are well within the semiconductor gain response time (~10 GHz). As such, it has been reported that use of a semiconductor gain medium in modelocked lasers suppresses the supermode levels by >10 dB [97–99]. Because the gain always saturates to a level near the net intracavity loss, the further the SCOW-COEO optical cavity is operated above threshold, the deeper the SCOWA operates into saturation (resulting in a larger intracavity power). The higher saturation level of the VC-SCOWPD system leads to an enhanced suppression of sidemode oscillation. Note that this suppression mechanism applies to all intensity noise processes below the inverse carrier lifetime of the SCOWA.

In order to provide a complete characterization of the SCOW-COEO system, we next describe our measurements of the oscillator's RF spectrum and output optical pulse train. The configuration used for both of these measurements is again the same as that of Fig. 6-1 with an

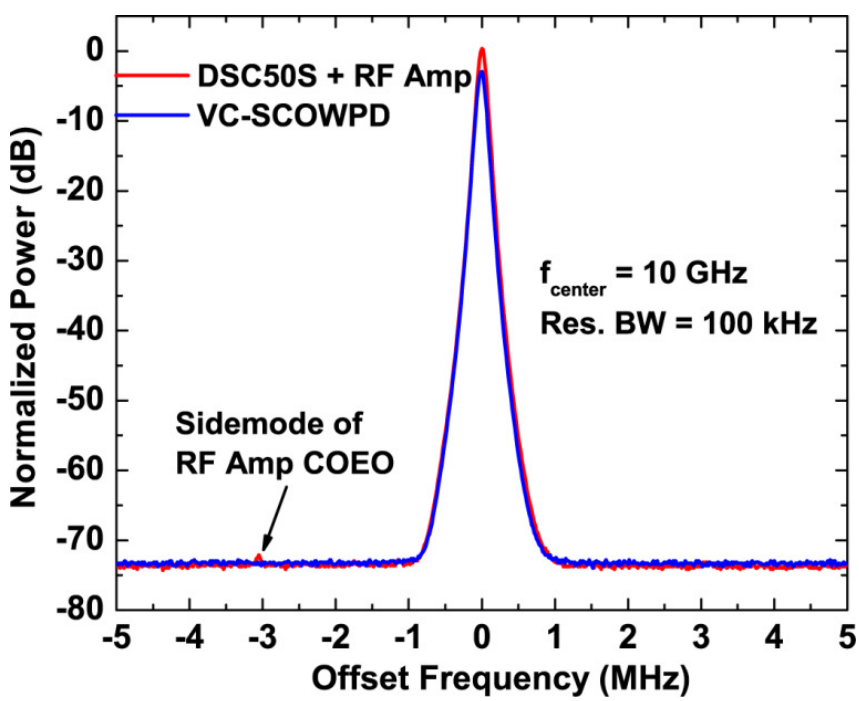

Figure 6-5: Measured normalized RF spectrum of a VC-SCOWPD SCOW-COEO system (blue dashed-line) and of a DSC50S + RF amplifier SCOW-COEO system (red line). The spectrum was centered at 10 GHz with a corresponding resolution bandwidth of 100 kHz.

80:20 coupler and V_π ~ 3.0 V (at 10 GHz) modulator. The RF spectrum is shown in Fig. 6-5 for both the cases of the RF-amplifier-free VC-SCOWPD system and the DSC50S + RF amplifier system. The operation conditions are the same as that of Fig. 6-4. The measured signal powers out of a 10-dB RF coupler are 0.5 dBm and -3.0 dBm (after calibration of losses) with and without RF amplification, respectively. The loss of signal power is due to the lower overall gain of the RF-amplifier-free configuration. Beyond ~1 MHz, the spectrum reaches the noise floor of the measurement system. With the VC-SCOWPD system, the sidemode spurs are below the noise-floor (-73.5 dBm) indicating a measurement-limited sidemode suppression of > 70.5 dB. However, with the DSC50S + RF amplifier configuration, a small sidemode peak (not noise) is visible at ~-3 MHz offset corresponding to a sidemode suppression of ~72.5 dB.

The SCOW-COEO system potentially allows access to both a low phase-noise RF tone and a low-jitter optical pulse train. So far, we have only performed measurements on its electrical output. Our goal now is to detail our characterization of the SCOW-COEO's optical pulse properties. Figs. 6-6 (a) and (b) show the uncompressed and compressed time-domain SCOW-COEO pulse shapes measured using an Agilent Infiniium DCA-J86100C oscilloscope with a 65 GHz Agilent 86116B optical sampling module. The optical output power of ~2 mW was compressed using 60 m of dispersion-compensating fiber (DCF). The compressed pulsewidths

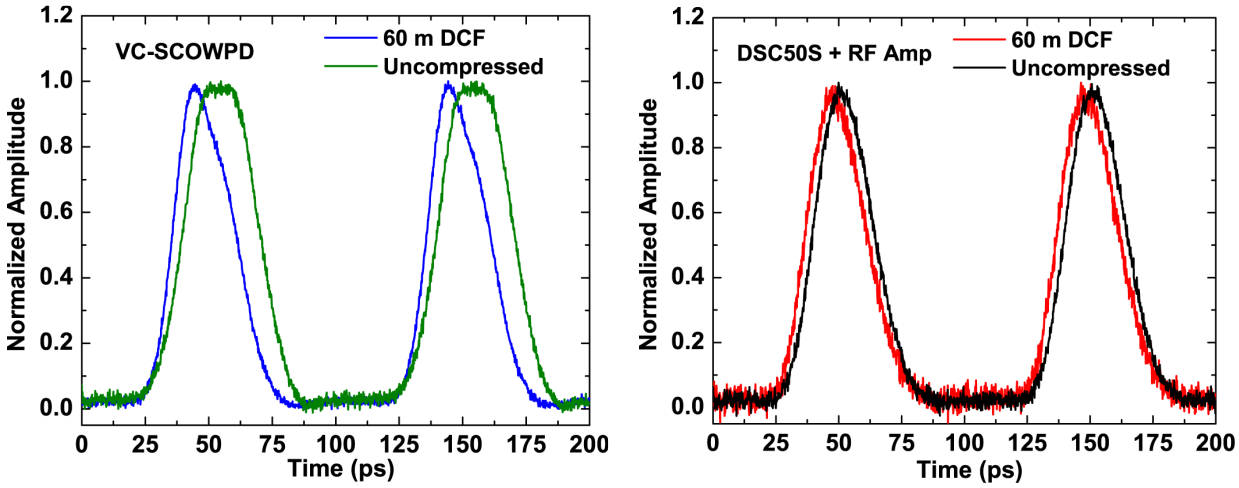

(a) (b)

Figure 6-6: Comparison of the SCOW-COEO optical pulses with and without 60 m DCF compression for (a) the VC-SCOWPD system and (b) the DSC50S + RF Amp system.

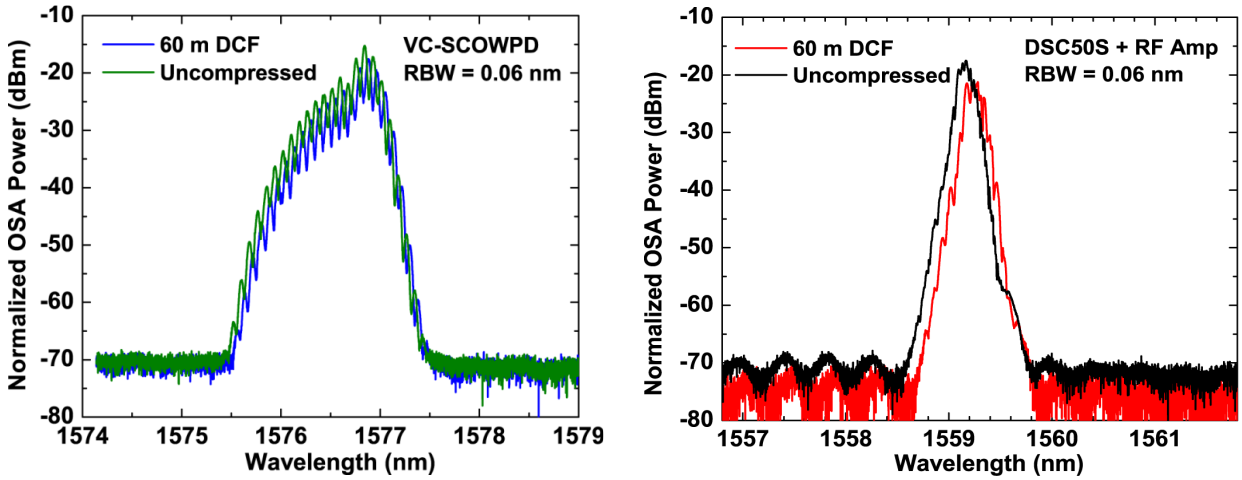

(a) (b)

Figure 6-7: Comparison of the SCOW-COEO optical spectra with and without 60 m DCF compression for (a) the VC-SCOWPD system and (b) the DSC50S + RF Amp system.

using the VC-SCOWPD and DSC50S + RF amplifier systems are both measured to be ~26.8 ps, while the corresponding uncompressed pulsewidths are ~32.2 ps and ~26.2 ps respectively. Note that the amplitudes of the pulses have been normalized to unity.

It is clear that DCF compression provides some benefit towards narrowing the pulse. However, to determine if the resulting pulses are optimal, we measure their corresponding optical bandwidths in Fig. 6-7. Figure 6-7 (a) presents a comparison of the optical spectra for the VC-SCOWPD system with and without 60 m DCF compression. The individual peaks comprising the comb spectrum are spaced by the pulse repetition frequency of 10 GHz. The compressed spectrum exhibits slightly lower optical power across all frequencies before reaching the measurement floor. This decreased power is due to signal attenuation propagating through 60 m of DCF. Other than the difference in optical power and also a slight shift in wavelength (due to variations of the COEO from trial-to-trial), both spectra appear to be identical. Their corresponding bandwidths are estimated to be 0.25 nm. Figure 6-7 (b) shows a comparison of the optical spectra for the SCOW-COEO system that operates off of the DSC50S photodiode + RF amplifier. Their overall shapes are both observed to be abnormal, with their individual comb lines barely resolvable. However, these comb lines must exist as Fig. 6-6 (b) shows the measured scope trace to be periodic. Once again, there is a decrease in optical power for the compressed

spectrum (due to signal attenuation) and also a slight shift in the center wavelength. The uncompressed spectrum exhibits a bandwidth of 0.15 nm while the bandwidth of the compressed spectrum is ~0.17 nm. These minute differences are likely in the noise of the measurement. Note that the origin of the ripples in the noise floor is currently unknown.

From the optical spectrum measurements of the VC-SCOWPD system, we find that the compression provided by the DCF is not optimal as the time-bandwidth product (TBP) is still ~1.8X transform-limited (~0.25 nm spectral bandwidth) assuming a Gaussian pulse-shape (0.44 time-bandwidth product). Longer lengths of DCF fiber were not tested because they were not available at the time of the measurement. For the DSC50S + RF amplifier system, the 60 m DCF fiber introduces additional chirp to the pulses. The corresponding TBPs are ~1.3X and ~1.1X transform-limited when the pulses are compressed and uncompressed, respectively. In this case, linear chirp does not significantly degrade the width of the measured optical pulses. The pulse widths measured compare well to that of other semiconductor-based COEOs but are significantly broader than those achieved by COEOs using either solid-state or fiber-based gain media. The pulse broadening experienced by semiconductor COEOs is usually attributed to nonlinearities of the semiconductor gain medium [100, 101].

6.2.2 SCOW-COEO Comparisons: Constant Intracavity Power

In the previous section, we showed that the performance of the SCOW-COEO improved with the use of a high-power VC-SCOWPD instead of a commercial DSC50S photodiode + RF amplifier. The configuration of the SCOW-COEO was maintained constant (Fig. 6-1) resulting in less intracavity optical power for the DSC50S + RF amplifier system (100 mW) compared to the VC-SCOWPD system (260 mW). In this section, we perform an alternative set of measurements where we keep the intracavity power as a constant between both systems. Figure 6-8 shows the measured phase-noise performance of a DSC50S + RF amplifier system using a 90:10 output coupler in the optoelectronic loop. The 90:10 coupler changes the distribution of power between the optical and optoelectronic cavities. Also shown in Fig. 6-8 is the comparison phase-noise of the previous VC-SCOWPD RF-amplifier-free SCOW-COEO system (80:20 coupler). Figures 6-8 (a) and 6-8 (b) differ primarily in measurement noise-floor

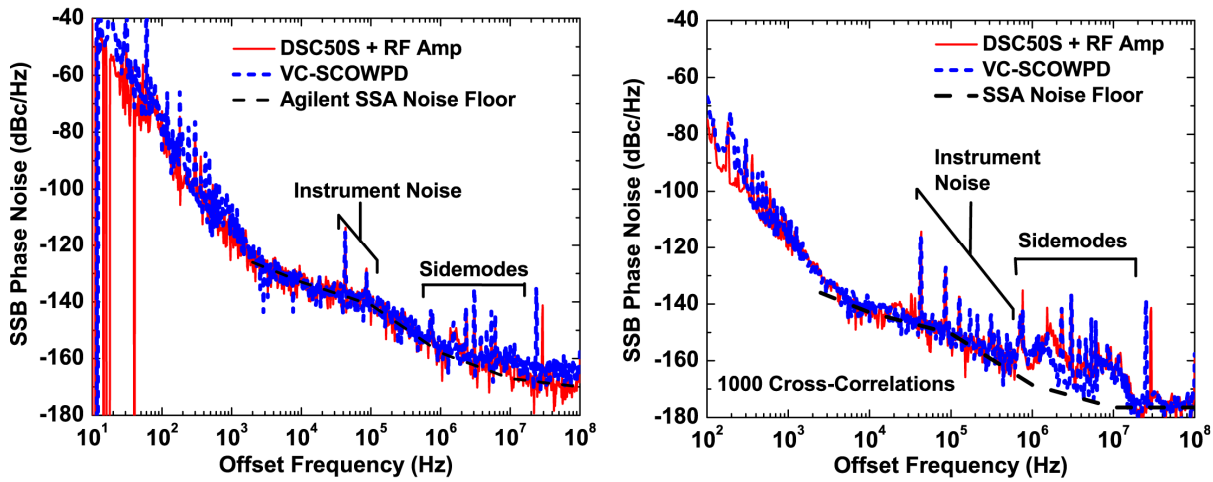

(b) (b)

Figure 6-8: Measured phase-noise of a DSC50S + RF amplifier SCOW-COEO system (red line) using a 90:10 coupler (a) without cross-correlation averaging and (b) with 1000 cross-correlation averaging. The measured phase-noise of the VC-SCOWPD system (80:20 coupler) is also shown for comparison (blue dashed-line). The measurement noise-floor is indicated by the black dashed-line.

and offset frequency range. In Fig. 6-8 (b), one-thousand (1000) cross-correlation averaging was used in order to reduce the system noise-floor. The offset frequency range was correspondingly reduced to prevent long averaging times (>10 minutes). The DSC50S system was operated at 21.9 mA average photocurrent yielding an intracavity optical power of ~270 mW, which is now close to that of the VC-SCOWPD system (260 mW). The measured phase-noise of the two systems compares well with each other (<-115 dBc/Hz at 1 kHz offset) and to other high-performance COEOs found in literature [11, 94, 95]. Furthermore, the sidemode levels are similar (<-135 dBc/Hz) as the intracavity power and saturation of the gain medium are comparable between the two systems. Note that photodiode amplitude-to-phase (AM-PM) noise conversion was not a limitation in any of our measurements. Typically, a photodiode must be operated at the photocurrent of zero conversion slope to prevent degradation from AM-PM noise processes [37, 102]. In general, the AM-PM null is dependent on the operating frequency and also on the characteristics of the waveform (modulated, pulsed, etc). We have measured this null for a modulated source and find no significant change when operated near its vicinity. We also

have experimentally swept the SCOW-COEO operation across multiple values of photocurrent to again verify no sudden change in performance.

In Chapters 4 and 5, we found that the sidemodes levels for an OEO degraded when an RF amplifier was introduced into the cavity. This degradation was largest for the sidemodes closest to the carrier (~135 kHz offset frequency), while the sidemodes farther away (~1 MHz offset frequency) appeared unaffected (see. Fig. 4-16). In contrast, here we observe no significant difference in the measured SCOW-COEO sidemodes with and without RF amplification. One possible explanation for this is that the sidemodes for the SCOW-COEO are naturally farther away from the carrier (5× shorter delay) and thus experiences less degradation from effects of RF amplification. This hypothesis can potentially be tested by increasing the delay length of the COEO while simultaneously monitoring the levels of the sidemodes. However, in practice, the proposed experiment is difficult to perform as the COEO becomes highly unstable at longer delay lengths. We will show a measurement of the SCOW-COEO's instability operating at an intracavity delay of 560 m in Section 6.2.4. Another possible explanation is that the SCOW-COEO's operation is intrinsically different from that of the SCOW-OEO and thus behaves differently under RF amplification. In Fig. 4-16, we observed that only the sidemodes (which are located at the frequencies coherent to the cavity) and not their surrounding noise were affected by the RF amplifier. In the SCOW-COEO, neither set of sidemodes (of the optical or optoelectronic cavity) is completely coherent within the system. Therefore, it is plausible that the sidemode degradation mechanism due to an amplifier may be fundamentally absent in a COEO system.

In Fig. 6-8, we observed that the COEO with larger intracavity optical power performed with lower phase-noise. The intracavity power is inherently related to the Q of the optical cavity. In steady-state, the gain provided by the optical amplifier must saturate close to but less than the level of total loss. The closer the saturated gain is to the level of loss, the higher the Q of the optical cavity and the larger the oscillator's circulating power [4, 29]. We next perform a set of experiments in order to specifically assess the dependence of COEO phase-noise on optical power. Figure 6-9 shows the phase-noise of the COEO as the intracavity optical attenuation is varied using a power-monitoring variable optical attenuator (VOA). The absolute level of loss added to the cavity is not known for certain as we can only monitor the intracavity power during

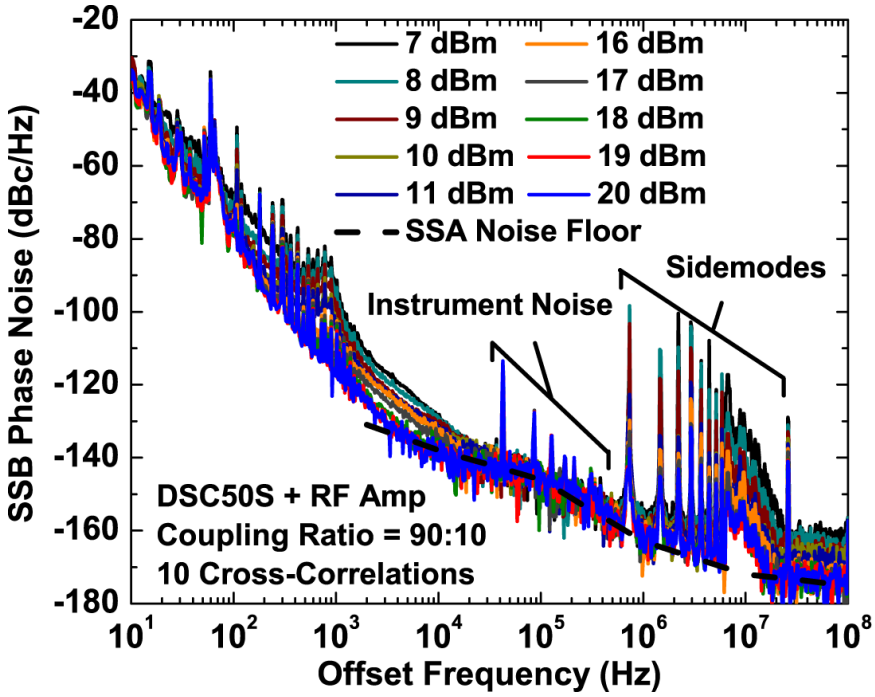

Figure 6-9: Measured phase-noise of a 90:10 output coupler DSC50S + RF amplifier SCOW-COEO system with varying intracavity optical power. The intracavity power was varied across two measurement trials (Trial 1: 7-11 dBm and Trial 2: 16-20 dBm).

the measurement. Our later calibrations, however, indicated that generally every 0.5 dB change in attenuation yields ~1 dBm change in optical power. Loss affects the signal during every roundtrip and thus greatly influences the cavity's optical power. In our experiments, attenuation levels corresponding to intracavity powers between 7 dBm and 20 dBm were tested as shown in Fig. 6-9. The tests were split over two trials (7–11 dBm) and (16–20 dBm) as we found mode hopping if the cavity was detuned too far from its initial operating point. For this measurement, we used the configuration of the SCOW-COEO comprising a DSC50S photodiode + RF amplifier with a 90:10 output coupler in the optical loop.

As expected from our previous discussion, we find the cavity Q to significantly affect the phase-noise performance of the SCOW-COEO. Figure 6-9 shows that with decreasing Q (increasing attenuation and decreasing intracavity power), both the phase-noise and the sidemode levels increase. The variation in phase-noise is as high as 14 dB near 2-kHz offset, while the

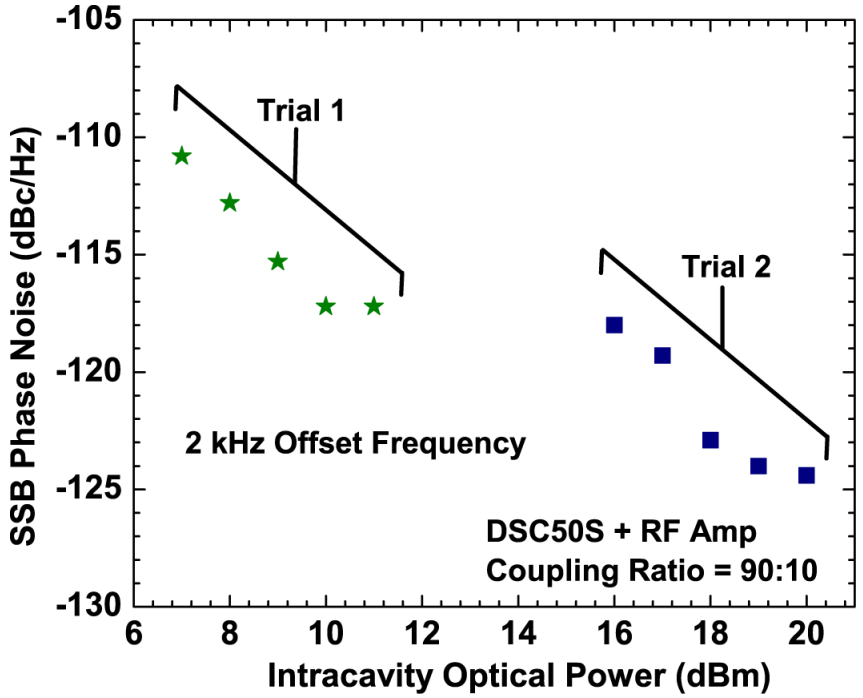

Figure 6-10: Measured phase-noise of a 90:10 output coupler DSC50S + RF amplifier SCOW-COEO system at 2-kHz offset frequency as a function of intracavity power. The intracavity power was varied across two measurement trials (Trial 1: 7-11 dBm and Trial 2: 16-20 dBm).

maximum variation in sidemode spurs is ~40 dB. Note that the apparent increase in phase-noise beyond 20 MHz (past the RF filter bandwidth) is an artifact of the SSA's degradation in minimum sensitivity when the input RF power becomes too low. At low frequencies (f < 100 Hz), we believe the COEO to be affected by noise that is common to all attenuation levels, such as noise due to modelocking instabilities or to the environment. Figure 6-10 shows the measured phase-noise at 2-kHz offset frequency as a function of the intracavity optical power. As expected, the measurements indicate a trend of decreasing phase-noise with increasing optical power. Finally, we have also performed experiments varying the bias current of the optical amplifier and also varying the coupling ratio in the optical loop that yielded similar results to that of Fig. 6-9.

6.2.3 SCOW-COEO Open-Loop Measurements

From our discussions of the previous section, it is clear that the Q of the optical cavity significantly impacts COEO phase-noise. However, we have not yet explained the relationship between the two. The case of the COEO is particularly difficult to analyze as any modification to the electrical or optical loops affects both cavities.

To address these issues, we perform two separate experiments on the SCOW-COEO that evaluates the impact of Q when the operations of the individual cavities are isolated. Of particular interest in this investigation is the role of the 'Q-enhancement effect' on the phase-noise of a COEO [9, 94, 103]. The Q-enhancement refers to the filtering of the RF signal by the optical cavity and can be most easily understood by breaking the electrical loop between the output coupler and modulator input in Fig. 6-1. A test RF input is applied into the modulator terminal and the electrical response at the output of the RF coupler is observed. The optical cavity only allows modelocking at frequency multiples of the mode spacing and rejects modulation at frequencies outside the modelocking bandwidth. Thus, we expect that certain frequency ranges of the input signal will become filtered by the optical cavity response. This picture agrees with our equivalent oscillator circuit in Fig. 6-2. The Q-enhancement effect has been characterized previously using S21 measurements to probe the electrical input-output relation of a COEO [94]. We have also performed S21 measurements on the SCOW-COEO (using DSC50S + RF amplifier) and found agreement only when both the electrical probe signal is small and the optical cavity is operated slightly above threshold. Ideally, a pump-probe experiment should be conducted with a large signal setting the modulation of the modelocked laser and a small signal probing the response of the cavity to noise perturbations. In practice, we found this measurement difficult to perform because the leftover pump signal power becomes comparable to that of the probe even after filtering.

In our next two tests, we adopt a similar strategy to that of the S21 measurements and break our electrical cavity between the photodiode output and the RF phase shifter (Fig. 6-11). We apply a 5 dBm RF tone to the RF amplifier input so that the optical cavity is modelocked at a level similar to the operating point of the COEO. We then evaluate the output of the photodiode in terms of phase-noise and amplitude-noise performance and compare these measurements to

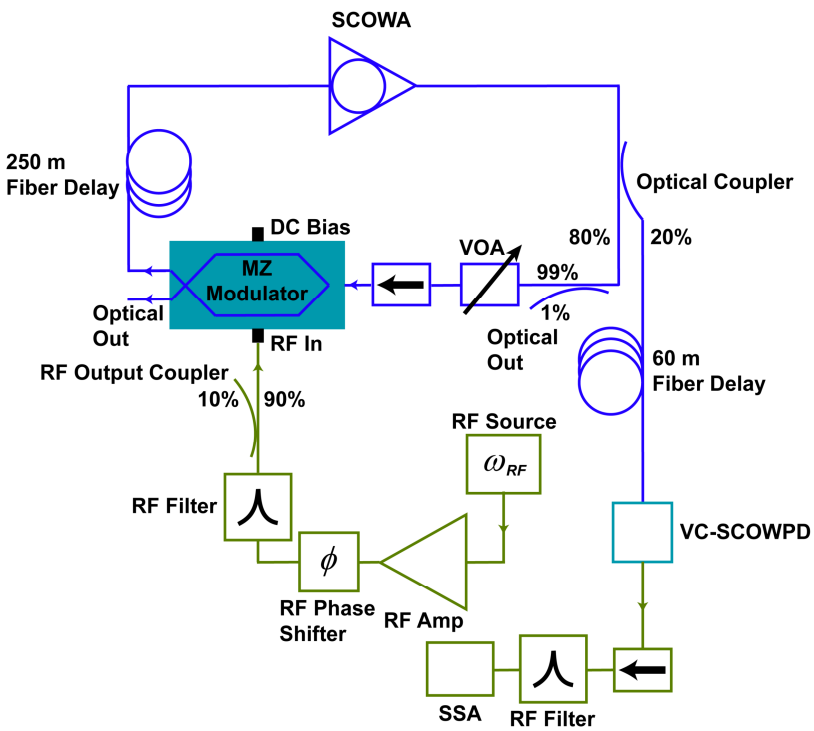

Figure 6-11: Schematic of the system used to probe the S21 response of the SCOW-COEO's optical cavity. The operating conditions of the individual components are maintained at their levels during COEO operation.

the noise of the RF source. Through this comparison, we can directly assess the filtering of the source's noise by the response of the optical cavity. Furthermore, by varying the attenuation of the optical cavity, we can also investigate the effects of optical cavity Q on the SCOW-COEO's open-loop response. The phase-noise and amplitude-noise measurements at the output of the photodiode are shown in Figs. 6-12 and 6-13 along with the corresponding noise of the reference source. Note that the output of the photodiode passes through a 20 MHz bandwidth RF filter (Fig. 6-11) to prevent power at higher order beat products from reaching the SSA. For our comparisons, we have also applied the same filter to the output of the RF source.

In Fig. 6-12, we vary the intracavity optical power (4 dBm to 20 dBm) by adjusting the attenuation of a VOA and measure the resulting phase-noise at the output of the photodiode. Similar to before, every 0.5 dB change in attenuation generally yields ~1 dB change in circulating power. The sidemodes clearly increase as attenuation is increased; however, the

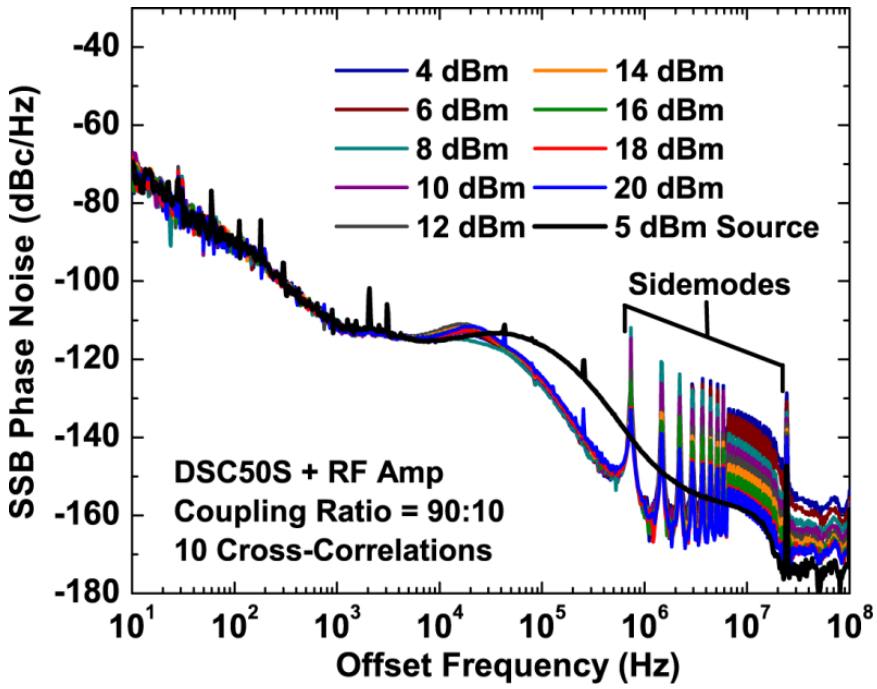

Figure 6-12: Measured open-loop phase noise of a 90:10 output coupler DSC50S + RF amplifier SCOW-COEO with varying intracavity optical power. Also provided is the noise of the reference RF source (black line) used as the probe for this measurement.

phase-noise at all other frequencies appears to be unaffected. The increase in sidemode levels at lower power is again due to a decrease in amplifier saturation. The RIN of the amplifier represents the injected noise and thus adds to both the phase-noise and amplitude-noise of the photodetected RF output. It is clear from Fig. 6-12 that the residual phase-noise added by the SCOWA is far below the phase-noise of the RF source. It is worth noting that none of the measurements taken were limited by the noise-floor of the SSA.

Furthermore, from the measurements in Fig. 6-12, we observe that the phase-noise of the optical pulse train follows that of the RF source until ~20 kHz offset. Beyond this frequency range, the source phase-noise becomes filtered by the optical cavity response. We find that the filtering effect of the optical cavity appears to contribute negligibly to the COEO's low-frequency phase-noise performance. In fact, the filtering of RF source noise is well-known in the modelocked laser literature [104, 105], and the filter frequency depends primarily on the length of the optical cavity. In addition to a filtering effect, the dispersion through a resonant system

generates additional group delay during signal propagation. From Figs. 6-4, 6-8, and 6-9, we see that this additional delay is also negligible as the sidemode frequencies (~710 kHz) are in agreement with the total expected delay of the system. The negligible effects of Q-enhancement on the COEO's performance agree with phase-noise measurements of a high-performance slab-coupled optical waveguide optoelectronic oscillator (SCOW-OEO) discussed in Chapter 4. The SCOW-OEO demonstrates ~-65 dBc/Hz phase-noise at 10 Hz offset for a 1.5 km length cavity, while the SCOW-COEO demonstrates ~-50 dBc/Hz at 10 Hz with a delay-length of ~310 m (Fig. 6-8 (a)). The phase-noise scaling is nearly 1/(delay time)^2 as according to theory.

Figure 6-13 shows the amplitude-noise spectrum tested with the same configuration and intracavity optical power range (4 dBm to 20 dBm) used in Fig. 6-12. Despite the limitation of the SSA noise-floor, it can be seen that the amplitude-noise generally decreases as the optical power increases towards +20 dBm. At lower intracavity powers, the amplitude-noise rises above that of the RF source due to the RIN of the SCOWA. In comparison to the phase-noise case, the

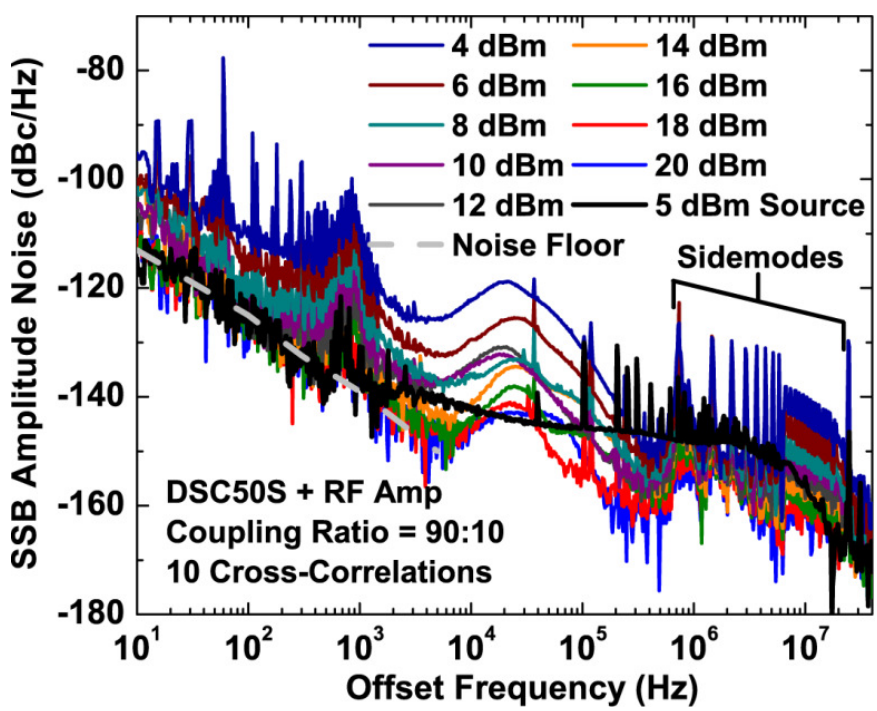

Figure 6-13: Measured open-loop amplitude noise of a 90:10 output coupler DSC50S + RF amplifier SCOW-COEO with varying intracavity optical power. The noise of the reference RF source (black line) and measurement noise-floor (gray dashed-line) are also provided.

added noise of the SCOWA can clearly be seen over the amplitude-noise of the RF source. This is in part due to the significantly lower amplitude-noise component of the RF source and also due to the higher sensitivity of the SSA's amplitude-noise measurement. The RIN of the optical amplifier decreases as the saturation of the amplifier increases. In the steady-state, the gain in the optical cavity must saturate to a level close to the total loss. With lower intracavity loss, the amplifier's saturation increases and thus its RIN decreases. This reduction in RIN directly reduces the amplitude-noise added to the RF source, as can be seen in Fig. 6-13 for higher intracavity optical powers. Near 1 kHz offset, the measurable amplitude-noise (at higher optical powers) appears to decrease below that of the RF source. This is due to the suppression of the source's intensity-noise by optical amplifier saturation. The sidemodes decrease at higher intracavity powers in agreement with the measured phase-noise spectrum of Fig. 6-12. Although not explicitly shown here, we observed that both the measurements of Fig. 6-12 and Fig. 6-13 are insensitive to the RF source over a wide range of input power levels.

Based on these results, we conclude that the degradation of SCOW-COEO phase-noise in

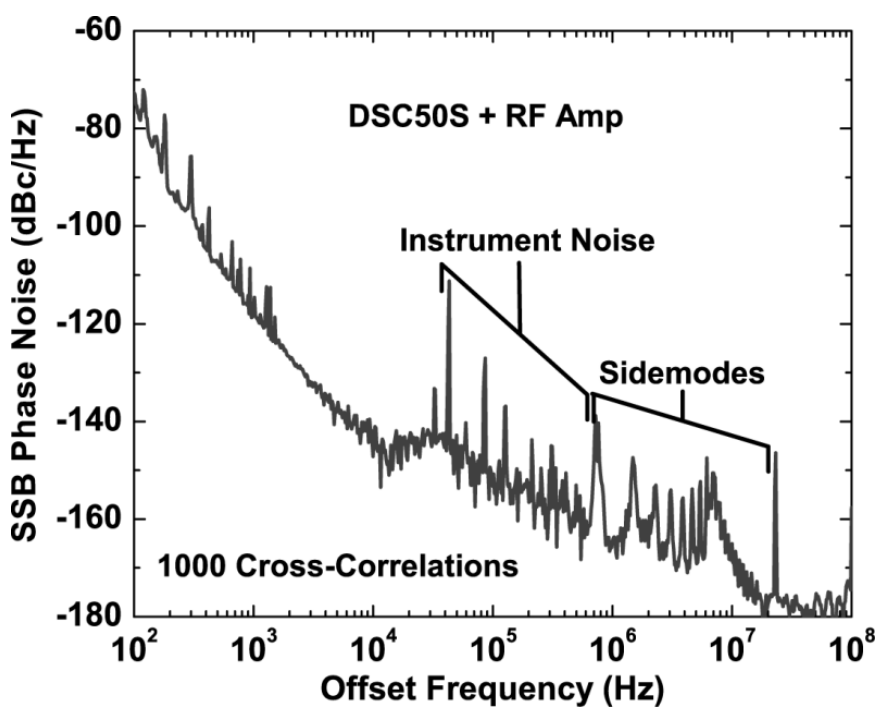

Figure 6-14: Measured phase-noise of a VC-SCOWPD SCOW-COEO system exhibiting a resonance near 30 kHz. The phase-noise floor (black dashed-line) is also provided.

Fig. 6-9 is due to the increase of SCOWA RIN when the Q of the optical cavity is decreased. The oscillation of a COEO initiates from an intensity fluctuation, which must have random phase. Once oscillation is reached, further injection of incoherent RIN on top of a coherent RF signal results in broadening (amplitude and phase) of the RF spectrum. Therefore, the optical amplifier RIN of a single roundtrip is critical to the phase-noise performance of a COEO. The increase in RIN with decreasing optical cavity Q cannot be observed in the phase-noise of Fig. 6-12 over the noise of the RF source. However, Fig. 6-13 clearly shows the degradation of RIN with cavity attenuation. The overall situation is analogous to a CW laser operating above threshold. As the bias is increased, the spontaneous emission becomes clamped while the majority of the power shifts into the oscillating mode. As such, the RIN decreases due to a reduction in the ratio of signal×spontaneous to signal× signal. In addition, the saturation of the gain medium further acts to suppress intensity noise effects. Before concluding this section, we wish to mention that the noise resonance located near 20 kHz offset in Fig. 6-13 is due to amplitude-noise resulting from timing differences between the RF source and the filtered optical pulse train [105]. Frequently, this noise also appears in the measurements of SCOW-COEO phase-noise (Fig. 6-14 near 30 kHz). In such cases, we usually tune the RF phase shifter to optimize the COEO around a different operating frequency. Note that this noise feature also appears in the measured COEO phase-noise (Fig. 4) of Ref. [11] and in the measured phase-noise of Ref. [95].

6.2.4 SCOW-COEO Optimization

In the previous sections, we presented the performance of our SCOW-COEO in its optimized configuration. Here, we will show the impact when the SCOW-COEO is slightly modified from this optimal geometry. It is our hope by the end that the reader will gain an appreciation for the complexities that arise from a coupled-cavity system. This section will also serve to highlight our optimization procedure that ultimately resulted in the configuration of Fig. 6-1.

We will first examine the impact of the optical delay used in the optoelectronic loop, comparing the optimized case of 60 m to two other cases of 21 m and 81 m. The optical delay length of the loop controls the Vernier between the optical and optoelectronic cavities, and thus is expected to influence the single-mode behavior of the COEO. Figures 6-15 (a) and (b) show these comparisons with the 60-m case kept constant in both plots. The photocurrent was

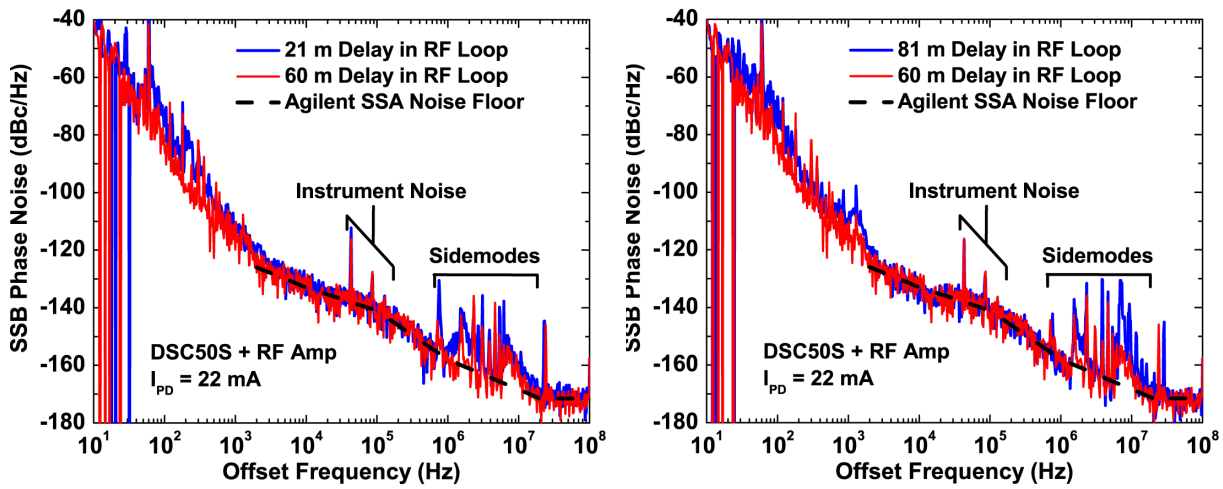

(a) (b)

Figure 6-15: DSC50S + RF amplifier SCOW-COEO phase-noise comparison for delays lengths of (a) 21 m and 60 m and (b) 81 m and 60 m delay in the optoelectronic loop. The measurement noise-floor (black dashed-line) is also provided.

maintained at 22 mA for each measurement. The general trend in Fig. 6-15 is that both the phase noise and sidemodes appear to be lowest for a delay of 60 m in the optoelectronic loop. Other delays were also tested but are not shown here as the data was not saved at the time of measurement. We will note however that the OEO behavior was highly unstable when this delay approached zero.

We next examine the operation of the SCOW-COEO as a function of the coupling between the optical and optoelectronic cavities. In the optimized version of the DSC50S+ RF amplifier SCOW-COEO presented in the previous sections, this coupling ratio was 90% into the optical cavity and 10% into the optoelectronic cavity. We showed experimentally in Fig. 6-4 the degradation in performance incurred when an 80-20 coupler is used. Our goal here is to evaluate the SCOW-COEO phase-noise as we vary the coupling ratio across a spectrum of values. This measurement is shown in Fig. 6-16 for coupling ratios ranging from 90:10 (the base case) to 30:70 in increments of 10%. The photocurrent was maintained at 19 mA for each of these trials.

From Fig. 6-16, it is clear that a large performance advantage is gained when the majority of the optical power is kept within the optical cavity. Both the phase noise and sidemodes degrade

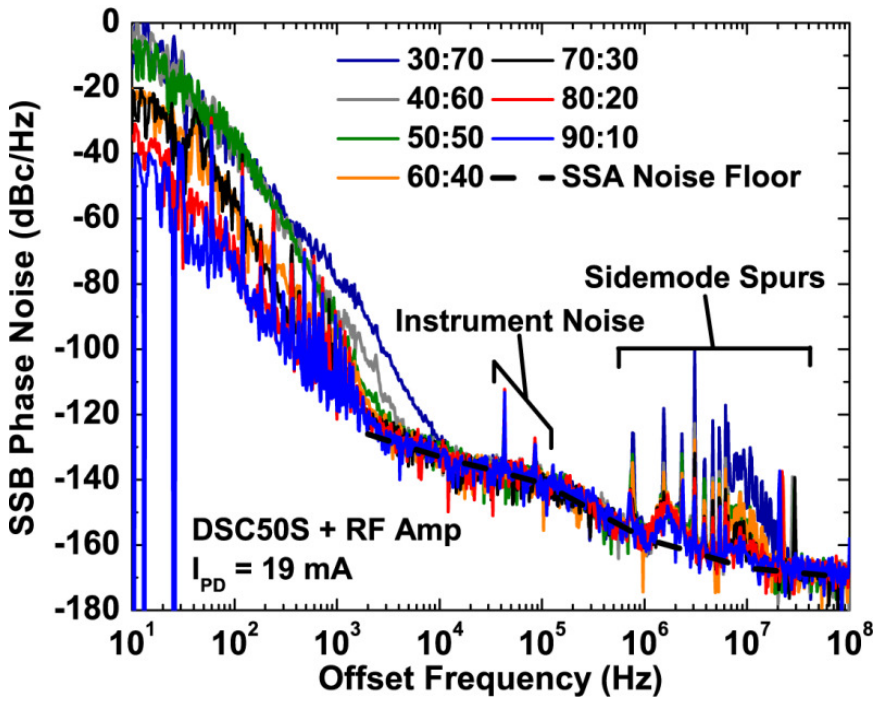

Figure 6-16: Measured DSC50S + RF amplifier SCOW-COEO phase-noise as a function of the coupling ratio between optical and optoelectronic cavities. The measurement noise-floor (black dashed-line) is also provided.

significantly when the coupling is near 30:70. In the previous section, we showed that the SCOW-COEO phase-noise is largely dependent on the losses within the optical cavity. With larger loss, the RIN added by the optical cavity degrades relative to the signal level. The situation here is even worse as not only is there additional loss due to the output coupling, but now this lost power is redirected towards the photodiode. If the photodiode is to be maintained at a specific photocurrent (or can only handle a specified value of photocurrent), this means that the SCOWA must be biased lower to compensate for the increase in coupling. This reduction of the SCOWA bias further acts to degrade the RIN of the optical cavity. Note that the RIN for a general laser improves with bias both due to intensity noise suppression from amplifier saturation and due to a decrease in the signal×spontaneous product relative to signal× signal. The result is a strong dependence of the SCOW-COEO performance on the coupling ratio used.

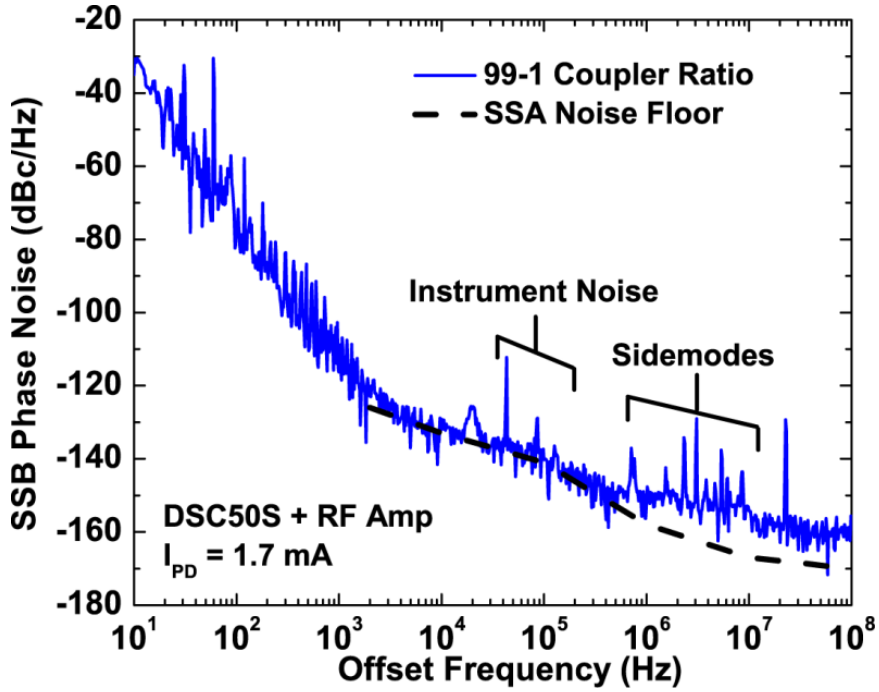

Figure 6-17: Measured DSC50S + RF amplifier SCOW-COEO phase-noise for a coupling ratio of 99-1 between optical and optoelectronic cavities. The measurement noise-floor (black dashed-line) is also provided.

The preceding analysis suggests that performance benefits may be gained from using a coupler which retains almost all of the optical power within the optical cavity. However, as the coupling ratio increases beyond 90:10, the oscillation condition becomes more difficult to achieve. For example, comparing a 99:1 coupler to a 90:10 coupler, the photocurrent would decrease by a factor of 10 resulting in a 20 dB decrease in RF gain. Ideally, the SCOWA should be operated at a higher bias so that a high intracavity power can be maintained while the optical power coupled out is increased. However, this would require ~2 W intracavity power to reach photocurrents ~20 mA. When the optical power available becomes a limitation, additional RF amplification would then be required to achieve net gain. Fig. 6-17 shows the performance of a SCOW-COEO that uses a 99:1 coupler. The photocurrent was 1.7 mA, and thus a second identical RF amplifier (G = 14 dB, P_{sat} = 28 dBm) was employed to achieve oscillation.

At low frequencies (<1 kHz), the phase-noise levels are comparable to that of the 90-10 coupling ratio SCOW-COEO shown in Fig. 6-16. Thus, there appears to be little advantage

gained in increasing the coupling ratio further. One reason for this is because the improvements in optical cavity loss become negligible compared to the other losses in the system. Furthermore, since the SCOWA bias current was maintained constant, both the intracavity optical power and the saturation level of the SCOWA do not change. The measured photocurrent was 1.7 mA here compared to 19 mA for the 90:10 coupler. The ratio of photocurrents is nearly 1:10 as expected if the intracavity power was kept constant. The SCOWA bias of 1.9 A can potentially be increased further to gain additional benefits of higher optical power. However, we did not go beyond 2.5 A in any of our measurements in order to prevent the SCOWA from being overly stressed. This SCOWA was the only of its kind exhibiting 30 dB gain and 400 mW in a packaged configuration. At higher offset frequencies, the phase noise becomes limited by shot noise and thus no longer reaches the same floor as it did in the measurements of Fig. 6-16.

We now consider one more potential approach to improving the SCOW-COEO phase-noise. This approach relies on using a longer delay, which was the foundation behind the concept of the

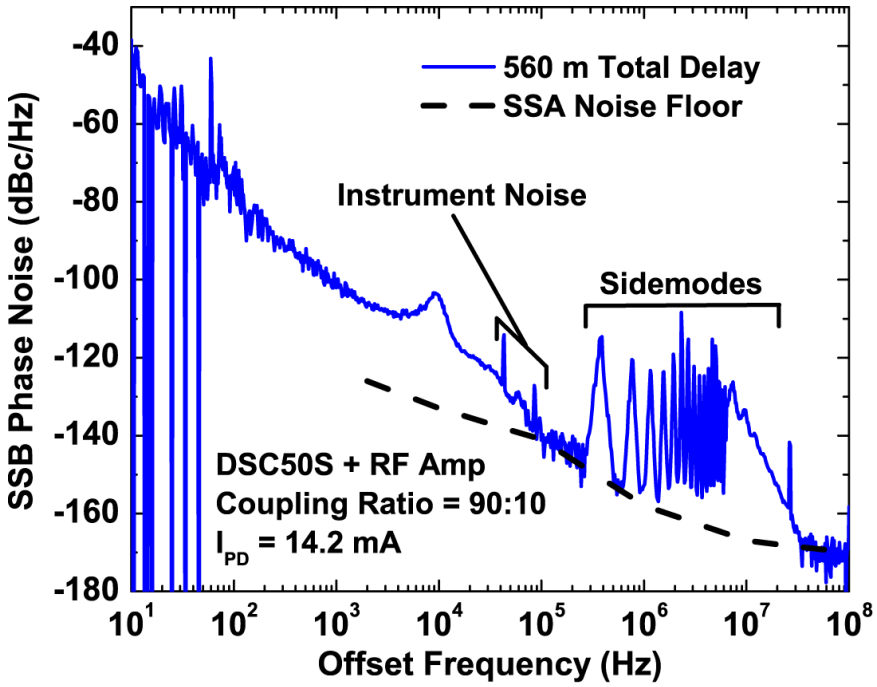

Figure 6-18: Measured DSC50S + RF amplifier SCOW-COEO phase-noise for a delay of 500 m in the optical loop and a delay of 60 m in the optoelectronic loop. The measurement noise-floor (black dashed-line) is also provided.

OEO in Chapter 4. Figure 6-18 shows the DSC50S + RF amplifier SCOW-COEO phase-noise with 500 m of delay in the optical loop and 60 m of delay in the optoelectronic loop. The SCOWA was operated at 1.7 A for this measurement yielding a photocurrent of 14.2 mA with a 90:10 coupling ratio. The sidemodes grow and appear at harmonics of 380 kHz corresponding to an effective delay of 525 m. The growth of the sidemodes is related to the inability of the Vernier effect to suppress the sidemode oscillation. That is, as the sidemode frequencies of one cavity become more and more finely spaced, it becomes more and more difficult to establish decoherence with the other cavity. As a result, the operation of the SCOW-COEO becomes unstable. It can be seen from Fig. 6-18 that the phase noise at higher offset frequencies (>100 Hz) degrades significantly compared to that of the optimized SCOW-COEO of Fig. 6-8. This sets an upper bound on the maximum delay length that can be practically implemented in a COEO. With a narrow enough RF filter, the sidemodes can be effectively eliminated, potentially extending the limits of delay length.

6.3 Conclusions

We have shown the operation of a high-performance RF-amplifier-free SCOW-COEO [106] operating at 10 GHz with low phase-noise (<-115 dBc at 1 kHz offset) and large sidemode suppression. The output optical pulses after compression were ~26.8 ps in width corresponding to 1.8X the transform-limit for a Gaussian pulse-shape. Furthermore, we found that the COEO phase-noise performance degrades significantly with attenuation in the optical cavity. Separate measurements probing the optical cavity response show this performance loss to be due to an increase in its output RIN. The Q enhancement provided by the coupled cavity configuration does not appear to contribute significantly to the performance of the COEO.

We have also illustrated the performance of the SCOW-COEO when its operating parameters are not at their optimum values. For example, we examined the case of deviations in the optoelectronic loop delay and showed the best sidemode suppression when an additional delay of 60 m was added to the cavity. We also demonstrated that the SCOW-COEO operation varied dramatically with the coupling ratio between the optical and optoelectronic cavities. These effects were mainly a consequence of the intracavity optical power with lower phase-noise being

achieved for higher optical powers. Finally, we showed the SCOW-COEO phase-noise and sidemode suppression to degrade for longer delay lengths (560 m). At these lengths, the SCOW-COEO is observed to operate on the edge of instability.

Chapter 7

Slab-Coupled Optical Waveguide Distributed Feedback Lasers (SCOW-DFBs)

The slab-coupled optical waveguide optoelectronic oscillator (SCOW-OEO) demonstrations of Chapter 4 consisted of large discrete components connected in a resonant configuration to achieve low-noise oscillation at 3 GHz. It is desirable that these components be integrated together so that a compact system can be realized. The first step is to miniaturize the pump laser which provides the microwave-photonic gain necessary for oscillation. It is desirable that this laser source have low relative intensity noise (RIN) near the performance level of the SCOW external cavity laser (SCOWECL) [~-120 dBc/Hz at 10-Hz offset] so that the noise injection can be made low. Related to this, it is also beneficial for the laser to operate single mode and with a damped relaxation oscillation response. Fortunately, the linewidth of the laser does not significantly impact the SCOW-OEO's operation as long as the accumulated chromatic dispersion is maintained at low levels. The output power of the laser source should also be larger than 200 mW so that the SCOW-OEO can reach oscillation without the need for additional optical or RF amplification.

To achieve these performance targets, we propose to apply the SCOW concept to conventional implementations of monolithic single longitudinal mode lasers. The single mode operation is usually obtained by virtue of frequency selective feedback within the optical cavity. The basic principle is to reduce the threshold gain for only one mode such that its threshold dominates the operation of the laser. Once the lasing threshold is reached, nominally all additional supplied power is consumed by the strongest mode. In this way, even a small amount of gain differential between modes is enough to yield large sidemode suppression.

In our laser design, we use etched semiconductor gratings to provide the frequency selective feedback necessary for single mode operation. These gratings provide coherent reflection of the optical mode if the frequency satisfies the 2π roundtrip phase condition within a grating period. For a first-order grating at 1550 nm, the next wavelength which satisfies this requirement occurs

at 775 nm. This wavelength is far outside the amplification bandwidth of the semiconductor gain, and thus only one mode has enough gain to oscillate.

The two primary designs of grating-based lasers reported in the literature are known as distributed feedback (DFB) and distributed Bragg reflector (DBR) lasers. In a DFB structure, the gain and grating sections overlap so that both amplification and reflection is achieved simultaneously as the mode propagates through the optical cavity. Alternatively, in a DBR structure, the grating forms a mirror at one or both ends of the laser cavity confining the mode to the centrally located semiconductor gain. Both designs have their own relative merits with simplicity and compactness usually favoring the DFB structure. However, one disadvantage of a DFB is that its standard structure allows for emission out of both facets, and thus half the laser power becomes inaccessible. A second important drawback is that the wavelength which satisfies the Bragg 2π phase condition is exactly antiresonant with the optical cavity. A cavity formed between any two grating boundaries will always result in an odd multiple of π phase shift during roundtrip propagation. As a result, the lasing becomes degenerate for the family of modes on either side of the Bragg wavelength. This mode degeneracy can be avoided from the use of a quarter-wave shift within the DFB grating structure. However, this requires additional fabrication complexity and does not solve the issue of the loss in collected output power. Both drawbacks can be simultaneously avoided by using high-reflection (HR) coatings for one facet of the DFB. However, this comes at the disadvantage of device yield, as we will discuss later.

In contrast to the DFB grating, DBR gratings allow for separate tuning of the grating mirrors, thereby enabling control of the operation wavelength. Besides complexity, the major disadvantage of DBR lasers is the required additional grating length in order to select a single longitudinal mode. The longer the gain section, the longer the grating must be to filter the sidemodes. For a 1 cm length gain section, the grating can effectively add ~1-10 mm to the overall chip length. In this thesis, we choose to demonstrate SCOW lasers operating in the DFB configuration primarily due to its inherent simplicity. We note that SCOW-DBR structures can also be readily realized with a re-optimization of the device and grating length. This chapter will describe the design, fabrication, and measurement results of low-confinement slab-coupled optical waveguide distributed feedback lasers.

7.1 Design of First Generation SCOW-DFB

Here, we describe our considerations for the design of high-power SCOW-DFB lasers. We first present a brief overview regarding the operation of a grating along with a summary of the relevant equations governing grating performance. We apply these equations to the analysis of the SCOW-DFB in order to specify the relevant parameters of the grating structure. BeamPROP simulations were carried out to optimize the grating strength (via its corrugation height) while maintaining single transverse mode behavior throughout the structure. In the following sections, specific attention will be paid toward designing for high power operation in a single transverse mode and over long semiconductor cavities.

7.1.1 Overview of DFB Grating Operation

Gratings in a laser structure represent periodic variations in the refractive index (real or imaginary) that result in coherent reflection of the optical wave over each period. Figure 7-1 shows an example of a grating stack from the perspective of an incident beam of light. The grating consists of alternating layers of dielectric material with refractive indices n_1 and n_2. The

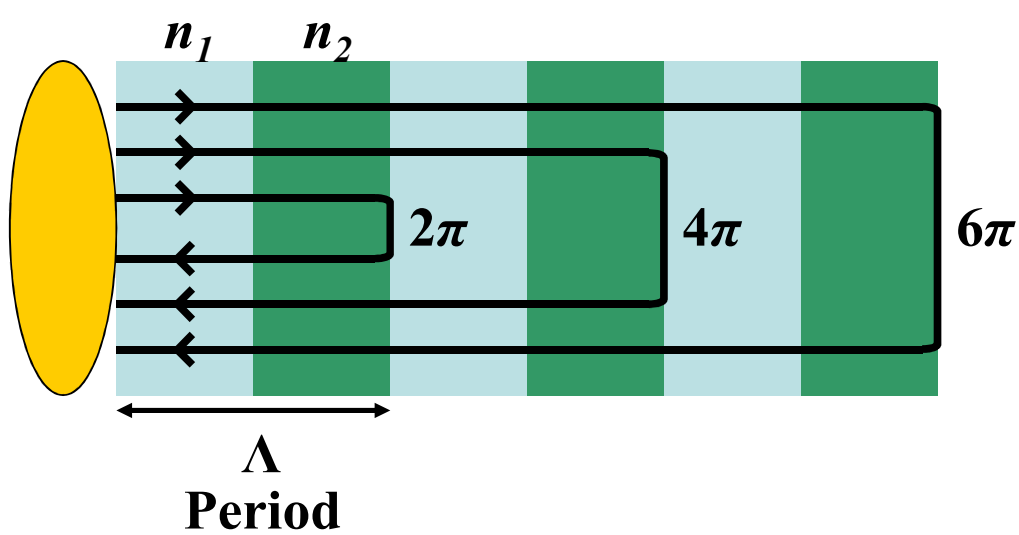

Figure 7-1: Grating structure from the perspective of the light beam consisting of two alternating refractive indices. The reflections from each period add constructively.

light is reflected at each dielectric discontinuity adding in phase with each period (length Λ) of the grating. The roundtrip phase shift accumulated from each successive grating period is a multiple of 2π referenced to the phase of the initial reflection. The reflections from the half-period interfaces also add in phase (for a 50% duty cycle grating) since the reflection boundaries introduce an additional π phase shift when traversing from a lower index to a higher index medium. This coherence of reflection only occurs for select wavelengths given by

$$\frac{2\pi\bar{n}}{\lambda}2\Lambda = l2\pi \text{ or } \lambda = 2\bar{n}\Lambda/l \tag{7.1}$$

Here, $\bar{n} = (n_1 + n_2)/2$ denotes the average effective index of the mode across the two grating cross-sections, Λ denotes the grating period, and l denotes the grating order. For operation at 1550 nm with typical $\bar{n} \sim 3.2$ and a first-order grating, we find that Λ should be half the wavelength in the medium or ~240 nm. This analysis specifies the designed grating period of our SCOW-DFB. The reasons for choosing a first-order grating over gratings of higher order will be made clear in Section 7.1.2.

In addition to the period, another dimension that can be manipulated in a grating structure is its duty cycle. The duty cycle controls the Fourier components of the permittivity at the grating orders. This can be intuitively seen in the spatial-frequency domain upon representing the grating permittivity as a rect function convoluted with a train of impulses spaced by the period of the grating (Fig. 7-2). In the spatial-frequency picture, the convolution transforms into a multiplication between a train of impulses and a sinc function. The impulses sample the sinc at the grating orders with the 0th order centered at DC. The duty cycle of the grating controls the width of the sinc and thus varies the amplitude of the permittivity at the grating orders. For a 50% duty cycle, the even order coefficients all become zero. When the grating duty cycle deviates from 50%, the reflected waves from the half-period interfaces are not perfectly coherent with the reflections at the integer-period boundaries and results in a slight cancellation of the first-order reflection. With these considerations in mind, it is apparent that a 50% duty cycle yields the optimum reflectivity for a first-order grating.

The characteristics of the grating can be described through a set of coupled-mode equations [30] with κ and L_g as parameters representing the forward-backward wave coupling per unit

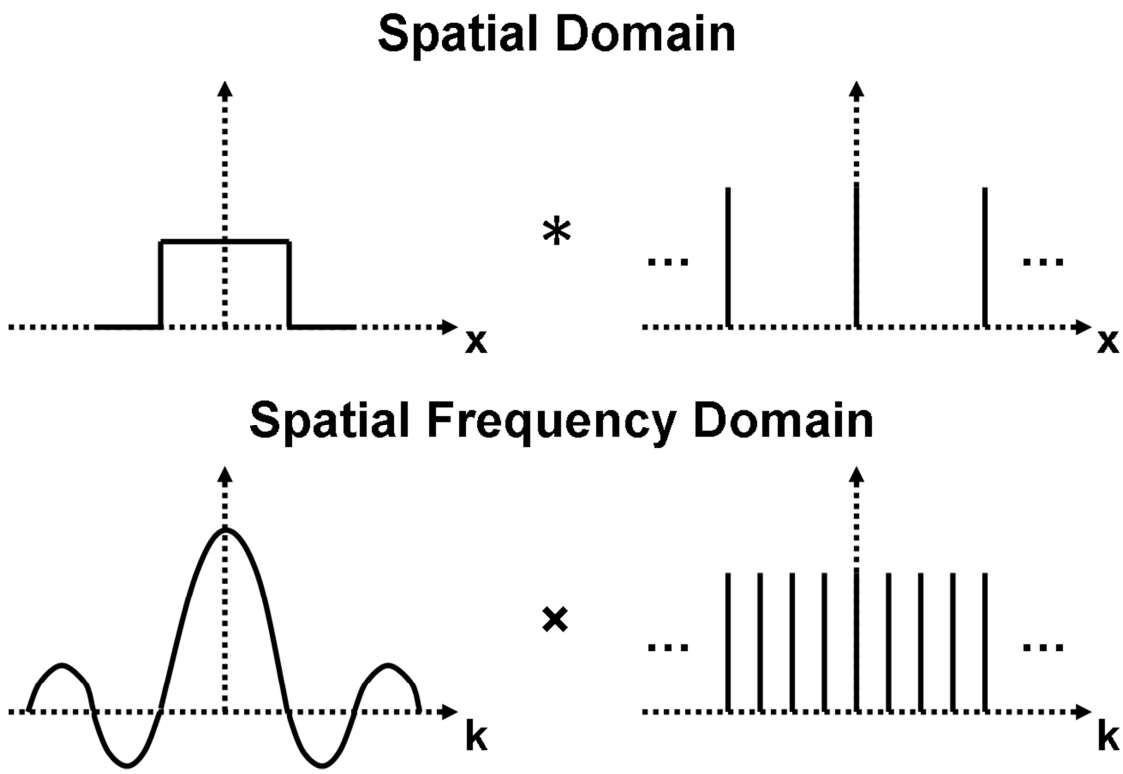

Figure 7-2: Grating analysis in spatial domain and spatial frequency domain. The grating can be spatially represented as a convolution of a rect function and a periodic impulse train. In the frequency domain, this becomes a multiplication of a sinc function with a second impulse train.

length and the grating length, respectively. Their product yields a measure of the total feedback experienced propagating through the grating. An equivalent concept can also be defined using principles of scattering matrices multiplying $r = \left|\frac{n_2 - n_1}{n_2 + n_1}\right|$ (the reflection at each grating discontinuity) by $2m$ (twice the number of grating periods) [29]. Equating the two expressions and simplifying with Eq. (7.1), one finds [29]

$$\kappa = \frac{2\Delta n}{\lambda l} \tag{7.2}$$

where $\Delta n = |n_2 - n_1|$ is the index difference between the two grating cross-sections. Typical values of κL_g for DFB lasers are in the range of unity. Once the grating length is known, the value of κ can be determined along with the index step of the mode in each grating cross-section. Due to the long lengths of the SCOW-DFB, this index step must be appropriately small to allow for efficient utilization of the entire cavity. We will see in the next section that Δn is on the order of 10^{-6} for the SCOW-DFB.

7.1.2 Selection of SCOW-DFB Grating Parameters

With Eqs. (7.1) and (7.2) defined, we would now like to specify the rest of the parameters relevant to the SCOW-DFB's operation. One important parameter is the grating order, which affects the waves coupled by the grating through

$$n_1 \sin(\theta_1) = n_2 \sin(\theta_2) + \frac{l\lambda}{\Lambda} \tag{7.3}$$

where θ_1 is the angle of incidence and θ_2 is the angle after diffraction. Equation (7.3) expresses a condition of momentum conservation with the grating supplying the extra momentum that couples two waves propagating at different angles. When $\theta_1 = \pi/2$ and $\theta_2 = -\pi/2$ denoting two counter-propagating waves, Eq. (7.3) reduces to Eq. (7.1). Higher-order gratings ($l > 1$) are lithographically easier to fabricate due to their larger periods but suffer from radiative losses at all the lower diffractive orders. For example using $l = 2$ for a constant λ, one can double the period to couple the same set of forward and backward waves. The wavelengths corresponding to grating orders $l > 3$ would be outside the bandwidth available for gain. However for $l = 1$, there is always an angle θ_2 at the operation wavelength that satisfies Eq. (7.3). The power into the $l = 1$ grating order represents loss for the DFB. In addition, a secondary disadvantage of using higher-order gratings is a reduction in the number of reflection interfaces for the same device length. For these reasons, we designed the SCOW-DFB for operation in the first grating order.

The length of the SCOW-DFB was designed to be 1 cm. This length was chosen based on traditional designs of SCOW amplifiers and lasers yielding ~14 dB single-pass gain at 1550 nm. The DFB length can be reduced or increased as needed and is upper-bounded by the size of the

chip. Through cutback measurements performed on SCOW Fabry-Perot structures, we determined the lower bound on device length to be ~4 mm. This is approximately the length when the gain differential between fundamental and higher-order transverse modes becomes too weak to ensure single-mode operation. We note that current simulation results do not predict the high-order transverse modes to play a significant role in the SCOW structure, as we will see in Section 7.1.3. The mode spacing decreases for longer cavity lasers, but the linewidth of the grating reflection is also reduced. This second effect allows for the selection of a single longitudinal mode even for SCOW laser cavities 1 cm in length. The disadvantages of longer device lengths include a lower value of κ required to achieve a specific κL_g and a higher susceptibility of the gratings to unintentional chirp or stitching errors along the device. Aside from problems with the controllability of the etch depth, a lower value of κ can also worsen issues with the integrity of the gratings after regrowth (see Section 7.4).

In an index-grating DFB laser structure, there is no mode that can lase at the Bragg wavelength as any optical cavity that can be formed between two reflections in the DFB will always undergo an odd multiple of π phase shift within one roundtrip. As a result, the two modes closest to the Bragg wavelength become the lasing modes of a DFB. These modes do not explicitly satisfy the Bragg condition but are still within the linewidth of the Bragg reflection. The modes are also degenerate causing multi-mode lasing unless perturbations are introduced to disrupt this degeneracy. As mentioned earlier in the introduction to this chapter, we break this degeneracy by introducing a HR coating to one of the DFB facets and using an anti-reflection (AR) coating for the other. The HR coating acts as a symmetry point where the cavity can be unfolded. This effectively doubles the path length of the last layer, which for quarter-wave thicknesses result in a configuration analogous to the quarter-wave shifted DFB. However, this approach has a significant disadvantage in that the position of the facet is uncontrollable and will yield an unpredictable phase shift with each cleave. As a result, the device yield with this technique is ~50%.

Typically, high-power HR-AR DFBs operate with $\kappa L_g \sim 1$. A high κL_g increases the grating reflectivity and thus confines the power to the center of the laser, whereas a low κL_g redistributes the peak in optical power to the facets. The local buildup of power is detrimental to DFB laser operation as the carrier density will also locally vary due to depletion of the gain

medium. These effects produce a spatial variation of refractive index causing the Bragg reflection to change along the device. This breakdown of single-wavelength lasing above threshold is well-known in the DFB and DBR literature and is termed spatial hole burning (SHB) [107, 108]. The effects of SHB are minimized when $\kappa L_g \sim 0.63$ for HR-AR facet reflectivities (or $\kappa L_g \sim 1.25$ for AR-AR facets [109]). Aiming for $\kappa L_g \sim 1$ traditionally has been the standard for achieving high power DFBs with low SHB. Aside from single-mode behavior, overly low and high values of κL_g may also cause degradations in other device metrics. A low κL_g increases the device threshold current, while a high κL_g may result in independent operation of various sections in the cavity. In this work, we similarly design for $\kappa L_g \sim 1$ noting that the long device lengths may require extremely small differentials in modal index. For $\kappa L_g \sim 1$ with L_g = 1 cm, we find κ to be 1 cm^{-1}. Using Eq. (7.2), we find Δn to be 7.75×10^{-5}. This value is ~1-2 orders of magnitude smaller than Δn of typical DFBs

7.1.3 Optimization of SCOW-DFB Structure

There are several locations in the SCOW structure where the gratings can be potentially introduced. These locations are (i) on the surface of the slab waveguide (ii) on the surface of the SCOW ridge (iii) within the bulk of the slab waveguide above the InP substrate (iv) within the bulk of the rib waveguide above the quantum wells. These regions are highlighted in Fig. 7-3. The surface etched gratings are attractive since they eliminate the need for regrowth over the etched grooves. The main disadvantage to gratings etched on the surface of the slab waveguide (configuration (i)) is that grating feedback will be provided to the higher-order modes residing in the slab. Moreover, the feedback for higher-order modes is expected to be even stronger as their overlap with the grating should be larger. Therefore, configuration (i) appears to be unsuitable for use in the SCOW-DFB structure. Relocating the gratings to the ridge (configuration (ii)) appears to resolve the issues of higher-order mode feedback. However, the gratings must now be etched through the 1.7 μm p-InP cladding in order to interact with the optical mode. These large etch depths along with their small error tolerance make the gratings of configuration (ii) difficult for use in the SCOW-DFB.

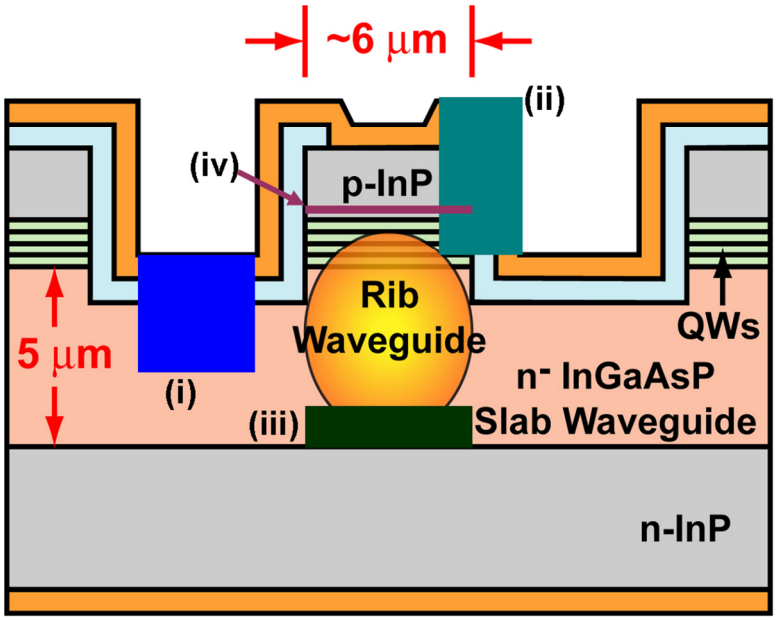

Figure 7-3: Possible grating locations in the SCOW-DFB structure: (i) surface of the slab waveguide, (ii) surface of the SCOW ridge, (iii) above n-InP substrate, (iv) above quantum wells.

Etching the gratings in the n-InGaAsP slab (configuration (iii)) would provide significant grating feedback to the higher-order transverse modes unless the grating can be confined to the center of the ridge. This confinement, however, requires the subsequent processing steps to be aligned with the gratings which can be difficult to accomplish once the full 7-μm structure is regrown. The other drawback of configuration (iii) is that the gratings must be located sufficiently far from the quantum wells so that the surface planarizes before the wells are grown. This is less of a concern for SCOW structures due to their inherently thick slab waveguide. The gratings located above the active region of configuration (iv) solves the problems of higher-order mode feedback that the previous configurations suffered from. No extra mask step is required to define the region where gratings are formed since the ridge waveguide definition removes the unwanted gratings in the field region. Regrowth over the etched grooves is required, but such processes are fairly standard in device fabrication. Finally, one additional advantage of configuration (iv) is that by using InGaAsP gratings over InP, any unwanted overetching of the gratings into the InP will be covered by the subsequent InP regrowth. As long as the InGaAsP

region is defined to be exactly the thickness required for the grating grooves, the variability of the grating structure can be made small.

To simulate the SCOW-DFB, we use a commercial RSoft BeamPROP package to solve for the guided modes in the structure. This simulation allows us to define the grating heights necessary to achieve $\Delta n \sim 7.75\text{x}10^{-5}$. A schematic of the simulated SCOW structure is shown in Fig. 7-4. From the n-InP substrate up to the quantum wells (QWs), the structure is exactly the same as standard SCOW amplifiers or lasers [21, 26]. The SCOW waveguide comprises 0.2 µm of n-InP on n-InP substrate, 1.0 µm n-InP with graded doping (1.0-0.3x10^{18} cm^{-3} S), and 5 µm n-InGaAsP doped 5x10^{16} cm^{-3} S (λ_g = 1.03 µm). Our active region is undoped and consists of 4 compressively strained (1%) QWs of 8 nm thickness (λ_g = 1.54 µm) separated by 3 tensile-strained (-0.3%) barriers of 12 nm thickness (λ_g = 1.22 µm). The bounding layers are the same as the barrier layers but are 15 nm thick. The grating is defined in an updoped InGaAsP layer (λ_g = 1.03 µm) buffered from the active region by an undoped InP layer. The layers are undoped to prevent unwanted diffusion of dopants into the active region during regrowth. The thicknesses of

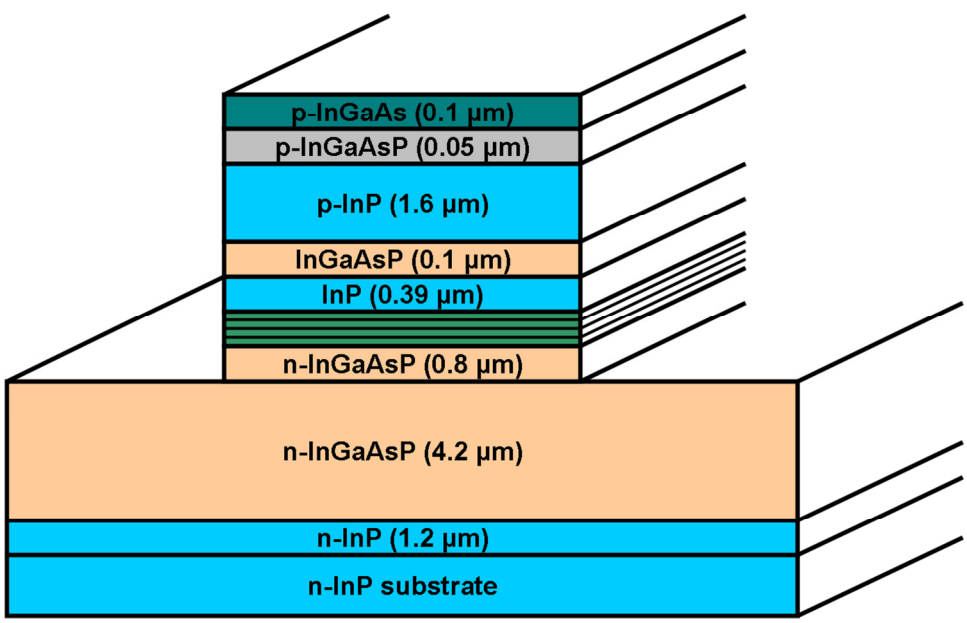

Figure 7-4: Structure of the SCOW-DFB with 0.1 µm InGaAsP grating layer above the quantum well active region.

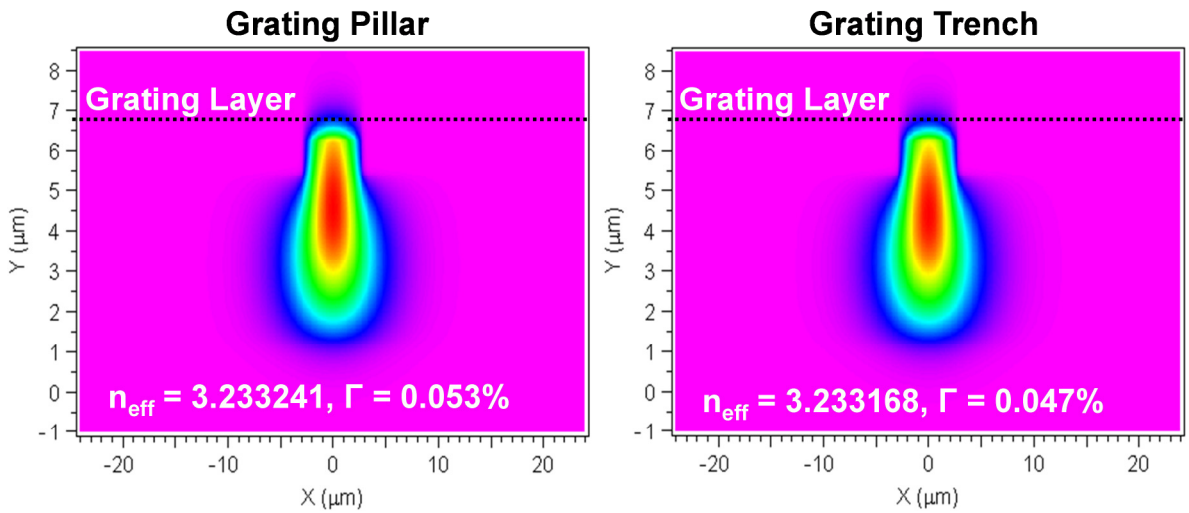

Figure 7-5: SCOW-DFB modes for both grating cross sections with the grating layer (dashed line) indicated. The values of the effective modal index are also provided.

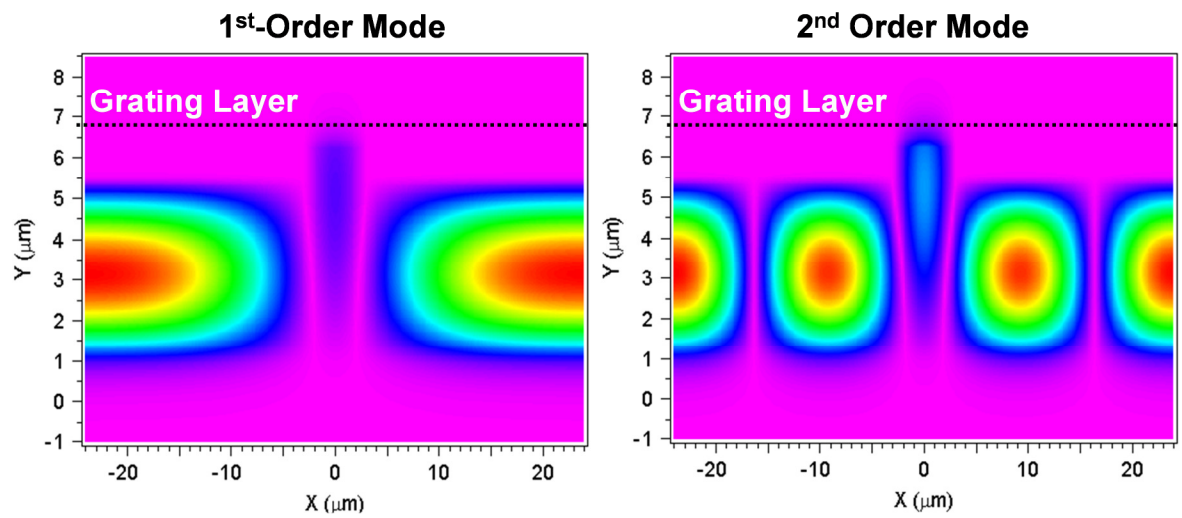

Figure 7-6: SCOW-DFB 1st and 2nd higher-order modes with the grating layer (dashed line) indicated.

the InGaAsP (0.1 μm) and InP (0.39 μm) layers were optimized via BeamPROP simulation to yield $\kappa L_g \sim 1$ while maintaining ~0.5% confinement factor and single transverse mode operation. The gratings are designed to be 100 nm thick and thus are etched through the entirety of the undoped InGaAsP layer. Above the grating layer are the overgrown p-cladding and

contact layers consisting of 1.0 μm of p-InP with graded doping (4-8x10^{17} cm^{-3} Zn), 0.6 μm of p-InP doped (1x10^{18} cm^{-3} Zn), 0.05 μm of p-InGaAsP (λ_g = 1.30 μm) doped (2x10^{18} cm^{-3} Zn) and 0.1 μm of p-InGaAs doped (2x10^{19} cm^{-3} Zn).

The simulated mode profiles for the two grating cross-sections are shown in Fig. 7-5. The position of the grating layer is indicated by the dashed horizontal line. The overlap of the optical mode with the gratings can be verified to be extremely small, as required for a 1 cm long device. The differential in modal index is 7.3x10^{-5} corresponding to $\kappa L_g = 0.94$. The overlap of the optical mode with the QWs is approximately 0.5%. The higher-order mode behavior of the SCOW-DFB structure can also be analyzed with BeamPROP. The simulated first and second higher-order modes are shown in Fig. 7-6. The overlaps of the higher-order modes with both the active region and grating region are insignificant. The bulk of the mode energy is located in the slab where neither gain nor grating feedback is present. Thus, we expect the designed SCOW-DFB structure to operate with a single transverse mode. However, as noted earlier, the simulations of the higher-order modes do not completely agree with experimental measurement.

7.2 SCOW-DFB Fabrication

Here, we outline the process used for fabrication of the SCOW-DFB. The grating recipe developed for this effort will be described in detail. In our developed process, we use photoresist to mask the grating etch, allowing etch depths <125 nm to be readily achieved. For larger etch depths, the grating pattern must be transferred to a secondary mask prior to etching into the semiconductor. We will also present a summary of the lithographic steps used in defining the SCOW structure. The procedure for fabricating the SCOW waveguide has been extensively developed previously at MIT Lincoln Laboratory. We combine these fabrication processes with our own grating process for the realization of a 1.55-μm SCOW-DFB.

7.2.1 SCOW-DFB Grating Process

The period of the grating (240 nm) is too small for standard contact lithographic techniques and must be defined using high-resolution (<90 nm) optical stepper, electron-beam (e-beam), or

interference lithography methods. High-resolution optical stepper lithography systems are usually designed for processing large (>6 in.) silicon wafers and cannot be used to process pieces of InP wafers. Furthermore, e-beam lithography is difficult and time-consuming for the fabrication of large grating structures as the writing field is 100 μm – 1 mm. Longer patterns such as that of the 1 cm SCOW-DFB structure require multiple exposures to be stitched together thus introducing further complications and stitching errors. For this work, we employ interference lithography for defining the SCOW-DFB gratings. In interference lithography, the surface of the InP chip is illuminated by a primary beam along with its reflection off a nearby mirror. The primary and reflected beams interfere at an angle set by the position of the mirror to yield a sinusoidal fringe pattern on the sample. The period of the grating is determined by the interference angle and can be readily scaled to the required 240 nm with a coherent short-wavelength laser source. The laser used in our interference lithography system emits at 325 nm. In this section, we will discuss the process developed for etching first-order gratings into the SCOW structure.

The grating process developed for our InP SCOW structure is based on etching gratings into InGaAsP masked by photoresist. The grating mask was formed using Shipley SPR 3012 photoresist in conjunction with MF-24A developer. At a spin speed of 5000 RPM, the

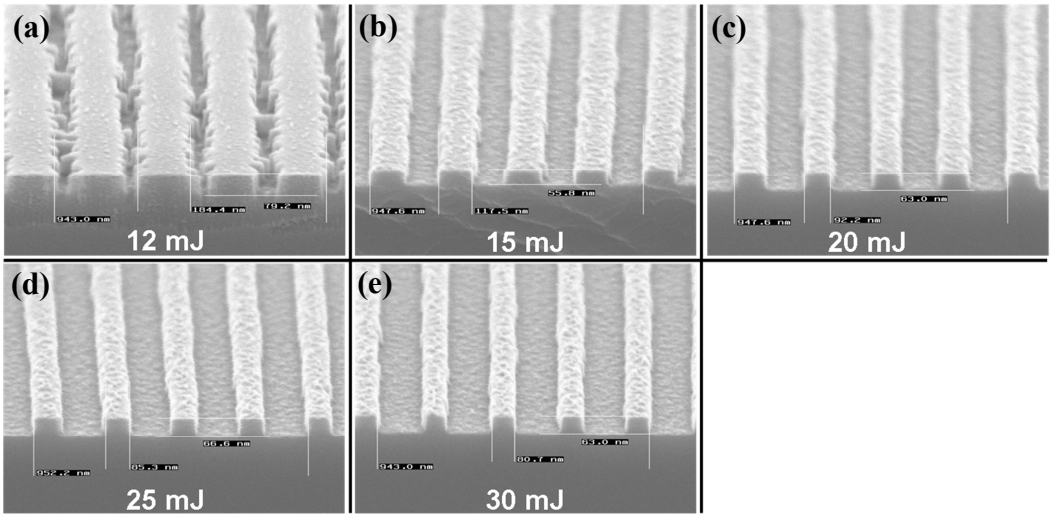

Figure 7-7: SCOW-DFB grating etch as a function of the exposure dose (12 mJ – 30 mJ).

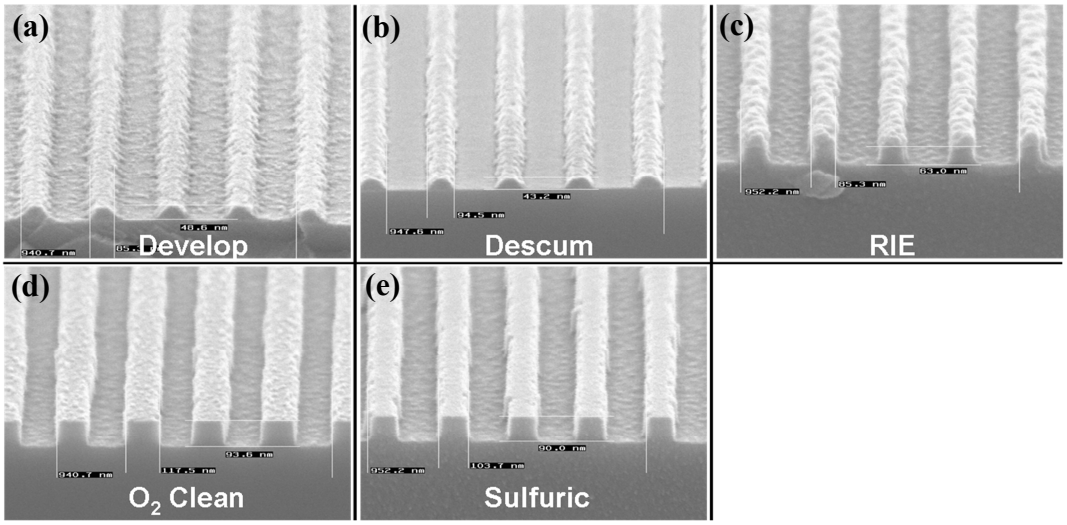

Figure 7-8: SCOW-DFB grating process beginning from the developing of the photoresist to the sulfuric clean of the grating grooves.

photoresist reaches a thickness of ~50 nm. The sample was baked at 115° C for 1 minute prior to spinning the photoresist and was baked at 95°C for 1 minute afterwards. Hexamethyldisilizane (HMDS) was also applied to promote adhesion of the photoresist to the surface of the sample. After the photoresist was spun onto the wafer, interference lithography was used for transferring the grating pattern into the photoresist. Various exposure doses were tested in order to optimize the gratings for 50% duty cycle. The results of this experiment are shown in the scanning electron microscope (SEM) images of Fig. 7-7. The gratings of Fig. 7-7 were etched under 2 minutes of Methane/Hydrogen/Argon (MHA) reactive ion etching (RIE). The etch depth across the different samples was approximately 60 nm, and the period averaged 237 nm. It is clear that exposure doses below 15 mJ were too low to properly define the trenches of the grating. The duty cycle was 50% at 15 mJ dose and decreased as the dose increased towards 30 mJ. This experiment shows that exposure doses > 15 mJ are suitable for defining gratings on an InP platform.

The entire grating process from start-to-finish can be represented concisely by the series of SEM images in Fig. 7-8. The images are shown in chronological order left-to-right and top-to-bottom for a 15 mJ exposure. Image (a) shows the surface of the InP sample right after the 20 second development. Rough strands of photoresist can be seen in the trenches of the grating

grooves. These strands were removed using a 7-15 second O_2 descum step at 10% power (image (b)). The short descum time is suitable for cleaning the trenches of the photoresist while leaving the photoresist mask intact. Image (c) shows that residual polymer is left behind after the 2 minute MHA RIE at 20% power. This polymer resides primarily on top of the grating pillars of which the majority can be removed by a 1 minute O_2 clean step at 30% power (image (d)). However, even with the O_2 clean, some residual polymer buildup is left behind. We perform one final step using a 45 second sulfuric dip to remove the excess polymer from the grating surface (image (e)). After this step, the grating is ready for the surface preparation treatment and subsequent regrowth over the grating.

In our finalized grating process, we made one modification to the process of Fig. 7-8. During the MHA RIE etch step, the RF power was reduced from 20% to 10% in order to decrease the damage inflicted on the sample prior to regrowth. The reduction of RIE power changes the MHA etch to a more chemical based etch thereby protecting the material surface from the bombardment of ions. This precaution helps to maintain a pristine interface for regrowth. A SEM photograph of the gratings fabricated under a 6 minute RIE etch is shown in Fig. 7-9. Note that

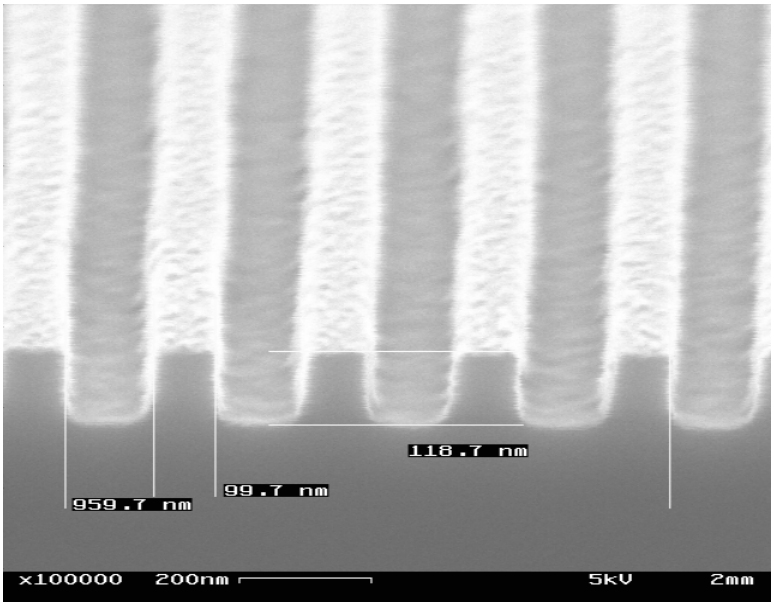

Figure 7-9: SEM photograph of a 6 minute SCOW-DFB grating etch under 10% RF power.

the final sulfuric dip was not performed on the gratings shown in the figure which would have removed the residue on the surface of the grating. The etch depth after 6 minutes was ~120 nm yielding an etch rate of 20 nm/minute. This is approximately a factor of 1.5 times less than the etch rate under 20% RF power. The foot at the edges of the sidewalls is more pronounced than in Fig. 7-8 and is indicative of the more chemical nature of the finalized etch.

7.2.2 SCOW-DFB Fabrication Process

The fabrication of the SCOW-DFB uses the standard procedures developed by MIT Lincoln Laboratory for fabricating SCOW structures. The main steps for this process are highlighted in Fig. 7-10. Initially, the chip consists of the SCOW structure up to the grating layer grown on an n-type InP substrate (image (a)). Using the interference lithography process described in Section 7.2.1, gratings are etched into the 0.1 µm InGaAsP layer with 240 nm period (image (b)).

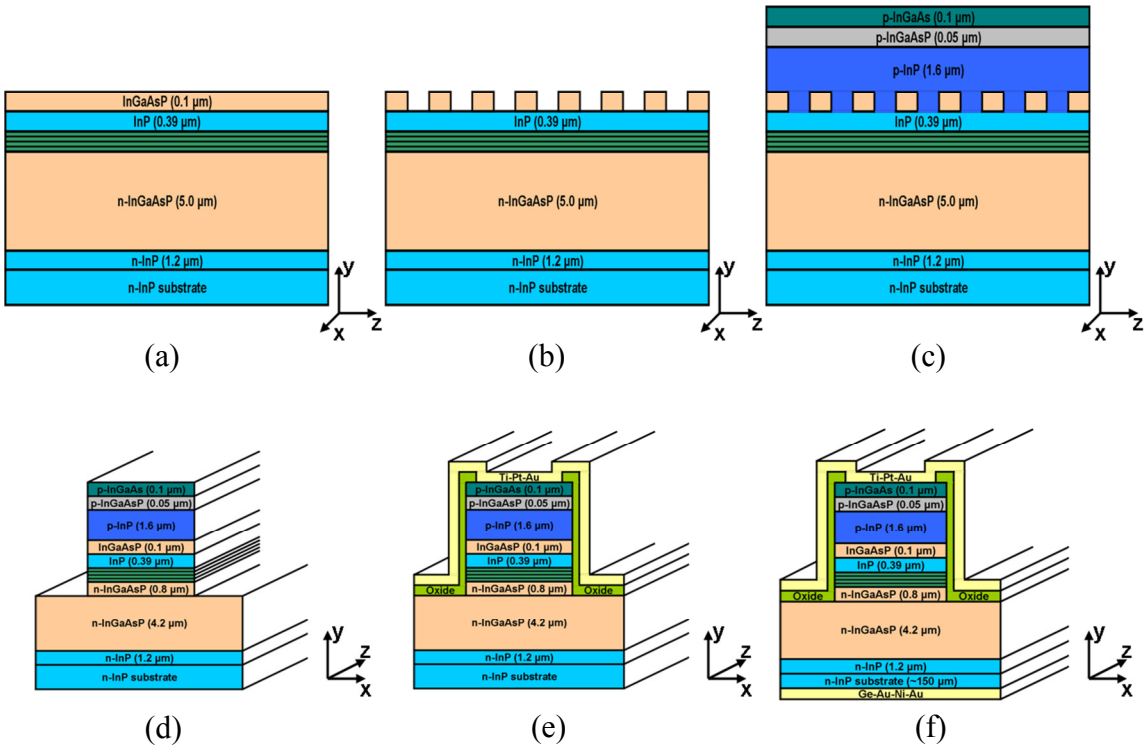

Figure 7-10: SCOW-DFB fabrication process starting from (a) an InP wafer grown up to the grating layer and ending with (f) the patterned and metalized SCOW-DFB structure.

Prior to regrowth, an hour-long UV ozone step is performed followed by a subsequent 5 second buffered-HF dip in order to clean the surface. The regrowth step is performed via metal-organic chemical vapor deposition (MOCVD) at 625 °C (image (c)). Ridges of 5.8 μm width were defined using inductively coupled plasma reactive ion etching (ICP-RIE) masked by aluminum oxide on nitride (image (d)). The mask is removed with a 12 minute 10:1 H2O:HF wet etch.

A bi-layer of oxide is then deposited on the newly formed ridge using a combination of pyrolytic oxidation (1.2 μm at 350 °C) and low pressure chemical vapor deposition (LPCVD) (1.7 μm at 275 °C). A 15 minute CF4 RIE etch step with the field masked off is performed to open vias to the underlying SCOW ridge. To pattern the p-metal, Ti (200 Å)-Pt (400 Å)-Au (1000 Å) is evaporated onto the surface and lifted off at the edges between devices. Prior to the evaporation, a 30 second NH_4OH:H_2O dip/blow dry step is performed to prevent oxidation of the semiconductor surface. After evaporation, a 30 second heat pulse step at 425 °C is used for alloying the semiconductor interface to the p-metal. The contact pads were formed through subsequent Ti-Au sputtering at thicknesses of 500 Å and 6000 Å respectively (image (e)). Finally, after thinning the surface of the backside to ~6 mil (~150 μm), Ge (300 Å)-Au (600 Å)-Ni (300 Å)-Au (2000 Å) is evaporated onto the backside to form the n-metal contact (image (f)). Alloying of the semiconductor and n-metal interface is performed at 350 °C for 30 seconds. A Ti (500 Å)-Pt (700 Å)-Au (500 Å) sputtering step is also used for solder metallization on the backside.

The SCOW-DFBs are mounted junction-up bonded to a Cu-W heatsink with AuSn (80:20) solder at 217 °C. The entire assembly is affixed to a copper submount using indium solder at 156 °C. The design of the mount allows for easy access to the n-metal and p-metal contacts while minimizing stress due to mismatch of thermal expansion.

7.2.3 SCOW-DFB Fabrication AFM Scans

Prior to the regrowth step, atomic force microscope (AFM) scans were taken on the device samples to verify the integrity of the etched gratings. The AFM scans were performed across three locations of the sample (bottom-right, center, and top-left) in order to ensure etch uniformity across the chip. The results of the scan are shown in Fig. 7-11 with the locations of the images denoting approximately where the scans were performed. The etch depths for all

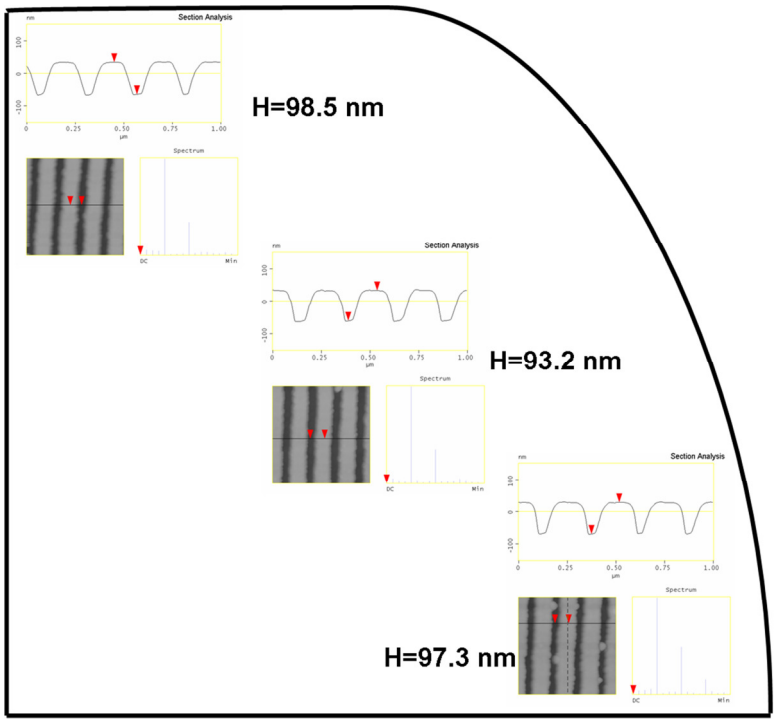

Figure 7-11: AFM images superimposed on the image of an InP chip indicating the location of the scans. The grating etch depths averaged 96.3 nm across the chip.

three scans are also provided. The gratings average 96.3 nm in height with only a +/- 3 nm variation across the chip. The trenches of the gratings appear narrow due to influence from the width of the AFM tip. A duty cycle of approximately 50 % was estimated based on the width of the flat region above the grating pillars. The exact grating period was unfortunately not measured during the time of the experiment but appears to be close to 240 nm based on the horizontal scale tick marks in each image.

7.3 First Generation SCOW-DFB Measurements

In the following sections, we describe the results of our measurements performed on the fabricated SCOW-DFBs. The overall performance of the DFBs was found to be relatively poor with high threshold currents and inconsistent lasing. The measurements that will be presented

include L-I-V measurements characterizing lasing operation and optical spectrum analyzer measurements characterizing lasing spectrum. The abnormal performance of the SCOW-DFB led us to conduct gain measurements characterizing the gain of the laser cavity. The gain measurements were performed on amplifiers cleaved and coated AR-AR using material from the DFB fabrication run. For completeness, we conclude with measurements of the SCOW-DFB mode profile. This will provide a further assessment of the degradation mechanisms occurring within the fabricated devices.

7.3.1 SCOW-DFB L-I-V

L-I-V measurements were performed on a bar of 7 DFBs mounted junction-up. The I-V data was collected with a 4-point measurement using a Keithley 2440 sourcemeter, and the L-I data was measured with an ILX optical power meter. Fig. 7-12 shows the L-I-V characteristics corresponding to one of the devices and for a current sweep from 0-5 A. The rest of the devices on the bar behaved similarly. The extracted turn-on voltage (V_0) and series resistance (R_S) are

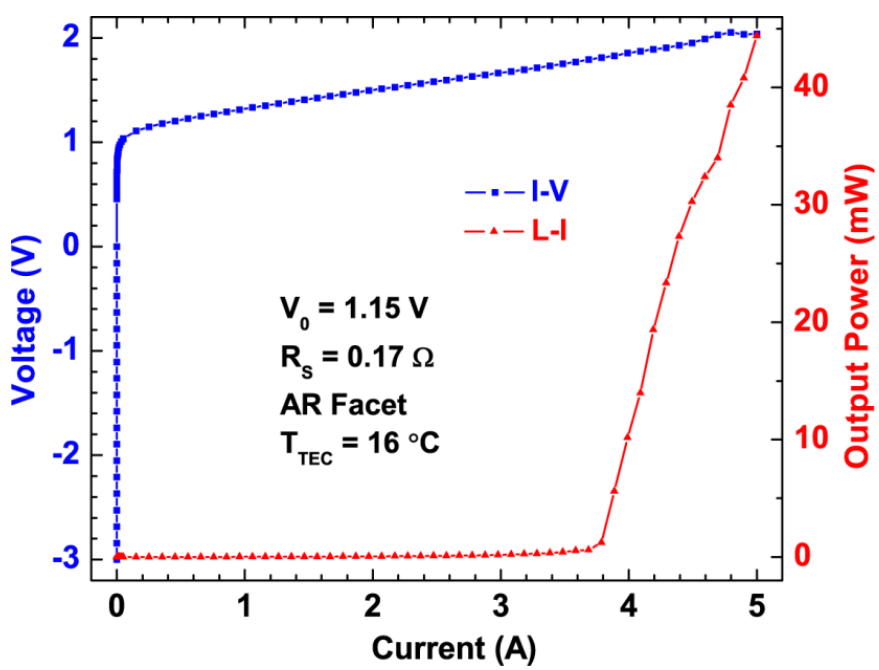

Figure 7-12: SCOW-DFB output light power (AR facet) and voltage versus bias current (0 A – 5 A). The extracted turn-on voltage and series resistance are also provided.

1.15 V and 0.09 Ω respectively. V_0 is typically expected to be around the bandgap (0.8 V) since the resistance of the diode goes to zero once flatband conditions are reached. This is indeed what is seen for typical SCOW devices but is 0.35 V lower than the V_0 measured for our SCOW-DFB. A higher turn-on voltage indicates the presence of a junction in series with that of our QW active region. This junction can result from several sources including a poor regrowth interface resulting in local trap sites for injected carriers or an unintentional potential barrier within the semiconductor layer stack. The series resistance of the SCOW-DFB is similar to that of typical SCOW devices at 1.55 μm.

The measured output power of the SCOW-DFB (~45 mW at 5 A) collected through a lensed fiber is much lower than expected considering the Watt-class power capabilities of SCOW amplifiers and lasers. The threshold current (~3.8 A) is also much higher than that of typical SCOW lasers. For example, the SCOWECL has a threshold of ~0.9-1 A. The slope efficiency is 37.5 mW/A and is about a factor of 5 lower than that of the SCOWECL. The wall-plug efficiency of the SCOW-DFB at 5 A is ~0.45 % and is a factor of 10 lower than the SCOWECL wall-plug efficiency. The poor efficiencies of the SCOW-DFB are due to its large threshold current and large turn-on voltage.

7.3.2 SCOW-DFB Optical Spectrum

We now present measurements of the optical spectra exhibited by the SCOW-DFB. Once again, the presented spectra are typical across the different devices on the bar. Figure 7-13 shows the spectrum measured above lasing threshold operating at a current bias of 4.5 A. The spectrum exhibits a broad peak near 1526 nm despite the original design of the SCOW-DFB gratings for 1550-nm operation. This suggests that the gratings are either misaligned by 4 nm from their original target period or that the gratings are not properly interacting with the optical mode. Of these possibilities, we believe the latter to be the more likely explanation. The optical feedback required for lasing is supplied from reflected light off of the lensed fiber rather than from any grating reflection. Even though the lensed fibers are themselves AR coated, we find that significant feedback can still occur when the position of the fibers are slightly detuned from the waveguide mode. We note that any evidence of lasing disappears when the lensed fiber is replaced with a free-space lens.

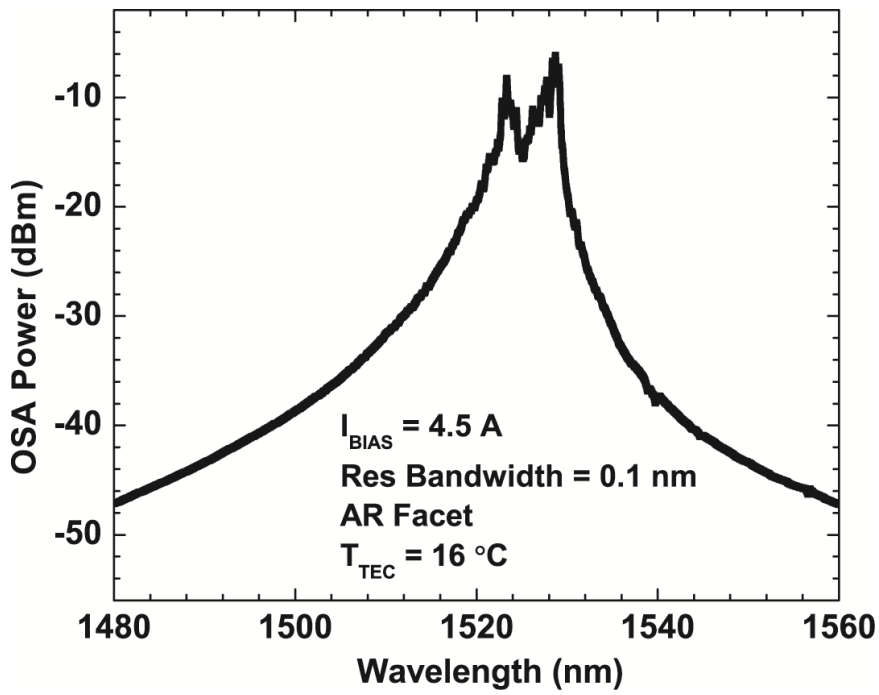

Figure 7-13: SCOW-DFB AR-facet optical spectrum for a bias current of 4.5 A.

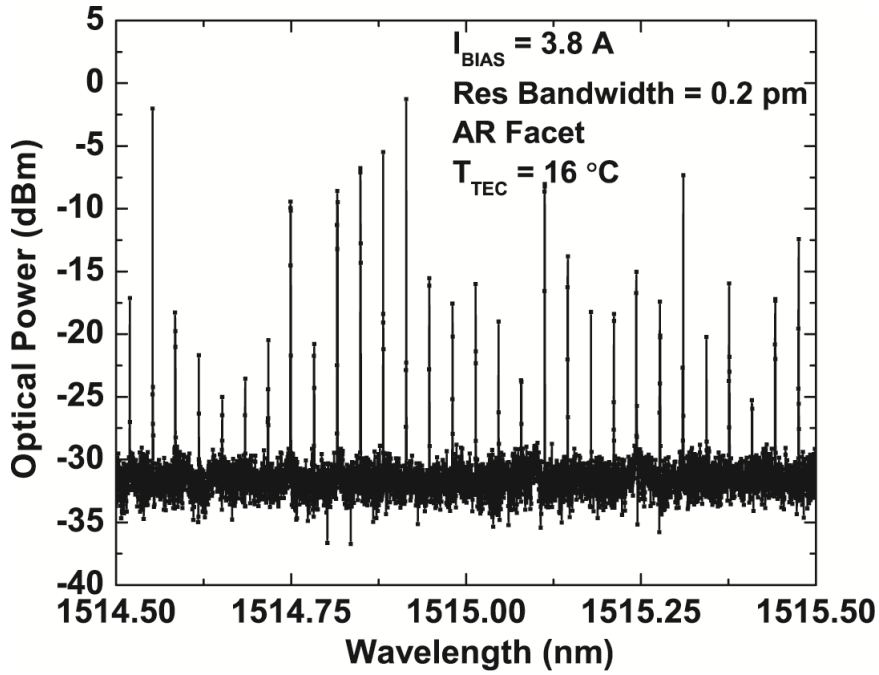

Figure 7-14: SCOW-DFB AR-facet optical spectrum for a bias current of 3.8 A. The resolution bandwidth for this measurement was 0.2 pm.

The capabilities of the optical spectrum analyzer (OSA) limit the resolution bandwidth of the measurement in Fig. 7-13 to values near ~0.1 nm. This prevents out ability to observe individual modes in the measured spectrum. The resolution limit can be substantially improved through OSAs operating by heterodyne means using a swept source. Figure 7-14 shows the optical spectrum captured by an Agilent 83453B high-resolution spectrometer. The resolution bandwidth for the measurement corresponds to 0.2 pm. The measurement is centered on 1515 nm which appears to be slightly off the peak in Fig. 7-13. However, the SCOW-DFB spectrum changes with bias current and also shifts around over time. The individual modes of the SCOW-DFB can be resolved in Fig. 7-14 and are separated by 4.3 GHz. It can be verified that this separation corresponds to the free-spectral range (FSR) of a 1 cm cavity with a group index of $n_g = 3.5$. Based on the results of this measurement, it is clear that the SCOW-DFB operation is strongly multi-moded.

7.3.3 SCOW-DFB Gain

In this section, we measure the gain of the SCOW-DFB structure. This measurement serves two purposes: 1) to explain the abnormally large threshold observed in the L-I-V of Fig. 7-12 and 2) to explain the lasing wavelength of 1520 nm in Figs. 7-13 and 7-14. As the original DFB structure consists of an HR coated facet, its gain is difficult to measure at high currents without the structure lasing. We instead prepared a second bar of similar devices but with their facets coated AR-AR. We measured the single-pass gain of these "amplifiers" by probing these devices with a tunable laser operated at low optical powers.

Fig. 7-15 shows the results of this gain measurement. The measurement wavelength spanned from 1454 nm to 1641 nm and was taken for current biases ranging from 0.5 A – 4 A. At 0.5 A bias, it is clear that the amplifier initially operates in a regime of loss, attenuating any input signal within the tested ~200 nm span. The net loss is comparable in magnitude to that measured of the packaged 0.8 W SCOWA in [22] signifying their mode overlaps with the active region ($\Gamma \sim 0.5\%$) to be similar. With increasing bias current, the gain peak shifts to shorter wavelengths and stabilizes near 1525 nm. This explains the ~1520 nm SCOW-DFB lasing wavelength in Figs. 7-13 and 7-14. The maximum single-pass gain occurs at 2 A – 3 A bias but

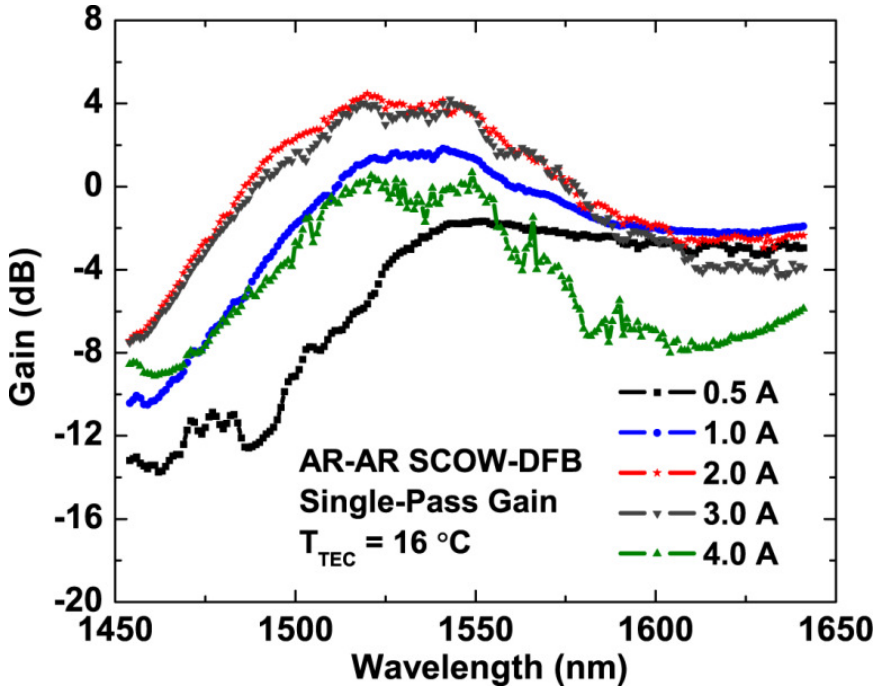

Figure 7-15: AR-AR SCOW-DFB single-pass gain for wavelengths between 1454 nm and 1641 nm. The gain spectrum was measured for bias currents ranging from 0.5 A to 4.0 A.

corresponds to a low value of gain (~4 dB). This explains the large SCOW-DFB threshold current. We will later show that this abnormally low gain is due to 1) low carrier injection efficiency into the quantum wells and 2) increased rates of free-carrier absorption (FCA). Both mechanisms are due to an unintentional carrier well introduced by the grating layer, as we will see in Section 7.4. From Fig. 7-15, it is clear that the net gain reduces dramatically at 4 A bias. This decrease in gain is another indication of the increase in FCA processes.

7.3.4 SCOW-DFB Mode Profile

In this section, we measure the mode profile of the SCOW-DFB across several bias currents. This serves to not only compare the SCOW-DFB mode to the modes of standard SCOW devices but also to track the evolution of the SCOW-DFB mode versus bias. Figure 7-16 shows the measured mode profiles for bias currents ranging from 1.5 A to 4.5 A. One clear trend in the modes is a steady decrease in X (horizontal) and Y (vertical) dimensions as the bias current

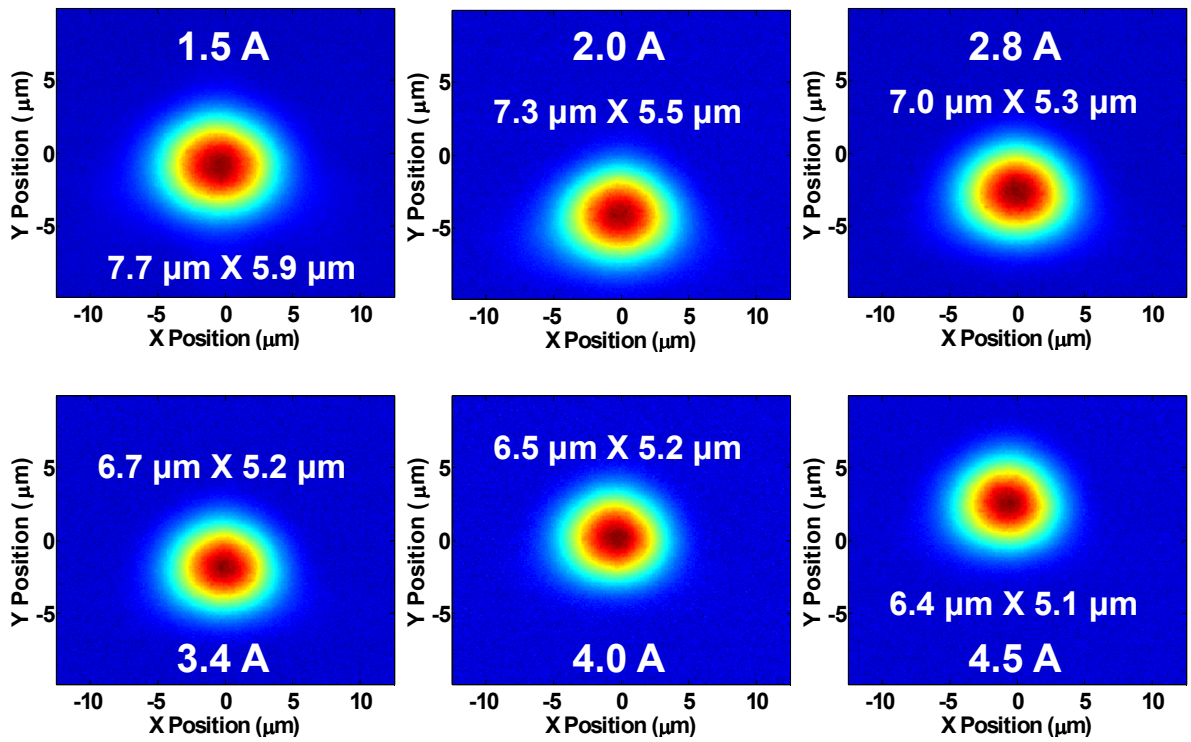

Figure 7-16: SCOW-DFB mode profiles as a function of bias for currents between 1.5 A and 4.5 A. The dimensions of the modes are also provided. The first number denotes the X dimension, whereas the second number denotes the Y dimension.

increases. The reduction in mode area occurs due to heat generated in the device causing the mode to become more and more confined. As the mode becomes confined, it experiences larger overlap with the unintentional carrier well resulting in a large decrease in gain at higher biases (Fig. 7-15). The mode dimensions of standard SCOW structures typically measure to be 7.5 µm X 5.5 µm. It can be verified that this agrees with the dimensions of the 1.5 A mode but is by a fair amount larger than the 4.5 A mode.

A second trend that can be observed in Fig. 7-16 is a gradual rising in the mode position with increasing current. This is especially apparent in the mode profiles beyond 2.0 A bias. The shifts in the mode are due to the thermal expansion of the assembly that which the device rests on. The 1.5 A profile was taken last (after the 4.5 A mode), which explains why its position is slightly above that even of the 3.4 A mode. We also expect the actual mode within the SCOW-DFB

structure to vary with bias due to changes in its confinement. However, these variations are likely to be smaller compared to the ~5 μm shifts seen in Fig. 7-16.

7.4 Analysis of First-Generation SCOW-DFB Deficiencies

In Section 7.3, it became clear that there were many problems related to the initial design of the SCOW-DFB. Here, we will present an analysis of these deficiencies. Our simulations previously considered only the optical structure of the DFB and thus optimized for modal overlap with the active region and gratings. In the upcoming sections, we supplement these optical simulations with electrical simulations of the device characteristics. We will show that these electrical simulations are necessary to account for the observed performance degradations of the SCOW-DFB. To conclude our analysis, we present scanning electron microscope (SEM) images of the completed structure. This will allow a direct comparison of the gratings before regrowth captured by the AFM scans of Fig. 7-11 to the gratings after fabrication captured by the SEM images.

7.4.1 SCOW-DFB Electrical Simulation

We are interested here in simulating the electrical behavior of the SCOW-DFB for diagnostic purposes. The engine we use is SimWindows with user-defined material parameters appropriate to the InP/InGaAsP system. The SimWindows package enables the simulation of band diagrams and device characteristics at arbitrary applied bias. This allows access to a large body of information regarding the operation of the SCOW-DFB.

Figure 7-17 shows the band diagram of the structure when the device is off (0 V) and when the device is beginning to turn on (1.2 V, see turn-on voltage of Fig. 7-12). The band diagrams illustrate the dilemma associated with our implementation of the grating layer. At 0 V, it can be seen that a potential well is formed by the grating layer sandwiched between the InP buffer layer and a graded p-doped region of InP. This potential well has the ability to trap carriers and thus reduce the injection efficiency of carriers into the quantum wells. Furthermore, as the grating and more importantly the InP buffer layers are undoped, any voltage applied also becomes dropped

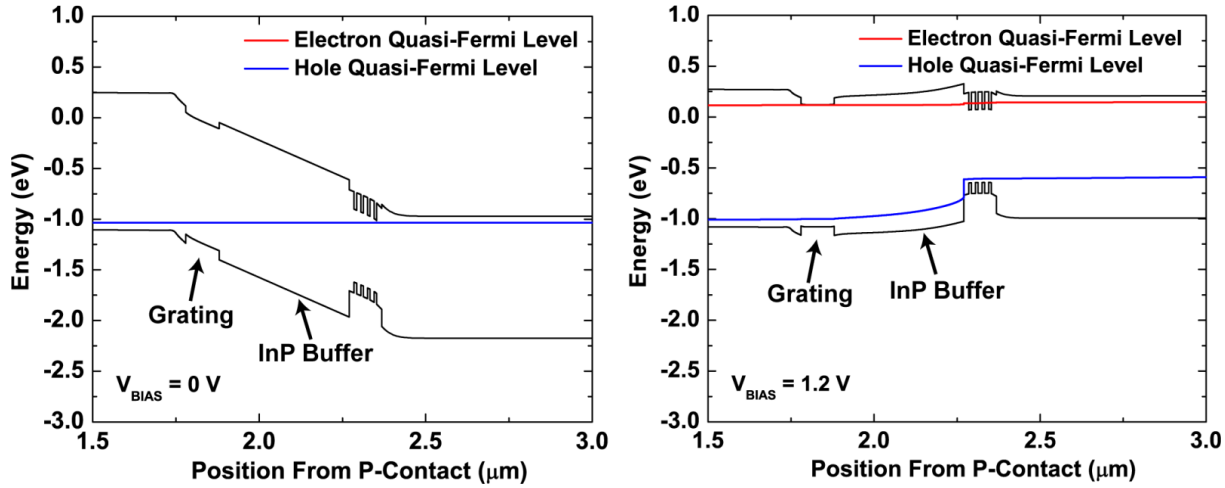

(a) (b)

Figure 7-17: Band diagram of the SCOW-DFB for operation at (a) 0 V bias and at (b) 1.2 V bias. The electron and hole quasi-Fermi levels are also provided.

across these layers. Since the bandgaps of these layers are large compared to the quantum wells, the applied voltage must be larger to counteract the potential gradient impeding electron and hole flow. The required additional voltage can be seen in the jump in the quasi-Fermi level difference near the InP buffer layer for a total applied voltage of 1.2 V (Fig. 7-17 (b)).

Based on the band diagram of Fig. 7-17, we identified two significant deficiencies of our previous SCOW-DFB design. One deficiency was related to the trapping of carriers by the potential well formed from the grating layer. The impact of this well can be assessed by simulating the carrier density profile as a function of the voltage bias. Figure 7-18 shows this simulation for biases between 0.9 V and 1.8 V and over the same range of positions as that shown in Fig. 7-17. There are two recognizable regions where carriers build up in the device. The region on the right (~2.3 μm) corresponds to the four separate quantum wells, while the region on the left (~1.8 μm) corresponds to the grating layer. It is clear that a larger carrier concentration builds up in the quantum wells but only by a small margin. This significantly reduces the injection efficiency achievable by the SCOW-DFB. Furthermore, the overlap of the mode with the grating layer, while necessary for DFB operation, becomes detrimental due to increased loss from FCA processes.

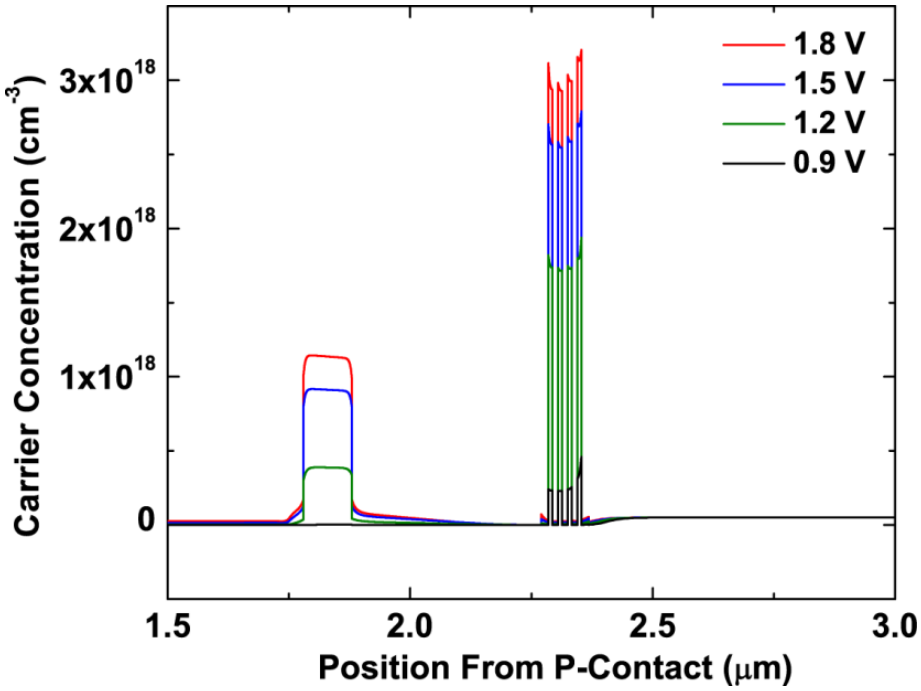

Figure 7-18: Carrier concentrations as a function of position within the SCOW-DFB structure for voltage biases of 0.9 V – 1.8 V.

The second deficiency in the SCOW-DFB structure was the additional voltage required to overcome the potential barrier of the grating and InP buffer layers. The impact of this barrier on the I-V relations can be seen from the simulations of Fig. 7-19. The standard SCOW structure is shown to yield a turn-on voltage of 0.92 V, which agrees well with typical measured V_0 of ~0.85 V. On the other hand, the I-V corresponding to the SCOW-DFB structure indicates a turn on voltage of 1.22 V. Again, this corresponds closely to measured V_0 values for the SCOW-DFB ($V_0 \sim 1.15$ V in Fig. 7-12). Note that the grating and InP buffer layers represent the only varied parameters between the simulations of the standard SCOW structure and of the SCOW-DFB. It is clear then that the difference observed in turn-on voltage is due to the additional potential barriers introduced by these layers. Before concluding this section, we wish to mention that the series resistance, which is related to the slope of the I-V curve, remains largely unaffected by these additional layers.

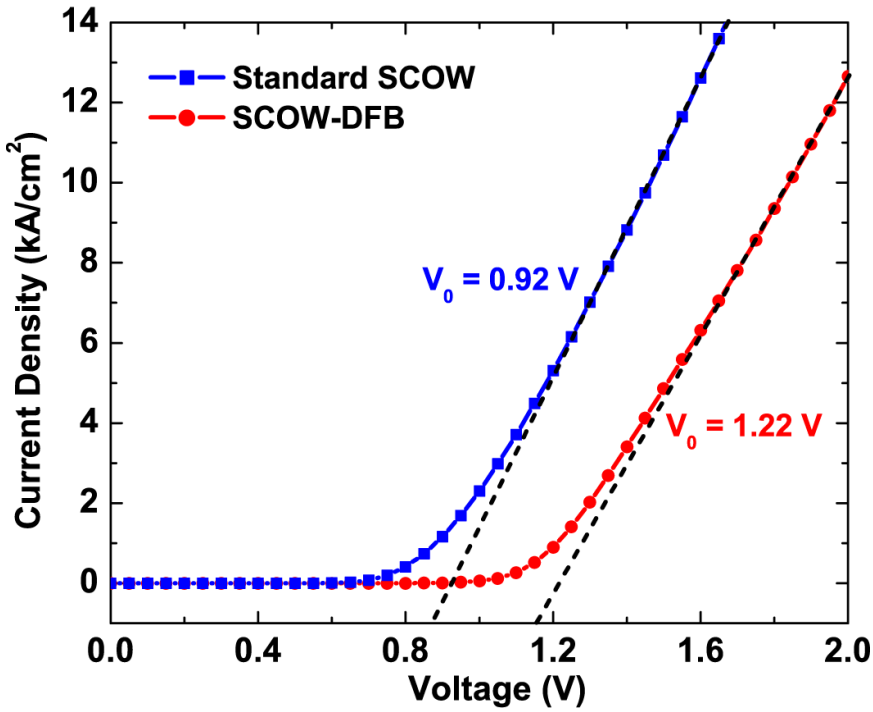

Figure 7-19: Simulated I-V relations for the standard SCOW structure and for the SCOW-DFB. The turn-on voltage for each respective device is also provided.

7.4.2 SCOW-DFB Post-Fabrication SEM Images

Since the gratings were defined in an intermediate step along the entire process, it is useful to examine the features of the gratings after the SCOW-DFB is fully fabricated. To accomplish this, we first etch the gratings along the edge of the chip to provide contrast between the InGaAsP gratings and the InP background. The solution used for the etch is a mixture of 10:1:1 H_2O:H_2SO_4:H_2O_2. The gratings are then imaged along the cleaved edge as can be observed in the SEM photograph of Fig. 7-20. From the image, we see that the gratings have an estimated period of 243 nm. Although this appears to deviate from the designed period of 240 nm, we believe the difference is most likely due to uncertainties in the lengths extracted from the SEM.

More importantly, we find that the gratings, which originally had a height of 96.3 nm (Fig. 7-11), have now reduced by 50% to a post-fabrication height of 49 nm. The shapes of the

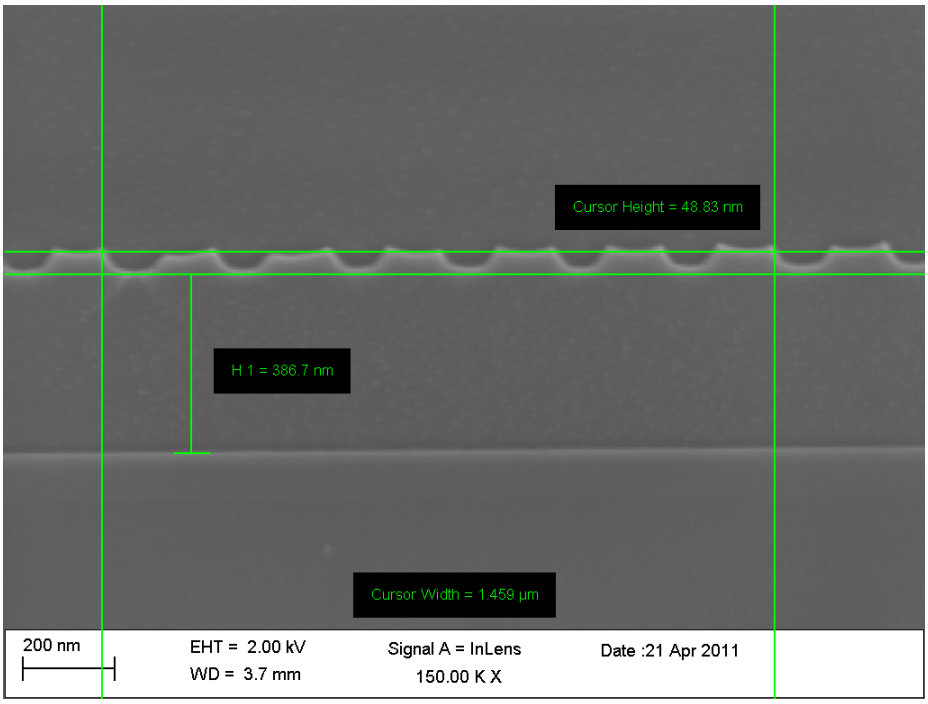

Figure 7-20: SEM image of the SCOW-DFB gratings after regrowth. The measured average grating height is indicated. The average grating period can be found from the measured length over 6 grating periods.

gratings are also deformed with a duty cycle that is now clearly >50 %. These structural changes are due to mass reflow during the regrowth process resulting from the elevated temperatures required for growth [110]. Typically, the Indium species becomes diffusive at growth temperatures (625 °C) and produce a smoothing to the grating shape and a reduction to the grating height. These effects decrease κ from the target specified by design. Thus in the end, not only do the SCOW-DFB gratings confine carriers and impede current flow, but they also are relatively poor at reflecting light.

To better understand the grating mass-transport process, we evaluated the effects of regrowth on the gratings across a range of material compositions. Three InGaAsP compositions were tested corresponding to wavelengths of 1055, 1256, and 1545 nm. The 1055-nm material is very close to the material originally used for the SCOW-DFB gratings. As the amount of Indium decreases, the wavelength increases to 1256 nm and eventually to 1545 nm.

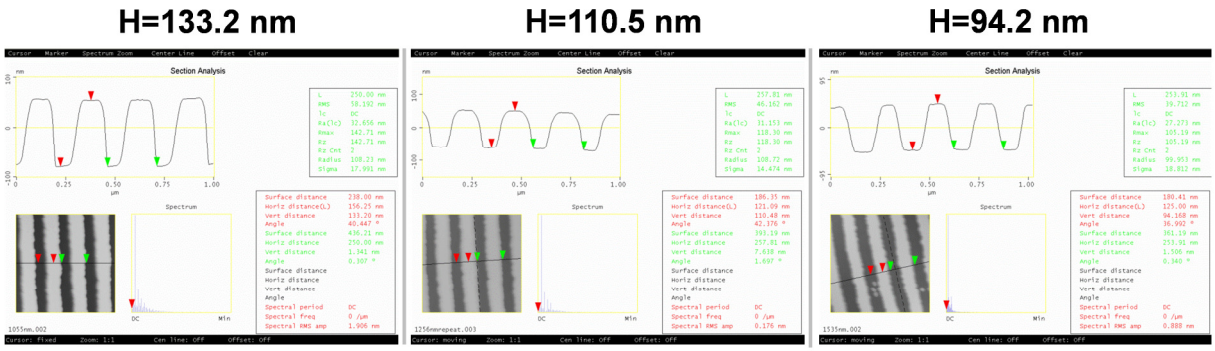

Figure 7-21: AFM scans for three different InGaAsP compositions with bandgaps corresponding to the wavelengths of (a) 1055 nm, (b) 1256 nm, and (c) 1545 nm. The grating heights (H) are provided in each case.

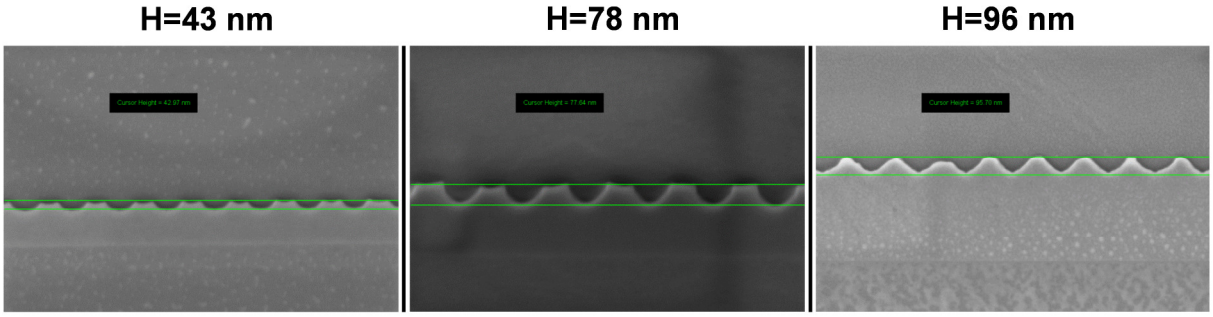

(a) (b) (c)

Figure 7-22: SEM scans for three different InGaAsP compositions with bandgaps corresponding to the wavelengths of (a) 1055 nm, (b) 1256 nm, and (c) 1545 nm. The grating heights (H) are provided in each case.

Figure 7-21 shows AFM scans of the three materials used in this study. The corresponding grating heights after a fixed duration MHA RIE etch are also provided. While the gratings are all near 100 nm, it is clear that the etch prefers the shorter wavelength materials by a fairly large margin. We compare these scans to SEM images of the same chips but after regrowth of the full structure. These SEM images are shown in Fig. 7-22 again with their respective grating heights provided. For the 1055, 1256, and 1545 nm materials, the gratings reduce to 32%, 70%, and ~100% of their starting heights, respectively. As expected, with decreasing Indium content, the

gratings retain more of their original features and size. Based on the results of this study, we would ideally then choose the grating material to have a bandgap of 1545 nm or lower. However, this narrow-bandgap layer has the possibility of introducing an additional potential well, thus trapping the injected carriers and preventing them from reaching the quantum wells. The bandgap of the grating material should therefore be designed large enough to prevent this undesirable accumulation of carriers. Furthermore, since smaller bandgap corresponds to larger refractive index, it is advantageous to keep the bandgap high to prevent significant increases to the mode confinement.

7.5 Design of Second Generation SCOW-DFB

Our previous approach of introducing gratings into the SCOW structure unfortunately resulted in significant degradations of the device performance. As we saw earlier, the carrier transport was obstructed by the additional grating layers, and the necessity for high regrowth temperatures distorted the dimensions and shapes of the gratings. Here, we present a revised design that addresses the flaws of the first-generation structure. In the upcoming sections, we will detail both optical and electrical simulations of the SCOW-DFB performance. In the end, we will see that the previous limitations are adequately resolved in our proposed redesign.

7.5.1 Second Generation SCOW-DFB Structure

Figure 7-23 shows a schematic of the second-generation SCOW-DFB. Most of the layers are identical to that of the previous SCOW-DFB and to that of typical SCOW designs. The top of the structure still comprises a 0.1 μm p-InGaAs / 0.05 μm p-InGaAsP contact layer with a graded p-InP cladding underneath. The grating layer consists of 0.04-μm thick InGaAsP with bandgap λ_g = 1.185 μm. This wavelength is larger and thus corresponds to lower InGaAsP Indium content. This is important to mitigate the effects of mass transport under regrowth conditions as observed in Figs. 7-21 and 7-22. The 0.04 μm thickness of the grating layer was chosen so that ~0.028 μm (70%) remains after regrowth. The width of the grating layer is nominally 1 μm to

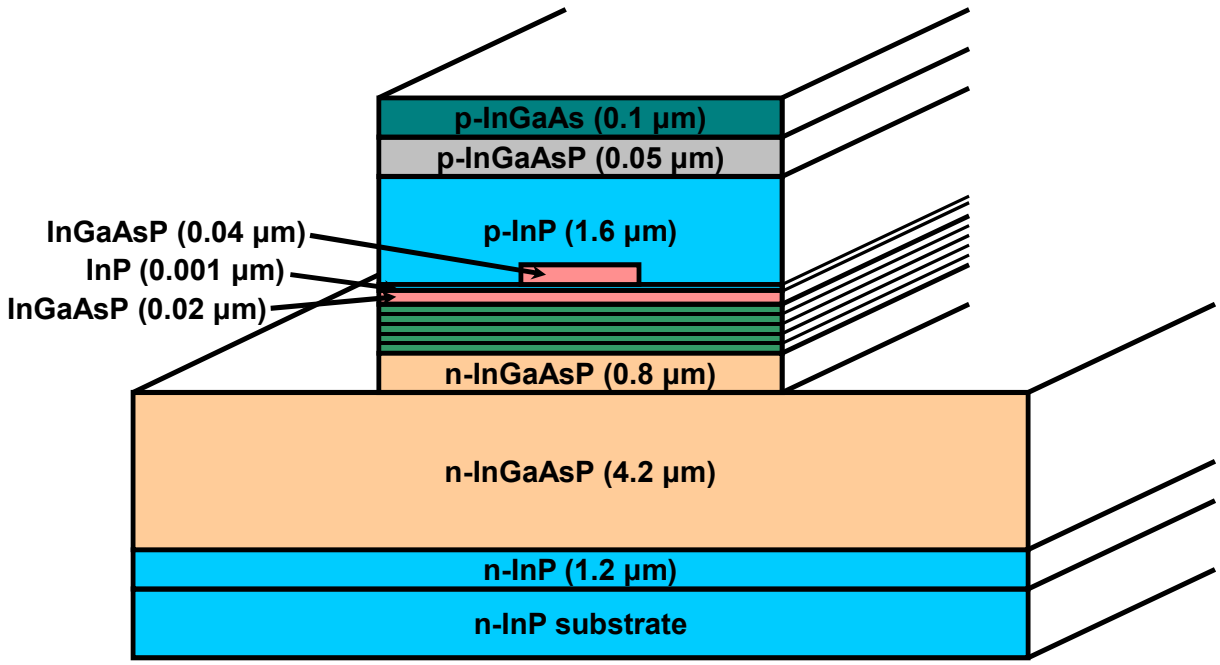

Figure 7-23: Revised SCOW-DFB structure with 0.02 µm InGaAsP buffer layer, 0.001 µm InP etch stop layer, and 0.04 µm variable-width InGaAsP grating layer.

limit the amount of grating feedback provided over the length of the structure but can be made wider to accommodate requirements for larger feedback.

Beneath the gratings, we use 1 nm of InP as an etch stop for the wet etching of the gratings. This layer should be thick enough to impede further etching but should also be thin enough for carriers to tunnel through. Underneath the etch stop is a second InGaAsP layer with λ_g = 1.185 µm. Besides replacing the previously undesirable InP buffer in the first generation SCOW-DFB, this buffer layer serves three additional purposes. First, it acts as a sacrificial layer should the InP etch stop prove insufficient in protecting the underlying structure. Second, the buffer layer helps to separate the gratings from the active region so that the grating feedback can be kept low over the length of the structure. Third, its relatively high index helps to increase the confinement of the optical mode to the quantum well active region. This is important in our second-generation design as we will be reducing the device length from 1 cm to 5 mm. This reduction in length is again necessary to limit the overall value of κL_g.

Directly below the InGaAsP buffer are the quantum well and barrier layers. We use five quantum wells and six barriers in this SCOW-DFB design for the purposes of increasing the active region confinement. The 5.0-µm thick InGaAsP waveguide (λ_g = 1.05 µm) lies underneath the active region along with a graded 1.2-µm thick n-InP epitaxial layer and eventually the n-InP substrate.

7.5.2 Second Generation SCOW-DFB Optical Simulations

In this section we discuss our optical simulations of the revised SCOW-DFB structure. These simulations mirror those of Section 7.1.3, and so we present only their main results here. Figure 7-24 shows the fundamental SCOW-DFB mode in both the grating pillar and grating trench cross-sections. The average confinement factor is ~1%, which is double the confinement of typical SCOW structures. This is necessary to compensate for the 50% reduction in device length. The effective index difference between the individual cross sections is $\Delta n_{eff} = 1.62 \times 10^{-4}$ yielding a κL_g of 1.05.

The simulated first two higher-order modes of the SCOW-DFB are shown in Fig. 7-25. As can be verified from the figure, the mode overlaps with the active region and gratings are both

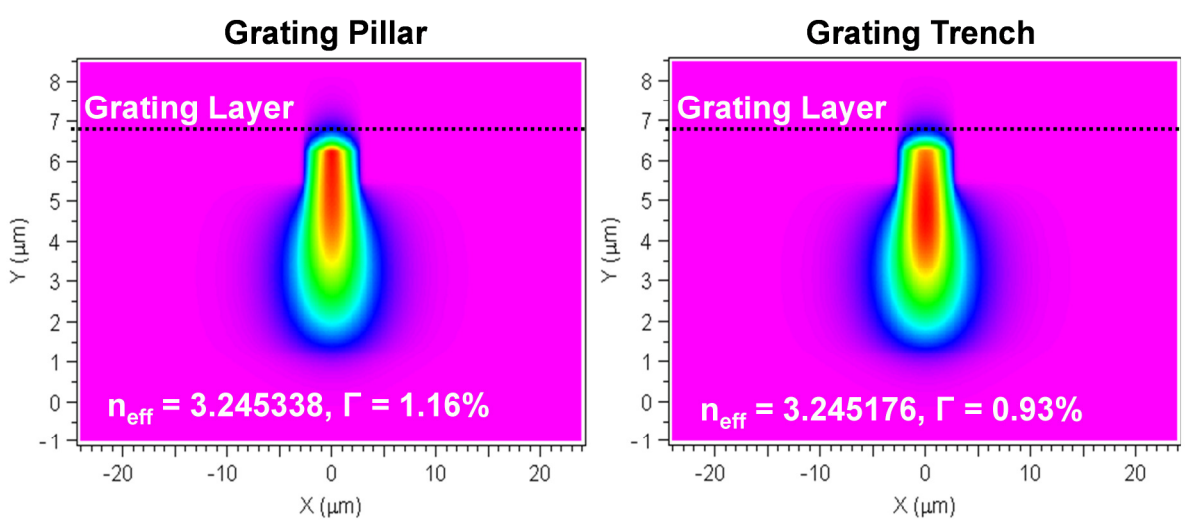

Figure 7-24: SCOW-DFB modes for both grating cross sections with the grating layer (dashed line) indicated. The values of the effective modal index are also provided.

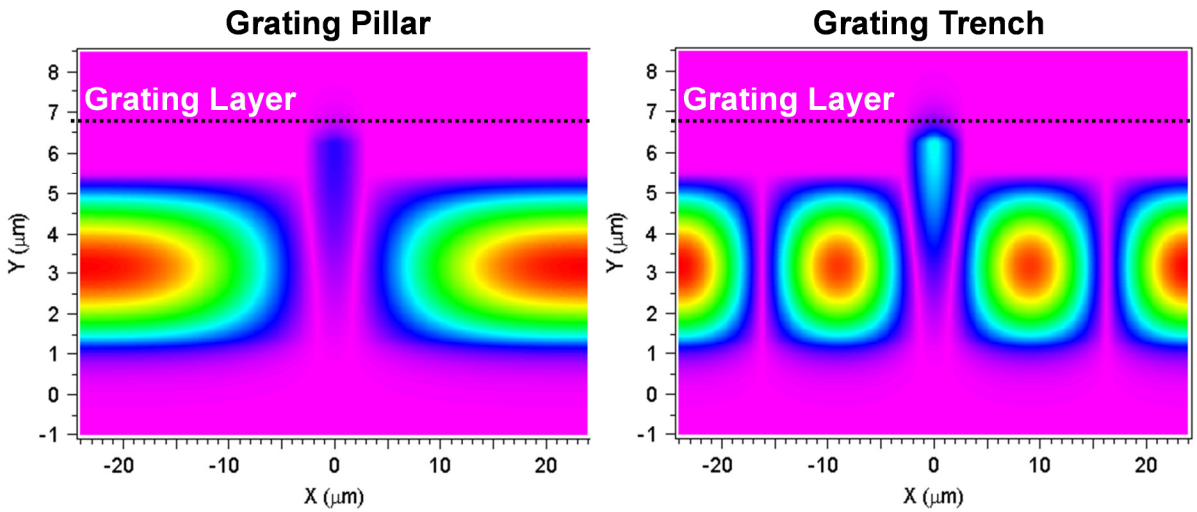

Figure 7-25: Higher-order SCOW-DFB modes for both grating cross sections with the grating layer (dashed line) indicated.

negligibly small. However, once again, we note that the simulations of the higher-order modes do not yield complete agreement with our experimental observations of the competition between SCOW modes.

7.5.3 Second Generation SCOW-DFB Electrical Simulations

Here, we discuss our electrical simulations of the revised SCOW-DFB structure. As was emphasized in the previous sections, these simulations are necessary to ensure proper functionality of the device. Figure 7-26 shows the band diagrams at biases of 0 V and 1.2 V. Note that the InP etch stop was removed during simulation as SimWindows has difficulty accounting for effects of tunneling. This can be readily verified through simulations of structures with barriers as thin as a few angstroms. Since the buffer and grating layers are formed from the same material, their cascade appears as a continuous band of energies in Fig. 7-26. It can be observed that the potential well introduced by the grating layer in Fig. 7-17 is no longer an issue in our revised design.

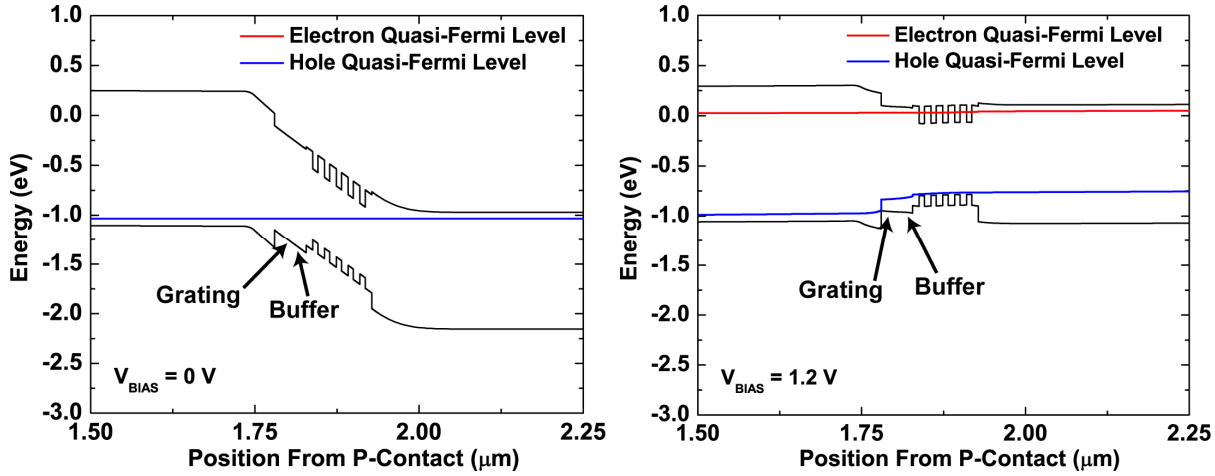

(a) (b)

Figure 7-26: Band diagram of the SCOW-DFB for operation at (a) 0 V bias and at (b) 1.2 V bias. The electron and hole quasi-Fermi levels are also provided.

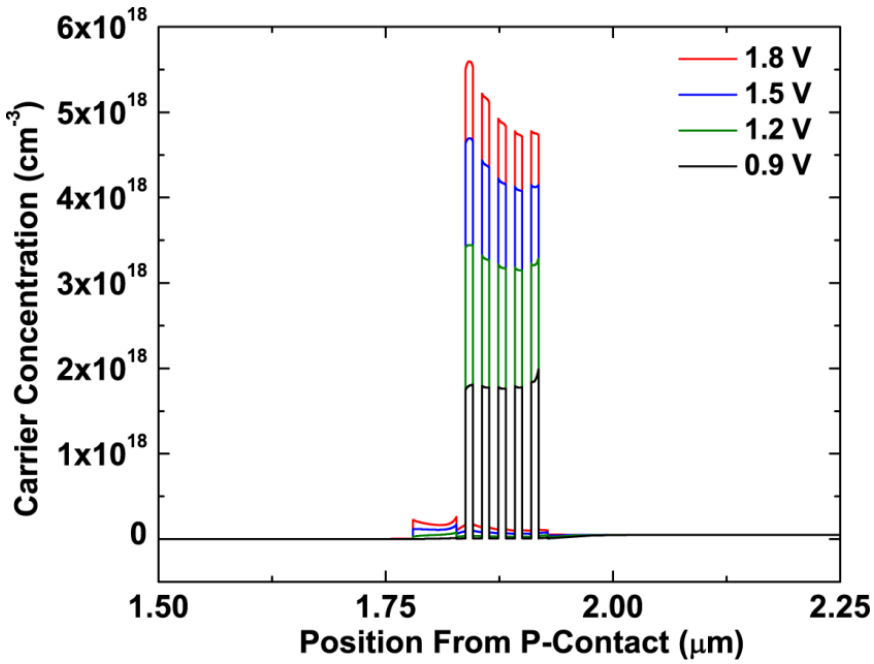

Figure 7-27: Carrier concentrations as a function of position within the SCOW-DFB structure for voltage biases of 0.9 V – 1.8 V.

The intrinsic InP adjacent to the grating layer is a result of our regrowth process and introduces a sharp discontinuity in the conduction and more importantly valence bands. This discontinuity results in a potential barrier that blocks holes from reaching the quantum wells. A voltage must be applied in order to overcome the effects of this barrier, as can be verified in the hole quasi-Fermi level of Fig. 7-26 (b). However, the effects of the intrinsic InP layer will likely be mitigated by dopant diffusion from later stages in the regrowth process.

Figure 7-27 shows the profile of the carrier concentration within the SCOW-DFB structure as a function of applied bias. The feature on the left corresponds to the carriers trapped within the grating and buffer layers, while the five peaks on the right correspond to the carriers injected into the quantum well. Compared to Fig. 7-18, the carrier concentrations within the wells are larger, while the carrier concentration confined to the grating layer is clearly reduced. Note that the level of carrier density in the grating and buffer layers is similar to that of the barriers and is below that of the doped p-InP in conventional SCOW structures.

To complete our electrical simulations, we show the predicted I-V relations of the SCOW-

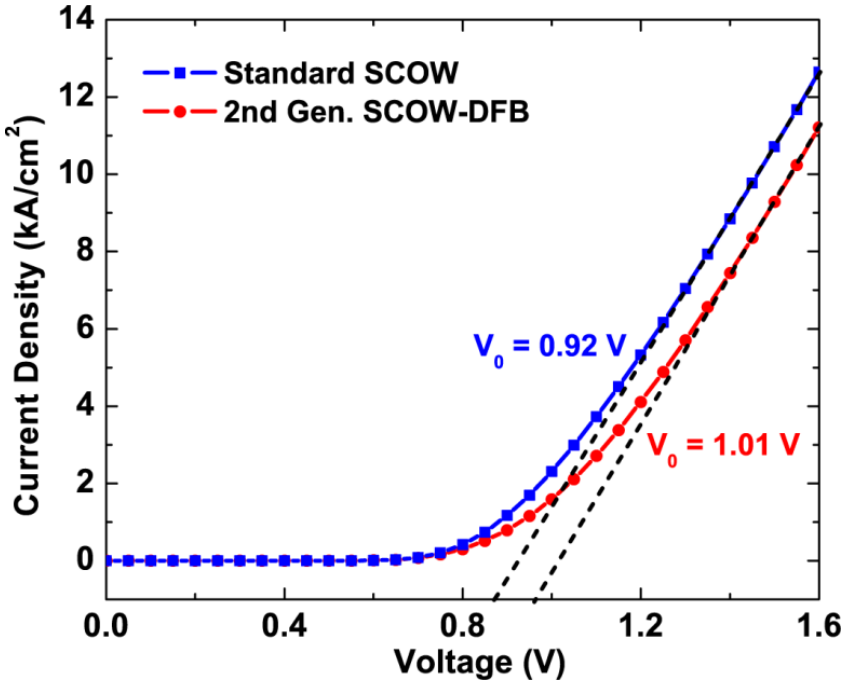

Figure 7-28: Simulated I-V relations for the standard SCOW structure and for the second-generation SCOW-DFB. The turn-on voltage for each respective device is also provided.

DFB in Fig. 7-28. The I-V characteristics corresponding to a standard five-quantum-well SCOW structure (no grating or buffer layers) is provided again for reference. With the revised SCOW-DFB design, the turn-on voltage decreases from 1.22 V (Fig. 7-19) to 1.01 V. The remaining voltage difference is consumed by the intrinsic InP layer introduced during regrowth. As expected, the series resistance is nearly identical between the SCOW-DFB and standard SCOW structure.

7.6 Fabrication of Second Generation SCOW-DFB

Here, we discuss our planned process for the fabrication of the second generation SCOW-DFBs. Most of the steps have already been detailed in Section 7.2.2 and follow standard processes developed at MIT Lincoln Laboratory. We will thus focus our attention on the areas that are new

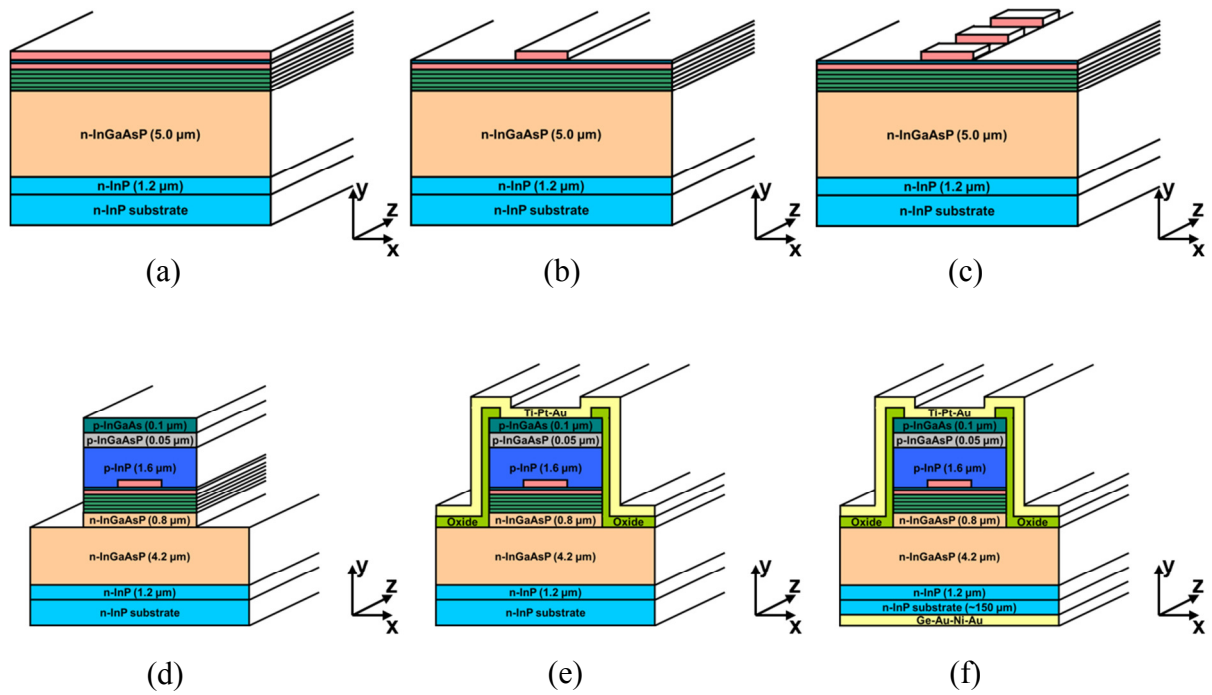

Figure 7-29: SCOW-DFB fabrication process starting from (a) an InP wafer grown up to the grating layer and ending with (f) the patterned and metalized SCOW-DFB structure.

in our second-generation design.

Figure 7-29 shows a summary of the planned process sequence. We begin with a 5.0-μm thick n-InGaAsP waveguide on an n-InP substrate (image (a)). Five quantum wells are located directly above the waveguide along with a 0.02 μm InGaAsP buffer layer, a thin 1 nm InP etch stop, and a 0.04 μm grating layer. Next, the grating layer is patterned into a stripe with variable width between 1 μm and 4 μm (image (b)). This patterning is performed using a selective wet etch with a nitride mask, stopping on the InP etch-stop layer. The next step is to define the grating pillars within this stripe (image (c)). There are three ways that we are currently exploring regarding how to accomplish this goal. One way is to use interference lithography to first pattern the grating features into a photoresist and then to subsequently transfer these features into the grating layer using the photoresist as a mask. This process of grating transfer is performed using a wet etch that again stops on the InP etch-stop layer. Should the etch penetrate this layer, the buffer and bounding layers serve as extra fodder preventing the etch from contaminating the quantum wells. The main concern of using photoresist as a mask is the peeling of the photoresist during the wet etch step, resulting in a lateral undercutting of the structure beneath the mask.

The second option for defining the gratings is to transfer the photoresist grating pattern into an oxide hard mask and then subsequently to transfer these features into the InGaAsP grating layer. The benefit is that the oxide mask does not suffer from issues of peeling that would normally occur when wet etching with a photoresist mask. However, the main issue with the oxide mask is the potential for extraneous reflections during the interference lithography exposure that can otherwise cancel the interference pattern in the gratings without the use of an anti-reflection coating (ARC) layer. This ARC layer was not needed with a pure photoresist mask due to the thickness of the photoresist (~40 nm) being much less than the wavelength of the exposing light (325 nm).

The third option we are exploring is the use of e-beam lithography to define the grating features. This technique is especially attractive as it simplifies steps (b) and (c) of Fig. 7-29 into a single lithography step. However, the main issue with the e-beam approach is the relatively small size of the writing field (~500 μm), which results in the need to stitch together multiple fields along the length of the 5 mm device. For the e-beam system being used, the stitching error between adjacent fields is measured to be <2.5 nm, which is a relatively small fraction of the overall grating period (240 nm).

The remainder of the process sequence follows similarly to that of Fig. 7-10. After the gratings are defined, regrowth is performed via MOCVD at 625 ºC to grow the rest of the SCOW-DFB structure (image (d)). This includes a 1.6 μm p-InP cladding layer along with the p-InGaAsP and p-InGaAs layers forming the contact to the metal. Next, ridges of 5.8 μm width are defined using ICP-RIE etching into the n-InGaAsP waveguide, masked by aluminum oxide on nitride. The mask is removed with a 12 minute 10:1 H2O:HF wet etch.

A bi-layer of oxide (image (e)) is then deposited over the ridge using a combination of pyrolytic oxidation (1.2 μm at 350 °C) and LPCVD (1.7 μm at 275 °C). The vias are opened along the center of the ridge using a CF4 RIE etch. Ti (200 Å)-Pt (400 Å)-Au (1000 Å) is subsequently evaporated to form the p-contact metal and is lifted off at the edges between devices. Finally, after thinning the surface of the backside to ~6 mil (~150 μm), Ge (300 Å)-Au (600 Å)- Ni (300 Å)-Au (2000 Å) is evaporated onto the backside to form the n-metal contact (image (f)).

7.7 Conclusion

In this chapter, we described the design, fabrication, and measurement of DFB lasers incorporating SCOW technology as a means to achieve both high-power and low-noise operation. Our design primarily focused on the optical waveguiding properties of the structure but neglected the carrier transport through the junction. The fabrication of the DFBs was performed using interference lithography in combination with standard SCOW processing techniques developed at MIT Lincoln Laboratory. Upon testing of the fabricated devices, we found large threshold currents (~3.8 A) along with multi-longitudinal mode lasing and poor I-V characteristics (turn-on voltage: 1.15 V). The single-pass gain of the SCOW structure was also separately measured to be 4 dB. Electrical simulations of the SCOW-DFB structure indicated the formation of a potential well, trapping injected carriers and generating excess free-carrier loss for the optical mode. Moreover, the intrinsic InP buffer layer acted as a barrier to carrier flow into the wells, resulting in an increase in the turn-on voltage necessary to counteract these effects. Finally, SEM imaging of the post-fabrication gratings showed that the grating pillars had reduced in height by a factor of 2 due to Indium migration at the temperatures of regrowth.

The problems associated with the first generation SCOW-DFB motivated us to redesign the grating and buffer layers so that the issues with electrical transport are remedied. In our second generation design, we replaced each of these layers with InGaAsP material of lower bandgap so that the transport of holes into the quantum wells is no longer inhibited. The use of lower bandgap, higher index material also leads to a decrease of Indium content and thus improves on the attrition of the grating pillars during regrowth. However, with a higher index, it becomes necessary to redesign the active confinement factor and mode overlap with the gratings so that both parameters are simultaneously optimized in the second generation structure. The fabrication and eventual testing of these SCOW-DFBs is currently underway.

Chapter 8

Conclusions and Future Work

This thesis merges together elements of semiconductor devices, microwave-photonic (MWP) systems, and oscillator phase-noise. The overall goal was to demonstrate a low phase-noise optoelectronic oscillator (OEO) that takes advantage of the capabilities afforded by high-power low-noise slab-coupled optical waveguide (SCOW) components. Our work on OEOs led us to investigate the unique properties of the gain experienced by signals transmitted over MWP links. Furthermore, our desire to understand the performance limitations of the OEO motivated us to formulate a unified description of phase noise applicable to any electromagnetic oscillator. Below we summarize the main points of this thesis and also provide possible avenues for future exploration.

Noise degrades the spectral purity of every oscillator system. Its influence on oscillators can be decomposed into perturbations of the oscillating field's amplitude and phase. As was discussed in Chapters 2 and 3, almost all oscillators are limited by phase noise rather than by amplitude noise. This was a consequence of an oscillator's intrinsic amplitude-noise limiting mechanisms (e.g., the saturation of the amplifier and negative feedback stabilization around the point of oscillation). In Chapter 2, we specifically addressed the influence of white-noise perturbations on oscillator behavior [46]. We showed that the end result was a broadened lineshape in the form of a Lorentzian. One key contribution from our work was a concept of noise partitioning such that each mode received a fraction of the available noise power. This partitioning occurs due to effects of confinement in an oscillator cavity. In the absence of a cavity, the noise emits into a continuum of modes and thus appears white over a broad range of frequencies. However, within the confines of a bounded cavity, the basis changes thereby forcing the noise to emit only into a discrete set of modes pertaining to the new system. The noise that perturbs any given oscillator mode is exactly the noise that becomes coupled into the mode. For the case of white noise, the noise power is equally coupled into all of the oscillator modes. With knowledge of the noise spectral density, signal power, and roundtrip delay, we showed both

theoretically and experimentally that the phase noise of any electromagnetic oscillator can be precisely determined.

In Chapter 3, we extended the treatment of oscillator phase-noise to noise perturbations characterized by $1/f^{\alpha}$ spectral shape [71]. This class of noise is commonly referred to as flicker noise and is especially important as it ultimately limits the phase noise of every oscillator, especially at low offset frequencies. The case of flicker noise is difficult to analyze for two reasons. First, one needs a clear picture of how low-frequency flicker noise can be upconverted onto the oscillating signal operating at frequencies in the RF or optical range. Second, one then requires an equivalent concept of partitioning that governs the noise that becomes coupled into the oscillating mode. This task is particularly difficult due to the divergence of the noise power at DC. We showed in Chapter 3 that the interpretation of flicker noise in an oscillator becomes greatly simplified if one views its upconversion from the perspective of a gain fluctuation. From here, we arrived at the appropriate form of the oscillator's instantaneous-frequency fluctuations and eventually derived an expression for its phase noise. Once again, excellent agreement was found between experiment and theory across a wide range of oscillators.

Beyond the advances offered by our treatment of oscillator phase-noise, there still remains significant territory left to explore. Many of the remaining challenges are related to understanding the interaction of noise with the oscillator, especially for the case of flicker-noise. In our analysis, we did not provide a complete interpretation regarding the partitioning of flicker noise into the oscillator's modes. It is likely that the resolution of this issue will lead to an understanding that can be universally applied to any noise process. Outside the realm of oscillators, the origin of flicker noise itself is still a perplexing issue that to this day remains a topic of research and debate.

Another possible area for future work is the extension of this model to non-electromagnetic oscillators. The concept of a mode is universal to any physical system, and thus an equivalent form of noise partitioning can in principle be defined for any oscillator. We anticipate the greatest challenge towards this will be quantifying the equivalent system parameters for these oscillators. Examples of other oscillator varieties include mechanical oscillators, biological oscillators, etc. One more area of interest pertains to the extension of our noise model to systems whose oscillation is non-sinusoidal. We note that any periodic oscillatory signal supported by the cavity can be formed from a superposition of the individual cavity modes. We anticipate the next

step is to assign the noise associated with the various cavity modes to the supermode formed by the oscillator. This is similar to the treatment of noise in gain-guided lasers [53].

In Chapter 4 we demonstrated an OEO formed from high power, low noise SCOW components [58]. The use of a SCOW external cavity laser (SCOWECL) [27] and a variable-confinement SCOW photodiode (VC-SCOWPD) enabled OEO oscillation without the need for additional amplification (i.e., optical or RF). This has the benefit of reducing the system noise and also lowering the overall size, weight, and power consumption of the OEO. Low phase-noise was achieved by virtue of the SCOWECL's low relative intensity noise (RIN) along with the long passive delay of the optoelectronic cavity. The SCOW-OEO demonstrated a measurement-limited <-120 dBc/Hz phase noise at 1-kHz offset frequency for a 1-km length of optical delay. Its corresponding sidemode suppression relative to the carrier was measured to be >88 dB, again limited by the measurement floor of our instrumentation. Throughout the chapter, we also demonstrated the importance of suppressing fiber nonlinearities and minimizing amplitude-to-phase (AM-PM) noise processes in the photodiode.

One open question during this work was the sudden increase in sidemode levels when either RF or optical amplification was employed within the OEO cavity. This phenomenon was primarily observed in the phase noise of the sidemodes, and the level of the increase appeared greater for sidemodes closer in frequency to the oscillating mode. It is possible that the flicker noise introduced by the amplifier (optical or RF) has a large impact on the sidemode phase-response, despite being much lower than the white noise at the corresponding frequencies of the sidemodes. However, this is for the most part speculation, and thus the exact mechanism governing this phenomenon requires further investigation.

One major limitation to the SCOW-OEO performance is the degradation of its noise properties at higher optical powers. This degradation occurs due to noise introduced from stimulated Brillouin scattering (SBS) when propagating over long lengths of optical fiber. The SBS process intensifies with increasing fiber length and thus becomes the primary obstacle preventing the use of longer fiber delays in the OEO system. Some techniques for suppressing SBS effects include phase modulation and also the use of specialty non-uniform or hollow-core fiber. However, even these approaches do not completely nullify the noise degradation mechanism and only serve to delay its onset. Many systems (including the OEO) can benefit

greatly if the SBS process can be effectively eliminated. This may be one possible avenue for future research.

To date, the current demonstrations of the SCOW-OEO have all been operated under free-running conditions. However, the highest performance achievable by any oscillator is typically obtained under locked conditions when there is active compensation for errors in phase or amplitude. The circuitry used for stabilizing traditional oscillators can in principle be applied to the OEO for the possibility of realizing orders of magnitude improvement in phase noise. The exact details on how to implement these schemes requires further investigation.

In Chapter 5, we discussed an interesting property of the gain exhibited by MWP systems. In particular, we showed that the MWP gain is "super-homogeneous" such that under the effects of saturation, the reduction in gain is lower for the saturating signal than it is for other weaker signals transmitted simultaneously [77]. To our knowledge, this property of gain is currently not known to exist in any other system. The significance is that for an OEO, any sidemodes transmitted with the dominant oscillating mode will experience higher intracavity loss and thus become attenuated to nearly zero over the course of several cavity roundtrips. This unique property inherently mitigates the problem of multi-moded behavior in an OEO, which would otherwise become significant due to the long OEO delay lengths used. In Chapter 5, we showed that the resulting sidemodes of the SCOW-OEO are attenuated nearly to the level of its background noise.

Our work on the super-homogeneous gain opens up the possibility of applying these unique properties to other physical systems that employ MWP gain. In Chapter 5, we showed one such application using the super-homogeneous gain as an infinitesimally narrowband filter that can provide discrimination against a larger signal in favor of a smaller signal [111]. These unique properties occur for two signals spaced arbitrarily apart in frequency and are enabled by the highly nonlinear photodiode response to modulation. We showed that 55 dB suppression of the larger tone can be achieved relative to the amplitude of the smaller tone. This suppression applies not only to the peak of the signal but also to its surrounding phase-noise sidebands, potentially allowing for the uncovering of smaller signals which would otherwise be buried below the phase noise of a larger tone. One challenge to exploiting these properties of the MWP gain is that the suppression is reliant on setting the amplitude of the larger signal to a specific level relative to V_π, within an accuracy of ~0.01 dB.

Our work in Chapter 5 leaves many areas open for future exploration. For example, the nonlinear gain properties of an OEO result in cross-injection of energy between the modes on the left and right halves of the spectrum. This cross-injection is a result of the intermodulation product ($2\omega_1 - \omega_3 = \omega_2$) and serves as a mechanism which locks the phase between the modes of an OEO. The phase-locking of the modes may be a potential enabler for other interesting applications or measurements. Note that this property requires the oscillation condition of the sidemodes to be first satisfied. Other future directions include exploring the possibility of using MWP links to perform nonlinear operations (such as wavelength conversion) as well as using super-homogeneous gain to strategically manipulate both the gain and phase of the transmitted signals.

In Chapter 6, we demonstrated a RF-amplifier-free coupled optoelectronic oscillator (COEO) comprising high-power, low-noise SCOW components [106]. To our knowledge, this represents the first demonstration of a RF-amplifier-free COEO. The specific components used consisted of a VC-SCOWPD operating at 10 GHz and a packaged Watt-class SCOW amplifier (SCOWA) [23]. The architecture of the SCOW-COEO is identical to that of a regenerative modelocked laser but is optimized for the purpose of achieving a low phase-noise RF signal at 10 GHz. Unlike the case of the SCOW-OEO, the SCOW-COEO does not suffer much from noise degradation due to effects of SBS. The reason for this is because the SCOW-COEO operates as an optical pulsed source, and thus the power per individual comb line is only a small fraction of the total power. Furthermore, we also did not observe any additional degradation due to AM-PM noise processes within the photodiode. The phase-noise performance was measured to be -115 dBc/Hz at 1-kHz offset frequency, while the sidemode suppression relative to the oscillation signal was >70 dB measurement-limited. The RIN of the SCOWA and the relatively short delay lengths achievable serve as the primary limitations to the SCOW-COEO performance.

Our work on the SCOW-COEO leaves several avenues open for continued research in the field. For example, both the OEO and COEO architectures have the capabilities to simultaneously generate outputs in both the optical and electrical domains. In the case of the COEO, this is especially beneficial as an optical pulsed source is inherently useful for many applications. Although our SCOW-COEO has achieved excellent performance in terms of RF phase-noise, we have largely ignored the optical pulse properties of the system. Preliminary measurements of these characteristics show relatively broad pulses in the range of 20 ps. In

principle, the pulses can be made far narrower with efficient use of the gain-bandwidth. Further investigations would be needed to accomplish these goals.

One of the major limitations to the SCOW-COEO performance is the relatively short fiber delays that can be practically achieved in the system. As was found in Chapter 6, the stability of the system degrades significantly for longer delay lengths. This instability was related to the large number of sidemodes that appear as a result of the decrease in free spectral range. Ideally, one desires the ability to arbitrarily increase the SCOW-COEO delay in order to achieve significant reductions in its phase noise. Further research is needed to determine if other possibilities exist that can suppress these sidemode instabilities. We showed in Chapter 5 that the OEO exhibits a mechanism of super-homogeneous gain that results in large attenuation of its sidemodes. Currently, no such analysis has been performed for the COEO system. This may be one possible path for future research that has the potential to solve the instability issue of the COEO sidemodes.

In Chapter 7, we attempted to miniaturize the OEO pump laser source into the form of a compact SCOW distributed feedback laser (DFB). The SCOW-DFB was designed for 1550 nm operation with single-mode behavior and high output power. However, due to issues associated with grating deformation and with electrical transport through the device structure, the resulting DFBs lased with low power and were highly multi-moded in the longitudinal dimension. Our electrical simulations of the structure showed that the grating layer formed a potential well which not only trapped the injected carriers but also provided a source of free-carrier loss. At the time of this writing, we have redesigned the SCOW-DFB structure to improve on the first-generation design in these areas. Our future work for the SCOW-DFB includes the fabrication and testing of our second-generation design. However, another potential area for exploration involves the tailoring of the grating strength along the device so that the optimal DFB performance can be achieved. Following the demonstration of the SCOW-DFB, one can then envision strategies to integrate the other components of the OEO.

Throughout this thesis, our overarching goal was to demonstrate a SCOW-OEO whose phase-noise performance improves on that of current state-of-the-art OEOs by an order of magnitude. While the noise properties of our pump laser readily met the requirements needed to achieve these goals, the overall phase-noise of our system became limited by the lengths of fiber delay that could be practically implemented. For frequencies close to the carrier, the highest

performing OEOs today [11] are currently comparable in phase noise to that of feedback stabilized sapphire-loaded cavity oscillators (SLCOs) [112]. However, at higher offset frequencies (> 10 kHz), the OEO's sidemodes spoil the noise performance of the system [11]. In comparison, the phase noise of the SCOW-OEO was found to be only slightly worse than that of the highest performing OEOs. The lower performance of the SCOW-OEO is due to its shorter intracavity delay by a factor >10 resulting in a >20 dB degradation in its phase noise. On the other hand, we found the SCOW-OEO's sidemodes to be on the level of noise and are thus far lower than that found in conventional OEOs.

The ultimate direction for this work was to integrate the OEO system onto a single chip of InP using high-power low-noise SCOW technology. In addition to the challenges of integrating the laser, modulator, and photodetector onto a common platform, one further complication arises from how to incorporate kilometer lengths of delay onto an OEO chip. The loss of optical waveguides would be too large to reach a kilometer of delay, while the physical size of optical fiber would reduce the benefits of an integrated approach. The length of delay that can be practically achieved serves as the fundamental limitation to the phase-noise performance of an integrated OEO. Although our vision of integrating the SCOW-OEO was not completely realized, significant progress was made in developing the OEO, in miniaturizing its pump laser, and in understanding the limitations of phase-noise governing oscillators in general.

Appendix A

Appendix: Chapter 2

A.1 Derivation of the Phase-Noise Spectrum

Starting from the electric field $E(t)$ of the oscillator

$$E(t) = \sqrt{2}\left[E_0 + \Delta E(t)\right]\cos\left(\omega_0 t + \phi(t)\right) \tag{A.1}$$

we can calculate the spectrum through application of the Wiener-Khinchin theorem [61]

$$S(\omega) = \mathrm{FT}\left\langle E(t)^* E(t+\tau)\right\rangle \tag{A.2}$$

Here, E_0 is the initial field amplitude, $\Delta E(t)$ is the time-dependent amplitude shift, ω_0 is the oscillation frequency, $\phi(t)$ is the time-dependent oscillator phase, τ is the time delay of observation, and FT denotes the Fourier transform operation. Note that $E(t)$ in Eq. (A.1) is normalized so that the average power is E_0^2. The autocorrelation is evaluated directly

$$\begin{aligned}\left\langle E(t)^* E(t+\tau)\right\rangle = &\left\langle \frac{\left[E_0 + \Delta E(t)\right]\left[E_0 + \Delta E(t+\tau)\right]}{2} e^{j\left(\omega_0\tau + \phi(t+\tau) - \phi(t)\right)}\right\rangle \\ &+ \left\langle \frac{\left[E_0 + \Delta E(t)\right]\left[E_0 + \Delta E(t+\tau)\right]}{2} e^{-j\left(2\omega_0 t + \omega_0\tau + \phi(t+\tau) + \phi(t)\right)}\right\rangle \\ &+ \left\langle \frac{\left[E_0 + \Delta E(t)\right]\left[E_0 + \Delta E(t+\tau)\right]}{2} e^{j\left(2\omega_0 t + \omega_0\tau + \phi(t+\tau) + \phi(t)\right)}\right\rangle \\ &+ \left\langle \frac{\left[E_0 + \Delta E(t)\right]\left[E_0 + \Delta E(t+\tau)\right]}{2} e^{-j\left(\omega_0\tau + \phi(t+\tau) - \phi(t)\right)}\right\rangle\end{aligned} \tag{A.3}$$

Since the second and third terms on the right-hand-side average to zero, the autocorrelation evaluates to

$$\left\langle E(t)^* E(t+\tau)\right\rangle = \left\langle \frac{1}{2}\begin{bmatrix} E_0^2 + E_0 \Delta E(t+\tau) + \\ E_0 \Delta E(t) + \Delta E(t)\Delta E(t+\tau) \end{bmatrix} \left(e^{j(\omega_0\tau+\Delta\phi)} + e^{-j(\omega_0\tau+\Delta\varphi)}\right)\right\rangle \tag{A.4}$$

Eq. (A.4) introduces the variable $\Delta\phi = \phi(t+\tau) - \phi(t)$ corresponding to the total phase shift occurring over a time delay τ. In general, the correlations between amplitude and phase in Eq. (A.4) are non-zero [41] as a single noise event generates both amplitude and phase fluctuations. However, the amplitude noise is usually greatly suppressed relative to phase noise due to the oscillator's intrinsic negative feedback and also to various amplitude-limiting elements in the cavity (e.g. the amplifier). The oscillator's autocorrelation is therefore approximately due to phase fluctuations and evaluates to

$$\left\langle E(t)^* E(t+\tau)\right\rangle = \left\langle \frac{E_0^2}{2}\left(e^{j(\omega_0\tau+\Delta\phi)} + e^{-j(\omega_0\tau+\Delta\varphi)}\right)\right\rangle \tag{A.5}$$

It is clear from Eq. (A.5) that the individual terms on the right-hand-side represent the positive and negative frequencies of the corresponding spectrum. We can thus represent the autocorrelation through a phasor with only positive frequencies explicit.

As the oscillator phase is defined through a series of many noise events, it is reasonable to expect from the central limit theorem that the phase distribution follows a Gaussian. Starting from the Fokker-Planck equation, Ref. [42] proves this to be exactly true for infinite observation time. Reference [42] also shows that only the cumulants of first and second order survive in $\Delta\phi$, and therefore the total phase shift is also Gaussian distributed. Evaluation of the expectation value then requires only the integration of Eq. (A.5) multiplied by a Gaussian probability density.

$$\left\langle E(t)^* E(t+\tau)\right\rangle = E_0^2 \left\langle e^{j(\omega_0\tau+\Delta\phi)}\right\rangle = \frac{E_0^2 e^{j\omega_0\tau}}{\sqrt{2\pi\sigma^2}} \int_{-\infty}^{\infty} e^{j\Delta\phi} e^{-\frac{\Delta\phi^2}{2\sigma^2}} d\Delta\phi = E_0^2 e^{j2\pi f_0\tau} e^{-\langle\Delta\phi^2\rangle/2} \tag{A.6}$$

In evaluating Eq. (A.6), we have used the fact that the average phase shift (first moment) is zero and thus the variance in phase shift σ^2 is given by its second moment $\left\langle \Delta\phi^2 \right\rangle$.

A.2 Vector Combination of Noise Sources

Here, we show that the vector of combined noise sources satisfies Eq. (2.9) for a single roundtrip of the oscillator. We begin with the total phase shift $\Delta\phi_{RT}$ due to M_{RT} noise events in a cavity roundtrip. The contribution of noise over a roundtrip yields a net phase shift

$$\Delta\phi_{RT} = \sum_{i=1}^{M_{RT}} E_n \frac{\sin\theta_i}{E_0} \tag{A.7}$$

Here, E_n is the field amplitude of a noise event, E_0 is the field amplitude of the signal, and θ_i is the phase of the noise relative to the oscillating field. We can equivalently combine the noise events over the time of a roundtrip into a combined noise vector ($E_{n,tot}$) through

$$E_{n,tot} = \sum_{i=1}^{M_{RT}} E_n e^{j\theta_i} = \sqrt{\left(\sum_{i=1}^{M_{RT}} E_n \cos\theta_i\right)^2 + \left(\sum_{i=1}^{M_{RT}} E_n \sin\theta_i\right)^2}\, e^{j\tan^{-1}\left(\sum_{i=1}^{M_{RT}} E_n \sin\theta_i \Big/ \sum_{i=1}^{M_{RT}} E_n \cos\theta_i\right)} \tag{A.8}$$

Applying Eq. (2.9), the combined phase shift ($\Delta\phi_{tot}$) is

$$\Delta\phi_{tot} = \frac{\left|E_{n,tot}\right|}{E_0} \sin\left(\angle E_{n,tot}\right) = \frac{\sum_{i=1}^{M_{RT}} E_n \sin\theta_i}{E_0} \tag{A.9}$$

The equivalence of Eqs. (A.7) and (A.9) establishes the validity of representing the roundtrip noise through a combined noise vector, even if the total amplitude and phase shift are no longer small compared to that of the oscillating field.

A.3 Effects of Oscillator Non-uniformity

Here, we wish to address one potential concern regarding the application of our phase-noise theory when the oscillator characteristics are non-uniform. In any given oscillator, the oscillation condition establishes the net gain to be near but slightly below the level of intracavity loss. However, there are no restrictions that the gain must balance the loss at every point within the cavity. It is easy then to imagine a scenario where the signal power is non-uniform within the oscillator so that the influence of noise changes along its length. We are interested in discussing whether or not our developed techniques can still be applied to these cases.

Consider the situation of Fig. A-1 depicting an oscillator whose gain comprises a cascade of three amplification stages. We expect the output power to increase after each amplifier stage so that the loss introduced by the RF filter and output coupler causes the power to stabilize to its steady-state value. It is clear that the magnitude of the signal vector changes along points (i), (ii), and (iii), which non-uniformly impacts its interaction with the noise. To begin, we consider an initial signal power of P_{in} at the input to the first amplifier. The output of the amplifier is

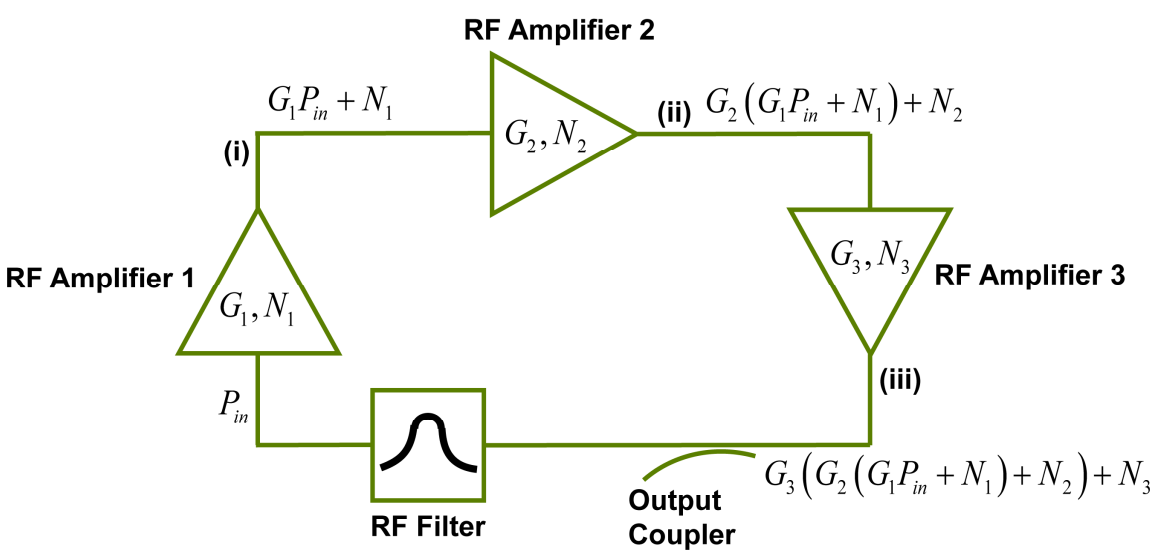

Figure A-1: RF oscillator consisting of three amplification stages, an RF filter, and an output coupler. Points (i), (ii), and (iii) label the outputs of RF Amplifiers 1, 2, and 3, respectively.

$G_1 P_{in} + N_1$ where G_1 represents the large-signal gain of Amplifier 1 and N_1 represents the noise of Amplifier 1. As per our analysis in this chapter, the perturbation of the oscillating field due to noise can be evaluated using Fig. 2-3. However, as the ratio of noise-to-signal is invariant under attenuation or gain, we can instead choose to hold these calculations until the very end.

Continuing on to Amplifier 2, we can represent its output as $G_2\left(G_1 P_{in} + N_1\right) + N_2$ where G_2, N_2 are the large-signal gain and noise of Amplifier 2. Here, the gain of the second amplifier boosts the signal power so that the interaction of N_2 with the oscillating field becomes weaker. Once again, we hold these calculations until the very end and instead continue on to Amplifier 3. The output of Amplifier 3 can be expressed as $G_3\left(G_2\left(G_1 P_{in} + N_1\right) + N_2\right) + N_3$ where G_3, N_3 are the large-signal gain and noise of Amplifier 3. Now, when we measure the total noise added in a cavity roundtrip, we would find $G_3 G_2 N_1 + G_3 N_2 + N_3$ which represents a weighted sum of the individual noise sources. The noise contributions which undergo more amplification would have a proportionally larger effect on the output signal $G_3 G_2 G_1 P_{in}$. The ratio of the total noise to the total signal is then

$$\frac{G_3 G_2 N_1 + G_3 N_2 + N_3}{G_3 G_2 G_1 P_{in}} = \frac{N_1}{G_1 P_{in}} + \frac{N_2}{G_2 G_1 P_{in}} + \frac{N_3}{G_3 G_2 G_1 P_{in}} \tag{A.10}$$

which is what one would intuitively expect. As long as the total output noise (including amplification) is measured, the effects of oscillator non-uniformity are exactly accounted for. Note that this analysis applies to oscillators comprising an arbitrary number of amplification stages and also to oscillators exhibiting gain that is distributed over an active length.

Appendix B

Appendix: Chapter 3

B.1 Derivation of the Mixer (IF) Voltage Output

We begin by considering the voltage of an oscillator defined through

$$V_{RF} = V_0 \sin\left(\omega_0 t + \theta_0(t)\right) \tag{B.1}$$

incident on the RF arm of an ideal mixer. Here, ω_0 defines the frequency of oscillation. In Eq. (B.1), we ignore the effects of amplitude noise on the oscillation amplitude V_0 and use $\theta_0(t)$ to account for fluctuations of the oscillator's phase. Imagine now that one wishes to measure the phase noise using a suitably low noise reference oscillator. The reference is sent into the LO arm of the mixer and is phase locked to the original oscillator waveform so that both oscillators share the same operating frequency. The mixer is also biased at quadrature enforcing the LO voltage at ω_0 to follow a cosine response pattern. The operation of the mixer then generates an IF voltage that consists of the product between the individual RF and LO signals

$$\begin{aligned} V_{IF} &= \alpha_m V_0 \sin\left(\omega_0 t + \theta_0(t)\right)\cos\left(\omega_0 t + \theta_{ref}(t)\right) \\ &= \frac{\alpha_m V_0}{2}\sin\left(\theta_0(t) - \theta_{ref}(t)\right) + \frac{\alpha_m V_0}{2}\sin\left(2\omega_0 t + \theta_0(t) + \theta_{ref}(t)\right) \end{aligned} \tag{B.2}$$

In Eq. (B.2), $\theta_{ref}(t)$ represents the phase fluctuations of the reference oscillator, which closely tracks $\theta_0(t)$ by action of the phase-locked loop. We have also introduced α_m to account for losses during the mixing process. The IF signal is subsequently low-pass filtered

$$V_{IF}^{LP} = \frac{\alpha_m V_0}{2}\sin\left(\theta_0(t) - \theta_{ref}(t)\right) \tag{B.3}$$

retaining only the contributions near DC. Detection of V_{IF}^{LP} using a spectrum analyzer yields the desired phase-noise spectrum of the oscillator.

Upon comparing Eq. (B.3) to (B.2), we see that V_{IF}^{LP} is a scaled, frequency-shifted, and *biased* version of the original oscillator voltage V_{RF}. If $\theta_{ref}(t)$ is independent from $\theta_0(t)$ and also much lower in magnitude, this measurement would yield approximately the phase-noise spectrum of the original oscillator. In other words, one can always beat two oscillators together and measure the noise of the lower-performing system. If however $\theta_{ref}(t)$ is correlated with $\theta_0(t)$ as would be the case using a phase-locked loop, then the measured spectrum becomes distorted by the degree of correlation. For perfect correlation ($\theta_{ref}(t)=\theta_0(t)$), V_{IF}^{LP} becomes 0. This means that the measured phase noise vanishes when one mixes an oscillator with its twin.

Under normal operating conditions, $\theta_{ref}(t)$ and $\theta_0(t)$ are only partially correlated and only within the phase-locked loop bandwidth. In these cases, $\theta_0(t)-\theta_{ref}(t)$ is small (but non-zero), and the measured phase-noise spectrum becomes suppressed for offset frequencies within the loop bandwidth. The significance is that measuring the spectrum of V_{IF}^{LP} is effectively equivalent to measuring the spectrum of $\theta_0(t)-\theta_{ref}(t)$ by virtue of the small-angle approximation. When the phase tracking of the reference oscillator is later accounted for in post-analysis by correcting for the distortion at low offset frequencies, the spectral density corresponding to $\theta_0(t)$ is recovered. Our analysis therefore shows that it is the spectral density of phase that is determined in an oscillator phase-noise measurement. Note that this is only true if both the small-angle approximation is applicable ($\theta_{ref}(t)$ tracks $\theta_0(t)$) *and* post-analysis correction is used on the measured spectrum. These conditions apply to most measurements of oscillator phase noise but do not apply when the spectrum is directly detected by a spectrum analyzer. In this case, no mechanism of phase tracking exists, and it is the spectral density of the field that is found.

Bibliography

[1] J. R. Vig, "Military applications of high accuracy frequency standards and clocks," *IEEE Trans. Ultrason., Ferroelectr., Freq. Control*, vol. 40, pp. 522–527, 1993.

[2] R. Th. Kersten, "Ein optisches nachrichtensystem mit bauelementen der integrierten optic für die übertragung hoher bitraten," *Archiv für Elektrotechnik*, vol. 60, pp. 353–359, 1978.

[3] H. F. Schlaak, A. Neyer, and W. Sohler, "Electrooptical oscillator using an integrated cutoff modulator," *Opt. Commun.*, vol. 32, pp. 72–74, 1980.

[4] X. S. Yao and L. Maleki, "Optoelectronic microwave oscillator," *J. Opt. Soc. Am. B*, vol. 13, pp. 1725–1735, 1996.

[5] X. S. Yao and L. Maleki, "Optoelectronic oscillator for photonic systems," *IEEE J. Quantum Electron.*, vol. 32, pp. 1141–1149, 1996.

[6] C. H. Cox III, *Analog Optical Links: Theory and Practice*. Cambridge University Press, 2004.

[7] X. S. Yao and L. Maleki, "Dual microwave and optical oscillator," *Opt. Lett.*, vol. 22, pp. 1867–1869, 1997.

[8] X. S. Yao, L. Davis, and L. Maleki, "Coupled optoelectronic oscillators for generating both RF signal and optical pulses," *IEEE J. Lightwave technol.*, vol. 18, pp. 73–78, 2000.

[9] A. B. Matsko, D. Eliyahu, P. Koonath, D. Seidel, and L. Maleki, "Theory of coupled optoelectronic microwave oscillator I: expectation values," *J. Opt. Soc. Am. B*, vol. 26, pp. 1023–1031, 2009.

[10] M. Nakazawa, E. Yoshida, and Y. Kimura, "Ultrastable harmonically and regeneratively modelocked polarisation-maintaining erbium fibre ring laser," *Electron. Lett.*, vol. 30, pp. 1603–1605, 1994.

[11] D. Eliyahu, D. Seidel, and L. Maleki, "Phase noise of a high performance OEO and an ultra low noise floor cross-correlation microwave photonic homodyne system," in *Proc. IEEE Frequency Control Symposium (FCS)*, 2008.

[12] X. S. Yao, L. Maleki, Y. Ji, G. Lutes, and M. Tu, "Dual-loop opto-electronic oscillator," in *Proc. IEEE Frequency Control Symposium (FCS)*, 1998.

[13] E. N. Ivanov, M. E. Tobar, and R. A. Woode, "Advanced phase noise suppression technique for next generation of ultra low-noise microwave oscillators," in *Proc. IEEE Frequency Control Symposium (FCS)*, 1995.

[14] T. M. Fortier, M. S. Kirchner, F. Quinlan, J. Taylor, J. C. Bergquist, T. Rosenband, N. Lemke, A. Ludlow, Y. Jiang, C. W. Oates, and S. A. Diddams, "Generation of ultrastable microwaves via optical frequency division," *Nature Photon.*, vol. 5, pp. 425–429, 2011.

[15] D. J. Jones, S. A. Diddams, J. K. Ranka, A. Stentz, R. S. Windeler, J. L. Hall, and S. T. Cundiff, "Carrier-envelope phase control of femtosecond mode-locked lasers and direct optical frequency synthesis," *Science*, vol. 288, pp. 635–639, 2000.

[16] E. A. J. Marcatili, "Slab-coupled waveguides," *Bell Systems Technical Journal*, pp. 645–674, 1974.

[17] J. N. Wapole, J. P. Donnelly, P. J. Taylor, L. J. Missaggia, C. T. Harris, R. J. Bailey, A. Napoleone, S. H. Groves, S. R. Chinn, R. Huang, and J. Plant, "Slab-coupled 1.3-µm semiconductor laser with single-spatial large-diameter mode," *IEEE Photon. Technol. Lett.*, vol. 14, pp. 756–758, 2002.

[18] J. P. Donnelly, R. K. Huang, J. N. Walpole, L. J. Missaggia, C. T. Harris, J. J. Plant, R. J. Bailey, D. E. Mull, W. D. Goodhue, and G. W. Turner, "AlGaAs–InGaAs slab-coupled optical waveguide lasers," *IEEE J. Quantum Electron.*, vol. 39, pp. 289–298, 2003.

[19] P. W. Juodawlkis, J. J. Plant, J. P. Donnelly, A. Motamedi, and E. P. Ippen, "Continuous-wave two-photon absorption in a Watt-class semiconductor optical amplifier," *Opt. Express*, vol. 16, pp. 12387–12396, 2008.

[20] A. R. Motamedi, J. J. Plant, J. P. Donnelly, P. W. Juodawlkis, and E. P. Ippen, "Ultrafast nonlinearities and gain dynamics in high-power semiconductor amplifiers," *Appl. Phys. Lett.*, vol. 93, 251106 , 2008.

[21] P. W. Juodawlkis, J. J. Plant, R. K. Huang, L. J. Missaggia, and J. P. Donnelly, "High-power 1.5-µm InGaAsP-InP slab-coupled optical waveguide amplifier," *IEEE Photon. Technol. Lett.*, vol. 17, pp. 279–281, 2005.

[22] P. W. Juodawlkis, J. J. Plant, W. Loh, L. J. Missaggia, K. E. Jensen, and F. J. O'Donnell, "Packaged 1.5-µm quantum-well SOA with 0.8-W output power and 5.5-dB noise figure," *IEEE Photon. Technol. Lett.*, vol. 21, pp. 1208–1210, 2009.

[23] W. Loh, J. J. Plant, J. Klamkin, J. P. Donnelly, F. J. O'Donnell, R. J. Ram and P. W. Juodawlkis, "Noise figure of Watt-class ultralow-confinement semiconductor optical amplifiers," *IEEE J. Quantum Electron.*, vol. 47, pp. 66–75, 2011.

[24] T. Akiyama, M. Ekawa, M. Sugawara, K. Kawaguchi, H. Sudo, A. Kuramata, H. Ebe, Y. Arakawa, "An ultrawide-band semiconductor optical amplifier having an extremely high penalty-free output power of 23 dBm achieved with quantum dots," *IEEE Photon. Technol. Lett.*, vol. 17, pp. 1614–1616, 2005.

[25] K. Morito, S. Tanaka, S. Tomabechi, and A. Kuramata, "A broad-band MQW semiconductor optical amplifier with high saturation output power and low noise figure," *IEEE Photon. Technol. Lett.*, vol. 17, pp. 974–976, 2005.

[26] J. J. Plant, P. W. Juodawlkis, R. K. Huang, J. P. Donnelly, L. J. Missaggia, and K. G. Ray, "1.5-µm InGaAsP-InP slab-coupled optical waveguide lasers," *IEEE Photon. Technol. Lett.*, vol. 17, pp. 735–737, 2005.

[27] W. Loh, F. J. O'Donnell, J. J. Plant, M. A. Brattain, L. J. Missaggia, and P. W. Juodawlkis, "Packaged, high-power, narrow-linewidth slab-coupled optical waveguide external cavity laser (SCOWECL)," *IEEE Photon. Technol. Lett.*, vol. 23, pp. 974–976, 2011.

[28] P. W. Juodawlkis, J. J. Plant, W. Loh, L. J. Missaggia, F. J. O'Donnell, D. C. Oakley, A. Napoleone, J. Klamkin, J. T. Gopinath, D. J. Ripin, S. Gee, P. J. Delfyett and J. P. Donnelly, "High-power, low-noise 1.5-µm slab-coupled optical waveguide (SCOW) emitters: physics, devices, and applications," *IEEE J. Sel. Top. Quantum Electron.*, vol. 17, pp. 1698–1714, 2011.

[29] L. A. Coldren and S. W. Corzine, *Diode Lasers and Photonic Integrated Crcuits*. John Wiley & Sons, 1995.

[30] H. Kogelnik and C. V. Shank, "Coupled-wave theory of distributed feedback lasers," *J. Appl. Phys.*, vol. 43, pp. 2327–2335, 1972.

[31] M. Faugeron, M. Tran, F. Lelarge, M. Chtioui, Y. Robert, E. Vinet, A. Enard, J. Jacquet, and F. Van Dijk, "High-power, low RIN 1.55-µm directly modulated DFB lasers for analog signal transmission," *IEEE Photon. Technol. Lett.*, vol. 24, pp. 116–118, 2012.

[32] R. Menna, A. Komissarov, M. Maiorov, V. Khalfin, L. DiMarco, J. Connolly, and D. Garbuzov, "High power 1550 nm distributed feedback lasers with 440 mW CW output power for telecommunications applications," in *Proc. IEEE Conference on Lasers and Electro-Optics (CLEO)*, 2001.

[33] S. M. Madison, J. Klamkin, D. C. Oakley, A. Napoleone, J. J. Plant, and P. W. Juodawlkis, "Limits to maximum absorption length in waveguide photodiodes," *IEEE Photon. J.*, vol. 3, pp. 676–685, 2011.

[34] J. Klamkin, S. M. Madison, D. C. Oakley, A. Napoleone, F. J. O'Donnell, M. Sheehan, L. J. Missaggia, J. M. Caissie, J. J. Plant, and P. W. Juodawlkis, "Uni-traveling-carrier variable confinement waveguide photodiodes," *Opt. Express*, vol. 19, pp. 10199–10205, 2011.

[35] K. S. Giboney, M. J. W. Rodwell, and J. E. Bowers, "Traveling-wave photodetector theory," *IEEE Trans. Microwave Theory Tech.*, vol. 45, pp. 1310–1319, 1997.

[36] T. Yamatoya and F. Koyama, "Noise suppression of spectrum-sliced light using semiconductor optical amplifiers," *Electron. Commun. Jpn. Part 2*, vol. 86, pp. 28–35, 2003.

[37] D. Eliyahu, D. Seidel, and L. Maleki, "RF amplitude and phase-noise reduction of an optical link and an opto-electronic oscillator," *IEEE Trans. Microw. Theory Tech.*, vol. 56, pp. 449–456, 2008.

[38] D. B. Leeson, "A simple model of feedback oscillator noise spectrum," *Proc. IEEE*, vol. 54, pp. 329–330, 1966.

[39] A. Hajimiri and T. H. Lee, "A general theory of phase noise in electrical oscillators," *IEEE J. Solid-state Circuits*, vol. 33, pp. 179–194, 1998.

[40] T. H. Lee and A. Hajimiri, "Oscillator phase noise: a tutorial," *IEEE J. Solid-state Circuits*, vol. 35, pp. 326–336, 2000.

[41] F. X. Kaertner, "Analysis of white and f^{α} noise in oscillators," *Int. J. Circuit Theory Appl.*, vol. 18, pp. 485–519, 1990.

[42] A. Demir, A. Mehrotra, and J. Roychowdhury, "Phase noise in oscillators: a unifying theory and numerical methods for characterization," *IEEE Trans. Circuits Syst. I, Fundam. Theory Applicat.*, vol. 47, pp. 655–674, 2000.

[43] A. L. Schawlow and C. H. Townes, "Infrared and optical masers," *Phys. Rev.*, vol. 112, pp. 1940–1949, 1958.

[44] M. Lax, "Classical noise V. noise in self-sustained oscillators," *Phys. Rev.*, vol. 160, pp. 290–307, 1967.

[45] C. H. Henry, "Theory of the linewidth of semiconductor lasers," *IEEE J. Quantum Electron.*, vol. 18, pp. 259–264, 1982.

[46] W. Loh, S. Yegnanarayanan, R. J. Ram, P. W. Juodawlkis, "Unified theory of oscillator phase noise I: white noise," *IEEE Trans. Microw. Theory Tech.*, vol. 6, pp. 2371–2381, 2013.

[47] P. W. Milonni and P. L. Knight, "Spontaneous emission between mirrors," *Opt. Commun.*, vol. 9, pp. 119–122, 1973.

[48] H. H. França, T. W. Marshall, and E. Santos, "Spontaneous emission in confined space according to stochastic electrodynamics," *Phys. Rev. A*, vol. 45, pp. 6436–6442, 1992.

[49] E. M. Purcell, "Spontaneous emission probabilities at radio frequencies," *Phys. Rev.*, vol. 69, pp. 681, 1946.

[50] S. D. Brorson, H. Yokoyama, and E. P. Ippen, "Spontaneous emission rate alteration in optical waveguide structures," *IEEE J. Quantum Electron.*, vol. 26, pp. 1492–1499, 1990.

[51] T. Baba, T. Hamano, F. Koyama, and K. Iga, "Spontaneous emission factor of a microcavity DBR surface-emitting laser," *IEEE J. Quantum Electron.*, vol. 27, pp. 1347–1358, 1991.

[52] T. Baba, T. Hamano, F. Koyama, and K. Iga, "Spontaneous emission factor of a microcavity DBR surface-emitting laser (II) — effects of electron quantum confinement," *IEEE J. Quantum Electron.*, vol. 28, pp. 1310–1319, 1992.

[53] K. Petermann, "Calculated spontaneous emission factor for double-heterostructure injection lasers with gain-inducing waveguiding," *IEEE J. Quantum Electron.*, vol. 15, pp. 566–570, 1979.

[54] Y. Yamamoto, S. Machida, and G. Björk, "Micro-cavity semiconductor laser with enhanced spontaneous emission," *Phys. Rev. A*, vol. 44, pp. 657–668, 1991.

[55] F. De Martini and G. R. Jacobovitz, "Anomalous spontaneous-stimulated-decay phase transition and zero-threshold laser action in a microscopic cavity," *Phys. Rev. Lett.*, vol. 60, pp. 1711–1714, 1988.

[56] H. Yokoyama *et al.*, "Controlling spontaneous emission and threshold-less laser oscillation with optical microcavities," *Opt. Quantum Electron.*, vol. 24, pp. S245–S272, 1992.

[57] L. Maleki, "Sources: the optoelectronic oscillator," *Nature Photon.*, vol. 5, pp. 728–730, 2011.

[58] W. Loh *et al.*, "Amplifier-free slab-coupled optical waveguide optoelectronic oscillator systems," *Opt. Express*, vol. 20, pp. 19589–19598, 2012.

[59] P. Maffezzoni and D. D'Amore, "Time-domain analysis of phase-noise and jitter in oscillators due to white and colored noise sources," *Int J. Circ Theor. App.*, vol. 40, pp. 999–1018, 2011.

[60] A. Demir and J. Roychowdhury, "On the validity of orthogonally decomposed perturbations in phase noise analysis," Bell Labs, Murray Hill, NJ, Tech. Memo., 1997.

[61] A. Khintchine, "Korrelationstheorie der stazionaren stochastischen Prozesse," *Math. Ann.,* vol. 109, pp. 604–615, 1934.

[62] A. E. Siegman, *Lasers*. University Science Books, 1986.

[63] E. Yablonovitch, "Inhibited spontaneous emission in solid-state physics and electronics," *Phys. Rev. Lett.*, vol. 58, pp. 2059–2062, 1987.

[64] H. T. Friis, "Noise figure of radio receivers," *Proc. IRE*, vol. 32, pp. 419–422, 1944.

[65] H. A. Haus, *Electromagnetic Noise and Quantum Optical Measurements*. Springer, 2000.

[66] M. J. O'Mahony, "Semiconductor laser linewidth broadening due to 1/f carrier noise," *Electron. Lett.*, vol. 19, pp. 1000–1001, 1983.

[67] L. B. Mercer, "1/f frequency noise effects on self-heterodyne linewidth measurements," *J. Lightwave Technol.*, vol. 9, pp. 485–493, 1991.

[68] A. Demir, "Phase noise and timing jitter in oscillators with colored-noise sources," *IEEE Trans. Circuits Syst. I, Fundam. Theory Applicat.*, vol. 49, pp. 1782–1791, 2002.

[69] A. Demir, "Computing timing jitter from phase noise spectra for oscillators and phase-locked loops with white and 1/f noise," *IEEE Trans. Circuits Syst. I, Reg. Papers*, vol. 53, pp. 1869–1884, 2006.

[70] R. Boudot and E. Rubiola, "Phase noise in RF and microwave amplifiers," *IEEE Trans. Ultrason. Ferroelec. Freq. Contr.*, vol. 59, pp. 2613–2624, 2012.

[71] W. Loh, S. Yegnanarayanan, R. J. Ram, P. W. Juodawlkis, "Unified theory of oscillator phase noise II: flicker noise," submitted *IEEE Trans. Microw. Theory Tech.*

[72] P. Langevin, "Sur la théorie de movement Brownien," *C. R. Acad. Sci. Paris*, vol. 146, pp. 530–533, 1908.

[73] H. Nyquist, "Thermal agitation of electric charge in conductors" *Phys. Rev.*, vol. 32, no. 1, pp. 110–113, Jul. 1928.

[74] B. M. Oliver, "Thermal and Quantum Noise" *Proc. IEEE*, vol. 53, no. 5, pp. 436–454, Jul. 1965

[75] S. Kogan, *Electronic Noise and Fluctuations in Solids*. Cambridge University Press, 1996.

[76] D. S. Elliot, R. Roy, and S. J. Smith, "Extracavity laser band-shape and bandwidth modification," *Phys. Rev. A*, vol. 26, pp. 12–18, 1982.

[77] W. Loh, S. Yegnanarayanan, R. J. Ram, and Paul W. Juodawlkis, "Super-homogeneous saturation of microwave-photonic gain in optoelectronic oscillator systems," *IEEE Photon. J.*, vol. 4, pp. 1256–1266, 2012.

[78] C. W. Nelson, A. Hati, and D. A. Howe, "Relative intensity noise suppression for RF photonic links," *IEEE Photon. Technol. Lett.*, vol. 20, pp. 1542–1544, 2008.

[79] P. S. Devgan, V. J. Urick, J. F. Diehl, and K. J. Williams, "Improvement in the phase noise of a 10 GHz optoelectronic oscillator using all-photonic gain," *IEEE J. Lightwave Technol.*, vol. 27, pp. 3189–3193, 2009.

[80] W. Zhou, O. Okusaga, C. Nelson, D. Howe, and G. Carter, "10 GHz dual loop opto-electronic oscillator without RF amplifiers," in *Proc. SPIE*, pp. 68970Z-1–68970Z-6, 2008.

[81] G. E. Obarski and J. D. Splett, "Transfer standard for the spectral density of relative intensity noise of optical fiber sources near 1550 nm," *J. Opt. Soc. Am. B*, vol. 18, pp. 750–761, 2001.

[82] A. David and M. Horowitz, "Low-frequency transmitted intensity noise induced by stimulated Brillouin scattering in optical fibers," *Opt. Express*, vol. 19, pp. 11792–11803, 2011.

[83] W. Zhou and G. Blasche, "Injection-locked dual opto-electronic oscillator with ultra-low phase noise and ultra-low spurious level," *IEEE Trans. Microw. Theory Tech.*, vol. 53, pp. 929–933, 2005.

[84] O. Okusaga, E. J. Adles, E. C. Levy, W. Zhou, G. M. Carter, C. R. Menyuk, and M. Horowitz, "Spurious mode reduction in dual injection-locked optoelectronic oscillators," *Opt. Express*, vol. 19, pp. 5839–5854, 2011.

[85] A. Yariv, H. Blauvelt, and S. Wu, "Reduction of interferometric phase-to-intensity conversion noise in fiber links by large index phase modulation of the optical beam," *J. Lightwave Technol.*, vol. 10, pp. 978–981, 1992.

[86] P. K. Pepeljugoski and K. Y. Lau, "Interferometric noise reduction in fiber-optic links by superposition of high frequency modulation," *J. Lightwave Technol.*, vol. 10, pp. 957–963, 1992.

[87] W. S. Chang, *RF Photonic Technology in Optical Fiber Links*. Cambridge University Press, 2002.

[88] B. H. Kolner and D. W. Dolfi, "Intermodulation distortion and compression in an integrated electrooptic modulator," *Appl. Opt.*, vol. 26, pp. 3676–3680, 1987.

[89] R. Olshansky, "Optimal design of subcarrier multiplexed lightwave systems employing linearized external modulators," *IEEE J. Lightwave Technol.,* vol. 10, pp. 378–382, 1992.

[90] W. Li and J. Yao, "An optically tunable optoelectronic oscillator," *IEEE J. Lightwave Technol.,* vol. 28, pp. 2640–2645, 2010.

[91] A. Hayat, A. Bacou, A. Rissons, and J.-C. Mollier, "2.49 GHz low phase-noise optoelectronic oscillator using 1.55 μm VCSEL for avionics and aerospace applications," in proc. *SPIE*, 2009, pp. 72290O-8.

[92] T. D. Anh and W. Dietel, "Homogeneous broadening in a 0.63 μm single mode He-Ne laser," *Opt. Quantum Electron.,* vol. 5, pp. 243–248, 1973.

[93] G. R. Huggett, "Mode-locking of CW lasers by regenerative RF feedback," *Appl. Phys. Lett.,* vol. 13, pp. 186–187, 1968.

[94] D. Eliyahu and L. Maleki, "Modulation response (S21) of the coupled opto-electronic oscillator," in *Proc. FCS*, 2005.

[95] E. Salik, N. Yu, and L. Maleki, "An ultralow phase noise coupled optoelectronic oscillator," *IEEE Photon. Technol. Lett.*, vol. 19, pp. 444–446, 2007.

[96] S. Ozharar, I. Ozdur, F. Quinlan, P. J. Delfyett, J. J. Plant, and P. W. Juodawlkis, "Ultra stable coupled optoelectronic oscillator based on slab-coupled optical waveguide amplifier," in *Proc. CLEO*, 2008.

[97] J. Maeda, D. Kurotsu, and S. Ebisawa, "Stable pulse generation from regenerative mode-locked fiber ring laser employing semiconductor optical amplifier," in *Proc. OECC*, 2010.

[98] W. Chiming and N. K. Dutta, "High-repetition-rate optical pulse generation using a rational harmonic mode-locked fiber laser," *IEEE J. Quantum Electron.*, vol. 36, pp. 145–150, 2000.

[99] L. Duan, C. J. K. Richardson, H. Zhaoyang, M. Dagenais, and J. Goldhar, "A stable smoothly wavelength-tunable picosecond pulse generator," *IEEE Photon. Technol. Lett.*, vol. 14, pp. 840–842, 2002.

[100] G. P. Agrawal and N. A. Olsson, "Self-phase modulation and spectral broadening of optical pulses in semiconductor laser amplifiers," *IEEE J. Quantum Electron.*, vol. 25, pp. 2297–2306, 1989.

[101] F. R. Ahmad, Y. W. Tseng, M. A. Kats, and F. Rana, "Energy limits imposed by two-photon absorption for pulse amplification in high-power semiconductor optical amplifiers," *Opt. Lett.*, vol. 33, pp. 1041–1043, 2008.

[102] J. Taylor, S. Datta, A. Hati, C. Nelson, F. Quinlan, A. Joshi, and S. Diddams, "Characterization of power-to-phase conversion in high-speed P-I-N photodiodes," *IEEE Photon. J.*, vol. 3, pp. 140–151, 2011.

[103] N. Yu, E. Salik, and L. Maleki, "Ultralow-noise mode-locked laser with coupled optoelectronic oscillator configuration," *Opt. Lett.*, vol. 30, pp. 1231–1233, 2005.

[104] D. R. Hjelme and A. R. Mickelson, "Theory of timing jitter in actively mode-locked lasers," *IEEE J. Quantum Electron.*, vol. 28, pp. 1594–1606, 1992.

[105] F. Quinlan, S. Ozharar, S. Gee, and P. J. Delfyett, "Harmonically mode-locked semiconductor-based lasers as high repetition rate ultralow noise pulse train and optical frequency comb sources," *J. Opt. A: Pure Appl. Opt.*, vol. 11, pp. 103001–103023, 2009.

[106] W. Loh *et al.*, "Low-noise RF-amplifier-free slab-coupled optical waveguide coupled optoelectronic oscillators: physics and operation," *Opt. Express*, vol. 20, pp. 19420–19430, 2012.

[107] R. Schatz, "Dynamics of spatial hole burning effects in DFB lasers," *IEEE J. Quantum Electron.*, vol. 31, pp. 1981-1993, 1995.

[108] G. Morthier, K. David, P. Vankwikelberge, and R. Baets, "A new DFB-laser diode with reduced spatial hole burning," *IEEE Photon. Technol. Lett.*, vol. 2, pp. 388-390, 1990.

[109] J. Carroll, J. Whiteaway, and D. Plumb, *Distributed Feedback Semiconductor Lasers*. The Institution of Electrical Engineers, 1998.

[110] T. Koui, Y. Sakata, Y. Sasaki, T. Matsumoto, and K. Komatsu, "Mass-transport effect on InP corrugation shape control of DFB-LDs under atmospheric pressure MOVPE," *J. Cryst. Growth*, vol. 195, pp. 503-509, 1998.

[111] W. Loh, S. Yegnanarayanan, R. J. Ram, and P. W. Juodawlkis, "Nonlinear narrowband filtering of signals using microwave-photonic links," in preparation.

[112] D. A. Howe, "Low-noise x-band oscillator and amplifier technologies: comparison and status," in *Proc. FCS*, 2005.